1995

Mathematical modelling of the heat treatment in the continuous processing of steel strip

David Marlow
University of Wollongong

Mathematical Modelling of the Heat Treatment in the Continuous Processing of Steel Strip

A thesis submitted in fulfilment of the
requirements for the award of the degree

DOCTOR OF PHILOSOPHY

from

UNIVERSITY OF WOLLONGONG

by

DAVID MARLOW, B.Sc.(Ma.)(Hons.)

Department of Mathematics

1995

Declaration

This thesis is submitted to the University of Wollongong, and has not been submitted for a higher degree at any other University or Institution.

David Marlow

September 1995.

Abstract

This thesis develops the solution of new time-dependent mathematical models for the operation of furnaces involved in the heat treatment and annealing of steel strip. In a practical context, it is necessary to know the variation of the strip temperature throughout each furnace, and most importantly, the strip temperature at the exit of the furnace. Also of practical relevance is the change in temperature (if any) across the width of the strip in the direct-fired furnace, particularly at the edges. Any significant differences between the actual temperature of the steel strip and the desired temperature can have adverse effects on the metallurgical qualities of the steel, and result in a final product that does not meet specified requirements.

In each case, the models developed suit the type and geometry of the particular furnace involved. For example, the models for the direct-fired furnace are designed to be run off-line, and the radiant tube furnace model is designed to run in an on-line capacity, so greater liberty is taken with some of the assumptions used. Mathematical equations are developed, or modified and improved, to model the heat transfer between the steel strip, the combusted gas mixture and the highly insulated furnace walls. Methods of solution are derived which are appropriate to each furnace situation, and numerical techniques are used in the solution process due to the non-linear form of the equations that are solved. Results show that the off-line direct-fired furnace model works well, although further testing against data is also required. The present work extends the existing steady-state model in order to examine the occurrence of transients in the furnace. The on-line radiant

tube furnace model uses a different approach to previous models of radiant tube-type furnaces. The present model is extremely rapid and, considering the assumptions that are made, gives very good results when tested against actual data from the furnace. Finally, the new work on the analysis of the temperature variation across the width of the strip in the direct-fired furnace provides some interesting results. In particular, the edges are always hotter than the rest of the strip during steady-state conditions, and the turn-around roll at the base of the furnace has a large influence on the transverse profile, especially when the strip width changes.

The practical aim of the thesis is to install devices that are able to accurately model the strip temperature variation during the heating process, in order to ensure that all of the steel that passes through the furnace is treated to specified requirements and is therefore not wasted due to incorrect treatment. All of the work included in this thesis applies existing mathematical techniques to real industrial problems. The work undertaken here will reduce the amount of improperly treated steel produced, and save costs resulting from this wastage.

Acknowledgements

Firstly, I would like to thank my supervisors, Associate Professor Jim Hill and Dr Bruce Morrison, for their contributions throughout the course of this project. Professor Hill, as my academic supervisor, was able to impart some enthusiasm for mathematics to me as well as encouraging me to work hard on my project. Dr Morrison, as my industrial supervisor, was very helpful to me throughout my thesis from the time he took over my industrial supervision, and was extremely patient with me when discussing areas which took me some time to fully comprehend. I am especially grateful for his assistance throughout the work on the radiant tube furnace model, especially in the early stages of its construction.

Many thanks are also given to BHP for their financial support and the provision of data, without which this thesis would not have been possible. Support from the National Teaching Company Scheme and the University of Wollongong at various stages of this project is also gratefully acknowledged.

Thanks must also go to many others who have contributed in some way during the thesis. To name several, Noel Thompson and Bruce Martire for their help in introducing me to the project; Keith Enever for his initial supervision and helpful advice, including during the last stages of this work; Peter Stone for his contribution in the initial stages of the radiant tube furnace work, as well as for the provision of data to test the models; John Noye for his useful suggestions on finite-difference methods; Tim Marchant and Cat Tu for their general assistance; Daniel Yuen for his help with the edge-drop effect; Warwick Grace for his proofreading assistance; Chris Coleman for reading

through the thesis; and Phil Broadbridge for his general contribution in the final stages.

A big thank you to my family and friends, too numerous to mention, who have supported me in every good way throughout the course of my project through their love, friendship and prayers.

Most of all, thanks to the Lord of all, Jesus Christ, who has been with me from start to finish, through the many highs and lows of these past years, and from whom I have learned so much and in whom I have matured so much. He is the one who has given me the ability to undertake these studies in the first place, and I am thankful.

This project is dedicated to all of those who have helped to make it possible.

Contents

List of Figures

List of Tables

Chapter 1

Introduction

This thesis describes the development, implementation, solution method and results of mathematical models for furnaces involved in the heat treatment and annealing of steel strip, operated and run by BHP Steel Sheet & Coil Products Division (SCPD). Three furnaces are modelled, these being:

- **CGL2 DFF** - the direct-fired furnace located on the No.2 continuous galvanising line at BHP SCPD's works at Port Kembla, NSW;
- **MCL6 RTF** - the radiant tube furnace found on the No.6 metal coating line — BHP SCPD's newest and most modern galvanising line — at Westernport in Victoria, and
- **MCL6 DFF** - the direct-fired furnace, distinct from the one on CGL2, which is also part of MCL6.

Two types of furnace are examined — the direct-fired furnace, where steel strip is cleaned of impurities and heated from room temperature to several hundred degrees C; and the radiant tube furnace, which immediately follows the direct-fired furnace in its position on MCL6 and which heats the steel further or maintains it at its current temperature. Results of each model are displayed,

and these are compared with measured data from the galvanising lines where this information is available.

Annealing of steel is a process by which the steel is heat treated, in order that the metallurgical properties of the steel attain a desired level. The heating of the steel during the annealing process is also designed to burn off any surface contaminants that the steel strip contracted in the preceding stages of its development from a thick steel slab, such as during the rolling process.

The continuous annealing process for steel strip is a relatively recent development. The main advantage that continuous annealing has over batch annealing is the uniformity of the heat treatment. A secondary advantage is the speed at which the steel is heated. In a continuous annealing furnace, the strip can be annealed in a matter of seconds — in a batch annealing furnace, a coil of steel 'sits' in a heating furnace in which the heating process can take hours or even days. Controlled rapid heating and cooling gives precise control over various aspects of metallurgical quality. These advantages justify the extra cost of continuous annnealing. BHP incorporates the continuous annealing process on all six of its galvanising lines in Australia. When the galvanising (or more generally, coating) of the strip is desired, the galvanising process immediately follows the annealing process.

The continuous annealing of thin steel strip is possible using both direct-fired methods (where the gas is combusted directly into the furnace) and indirect-fired methods (such as the radiant-tube furnace, where the gas is combusted within tubes and the heat generated is radiated into the furnace). On MCL6, these methods are used in tandem, but other companies may use only radiant tube heating in their annealing process. The direct-fired furnaces modelled in this thesis were developed by the Selas corporation of America [14]. When released in the early 1950's, Selas' vertical direct-fired annealing

furnace represented a breakthrough in continuous annealing technology.

The literature contains papers on a wide range of topics in annealing furnaces and furnace modelling. These topics include studies on furnace efficiency and furnace design, as well as the influence of various factors on furnace performance. There are also some mathematical models for both sample furnaces and real-life furnaces, ranging from steady-state models to on-line control models.

A review of continuous annealing technology by Mould [30] compares continuous annealing to batch annealing, especially the differences in the metallurgical properties that result, and the implications of continuous annealing to the steel industry are considered. Another review by Imose [18] includes specific in-depth sections on both radiant tube furnaces and direct-fired Selas-type furnaces.

Articles on the Selas furnace describe its introduction as a revolutionary method of continuous annealing in the early 1950's to its present day applications and new development. These include an overview of the Selas furnace, [14], with a good description of its history, purpose and operation. Another descriptive article by Ottersbach [34], looks specifically at the construction of BHP Steel SCPD's recently completed No. 6 MCL (metal coating line) at Westernport, and includes a brief section on the Selas furnace. Wang [60] looks briefly at the effect that a direct-fired furnace has on steel strip that is passed through it, and suggests that a vertical Selas-type furnace achieves an efficiency of up to 70%. Other papers focussed on the use of Selas furnaces on the annealing and galvanising lines of NKK in Japan. A synopsis of a recently installed annealing line by Kanetoh *et al.* [21] includes a small section describing a direct-fired furnace, with an additional short description of an on-line control model of the heat transfer. Nakayama *et al.* [32] summarise the application of Selas technology to NKK's continuous annealing and galvanising

lines and its advantages over other furnace heat treatment methods, as well as some advances that NKK has made in developing the process further to suit their own requirements. Sekiguchi *et al.* [45] also detail an NKK galvanising line which includes a Selas-type direct-fired furnace.

Several articles on radiant tubes were found in the literature, from models of the tubes only, to control models of furnaces containing such tubes, and also general overviews of tube operation. A good overview of gas-fired radiant tubes is found in Harder *et al.* [13], including analyses of different types of tubes, such as the U-type and W-type which are both mentioned briefly. Mathematical models for the simpler tube designs are also included, such as for the straight-through type, where the gas and air enter at one end, are combusted in the tube and exhausted at the other end. The thermal efficiency was found to increase with an increase in the diameter or length of the straight-through tube design. Another paper by Goman & Krivosheev [10] examines the optimal arrangement of radiant tubes in a furnace for uniform heating of the furnace load. It is found that the the distance between the tubes should be less than twice the distance from the centre of the tubes to the load for favourable uniform heating. A further paper by Ramamurthy *et al.* [42] contains a detailed mathematical model of radiant tubes and a load in a one-pass continuous reheating furnace, in which heat transfer is modelled between the tubes, the wall, the load and the gas present in the furnace. Parametric investigations of such relationships as load emissivity to load temperature give generally expected results. A similar analysis of a radiant-tube heated batch furnace is undertaken by the same authors [41]. Two further papers, Somers *et al.* [48] and Somers & Pallone [47], use a steady-state model to predict strip temperature in a 10-pass radiant tube annealing furnace. The first paper [48] develops the model, and the follow-up paper [47] verifies it by testing it on a continuous annealing line furnace, finding that the model displays excellent

agreement with measured strip temperatures for a real furnace. Measured gas and tube temperatures are used as input to the model to test its accuracy. Finally, Mizikar & Upton [29] describe an off-line time-dependent model for the heat transfer in a one-pass radiant tube furnace as part of a model for a complete Hennepin galvanising line, also with good results.

Papers by Yoshitani [63], Yahiro *et al.* [62] and Taya *et al.* [52], all detail on-line control models for annealing lines at Japanese steel works. An article by Paulus *et al.* [37] describes the application of a computerised technique to some annealing lines heated by radiant tubes, including explanations of procedures in the entry and exit sections, and the process section (including the heating furnace). The section on the heating furnace includes details on how to implement section and cycle changes, both of which are explained later.

Other papers, such as Docherty & Tucker [9] examined the influence of the wall emissivity on the efficiency of a furnace, using mathematical models of a continuous reheating furnace and a single zone batch reheating furnace. They found that the efficiency does increase with increasing emissivity, but this influence is negated under transient conditions and for low values of wall thermal conductivity, and is nullified if the furnace gas is grey. Jamaluddin & Fiveland [20] looked at the influence of a specular component of reflection for radiant heat transfer to a wall, finding that a higher component of specular reflection increases the heat flux from the wall in the examples of two and three-dimensional furnaces analysed. In a study on the interaction of radiation with turbulence in combustion systems, Song & Viskanta [49] examined any effect that this interaction may have in different combustion furnaces by using a parametric study. The effect of any interaction can be significant, but reduces to negligible levels when the flame occupies a small volume proportion of the furnace. Pikashov & Velikodnyy [39] examined the effect that the emissivity of a surface can have on the effective radiation in several kinds of furnaces. For

a direct-fired type furnace, the effective radiation depends on the relationship between the heat conducted through the wall and the convective heat flux to the wall — if the conductive flux is the lower of the two, the radiation is found to increase.

Most of the papers found in the literature review look at mathematical models of a furnace. Most make use of Hottel's zone method from Hottel & Sarofim [17] to model the radiation in the furnaces. Of these models, a paper by Chapman *et al.* [7], was found to be the most similar to this furnace model. A direct-fired continuous furnace with flames providing heat to the load was modelled. A parametric study examined the relationship between such parameters as the load heat flux and temperatures of the gas and the load. Another model of a direct-fired batch-reheating furnace by the same authors [6] uses a virtually identical procedure and conducts further investigations on the dependence of various furnace parameters on each other. A paper by van Dongen [58] describes a heat transfer model for a gas-fired flame furnace, also examining the effect that parameters such as the air-to-fuel ratio and furnace dimensions have on the heat flux distribution in the furnace.

The emphasis of a paper by Tucker & Lorton [57] is to predict the thermal efficiency of a furnace and also to assist in furnace design. Both steady-state and transient models are constructed for a high temperature load-recuperative furnace with favourable results. Song & Viskanta [50] also look at predicting thermal performance of a gas-fired furnace by conducting parametric investigations on a sample two-dimensional gas-fired furnace. Khalil & Truelove [23] use conservation equations to develop models of heat transfer in a furnace. The results shown compare reasonably well with experimental values and other models. Using virtually the same basic equations, Khalil *et al.* [22] tested the model on real gas-fired furnaces using previously published experimental results, again finding good agreement, with average discrepancies

in the model around 10% in the maximum values.

This is an industrial mathematics thesis. The main object of the project was to find real solutions to industrial problems that BHP Steel encounter on the annealing furnace sections of their galvanising lines. These problems involve the transfer of heat in a high temperature environment. As a result, radiation is the dominant mode of heat transfer within these furnaces. Because the heat flux from radiation varies with the fourth power of temperature, the equations that need to be solved are non-linear in form. This, combined with the required boundary conditions for the furnace, makes the search for analytical solutions very difficult. Because of the type of equations encountered, numerical methods are used almost exclusively; analytical solutions are included only to indicate some kind of trend or phenomenon in the furnace within a certain region.

Related to the above, the major aim of the project was to develop realistic and efficient models that could be used by the sponsor — ie, BHP. The company will have access to all of the results, with the computer program constructed for the radiant tube furnace model undergoing implementation on MCL6 at the time of writing. The outcome of the work on the strip edges is also certain to be of major significance to BHP in their annealing operations.

The thesis can be divided into three distinct parts. The first part concentrates on the development, implementation and results of the model for the direct-fired furnace (DFF) on CGL2. This includes a study of the effect of the heat flux from the wall on the furnace operation, using an integral method to show that the adiabatic wall assumption used in the steady-state model [55] is inadequate for the transient model. The method of solution is outlined, including a study of the reasons for the eventual choice of the finite-difference method used. Then, the results are shown. First, the transient equations are solved for an adiabatic wall, in order to show that the model can successfully

progress through a transient stage from one steady-state to another, using data obtained from the steady-state program. Finally, the model is extended to the case of the dynamic wall, and solutions using input data from the steady-state model are compared with measured data obtained by hand from CGL2 for various transients. The results show that the transient model is adequate for predicting the variation of the strip temperature for either cycle changes or section changes.

The second part (chapter 3) describes the on-line control model for the radiant tube furnace (RTF) on MCL6. Here, the model emphasis is on speed of execution rather than accuracy, and as a result a simple model is constructed for the five-pass RTF which can run on a SUN sparc 10 workstation in around 10-20 seconds for a data set of a duration up to four hours. A filtering technique is also used to improve the overall accuracy of the model. Results are compared with real-time data obtained from MCL6. The comparison reveals that the model works well for the purposes for which it was designed.

The final part includes the adaptation of the DFF model for CGL2 to the DFF on MCL6, as well as an examination of the temperature variation across the strip width. The original DFF model from CGL2 is extended to run over the same long-duration data sets as for the RTF model on the DFF at MCL6, using a core model that is almost identical to the one used from CGL2. For this model, such parameters as the strip emissivity are changed according to the values given in [51]. In this case the model follows the trends of the data well, but suffers from a large underprediction in temperature which will need to be corrected if the model is to be utilised in an off-line capacity. This adaptation also acts as a prelude to the analysis of the temperature variation of the strip across its width. The DFF model is now extended to two dimensions across the strip surface. It is found that in steady-state operations the edge temperature is substantially hotter than the centreline temperature. During

transients, the temperature difference is sometimes even more pronounced. The increase at the edge is found to be caused by the extra surface area at the edge absorbing heat, and this is enhanced if the steel strip suffers from edge-drop, where the strip thickness is less near the edge than at the centre — a phenomenon that occurs during the process of reducing the strip to its final thickness. The rolls in the furnace have a significant effect during transients especially, when an increase in the width of the strip leads to a covering of and interaction with a part of the roll that was at a different temperature. A hotter roll temperature causes a rise not just at the edges but also over the extra width of strip now in the furnace. A cooler roll temperature causes a double peak in the strip temperature for a short period of time — one at the new strip edge, and one over the position where the strip edge was previously. All of these factors can have significant effects on the quality of the steel where these phenomena occur.

The work contained in this thesis applies existing mathematical techniques to real industrial problems in steel processing. The direct-fired furnace modelled in this thesis has not been studied before according to the literature, and the radiant-tube furnace model uses a different approach to other models; both models are tested for validity against real data from the lines. The study of the hotter strip edges in a direct-fired furnace is new work which is very important for the steel processing industry. The aim of all of these models is to increase the performance of BHP's galvanising lines and to assist in achieving the minimum amount of non-prime first-time (NPFT) steel produced; that is, steel that is not properly treated to customer's requirements. It is believed that the aim has been substantially achieved and that the work will provide the basis for both off-line model testing for the direct-fired furnace model, and real-time process control for the radiant tube furnace model. The study of the edge effects has also provided valuable insight into the causes of

the temperature variation across the strip width, as well as the extent of this variation. The models will assist BHP in saving the cost of lost prime product on their galvanising lines.

Chapter 2

Modelling of the direct-fired furnace (DFF)

2.1 Introduction

The Selas direct gas-fired furnace is an integral part of the galvanising lines of BHP Steel Sheet & Coil Products Division (SCPD) at Port Kembla, NSW and Westernport, Victoria. Steel strip is passed through the furnace in order to clean the surface of any oils or other impurities, as well as to heat the strip to a desired temperature in preparation for coating with either GALVABOND© (a zinc coating), ZINCALUME© (a coating $\approx$ 55% aluminium and 45% zinc) or terne (a lead/tin mixture). The aim of this section is to model the furnace in order to make predictions of how different types of strip are affected when passing through the furnace, and to assist the operators in determining what values the furnace parameters should take for various cycles and strip dimensions. More specifically, the interest is in a transient state when a major change in the heat treatment of the product strip (called a cycle change) or the width and/or thickness of the product strip (called a section change) is introduced to the system, to analyse what must be done to minimise wastage

from incorrect parameter settings in the furnace.

The Selas furnace is so named after the company that developed it in the early 1950's. Furnaces made by Selas have been installed around the world, and BHP has one on each of its six operating galvanising lines — three at Port Kembla and three at Westernport, the most recent of which (No. 6 Metal Coating Line, or MCL6) came on line in August of 1992. A diagram of MCL6 is displayed in Figure 2.1.

The Selas researchers wanted to find a process that would heat treat and clean the strip at the same time. What was constructed, as described in [14], was a vertical furnace in which steel strip enters continuously from the top and passes through the furnace, burning a natural gas/air mixture with a composition that prevents oxidation (blueing) of the steel surface. The gas burners are separated into several zones of unequal length, and the burners are arranged axisymmetrically to ensure that the strip is heated uniformly over its surface. The steel strip is both cleaned of surface contaminants (rolling oils) as well as heat treated by the process, and so the steel exits the Selas furnace with a shiny, reflective appearance due to the cleaning, and also at the required temperature. During line operation, the bottom zone of the furnace has the gas continually on. The higher zones are only switched on during the annealing of soft-iron product or when there is a greater load in the furnace.

In this section, the aim is to derive a mathematical model for the operation of a Selas furnace. The furnace that is modelled is located on SCPD's CGL2 (No.2 continuous galvanising line) at its Springhill works at Port Kembla. The furnace is about 12.7 m high, 2 m wide and 0.5 m thick, and steel strip passes through at a maximum speed of about 85 metres per minute. A simple diagram of a Selas-type furnace is shown in Figure 2.2 [54].

Deriving a mathematical model for the process would contribute to the furnace being run more smoothly and accurately. Currently, the re-

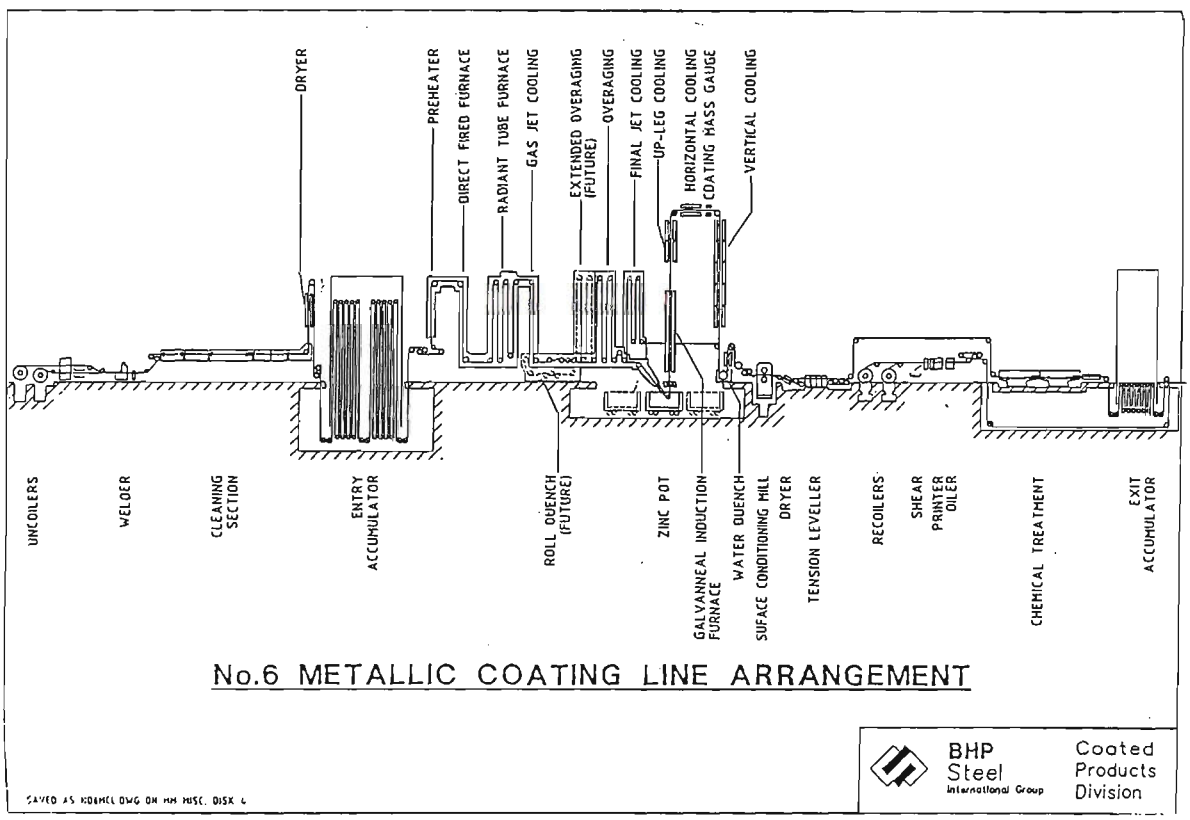

Figure 2.1: Diagram of MCL6 at Westernport

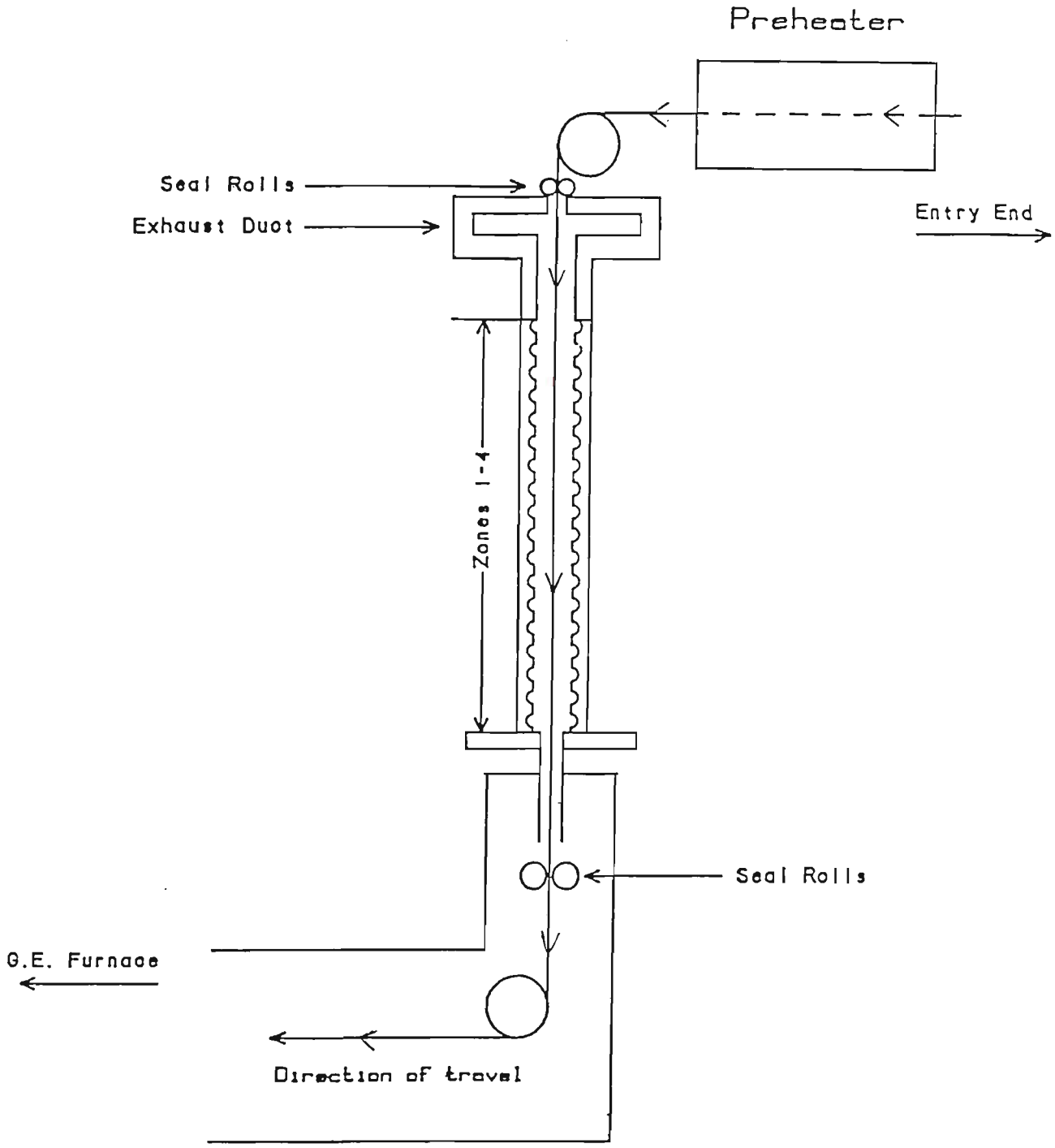

Figure 2.2: Simple diagram of a typical Selas furnace

sponsibility falls on the operators regarding changes to the furnace parameters — line speed and/or gas flow rate — hence the possibility of error is large, especially for such things as:

- **cycle changes** : this is where the parameters are set so that the furnace conditions change from running for a hard iron cycle to a soft iron cycle (or vice versa). A hard iron cycle is that for which the steel is heated below its recrystallisation temperature ($\approx 530°C$) to retain its hardness (ie, it is recovery heat treated), whereas in a soft iron cycle the steel does recrystallise (ie, its internal properties change) and becomes more ductile (ie, it is fully annealed).

- **section changes** : this is where the thickness and/or width of the strip is altered to satisfy the needs of the customer for whom the steel is made. Section changes alter the loading in the furnace.

Line operators use a table of operating conditions to estimate not only the new parameter settings for a cycle change or section change, but *when* to change the parameters. If the values are not set correctly, the steel is not successfully heat treated and must be downgraded or scrapped. New material must be produced to satisfy the original customer, so time and money are wasted. This is known as "non-prime first time" (NPFT) or "non-prime to schedule" steel and causes BHP large losses. The aim of the mathematical model is to relieve the responsibility from the operators and to indicate to them when to change the furnace parameters and by how much, depending on the conditions at the time. It would remove much of the guesswork involved and would give accurate information about the optimal operation of the furnace in order to minimise wastage and NPFT product.

Much of the background work for this section was done by Thompson & Martire, [54] & [55], Martire, [28], and by the participants at the 1990

CSIRO Mathematics-in-Industry Study Group, [1]. That work involved the first detailed study of the furnace and its operation, followed by the development of a steady-state mathematical model with its computer program and implementation, to the first construction of a transient model for the process. The steady-state model for the operation of CGL2 is currently set up on the line, but is not in use and has not been tuned. It was also the base for this work in the assumptions used, in the equations used and in the outline of the program. The assumptions for the steady-state model were derived from the work on the qualitative study of the Selas furnace (Thompson & Martire, [54]). The assumptions are described in Thompson & Martire [55], some of which are

- there is negligible heat conduction in the strip in the longitudinal direction, and the strip is a uniform temperature through its thickness (ie, infinite conduction there),
- the furnace walls are adiabatic,
- the gas flow is turbulent at all times, and
- all radiative heat transfer is assumed to take place in the plane perpendicular to the direction of strip flow.

All of these simplify the steady-state model down to one variable, that being the furnace height x. The transient model described here makes use of these assumptions (except for the adiabatic wall, although this is included initially), and also studies the variation of the parameters with time.

The steady-state model is designed to indicate the necessary line speed, gas flows, strip width and thickness for one whole coil being passed through the line. It is not concerned with the changes from one steady-state to another when a different coil comes in, as this is the task of the transient

model. The steady-state model is run once for one particular coil only; for the output of any other coil of different dimension and hardness, the program is run separately.

The equations used to solve the steady-state model are as follows:

$$\frac{dT_s}{dx} = \frac{Q_{gs}}{-\dot{m}_s c_{ps}}, \tag{2.1}$$

$$\frac{dT_g}{dx} = \frac{\dot{M}(h_{ad} - h_g) - Q_{gs}}{\dot{m}_g c_{pg}}, \tag{2.2}$$

$$B_{gw} - B_w + q_{w,c} = 0, \tag{2.3}$$

with $\dot{m}_s, \dot{m}_g > 0$, where

$$\dot{M} = d\dot{m}_g/dx, \tag{2.4}$$

$$Q_{gs} = P_s(B_{gs} - B_s + q_{s,c}). \tag{2.5}$$

Therefore, the strip receives heat from the gas, and the gas loses heat to the strip and receives heat from combustion. Appendix A contains a description of the major variables used in this thesis. The radiosities B are functions of T_s, T_g and T_w, and the convective flux terms $q_{s,c}$ and $q_{w,c}$ are functions of T_s and T_g, and T_w and T_g respectively.

This system represents three equations in three unknowns — the strip temperature, gas temperature and wall temperature. There are two differential equations (those for the strip and the gas temperatures, equations (2.1) and (2.2)), and one polynomial equation (to calculate the wall temperature, equation (2.3)).

The steady-state model uses a shooting method to find the solution to the problem. The desired strip temperature at the furnace base is known, and the gas temperature at the base of the furnace is guessed using the boundary condition that $\dot{m}_g(0) = 0$; ie, there is no gas flow at the base of the furnace. This is not strictly correct, as there is some gas that leaks in from an adjoining furnace. However, this boundary condition does give reasonable

results. The consequence of this is that the numerator of the right-hand side of equation (2.2) is equal to zero also, and so the boundary condition becomes

$$\dot{M}(h_{ad} - h_g) - Q_{gs} = 0 \tag{2.6}$$

at $x = 0$. Coupling this equation with the adiabatic wall equation (2.3) gives the gas and wall temperatures for the furnace boot. The temperatures for the rest of the furnace are then calculated for the initially chosen values of the line speed and gas flow rates. If these values converge to within a few degrees of the desired strip temperature at the top of the furnace (eg, 20°C), then the solution has been found and the program stops. If convergence has not been achieved, then one of either the line speed or the gas flow rate is fixed, and the other varied, until the values of both result in convergence of the steady-state program to the specified strip temperature at the top of the furnace. A maximum number of iterations is given within which to work, and if the values do not converge within this time then an error message is given. The transient model is an extension of the steady-state model in most respects, except that the adiabatic wall condition is dropped for the more realistic case of a dynamically acting wall.

The model is now likely to be used as an off-line model, with its usefulness being in its accuracy in predicting the variance of the boot strip temperature (ie, the temperature of the strip at the bottom of the Selas furnace) for transient operation of the furnace. It is able to predict accurately how the boot strip temperature should vary for any type of cycle or section change that may occur, and can be used to compare these results with those from other models (for example, Stone & Morrison [51]). The main function of the off-line model is to provide accuracy, but it is much slower than on-line models. However, for a sample 10-minute simulation of a transient in the furnace, the program for the CGL2 DFF described here takes around 3-6 minutes to run on a SUN workstation, depending on some parameters such as the gas

flow rates. This length of execution is sufficient for an off-line model.

2.2 Analytical study of the heat flux from the wall

An analytical study of the influence of the wall heat flux is undertaken to establish whether the adiabatic wall assumption used for the steady-state model is adequate for the transient model. It is shown, by calculating some time constants in the furnace, that the heat flux from the wall is considerable and that its effect must be included in the basic transient model equations to model the system accurately.

The transient model equations are

$$\frac{\partial T_s}{\partial t} - V_s \frac{\partial T_s}{\partial x} = \frac{Q_{gs}}{\rho_s w_s d_s c_{ps}} \tag{2.7}$$

$$\frac{\partial T_g}{\partial t} + V_g \frac{\partial T_g}{\partial x} = \frac{\dot{M}(h_{ad} - h_g) - Q_{gs} - Q_{gw}}{\rho_g (w_f d_f - w_s d_s) c_{pg}} \tag{2.8}$$

where

$$V_g = \dot{m}_g / (\rho_g (w_f d_f - w_s d_s)) \tag{2.9}$$

$$V_s = \dot{m}_s / (\rho_s w_s d_s), \tag{2.10}$$

$$Q_{gw} = P_w (B_{gw} - B_w + q_{w,c}), \tag{2.11}$$

where Q_{gw} is the heat flow rate per metre from the gas to the wall via radiation (the B terms) and convection (the q terms). The similarities between the transient equations (2.7) and (2.8) and the steady-state equations (2.1) and (2.2) are obvious. The steady-state model does not include a term involving the wall heat flux, because it is assumed that the wall is adiabatic under normal operating conditions. The aim of this section is to show that the Q_{gw} term is relevant and is needed in the transient equations.

Consider a cycle change in the Selas furnace from a soft iron cycle (where the steel is recrystallised and heated to around 650°C) to a hard iron cycle (where the steel is heated to around 500°C and retains its original crystal structure). For the purpose of this exercise, "into the wall" is considered as the z direction, with $z = 0$ as the wall/furnace interface. Hence the heat conduction equation is

$$\kappa \frac{\partial^2 T}{\partial z^2} = \frac{\partial T}{\partial t} \tag{2.12}$$

where T is the wall temperature and κ is the thermal diffusivity. The boundary condition at $z = 0$ is

$$-k \frac{\partial T}{\partial z} = q(t) \tag{2.13}$$

where k is the thermal conductivity and $q(< 0)$ is the flux from the wall. Because the greatest temperature difference occurs between the interior and exterior of the wall, the comparatively small heat flow in the plane of the wall is ignored.

This problem is similar to the Stefan problem in that, as the wall cools, the initial wall temperature $T = T_\infty$ at the start of the hard-iron cycle ($t = 0$) begins falling at the surface, but does not cool as quickly at the interior of the wall due to its low thermal diffusivity. For simplicity, there is assumed to be a "moving boundary" of thickness $\delta(t)$, called the *penetration distance*, with

$$T(\delta(t), t) = T_\infty, \tag{2.14}$$

and

$$\frac{\partial T}{\partial z}(\delta(t), t) = 0; \tag{2.15}$$

ie, there is negligible heat flow past the point $z = \delta(t)$, and

$$T(z, t) = T_\infty, \tag{2.16}$$

for $z > \delta(t)$. The above conditions are similar to those used in the Stefan problem, except in this case, there is no latent heat condition. A simple

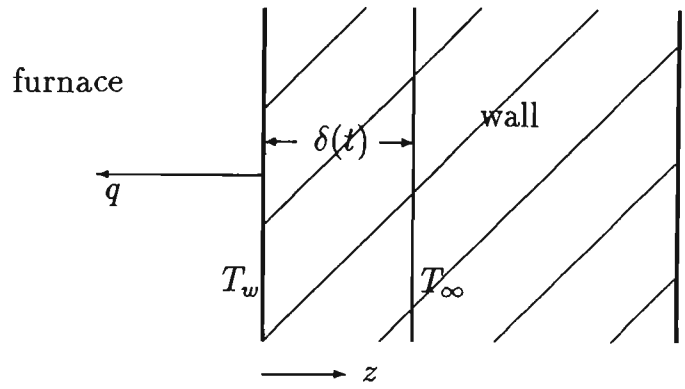

Figure 2.3: Diagram of analytical wall model

diagram of the wall model is shown in Figure 2.3, where the isotherm for T_∞ is not necessarily straight.

An integral method is now employed to assist in getting an analytical solution to the problem. Applications of this technique to find approximate solutions to the heat conduction equation can be found in Goodman [11] and Özişik [36] among others. If the heat conduction equation is integrated over the penetration distance, then

$$\begin{aligned} \frac{d}{dt}(\theta - T_\infty \delta) &= \kappa\left(\frac{\partial T}{\partial z}(\delta, t) - \frac{\partial T}{\partial z}(0, t)\right) \\ &= -\kappa \frac{\partial T}{\partial z}(0, t) \text{ since } \frac{\partial T}{\partial z}(\delta, t) = 0 \end{aligned} \tag{2.17}$$

$$\text{with } \theta = \int_0^{\delta(t)} T \, dz. \tag{2.18}$$

It is now assumed that T takes the form of a cubic polynomial in this region, ie $T = \beta_0 + \beta_1 z + \beta_2 z^2 + \beta_3 z^3$. By applying the conditions given and a curvature condition,

$$\frac{\partial^2 T}{\partial z^2}(\delta, t) = 0, \tag{2.19}$$

T becomes

$$T(z, t) = T_\infty + \frac{q(t)}{3k\delta^2}(\delta - z)^3. \tag{2.20}$$

Substituting this into (2.18) gives

$$\theta = T_\infty \delta + \frac{q(t)}{12k}\delta^2, \tag{2.21}$$

and so

$$\begin{aligned} \frac{d}{dt}(\theta - T_\infty \delta) = \frac{d}{dt}\left(\frac{1}{12k} q\delta^2\right) &= \frac{\kappa q}{k} \\ \Rightarrow \frac{d}{dt}(q\delta^2) &= 12\kappa q \end{aligned} \tag{2.22}$$

where both q and δ are dependent on the time t.

The wall flux $q(t)$ is taken to be a simple expression,

$$q(t) = -\varepsilon_W \sigma T(0,t)^4,$$

where σ is the Stefan-Boltzmann constant and ε_W is the effective wall emissivity. This is different from the wall emissivity ε_w, in that the effective wall emissivity takes account of multiple reflections. Hence the effective wall emissivity, denoted as ε_W, takes the form

$$\varepsilon_W = \frac{\varepsilon_w \varepsilon_s}{1 - \rho_w \rho_s} = \frac{\varepsilon_w \varepsilon_s}{1 - (1 - \varepsilon_w)(1 - \varepsilon_s)} \tag{2.23}$$

where $\varepsilon_w = 0.8$ and the ρ terms are reflectivities here. The shape factor, which governs the geometrical influence on how much radiation is transmitted from one surface to another, is therefore implicitly set equal to one (infinite parallel plate approximation).

By using this expression for q, the gas in the furnace is being ignored, since there is no convection term in q, nor any inclusion of the gas temperature. Hence the model is simply of a wall by itself, with the presence of the strip only indicated by the usage of the strip emissivity in the wall heat flux term.

The initial condition (IC) for the wall heat flux is $q(0) = -\varepsilon_W \sigma T_\infty^4$. The other initial conditions are $\delta(0) = 0$ and $T(z,0) = T_\infty$. It is known that $T(0,t) = T_w(t)$ where T_w is the wall temperature, and so, from (2.20), at $z = 0$,

$$\begin{aligned} T_w &= T_\infty + \frac{q(t)}{3k\delta^2}\delta^3 \\ \Rightarrow q(t) &= \frac{3k(T_w - T_\infty)}{\delta(t)} \end{aligned} \tag{2.24}$$

This leaves three equations in three unknowns, ie

$$q = -\varepsilon_W \sigma T_w^4 \tag{2.25}$$

$$q = 3k(T_w - T_\infty)/\delta \tag{2.26}$$

$$d(q\delta^2)/dt = 12\kappa q \tag{2.27}$$

where the unknowns are the wall heat flux q, the penetration distance δ, and the wall temperature T_w; all functions of time t.

By various substitutions, an expression can be obtained for one of the above variables in terms of t, and hence some estimations can be made for the time constant for the wall. If δ is eliminated, (2.26) can be rearranged so that

$$\delta = \frac{3k(T_w - T_\infty)}{q} = \frac{3k\tau}{q} \tag{2.28}$$

where $\tau = T_w - T_\infty$, and then by substituting this into (2.27),

$$\frac{d}{dt}\left(\frac{\tau^2}{q}\right) = \frac{4}{3}\frac{\kappa q}{k^2} \tag{2.29}$$

is obtained. By expanding this derivative and combining like terms, this becomes

$$\left(\frac{2\tau}{q^2} - \frac{\tau^2}{q^3}\frac{dq}{d\tau}\right) d\tau = \frac{4}{3}\frac{\kappa}{k^2} dt$$

which can be integrated over time. From (2.25),

$$q = -\varepsilon_W \sigma T_w^4 = -\varepsilon_W \sigma (\tau + T_\infty)^4, \tag{2.30}$$

which means that

$$\frac{dq}{d\tau} = -4\varepsilon_W \sigma (\tau + T_\infty)^3, \tag{2.31}$$

and so

$$\Rightarrow \int_0^\tau \left(\frac{2\tau}{\varepsilon_W^2 \sigma^2 (\tau + T_\infty)^8} - \frac{\tau^2}{-\varepsilon_W^3 \sigma^3 (\tau + T_\infty)^{12}}(-4\varepsilon_W \sigma (\tau + T_\infty)^3)\right) d\tau = \frac{4}{3}\frac{\kappa}{k^2} t$$

which becomes, after integrating and rearranging,

$$\Rightarrow t = \frac{3}{2}\frac{k^2}{\kappa \varepsilon_W^2 \sigma^2} \int_0^\tau \frac{\tau(T_\infty - \tau)}{(\tau + T_\infty)^9} d\tau. \tag{2.32}$$

By replacing τ with $T_w - T_\infty$ as before, the right hand side (RHS) can now be integrated. This gives

$$\begin{aligned} t &= \frac{3}{2}\frac{k^2}{\kappa\varepsilon_W^2\sigma^2}\left(T_\infty\int_{T_\infty}^{T_w}\frac{T_w - T_\infty}{T_w^9}dT_w - \int_{T_\infty}^{T_w}\frac{T_w^2 - 2T_wT_\infty + T_\infty^2}{T_w^9}dT_w\right) \\ &\vdots \\ &= \frac{3}{2}\frac{k^2}{\kappa\varepsilon_W^2\sigma^2}\left[T_\infty\left(-\frac{1}{7}\frac{1}{T_w^7} + \frac{1}{8}\frac{T_\infty}{T_w^8} + \frac{1}{7}\frac{1}{T_\infty^7} - \frac{1}{8}\frac{T_\infty}{T_w^7}\right)\right. \\ &\quad \left. - \left(-\frac{1}{6}\frac{1}{T_w^6} + \frac{2}{7}\frac{T_\infty}{T_w^7} - \frac{1}{8}\frac{T_\infty^2}{T_w^8} + \frac{1}{T_\infty^8}\left(\frac{1}{6} - \frac{2}{7} + \frac{1}{8}\right)\right)\right] \\ &= \frac{3}{2}\frac{k^2}{\kappa\varepsilon_W^2\sigma^2}\frac{1}{T_\infty^6}\left[\frac{1}{6}\left(\frac{T_\infty}{T_w}\right)^6 - \frac{3}{7}\left(\frac{T_\infty}{T_w}\right)^7 + \frac{1}{4}\left(\frac{T_\infty}{T_w}\right)^8 + \frac{1}{84}\right] \end{aligned} \tag{2.33}$$

which gives a time constant in terms of the wall temperature T_w.

An equivalent expression can be derived in terms of the wall heat flux q. Because $q = -\varepsilon_W\sigma T_w^4 = -\varepsilon_W\sigma(\tau + T_\infty)^4$,

$$\tau = \left(\frac{q}{-\varepsilon_W\sigma}\right)^{\frac{1}{4}} - T_\infty, \tag{2.34}$$

recalling that q is negative. Starting with equation (2.29) and substituting in

$$\tau^2 = \left(\frac{q}{-\varepsilon_W\sigma}\right)^{\frac{1}{2}} - 2T_\infty\left(\frac{q}{-\varepsilon_W\sigma}\right)^{\frac{1}{4}} + T_\infty^2 \tag{2.35}$$

this gives

$$\frac{1}{q}d\left(\frac{1}{(-\varepsilon_W\sigma)^{\frac{1}{2}}}q^{-\frac{1}{2}} - \frac{2T_\infty}{(-\varepsilon_W\sigma)^{\frac{1}{4}}}q^{-\frac{3}{4}} + T_\infty^2 q^{-1}\right) = \frac{4}{3}\frac{\kappa}{k^2}dt$$

$$\Rightarrow \frac{1}{(-\varepsilon_W\sigma)^{\frac{1}{2}}}\left(-\frac{1}{2}\right)q^{-\frac{5}{2}}dq - \frac{2T_\infty}{(-\varepsilon_W\sigma)^{\frac{1}{4}}}\left(-\frac{3}{4}\right)q^{-\frac{11}{4}}dq - T_\infty^2 q^{-3}dq = \frac{4}{3}\frac{\kappa}{k^2}dt$$

Integrating over time gives

$$\frac{1}{(-\varepsilon_W\sigma)^{\frac{1}{2}}}\frac{1}{3}(q^{-\frac{3}{2}} - q_0^{-\frac{3}{2}}) - \frac{2T_\infty}{(-\varepsilon_W\sigma)^{\frac{1}{4}}}\frac{3}{7}(q^{-\frac{7}{4}} - q_0^{-\frac{7}{4}}) + \frac{1}{2}T_\infty^2(q^{-2} - q_0^{-2}) = \frac{4}{3}\frac{\kappa}{k^2}t$$

or

$$\begin{aligned} t &= \frac{3k^2}{4\kappa}\left[\frac{1}{(-\varepsilon_W\sigma)^{\frac{1}{2}}}\frac{1}{3}(q^{-\frac{3}{2}} - q_0^{-\frac{3}{2}}) - \frac{2T_\infty}{(-\varepsilon_W\sigma)^{\frac{1}{4}}}\frac{3}{7}(q^{-\frac{7}{4}} - q_0^{-\frac{7}{4}})\right. \\ &\quad \left. + \frac{1}{2}T_\infty^2(q^{-2} - q_0^{-2})\right] \end{aligned} \tag{2.36}$$

which can be shown to be identical to equation (2.33) by simple substitution.

Having derived expressions for the time constants, they can now be determined. The numerical values for the constants in the equations are:

- thermal conductivity, $k = 0.2$ W m^{-1} K^{-1}
- thermal diffusivity, $\kappa = 0.3 \times 10^{-6}$ m^2 s^{-1}
- Stefan-Boltzmann constant, $\sigma = 5.67 \times 10^{-8}$ W m^{-2} K^{-4}

The values for the wall temperature were chosen from runs done with the steady-state equations using the computer program found in Martire [28]. A run was done for both a soft-iron and hard-iron cycle and the results are shown in Table 2.1. It should be noted that some of these temperatures are unrealistically high, because the strip emissivity function overestimates the actual wall temperatures. The strip emissivity values shown in Table 2.1 are higher than real furnace values also (which are generally around 0.3), but they are sufficient for the purpose of this section. By examining some of these temperatures, it can be determined how long it takes for the wall to cool to a certain temperature, or more specifically, how long it takes for the initial wall heat flux to decrease by 50% and by 90%.

Firstly, consider the top of the furnace, where $T_w = 503°$C for a hard iron cycle. This means that the value for $\varepsilon_s = 0.8$, so $\varepsilon_W = 0.67$ from equation (2.23). Also, $T_\infty = 776$ K, and for this initial wall temperature,

$$q = q_0 = -\varepsilon_W \sigma T_\infty^4 = -13.8 \text{ kW m}^{-2}$$

Now for the flux q to equal half of the initial flux q_0, the temperature T_w must reduce to $T_w = 653$ K.

Rather than substituting in these values and tediously doing every calculation, it is noticed that, if $q = \frac{1}{2}q_0$, then the ratio $T_\infty : T_w$ is $\sqrt[4]{2}$, which

x (m)	T_w (soft iron) (°C)	T_w (hard iron) (°C)	ϵ_s
0.00	1700	1290	0.20
1.06	1640	1241	0.25
2.11	1570	1162	0.30
3.17	1498	1064	0.35
4.22	1422	949	0.40
5.28	1345	856	0.45
6.33	1252	779	0.50
7.39	1166	714	0.55
8.44	1080	659	0.60
9.50	1002	612	0.65
10.55	935	571	0.70
11.61	874	535	0.75
12.66	818	503	0.80

Table 2.1: Wall analysis - wall temperatures for soft and hard-iron cycles

means that the time taken for the wall heat flux to be halved can be calculated by modifying equation (2.33) to become

$$t = \frac{3}{2}\frac{k^2}{\kappa\varepsilon_W^2\sigma^2}\frac{1}{T_\infty^6}\left(\frac{1}{6}(2\sqrt{2}) - \frac{3}{7}\left(\frac{4}{\sqrt[4]{2}}\right) + 1 + \frac{1}{84}\right)$$

such that t is dependent only on the initial values of ε_W and T_∞. A similar technique is possible for a reduction in q to 10% of its original value, ie

$$t = \frac{3}{2}\frac{k^2}{\kappa\varepsilon_W^2\sigma^2}\frac{1}{T_\infty^6}\left(\frac{1}{6}(10\sqrt{10}) - \frac{3}{7}\left(\frac{100}{\sqrt[4]{10}}\right) + 25 + \frac{1}{84}\right)$$

The numerical expression for t in the 50% reduction case is

$$t = (2.5986 \times 10^{18})\varepsilon_W^{-2}T_\infty^{-6}$$

Therefore, for the values of $\varepsilon_W = 0.67$ and $T_\infty = 776$ K, this gives

$$t = 26.5 \text{ s}$$

to reduce to 50% of its initial flux. For the 90% reduction case,

$$t = (3.8458 \times 10^{20})\varepsilon_W^{-2}T_\infty^{-6}$$

and so in this case, for the same ε_W and T_∞, $t = 66$ minutes. Both of these results indicate a rather high influence from the wall for quite some time immediately after a cycle change.

At the base of the furnace, $T_w = 1290^oC$ and $\varepsilon_s = 0.2$, causing $\varepsilon_W = 0.19$ and $T_\infty = 1563$ K. For a 50% flux reduction,

$$t = 4.9 \text{ s}$$

and for 90%, $t = 12.2$ minutes.

At the middle of the furnace, $T_w = 779^oC$ and $\varepsilon_s = 0.5$, and so $\varepsilon_W = 0.44$ and $T_\infty = 1052$ K. Hence a 50% reduction in wall heat flux gives $t = 9.9$ s, and a 90% reduction gives $t = 24.4$ minutes.

The actual radiative flux from the wall in the furnace, given by B_w in equation (2.42), is of the same order of magnitude as the radiation emitted by the gas to the strip, B_{gs}, and to the wall, B_{gw}. This fact, coupled with the results described above, clearly indicate that the heat flux from the wall after a cycle change has a large influence on the total heat flux in the furnace. Considering that a piece of steel strip takes about 8 seconds to pass through the furnace, these time constants show that the wall heat flux affects the strip temperature to some extent — something not allowed for in the steady-state equations. There will almost always be a loss of some strip at a cycle change, but these losses can be minimised if there is a better knowledge of how the furnace is operating. Having learned that the wall is emitting a significant amount of radiation for a substantial time after a cycle change, this increased knowledge must be applied to the transient model equations. A model for the wall therefore needs to be implemented, and this is done in a later section. The adiabatic wall condition is hence found to be inaccurate for a transient situation in the furnace, although it is a good starting point to derive some results. Some of these results are shown in the next section of this report.

2.3 Solving the transient equations. Part 1 - adiabatic wall

2.3.1 The adiabatic wall equations

Recall the form of the transient equations from section 2.2, ie,

$$\frac{\partial T_s}{\partial t} - V_s \frac{\partial T_s}{\partial x} = \frac{Q_{gs}}{\rho_s w_s d_s c_{ps}} \tag{2.37}$$

$$\frac{\partial T_g}{\partial t} + V_g \frac{\partial T_g}{\partial x} = \frac{\dot{M}(h_{ad} - h_g) - Q_{gs} - Q_{gw}}{\rho_g (w_f d_f - w_s d_s) c_{pg}} \tag{2.38}$$

This is a coupled system of one-dimensional advection equations, with both the strip partial differential equation (PDE) (2.37) and the gas PDE (2.38) hyperbolic in form. As well as these equations, the solution requires initial and boundary conditions. Finding appropriate initial and boundary conditions was part of the construction of the problem.

As a result of the complexity of the problem, it was decided initially to look for solutions of the above set of equations by assuming that the wall is adiabatic — ie, whatever heat is transferred into the wall is reflected back into the furnace again. In this sense, the wall acts like a 'mirror', and the results of the effects of the wall in the operation of the furnace as shown in section 2.2 are ignored. The main reasons for doing this were, firstly, for simplicity, so that some results could be obtained without having to include the more complicated case of the dynamic wall, and secondly, for reasons of comparison. It may be recalled that the steady-state model also uses an adiabatic wall condition, and hence the results from the steady-state model can be used as a check on the transient model, because the transient model is designed to move from one steady-state to another. If the transient model agrees with the steady-state model in the limit, then the transient model is assumed to be working and so the next stage of the project — the inclusion of the wall effect — can be considered.

Because of the balance between the amount of heat transferred into and out of the wall, the Q_{gw} term in the above set of equations, which represents the net heat transferred from the gas to the wall, is equal to zero. Hence this term can be removed from the gas equation and included as a separate equation of $Q_{gw} = 0$. This results in three equations in three unknowns, these being the strip, gas and wall temperatures. It is pertinent at this stage to point out that both Q_{gs} and Q_{gw} can be written in terms of T_s, T_g and T_w, ie,

$$Q_{gs} = \alpha T_s^4 + \beta T_g^4 + \gamma T_w^4 + H_s(T_g - T_s) \tag{2.39}$$

$$Q_{gw} = \mu T_s^4 + \nu T_g^4 + \xi T_w^4 + H_w(T_g - T_w) \tag{2.40}$$

where the coefficients contain such parameters as the Stefan-Boltzmann constant, shape factors, and radiation-effecting terms such as emissivity and absorptivity. The major influencing factors in the heat transfer can be clearly seen with the T^4 terms representing the radiation heat transfer and the linear T terms representing the convective heat transfer.

A derivation of how the coefficients in equations (2.39) and (2.40) can be obtained from first principles is now given. Consider a cross-sectional view of the MCL6 DFF, similar to the CGL2 DFF, from above the furnace, as shown in Figure 2.4. The whole furnace includes the strip, the furnace walls, and the gas located everywhere in between the walls and the strip. The strip and walls extend about 12.7 metres down 'into the page' on the CGL2 DFF, and the approximation is made that the strip and walls have infinite length 'into the page'. As a result, the strip and wall perimeters can be used, rather than surface areas, to calculate how much heat enters and leaves a particular surface. This removes the need to calculate difficult values of shape factors using three dimensions. It also allows for the strip to be taken as one surface and for the wall to be taken as one whole surface, rather than separating the front-on wall from the side-on wall for example. This separation is done in chapter 5 when studying the temperature variation across the strip width.

The modes of heat transfer between the gas, the strip and the wall are radiation and convection. The strip radiates heat to the gas and the wall, and there is heat conduction across its surface, which is included in the analysis of the edges. The wall also radiates heat to the gas and the strip, and loses heat via conduction through the wall to the ambient surroundings, although for the moment the wall is assumed to be adiabatic. The heat loss through the wall is included in the following chapter.

The radiation heat transfer between the two different surfaces and

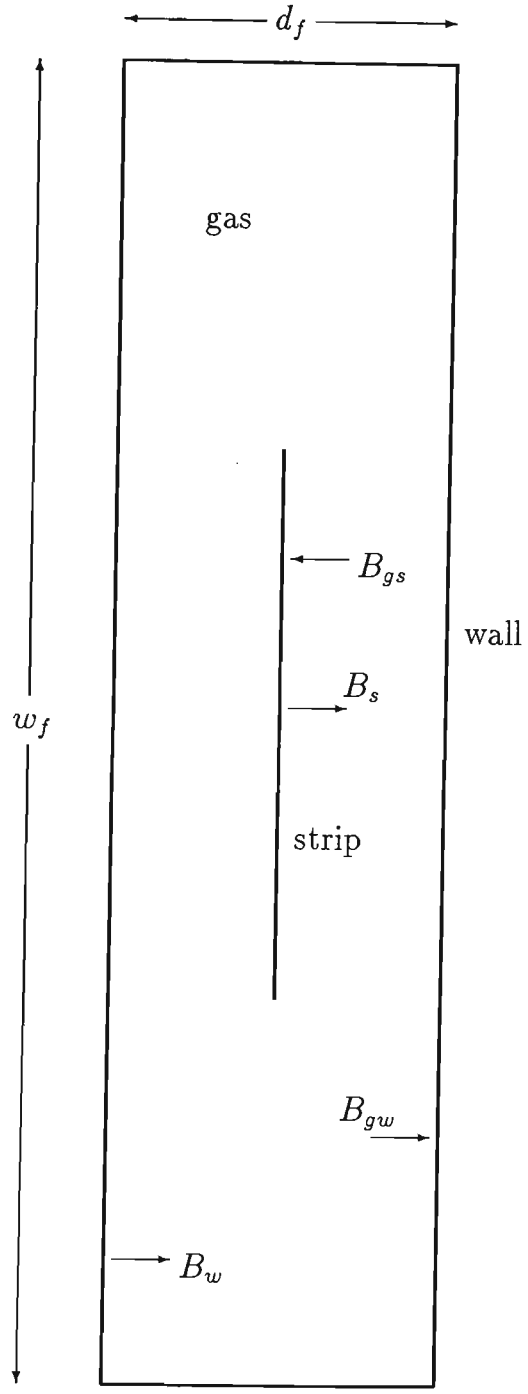

Figure 2.4: Cross-section of MCL6 DFF

the gas medium is modelled here using radiosities, a method found in Holman [16] for example. In the diagram in Figure 2.4, the terms B_{gs}, B_s, B_{gw} and B_w all represent an amount of radiation leaving one surface or medium. In mathematical form, the net amount of radiation from the strip, B_s, is represented by

$$P_s B_s = P_s \varepsilon_s \sigma T_s^4 + P_s \rho_s B_{gs}; \tag{2.41}$$

that is, the emitted radiation from the strip, plus that amount that the strip reflects from the incoming gas radiation. Similarly the amount of radiation from the wall, B_w, is

$$P_w B_w = P_w \varepsilon_w \sigma T_w^4 + P_w \rho_w B_{gw}. \tag{2.42}$$

The arrows in Figure 2.4 simply show the (rough) direction of the heat transfer. The gas radiates its own heat to the strip, and transmits heat from the wall to the strip also, and so the radiation from the gas to the strip, B_{gs}, is given by

$$P_s B_{gs} = P_s \varepsilon_g \sigma T_g^4 + P_w F_{ws} \tau_g B_w. \tag{2.43}$$

In a similar way, the gas radiates heat from itself to the wall, as well as transmitting heat through itself from the strip and from the rest of the wall, and so the radiation from the gas to the wall, B_{gw}, is

$$P_w B_{gw} = P_w \varepsilon_g \sigma T_g^4 + P_s F_{sw} \tau_g B_s + P_w F_{ww} \tau_g B_w. \tag{2.44}$$

where the F terms are shape factors. Using the geometry of the furnace as shown in Figure 2.4, the calculation of the shape factors is quite simple using shape factor algebra, described in Holman [16], and Siegel & Howell [46], among others. For example, it is quite obvious that the only other surface that the strip 'sees' is the wall. Therefore all of the radiation leaving the strip will reach the wall (when there is no radiatively-active gas present), meaning that

$$F_{sw} = 1. \tag{2.45}$$

The furnace wall either sees itself or the strip. In algebraic terms,

$$F_{ww} + F_{ws} = 1. \tag{2.46}$$

Shape factor algebra also includes the reciprocity condition, which holds for any two surfaces i and j and relates the shape factors, F_{ij} and F_{ji}, to their surface areas, ie,

$$A_i F_{ij} = A_j F_{ji}. \tag{2.47}$$

The reciprocity relation is equivalent to this when using perimeters instead of surface areas. Here, the strip perimeter P_s is given by $P_s = 2(w_s + d_s)$, and the wall perimeter P_w by $P_w = 2(w_f + d_f)$. Using equations (2.46) and (2.47), the shape factors become

$$F_{ws} = \frac{w_s + d_s}{w_f + d_f}, \tag{2.48}$$

$$F_{ww} = 1 - \frac{w_s + d_s}{w_f + d_f}. \tag{2.49}$$

For simplification, lowercase f terms are used to denote the products of the shape factors with the perimeters of the strip and the wall and the gas transmissivities. Therefore

$$\begin{aligned} f_{ws} &= \frac{P_w}{P_s} F_{ws}\tau_g \equiv F_{sw}\tau_g, \\ f_{sw} &= \frac{P_s}{P_w} F_{sw}\tau_g \equiv F_{ws}\tau_g, \\ f_{ww} &= \frac{P_w}{P_w} F_{ww}\tau_g = F_{ww}\tau_g. \end{aligned}$$

The expressions for B_{gs} and B_{gw} can now be obtained by rearranging equations (2.41)-(2.44), ie,

$$B_{gs} = \frac{\varepsilon_s \sigma T_s^4 (f_{sw}\rho_w f_{ws}) + \varepsilon_g \sigma T_g^4 (1 - \rho_w (f_{ww} - f_{ws})) + \varepsilon_w \sigma T_w^4 f_{ws}}{1 - \rho_w (f_{ww} + f_{ws}\rho_s f_{sw})}, \tag{2.50}$$

$$B_{gw} = \frac{\varepsilon_s \sigma T_s^4 (f_{sw}) + \varepsilon_g \sigma T_g^4 (1 + \rho_s f_{sw}) + \varepsilon_w \sigma T_w^4 (f_{ww} + f_{sw}\rho_s f_{ws})}{1 - \rho_w (f_{ww} + f_{ws}\rho_s f_{sw})}. \tag{2.51}$$

The other coefficients in equations (2.39) and (2.40) are those for convection, H_s and H_w. Hereafter, the value of the heat transfer coefficient is that derived for a fully-developed turbulent flow in a tube, as given in Rogers & Mayhew [44] and Holman [16], as shown below

$$h = k_g \mathrm{Nu}/D_H. \tag{2.52}$$

The hydraulic diameter D_H for this type of configuration is taken to be four times the cross-sectional area of the flow domain divided by the perimeter of the surfaces in contact with the gas, ie,

$$D_H = 4A_f/P_f \equiv \frac{4(w_f d_f - w_s d_s)}{2(w_f + d_f) + 2(w_s + d_s)}, \tag{2.53}$$

and the Nusselt number Nu is given by

$$\mathrm{Nu} = 0.023 \mathrm{Re}^{0.8} \mathrm{Pr}^{0.4}, \tag{2.54}$$

for this type of flow. Previous analysis by Thompson & Martire [54] has shown that the flow is always turbulent when gas is present. The Reynolds number Re and the Prandtl number Pr are given by

$$\mathrm{Re} = \frac{4\dot{m}_g}{P_f \mu_g} \equiv \frac{\rho_g V_g D_H}{\mu_g} \tag{2.55}$$

$$\mathrm{Pr} = \frac{c_{pg}\mu_g}{k_g} \tag{2.56}$$

From the value of h therefore, the total convective heat flow rate per metre to the surfaces can be calculated using $H_s = P_s h$ and $H_w = P_w h$. The derivations for all of these expressions are also found in Thompson & Martire [55].

The three equations in three unknowns that are to be solved therefore take the following form

$$\frac{\partial T_s}{\partial t} - V_s \frac{\partial T_s}{\partial x} = \frac{\alpha T_s^4 + \beta T_g^4 + \gamma T_w^4 + H_s(T_g - T_s)}{\rho_s w_s d_s c_{ps}} \tag{2.57}$$

$$\frac{\partial T_g}{\partial t} + V_g \frac{\partial T_g}{\partial x} = \frac{\dot{M}(h_{ad} - h_g) - \alpha T_s^4 - \beta T_g^4 - \gamma T_w^4 - H_s(T_g - T_s)}{\rho_g (w_f d_f - w_s d_s) c_{pg}} \tag{2.58}$$

$$0 = \mu T_s^4 + \nu T_g^4 + \xi T_w^4 + H_w(T_g - T_w) \tag{2.59}$$

The next section deals with the development of this solution method.

2.3.2 Development of solution method

Because of the nature of the problem, the options for solving the equations are limited. Many things must be considered, and each one of these contributes to reducing options for solution.

There is quite a range of methods which can be used to solve a simple 1-D advection equation of the form

$$\frac{\partial \tau}{\partial t} + u\frac{\partial \tau}{\partial x} = 0, \tag{2.60}$$

where τ is the temperature and u the velocity. Most of the finite-difference techniques that can be employed are found in Noye [33]. However, because of the complicated structure of the problem, the range of choices is reduced. A method was desired that was easy to implement, had a reasonably high order of accuracy and was stable over a reasonable range of values. The simplest finite-difference method (FDM) for the advection equation is the upwind method, which takes the form

$$\tau_j^{n+1} = c\tau_{j-1}^n + (1-c)\tau_j^n$$

where c, the Courant number, is given by

$$c = u\triangle t/\triangle x,$$

where $\triangle t$ is the size of the time step and $\triangle x$ is the size of the grid spacing. The upwind method is stable provided that

$$0 < c \leq 1.$$

One drawback of the upwind method is that it is only a first-order method. This means that the numerical accuracy of the method is only of the order of the size of the grid spacing; ie, $O(\triangle x)$. Also, the upwind method contains a numerical diffusion term which causes large amounts of damping to the solution, and hence affects the accuracy of the final result.

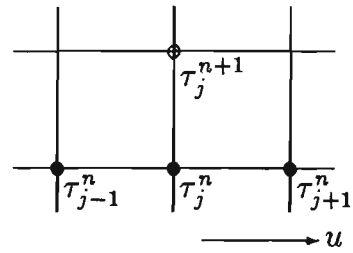

Figure 2.5: Computational stencil for the Lax-Wendroff method

There are several higher-order explicit methods also. One of these is the Lax-Wendroff method (found in Richtmyer & Morton [43]). Because it is a second-order method, its truncation errors are $O\{(\triangle x)^2\}$. Also, higher order methods require more grid points, and so the Lax-Wendroff method uses a $(1,3)$ computational stencil (ie, one point on the $(n+1)$th time step and three on the (n)th time step), as opposed to the $(1,2)$ computational stencil used in the upwind method. A diagram of the stencil is shown in Figure 2.5. The Lax-Wendroff equation has the form

$$\tau_j^{n+1} = \tfrac{1}{2}c(1+c)\tau_{j-1}^n + (1-c^2)\tau_j^n - \tfrac{1}{2}c(1-c)\tau_{j+1}^n \tag{2.61}$$

which is also stable in the range $0 < c \leq 1$.

A further second-order explicit method is the second-order upwind method. This has a similar form to the first-order upwind method, but it uses a grid point at position $(n, j-2)$ rather than at the $(n, j+1)$ position, making it too a $(1,3)$ stencil. A diagram for this method is shown in Figure 2.6. The finite-difference equation for the second-order upwind method is

$$\tau_j^{n+1} = -\tfrac{1}{2}c(1-c)\tau_{j-2}^n + c(2-c)\tau_{j-1}^n + \tfrac{1}{2}(1-c)(2-c)\tau_j^n \tag{2.62}$$

which is stable for $0 < c \leq 2$.

Another difference between this problem and the example equation (2.60) is that these equations are non-homogeneous. Therefore, the ad-

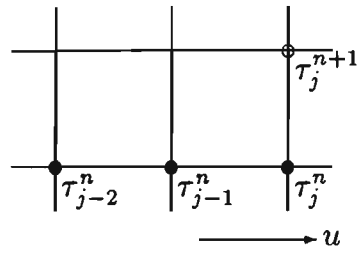

Figure 2.6: Computational stencil for the second-order upwind method

vection equation is not exactly equation (2.60), but it is more like

$$\frac{\partial \tau}{\partial t} + u\frac{\partial \tau}{\partial x} = f(\tau). \tag{2.63}$$

As a result, the Lax-Wendroff equation, (2.61), looks like

$$\tau_j^{n+1} = \tfrac{1}{2}c(1+c)\tau_{j-1}^n + (1-c^2)\tau_j^n - \tfrac{1}{2}c(1-c)\tau_{j+1}^n + \triangle t(f(\tau))_j^n, \tag{2.64}$$

and the second-order upwind method, (2.62) looks like

$$\tau_j^{n+1} = -\tfrac{1}{2}c(1-c)\tau_{j-2}^n + c(2-c)\tau_{j-1}^n + \tfrac{1}{2}(1-c)(2-c)\tau_j^n + \triangle t(f(\tau))_j^n. \tag{2.65}$$

The non-homogeneity can affect the accuracy, stability and computation time for the model.

These higher-order explicit methods give far more accurate results than the first-order upwind method for the same cell size, and because of this greater accuracy, they can be run with a longer time step; hence they are computationally faster than a first-order method for the same accuracy. There are other higher-order methods too, involving more and more grid points, but the choice is constrained by the shape of the furnace. Implicit methods were considered for the advection equation also, such as the box method described in Noye [33], but they were found to be difficult to implement. In the case of the box method, the non-homogeneity of the equation means that temperatures for the strip, gas and wall (and the values of the parameters that depend on the temperatures) are required at the $(n+\frac{1}{2})$ time step and the $(j-\frac{1}{2})$ grid

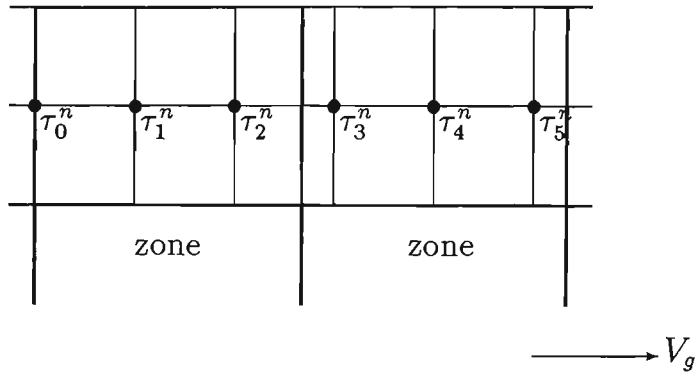

Figure 2.7: Uniform grid showing zonal boundaries

point, which are not accurately determined when the finite-difference method is solved.

The geometry of the furnace also poses difficulties. As was briefly mentioned in the introduction, the Selas furnace on CGL2 consists of zones of gas burners (though the top zone, zone 7, contains no gas burners), where these seven zones are of unequal length. When constructing a grid for a finite-difference method, it is preferable to retain a uniform grid spacing across the domain of the grid. In this problem, however, difficulties arise at the zonal boundaries. If the furnace is partitioned into uniformly-spaced grid points, these grid points *do not* fall on the zonal boundaries. An example of how the grid spacing appears in relation to the zones is shown in Fig 2.7. It is observed that if a uniform grid spacing is used throughout the entire furnace, then accurate results cannot be obtained around the zonal boundaries. In fact, when a uniform grid spacing was used throughout the whole furnace, and the program described later was run, the results were as expected for the strip, gas and wall after the first time step, but there were very large discrepancies in the temperatures of the gas across a zonal boundary.

The reason for this is found by considering the transient gas equa-

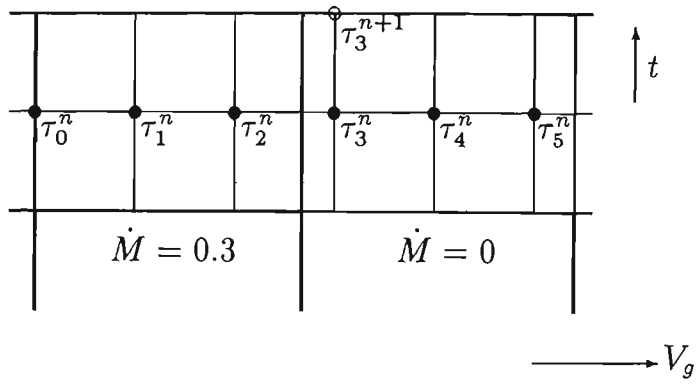

Figure 2.8: Grid stencil for one zone on, one zone off

tion (2.38) from earlier in the chapter,

$$\frac{\partial T_g}{\partial t} + V_g \frac{\partial T_g}{\partial x} = \frac{\dot{M}(h_{ad} - h_g) - Q_{gs} - Q_{gw}}{\rho_g(w_f d_f - w_s d_s)c_{pg}}.$$

The crucial term here is that involving $\dot{M}$, the gas addition rate. It describes the rate at which gas is being added to the furnace from the burners in the wall, and has units of kg m^{-1} s^{-1}. If a zone in the furnace is turned on, then the value of $\dot{M} \neq 0$, and if the zone is turned off, then $\dot{M} = 0$. Therefore, if a uniform grid spacing is used throughout the whole furnace, there are major discrepancies over the zonal boundaries where one zone is turned off and another is turned on. This problem is clearly shown in Fig 2.8, where the finite-difference method (in this case the upwind method) must evaluate the gas temperature at the point $(n+1, 3)$, by using those values known at the points $(n, 2)$ and $(n, 3)$. As can be seen, the value of $\dot{M}$ in this case is given as 0.3 kg m^{-1} s^{-1} in one zone, but $\dot{M} = 0$ in the zone after it. Because the zonal boundary is ignored, the value of T_g at the point $(n+1, j)$ is incorrect. What is required here is the *known* value of T_g at the zonal boundary if the error in T_g at $(n+1, j)$ is to be reduced.

Hence, if the values of the temperatures at the zonal boundaries are desired, then there are at least two ways of obtaining them.

- Use an interpolation function of some sort, eg, Lagrangian interpolation,

or

- Change from a uniform grid spacing throughout the whole furnace to another arrangement, such as a uniform grid spacing throughout each zone.

The first option would involve additional calculations at each time step, adding to the computation time. Also, the interpolation formula should be two orders of accuracy higher than the finite-difference method used [33] to retain the overall accuracy of the method, and different formulae may need to be used at different zonal boundaries to ensure that each interpolation formula is stable. Because of these difficulties, the second option was chosen.

An alternative method of coping with this problem is to simply move the zonal boundaries so that they fall on points that are exact multiples of the grid spacing. This is the method used by BHP [51], and it means that it is not necessary to reset the grid spacing to be variable throughout the furnace. This assumption is valid because the gas does not enter the furnace uniformly, and so adjusting the boundaries of the zones still represents the actual gas flow well.

The choice of a variable grid spacing can introduce problems, as was discovered by Crowder & Dalton [8], in a paper in which the benefits of using a non-uniform mesh to solve a particular problem in Poiseuille flow were analysed, and no accuracy advantages were found. In response, Blottner & Roache [3], indicated that the problem was not with non-uniform meshes in general, but in both the type of problem that they were studying, and the choice of mesh which they had used. Blottner & Roache [3] showed that, if a change in the grid spacing is to be made, then it must be made as small as possible in order for the truncation error to stay of the same order as for the previous grid spacing. In mathematical terms, if the truncation error from the i^{th} grid is of order $(\triangle x)^2$, then to keep it of this order for the $(i+1)^{th}$ grid,

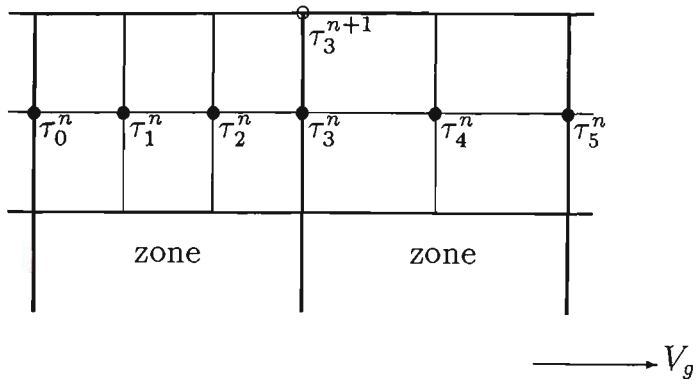

Figure 2.9: Uniform grid within each zone

the grid must satisfy the condition

$$\triangle x_{i+1} = f \triangle x_i$$

where $f = (1 + \alpha \triangle x_i)$, or in other words,

$$\triangle x_{i+1} - \triangle x_i = O\{(\triangle x_i)^2\}, \tag{2.66}$$

where α is of order 1. Therefore, care must be taken to ensure that any variable grid chosen must not destroy the order of accuracy of the whole method by changing too much from one zone to the next. The layout of the furnace makes satisfying the above condition (2.66) difficult to meet, due to the zones being of substantially uneven length.

However, consider the diagram in Figure 2.9. In this example, the grid from Figure 2.8 has been rearranged to allow the grid points τ_3^{n+1} and τ_3^n to fall on a zonal boundary. The two zones shown also have a uniform grid within each zone. If τ_3^{n+1} was to be determined from τ_2^n, τ_3^n and τ_4^n using the Lax-Wendroff method, then the condition (2.66) would need to be satisfied to retain accuracy. If, however, the second-order upwind method was used to determine τ_3^{n+1}, then the grid spacing is uniform for all of the grid points needed in this calculation (ie, τ_1^n, τ_2^n and τ_3^n). Therefore, the condition (2.66) is not relevant if the grid points used to solve the FDM in one zone are uniformly spaced within that zone. Numerical tests showed that taking grid spacings which differed in

a minimal way between each zone gave similar results to a situation where the number of grid points in only one zone was changed, being given up to eight times the number of grid points as before. Because of the forms of the two second-order finite-difference methods, both are required within each zone if only the grid points within each zone are used.

The errors around the zonal boundaries were greatly reduced when using the uniform-grid-in-a-zone approach compared with using the uniform grid spacing throughout the furnace. Where, with the latter approach, the temperatures varied by as much as 20 K after one time step, they now varied by less than 1 K.

A further difference between the advection equations to be modelled [(2.57) and (2.58)] and the simple advection equation (2.60) is that the velocity is a function of time (as well as position for the gas). This variation means that the gas velocity needs to be updated after every time step as well as for every position, which is costly in terms of computation time.

The velocity of the gas is given by

$$V_g = \frac{\dot{m}_g}{\rho_g(w_f d_f - w_s d_s)},$$

where $\dot{m}_g$ is the gas mass flow rate. The gas density is assumed to vary with the temperature of the gas following the ideal gas law, ie,

$$\rho_g T_g = \rho_{ad} T_{ad}$$

and hence, the new value of the gas density depends on the current gas temperature, so

$$\rho_g = \frac{\rho_{ad} T_{ad}}{T_g}.$$

Because this is updated on every time step, the gas velocity needs updating at every time step also.

The variability of the gas velocity also affects the stability condition, which therefore needs to be updated for every time step. The Courant

number for the gas, c_g, is

$$c_g(x,t) = \frac{V_g(x,t)\triangle t}{\triangle x},$$

so with the gas velocity varying, there is a danger that the finite-difference equation for the gas may show instability after a period of time, even if it is initially stable. The biggest danger of instability is during a change from a hard to a soft-iron cycle, which generally involves an increase in the gas flow rate in the furnace. As a result, care must be taken to ensure that the time interval is small enough to enable the stability condition to be met. A procedure for this is explained on page 59.

However, the varying gas velocity does cause other problems. These problems include the accuracy of the method and the consistency of the finite-difference equation(s) used. A test for the accuracy and consistency of a finite-difference method can be completed by finding the modified equivalent partial differential equation (MEPDE), explained by Noye [33]. The MEPDE gives the truncation error of the finite-difference method in terms of the grid spacing $\triangle x$ only. Obtaining the MEPDE requires progressively eliminating the time derivatives and the $\triangle t$ terms of the partial differential equation equivalent to the original FDM. This includes taking time and/or spatial derivatives and multiplying by terms involving $\triangle t$. The MEPDE for the Lax-Wendroff equation shown in equation (2.61), without accounting for the variable gas velocity, is

$$\frac{\partial \tau}{\partial t} + u\frac{\partial \tau}{\partial x} + \frac{u(\triangle x)^2}{6}(1-c^2)\frac{\partial^3 \tau}{\partial x^3} + \frac{u(\triangle x)^3}{8}c(1-c^2)\frac{\partial^4 \tau}{\partial x^4} + O\{(\triangle x)^4\} = 0,$$

and for the second-order upwind method in equation (2.62) with constant velocity, it is

$$\frac{\partial \tau}{\partial t} + u\frac{\partial \tau}{\partial x} - \frac{u(\triangle x)^2}{6}(1-c)(2-c)\frac{\partial^3 \tau}{\partial x^3} + \frac{u(\triangle x)^3}{8}(1-c)^2(2-c)\frac{\partial^4 \tau}{\partial x^4} + O\{(\triangle x)^4\} = 0.$$

Clearly both of these methods are second-order accurate.

These MEPDEs are given for the case when the velocity is assumed to be constant. In fact, due to the extra derivatives that result from the varying velocity, elimination of the $\triangle t$ terms is not possible when obtaining the MEPDE for these second-order methods in $\triangle x$. Therefore the variable velocity causes the method to be first-order accurate in $\triangle t$, although the small size of the time step ensures that its effect on the accuracy is small. Hence the variable velocity has a double effect, both on the computing time in having to consistently calculate values, and on the finite-difference method also, in that it affects the accuracy of the method used.

Not only does the variable velocity affect the accuracy of the FDM, but so too does the non-homogeneity of the PDE. The right hand side of equations (2.57) and (2.58) include terms to the fourth power in the strip, gas and the wall temperatures, all of which are functions of time and position. This also causes extra $\triangle t$ terms in the MEPDE which cannot be eliminated, again making the finite-difference equation first-order accurate in $\triangle t$. However, the small size of the time interval ensures no large problems with accuracy.

Another of the difficulties with constructing the model for the Selas furnace involves the opposite directions of motion of the strip and the gas. Naturally, it is preferred for both to be travelling in the same direction for ease of calculation, but this, unfortunately, is not the case. Therefore, to determine the new values of the strip and the gas temperature, each must be solved in its own direction of motion — from top to bottom for the strip, and from bottom to top for the gas. If both were travelling in the same direction, then only one pass through the furnace would be required.

Any attempts to solve the equations in the same direction are futile, because the form of the finite-difference method makes it impossible. With the coupled set of advection equations that describes the furnace, each quantity must be solved in its direction of motion, because each new value that

is calculated depends on the value at the previous position; ie, the position that is 'upwind' from the new one. Therefore, trying to determine the strip temperature at the top of the furnace by using the point directly below it is meaningless, because the strip is travelling downwards through the furnace, not upwards. The temperature of the gas at the bottom of the furnace cannot be determined by the temperature at any point above it for the same reason.

Because of these facts, the equations must be solved separately. However, the equations are also coupled, which means that the value of one depends on the other; they are functions of each other. This means that terms involving the gas (and wall) temperatures must be included in the strip equation, while terms involving the strip and wall temperatures must be included in the gas equation. Because an explicit method is used, the new strip temperature is calculated from the old strip, gas and wall temperatures, as well as from any other variable parameters, including the strip speed, thickness, and the gas flow rates, so that

$$T_s{}^{n+1} = f(T_s{}^n, T_g{}^n, T_w{}^n, \dot{M}, V_s, d_s, w_s).$$

In a similar way, the gas temperature is found,

$$T_g{}^{n+1} = f(T_s{}^n, T_g{}^n, T_w{}^n, \dot{M}, V_s, d_s, w_s).$$

The stability of the finite-difference method used here is mainly dependent upon the velocity of the gas, which is anywhere up to 20 times greater than the velocity of the strip. Because of this dependence of the time interval on the gas velocity, the gas critical time is almost always shorter than the strip critical time, so both the gas and strip temperatures can be calculated using the gas time interval.

Having determined the new values of the strip and the gas temperatures, the new values for the wall temperatures can be calculated. Because the adiabatic wall case is being considered at this stage, it must satisfy the

condition that the net heat flow rate to the wall is zero, and so

$$T_w{}^{n+1} = f(T_s{}^{n+1}, T_g{}^{n+1}, T_w{}^{n}, \dot{M}, V_s, d_s, w_s).$$

In the MCL6 progress report by Stone & Morrison [51], the gas temperatures are calculated first, then the strip temperatures using the new value of the gas temperatures, and then the wall temperatures using the new values of the strip and the gas temperatures. The reason for the above order has to do with the relative time constants of the three quantities — the gas is extremely fast, and the wall effects far slower in the transfer of heat.

The model must also be able to track the position of the weld in the furnace. When the weld enters the furnace, the strip dimensions may change, and if this is the case, so will such parameters as the strip perimeter and strip-dependent shape factors. The model follows the position of the weld in the CGL2 model by incrementing the distance at every time step by an amount dependent on the strip velocity. If the weld is in the furnace, the model records its position at each time step. During the calculations at each time step for the strip, the strip dimensions for the new coil are used until the weld is encountered, and the dimensions for the old coil once the weld is passed. The opposite applies for the gas, since the direction of solution is from the bottom of the furnace to the top as already noted.

Two boundary conditions (BCs) are required for this set of equations : one for the strip at the top of the furnace, and one for the gas at the boot of the furnace. For the strip, a value of $T_s(l,t)$ is sought, where l represents the point at the top of the furnace. It is assumed that the incoming strip temperature remains unchanged over time, ie,

$$T_s(l,t) = T_{s0}(l). \tag{2.67}$$

The gas BC is more difficult to establish. Because of the structure of the furnace, it is impossible to say that the gas temperature at the base of the

furnace takes on a fixed value with time. The assumption for the steady-state problem [28] was to set the gas temperature so it is equal to the strip temperature at the furnace base, the justification for this being that there is so little gas at the furnace base that its contact with the strip would cause it to take the same temperature as the strip. Another BC, which uses a similar line of thought, was constructed at the 1990 MISG, [1]. Recall the steady-state gas equation (2.2), ie

$$\dot{m}_g c_{pg} \frac{dT_g}{dx} = \dot{M}(h_{ad} - h_g) - Q_{gs}. \tag{2.68}$$

The idea here is that, because there is so little gas at the boot of the furnace, then the gas flow rate $\dot{m}_g$ is negligible there. As can be seen, setting $\dot{m}_g = 0$ makes the right hand side equal to zero, so that the gas boundary condition at the furnace boot becomes

$$\dot{M}(h_{ad} - h_g) - Q_{gs} = 0.$$

The extension of this idea to the transient model is not difficult. The transient gas equation, (2.38), is

$$\frac{\partial T_g}{\partial t} + V_g \frac{\partial T_g}{\partial x} = \frac{\dot{M}(h_{ad} - h_g) - Q_{gs}}{\rho_g (w_f d_f - w_s d_s) c_{pg}}. \tag{2.69}$$

Therefore, if it is again said that there is negligible gas flow at the furnace base, then this sets $V_g (= \dot{m}_g / \rho_g (w_f d_f - w_s d_s)) = 0$, and hence the spatial derivative term vanishes. This leaves the boundary condition for the gas at the base of the furnace as used in this program, ie,

$$\frac{\partial T_g}{\partial t} = \frac{\dot{M}(h_{ad} - h_g) - Q_{gs}}{\rho_g (w_f d_f - w_s d_s) c_{pg}}, \tag{2.70}$$

evaluated at $x = 0$.

2.3.3 Solution method

The final choice for solving the equations was as follows:

- a combination of two second-order finite-difference methods: the Lax-Wendroff method and the second-order upwind method,
- a variable grid, with the grid spacing constant in a particular zone, but differing between each zone, and
- the strip and the gas equations are solved separately, and these results used to obtain the wall temperature.

The mixture of the two second-order methods was necessary because the computation of just one or the other did not fit the grid arrangement that was chosen. However, the alternative was returning to a first-order method, and a combination of two more accurate second-order methods was preferable. The choice of the variable grid was found to be superior to that of the uniform furnace grid generally, especially for the first iteration, where the uniform grid caused large errors around zonal boundaries due to the sudden change in values of gas velocity and other parameters. The most desirable variable grid is the one with the smallest number of grid points, for this allows the choice of the time step $\triangle t$ to be larger while computation time is smaller. A diagram of the furnace showing the grid points for a 39 point furnace is shown in Figure 2.10.

In the model, the equations are solved for the strip first, from top to bottom in the furnace, then the gas, from bottom to top (although the strip-first, gas-second order is not important because of the solution method chosen); then the new temperatures of the wall are calculated by finding the zero of the wall equation (2.59), since the equation is of the form $f(T_w) = 0$. A NAG library routine [31] was used to accomplish this. The iteration continues until the final solution is obtained, which for the adiabatic wall model is when the temperatures have converged.

The initial conditions used in the program which solves the equations come directly from the steady-state model [28]. In other words, the

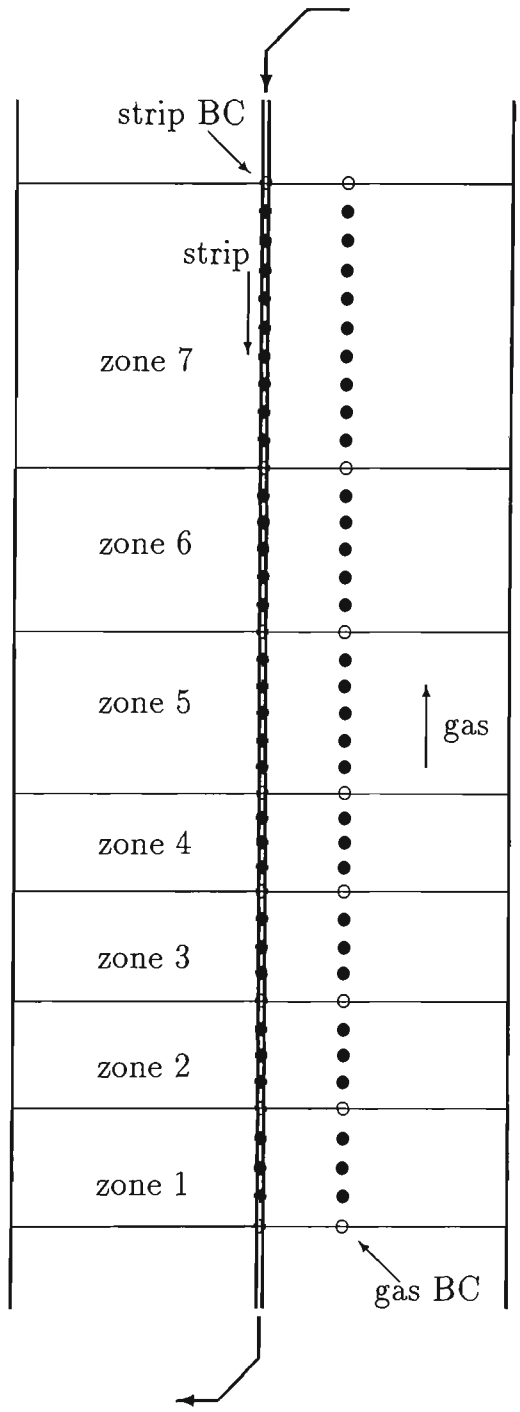

Figure 2.10: Furnace showing grid spacings for 39 grid points

output from a run of the steady-state model is used as the input for the transient model. In the steady-state model, the user can choose the type of cycle to run, and one of either the line speed V_s or the gas addition rate $\dot{M}$ for each zone. The steady-state program outputs results for points in the furnace as chosen by the user, as well as values of temperatures, velocities and heat transfer coefficients at each zonal boundary. It also performs an energy balance on the furnace as a check on the calculations. The relevant parts of this output are written to a file from within the steady-state program, and the transient program then reads from this same file to use these values as input. It then prompts the user for new values of V_s and $\dot{M}$ and also strip thickness d_s and strip width w_s if necessary, and the program runs until a new steady-state is reached. To check whether the steady-state to which the transient model program has converged is correct, a steady-state run can be done using the new values that were input to the transient program, and the results from the two runs compared.

Therefore, the initial conditions can be written as

$$\begin{aligned} T_s(x,0) &= T_{s0}(x), \\ T_g(x,0) &= T_{g0}(x), \\ T_w(x,0) &= T_{w0}(x), \\ V_g(x,0) &= V_{g0}(x), \\ h(x,0) &= h_0(x), \\ \dot{m}_g(x,0) &= \dot{m}_{g0}(x), \end{aligned}$$

and the boundary conditions, as have been shown before, given by

$$T_s(l,t) = T_{s0}(l), \tag{2.71}$$

for the strip, and

$$\frac{\partial T_g}{\partial t} = \frac{\dot{M}(h_{ad} - h_g) - Q_{gs}}{\rho_g(w_f d_f - w_s d_s)c_{pg}} \text{ at } x = 0, \tag{2.72}$$

for the gas.

The final form of the finite-difference equations to be solved is now given. The Lax-Wendroff equation is used within a zone, and the second-order upwind method is used on the zonal boundaries. The Lax-Wendroff equation for the strip is slightly different from that for the gas because the strip flows in the opposite direction to the positive. It takes the form

$$\begin{aligned} T_{s_j}^{n+1} &= \tfrac{1}{2}c_{s_j}^n(1+c_{s_j}^n)T_{s_{j+1}}^n + (1-\{c_{s_j}^n\}^2)T_{s_j}^n \\ &\quad - \tfrac{1}{2}c_{s_j}^n(1-c_{s_j}^n)T_{s_{j-1}}^n + \triangle t^n(\mathrm{RHS}_s)_j^n, \end{aligned} \tag{2.73}$$

and for the second-order upwind method,

$$\begin{aligned} T_{s_j}^{n+1} &= -\tfrac{1}{2}c_{s_j}^n(1-c_{s_j}^n)T_{s_{j+2}}^n + c_{s_j}^n(2-c_{s_j}^n)T_{s_{j+1}}^n \\ &\quad + \tfrac{1}{2}(1-c_{s_j}^n)(2-c_{s_j}^n)T_{s_j}^n + \triangle t^n(\mathrm{RHS}_s)_j^n. \end{aligned} \tag{2.74}$$

The gas equation for the Lax-Wendroff method is,

$$\begin{aligned} T_{g_j}^{n+1} &= \tfrac{1}{2}c_{g_j}^n(1+c_{g_j}^n)T_{g_{j-1}}^n + (1-\{c_{g_j}^n\}^2)T_{g_j}^n \\ &\quad - \tfrac{1}{2}c_{g_j}^n(1-c_{g_j}^n)T_{g_{j+1}}^n + \triangle t^n(\mathrm{RHS}_g)_j^n, \end{aligned} \tag{2.75}$$

and for the second-order upwind method,

$$\begin{aligned} T_{g_j}^{n+1} &= -\tfrac{1}{2}c_{g_j}^n(1-c_{g_j}^n)T_{g_{j-2}}^n + c_{g_j}^n(2-c_{g_j}^n)T_{g_{j-1}}^n \\ &\quad + \tfrac{1}{2}(1-c_{g_j}^n)(2-c_{g_j}^n)T_{g_j}^n + \triangle t^n(\mathrm{RHS}_g)_j^n, \end{aligned} \tag{2.76}$$

where $c_{s_j}^n = |V_s|^n \triangle t^n / \triangle x_j$, and $c_{g_j}^n = V_{g_j}^n \triangle t^n / \triangle x_j$. The right hand side for the strip equation (RHS_s) is given by

$$\mathrm{RHS}_s = \frac{\alpha T_s^4 + \beta T_g^4 + \gamma T_w^4 + H_s(T_g - T_s)}{\rho_s w_s d_s c_{ps}} \tag{2.77}$$

and the right hand side of the gas equation (RHS_g) by

$$\mathrm{RHS}_g = \frac{\dot{M}(h_{ad} - h_g) - \alpha T_s^4 - \beta T_g^4 - \gamma T_w^4 - H_s(T_g - T_s)}{\rho_g(w_f d_f - w_s d_s)c_{pg}}. \tag{2.78}$$

The program that includes the model should run as quickly as possible. To minimise execution time, the time step is varied throughout the duration of the program so that it is always at its maximum value within the stability range of each relevant parameter. After each time step, the model checks that the parameters affecting stability, such as the gas velocity, are still at values that ensure stability. If the gas velocity has increased and the time step is such that the value of c_g is just within the stability range, then the time step must be decreased to meet the stability requirements. If the gas velocity has decreased, then the time step may be increased (provided that no other parameters have changed that adversely affect stability) and the program is able to run faster. For this model, the method will be stable provided that the conditions

$$\triangle t \leq \triangle x/V_g, \tag{2.79}$$

$$\triangle t \leq \triangle x/V_s, \tag{2.80}$$

are satisfied at each time step and at each grid point, using the Lax-Wendroff stability criterion that $0 < c \leq 1$. The program checks every value of the gas velocity at each grid point in the furnace to ensure stability, since both the gas velocity and the grid spacing vary from point to point and zone to zone.

2.3.4 Results

Some results of runs of the adiabatic wall model are shown in this section. The results from two runs are displayed: a cycle change from a hard to soft-iron cycle, then a cycle change from a soft to hard-iron cycle. This required two runs of the steady-state program — one for a hard-iron cycle, the other for a soft-iron cycle — to provide the input data and to test the model. The values used for the steady-state program runs for each of the cycles are shown in Table 2.2.

quantity	hard iron	soft iron
line speed (m/min)	78.4224	70.4402
zone 1 gas flow (m^3/hr)	160	200
zone 2 gas flow (m^3/hr)	50	150
zone 3 gas flow (m^3/hr)	0	0
zone 4 gas flow (m^3/hr)	0	0
zone 5 gas flow (m^3/hr)	0	0
zone 6 gas flow (m^3/hr)	0	0
strip thickness (mm)	0.6	0.6
strip width (mm)	1175	1175
set point temp (^{o}C)	450	650
air:fuel ratio	9.5:1	9.5:1

Table 2.2: Adiabatic wall model : settings for the two steady-states

The adiabatic model is successful if it can accurately predict the temperatures of the new steady-state from the previous steady-state. Therefore, if the furnace is initially running a hard-iron cycle, then the model should accurately predict the temperatures for the soft-iron cycle if the new values of the line speed and gas flow rates, as given in Table 2.2, are input to the transient model. The reverse is true for a cycle change from a soft-iron cycle to a hard-iron cycle.

The results for a cycle change from a hard to soft-iron cycle are displayed for the strip, gas and wall temperatures for each point in the furnace after the program has converged to the new values of these temperatures. Strip, gas and wall temperatures are shown in Figures 2.11, 2.12 and 2.13 respectively. The solid lines in these graphs represent the values given by the steady-state program for each point in the furnace, and the dashed lines represent those temperatures calculated by the transient program. The solid line showing the

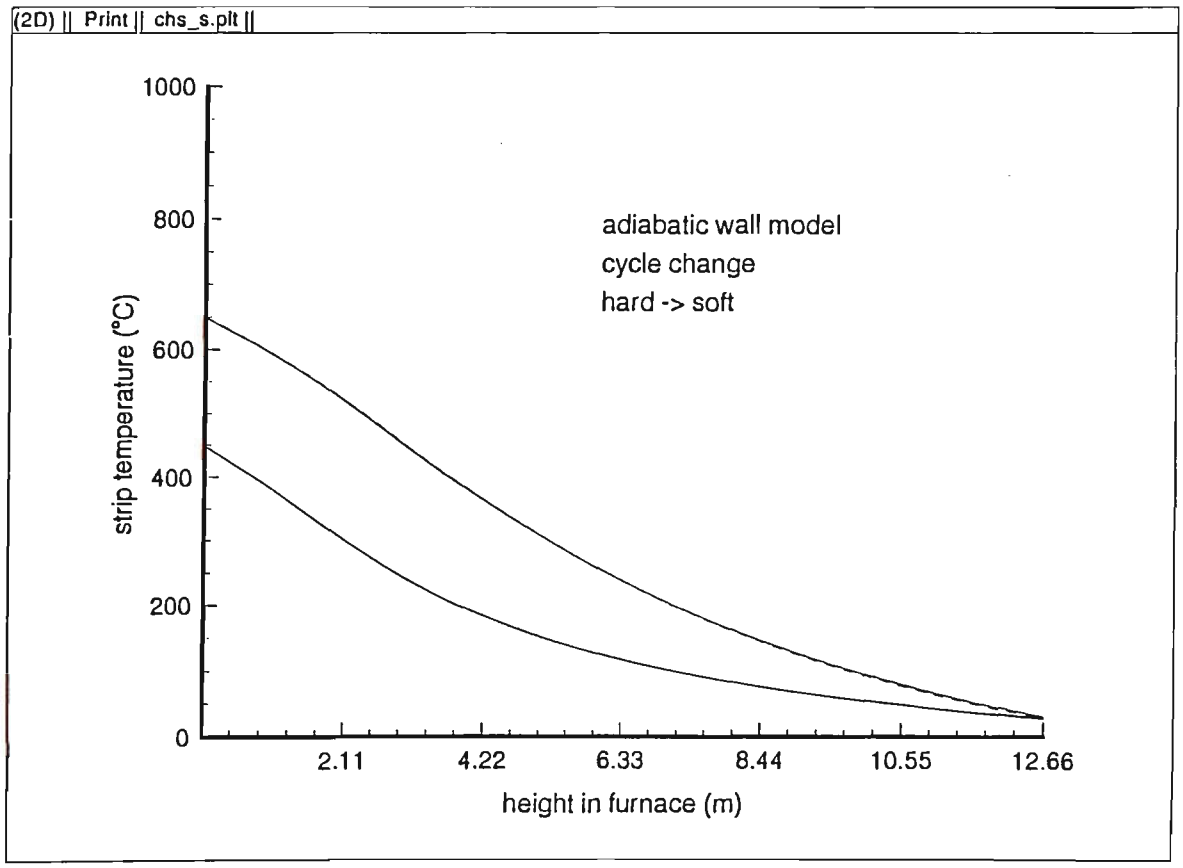

Figure 2.11: Adiabatic wall model : strip temperature - cycle change, hard to soft

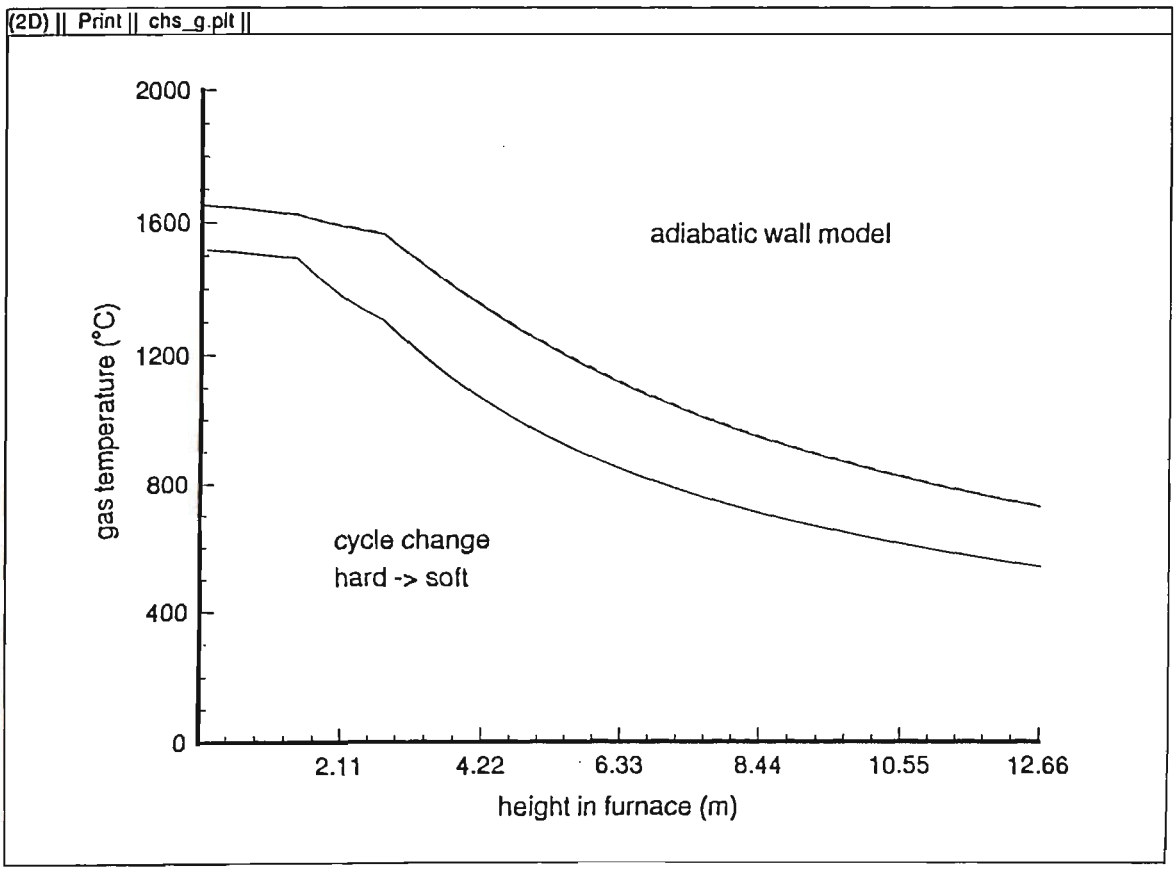

Figure 2.12: Adiabatic wall model : gas temperature - cycle change, hard to soft

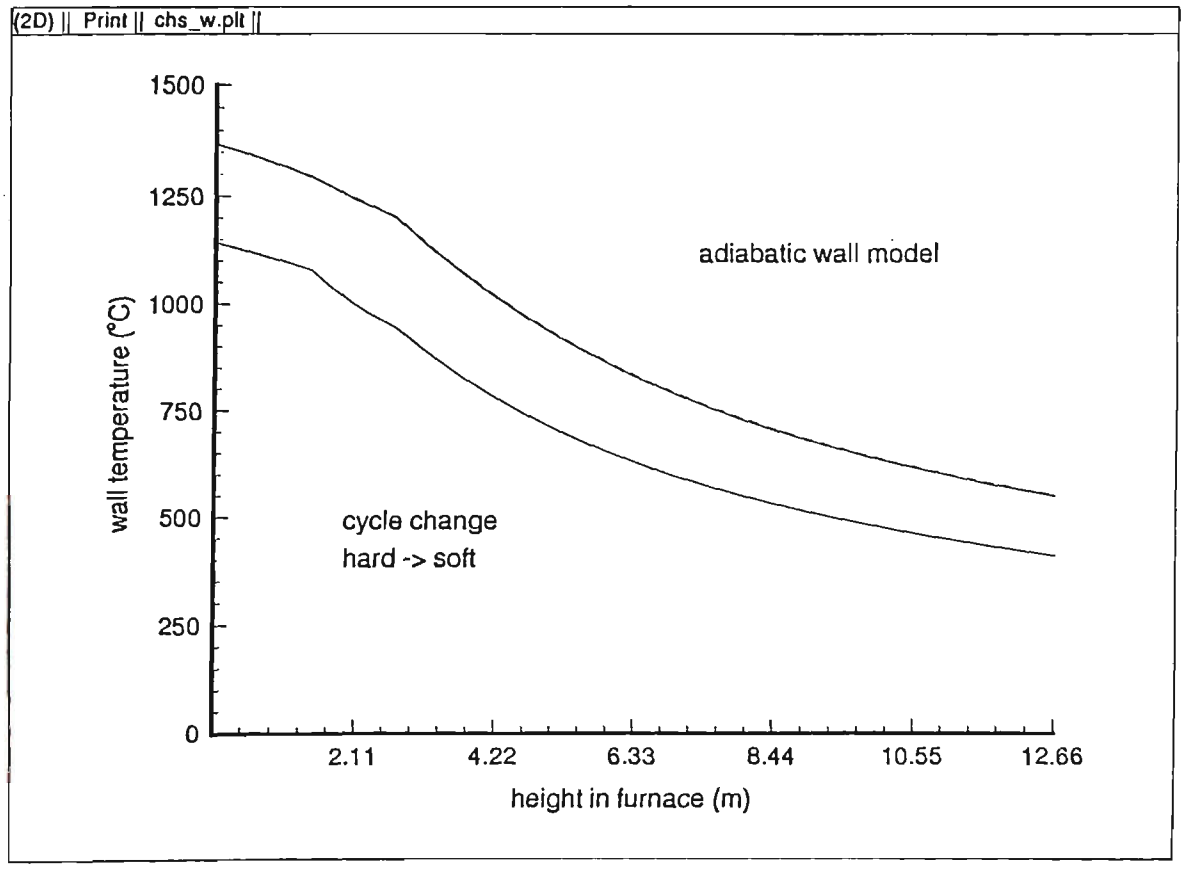

Figure 2.13: Adiabatic wall model : wall temperature - cycle change, hard to soft

higher values therefore represents the soft-iron cycle temperatures, and the solid line showing the lower temperatures are those for the hard-iron cycle.

As is clearly seen, the results that the adiabatic wall model gives in moving from one steady-state to another are very good. In each case, the dashed line closely follows the solid line for the strip, gas and wall temperatures right throughout the furnace, with perhaps the largest deviation about 5-10 K, which is quite acceptable. The difference in strip temperature at the top of the furnace results from the steady-state runs for each cycle converging to slightly different values for T_{s0} in equation (2.67). The slight humps in the gas and wall temperature graphs are found at the zonal boundaries because of the abrupt changes in the gas addition rates found there, as was explained earlier in this chapter.

The second set of results is for a cycle change in the opposite direction, from a soft-iron cycle to a hard-iron cycle. In this instance, therefore, the dashed line of the transient model is compared against the lower solid line of the steady-state model, with the higher solid line providing the input for the transient model. The results are shown in graphical form, as before, for the strip, gas and wall temperatures, in Figures 2.14, 2.15 and 2.16 respectively.

Again the results are extremely good, with the dashed line following the solid line very closely. The different values for T_{s0} obtained by the steady-state runs again cause the strip temperature there to vary slightly from the actual temperature. The gas and the wall temperatures are also followed accurately, even at the zonal boundaries.

2.3.5 Conclusion

These results from the transient model for an adiabatic wall are very good, being in excellent agreement with the results from the steady-state model. This close agreement does not prove that they are both good models, however,

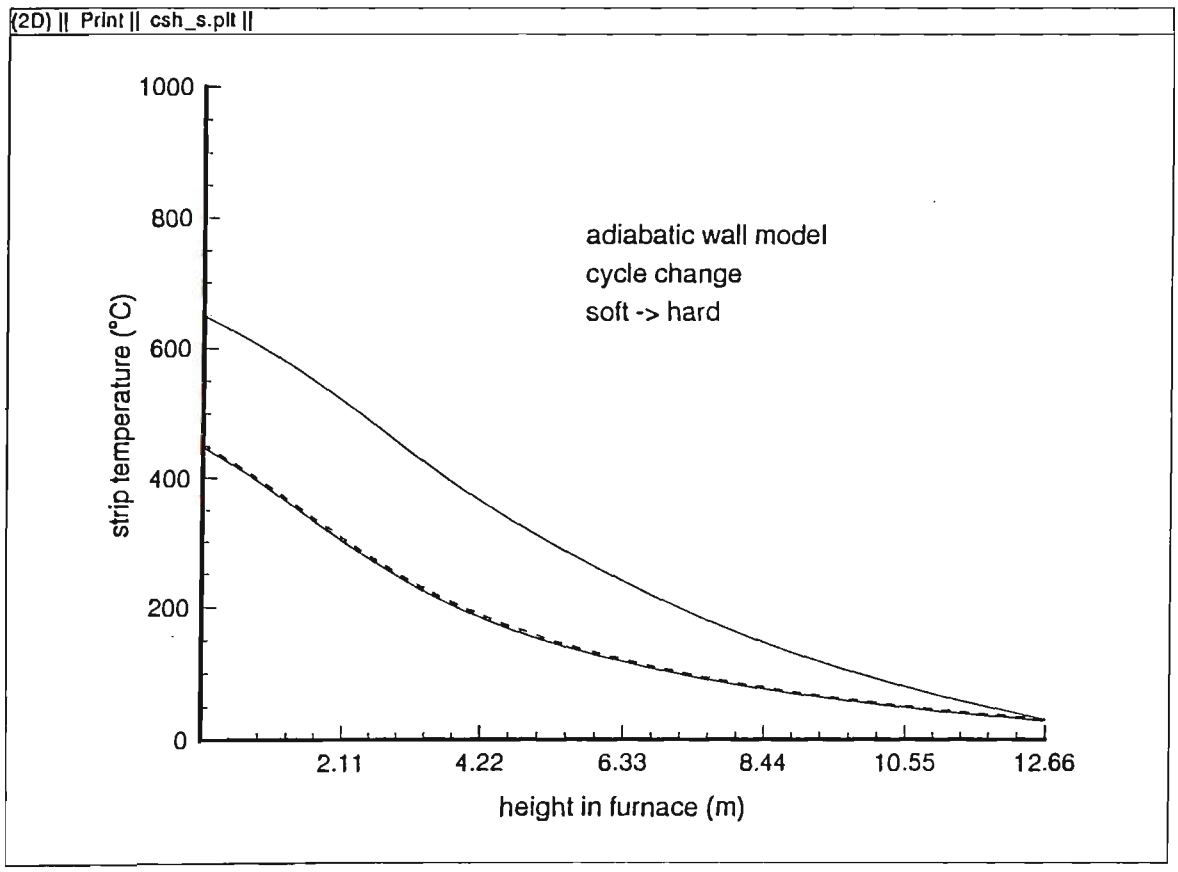

Figure 2.14: Adiabatic wall model : strip temperature - cycle change, soft to hard

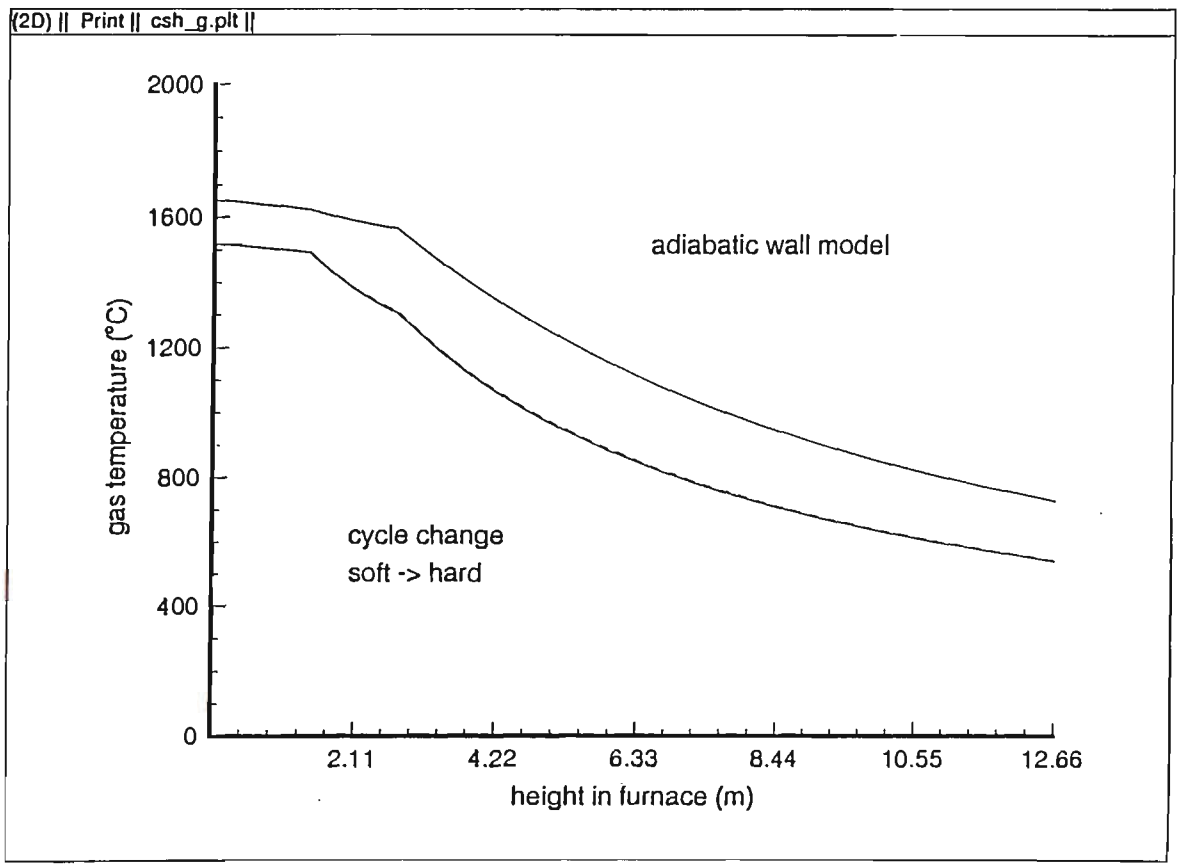

Figure 2.15: Adiabatic wall model : gas temperature - cycle change, soft to hard

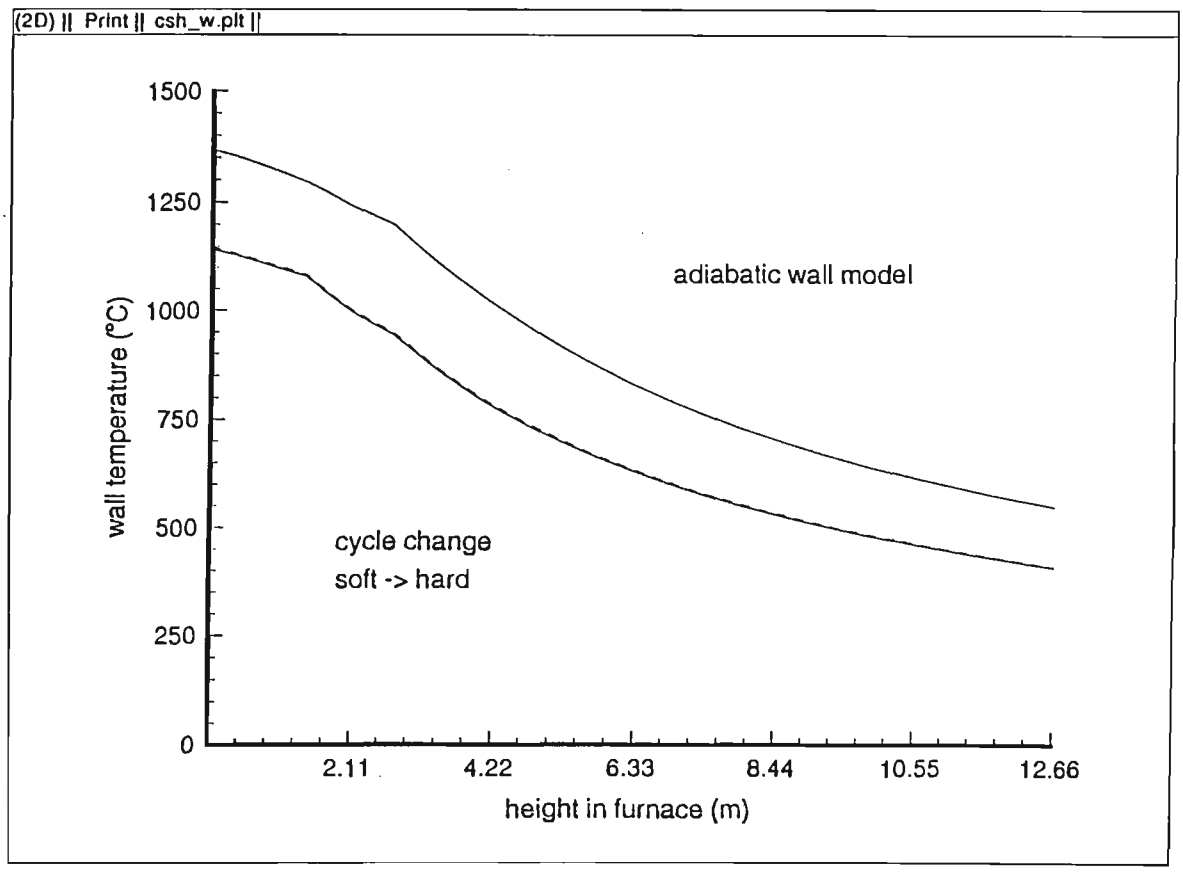

Figure 2.16: Adiabatic wall model : wall temperature - cycle change, soft to hard

because they are based on the same assumptions, and if the assumptions are not good, then they will give the same incorrect results. What it does show is that, using these assumptions, the transient model works well in moving from one steady-state to the next. The adiabatic wall model was invaluable in gaining initial solutions to the equations and, because of its accuracy, was an excellent foundation for the more relevant work on the dynamic wall model.

2.4 Solving the transient equations. Part 2 - dynamic wall

Having completed the analysis of the furnace for an adiabatic wall, the more realistic case of a dynamic wall is considered. The reason why the wall is so important in the dynamic response of the furnace is because of its ability to store heat via radiation and convection from the gas and, to a lesser extent, the strip, as was shown in section 2.2. An example of this effect is seen when comparing the results of a run of the model using the adiabatic wall and the dynamic wall. For a cycle change, which involves a step change in gas flow, line speed, etc, the adiabatic wall model indicates that it takes about 30 seconds of real time for the strip temperature to change by around 200 K, which is the correct temperature range for a cycle change. The dynamic wall model, however, suggests that it takes several minutes to fall by less than 200 K. Experimental data taken from the galvanising lines at BHP for the boot strip temperature indicate that the latter model is far more realistic.

2.4.1 Wall finite-difference method

A finite-difference method was sought as the most appropriate means for modelling the wall effects. Because of the high insulation of the wall, most of the heat interaction is expected to occur at or near the wall boundary at the inte-

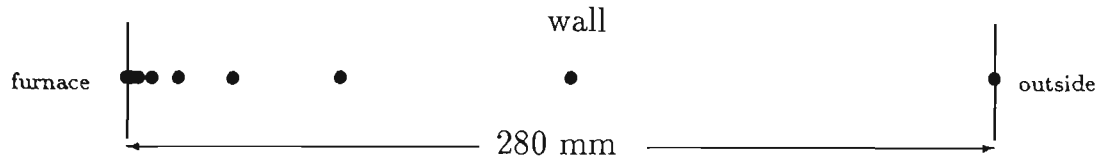

Figure 2.17: Interior grid spacing for the wall

rior of the furnace, with very little heat flow elsewhere in the wall. To model this, the grid spacing was chosen to double in size from the wall/furnace interface to the wall/ambient interface. This is similar to the technique used by Stone & Morrison [51], where a finite element method is used instead, and the temperature at the wall/furnace interface is determined by extrapolation. The advantage of this method is that it substantially reduces the number of grid points required and hence the computation time for the model. A diagram of the grid spacing used for the wall is shown in Figure 2.17.

The basic equations used are the typical 1-D Fourier heat conduction equation with constant thermal diffusivity, ie,

$$\kappa_w \frac{\partial^2 T_w}{\partial z^2} = \frac{\partial T_w}{\partial t}, \tag{2.81}$$

with the boundary condition at the wall/furnace interface ($z = 0$),

$$-k_w \frac{\partial T_w}{\partial z} = Q_{gw}/P_w. \tag{2.82}$$

These equations hold for all x in the furnace. The simple forward-time, centred-space (FTCS) construction (Hildebrand [15]) for the wall equation results in a finite-difference equation for a uniform grid of the form

$$T_{wj,l}^{n+1} = s_w T_{wj,l+1}^{n} + (1 - 2s_w) T_{wj,l}^{n} + s_w T_{wj,l-1}^{n} \tag{2.83}$$

with $s_w = \kappa_w \triangle t/(\triangle z)^2$, and $l = 0, L$ (the wall/furnace boundary to the outside wall). However, a geometrically increasing grid spacing is desired, and so

according to Noye [33], the spatial second derivative is expanded as

$$\frac{\partial^2 T_w}{\partial z^2} = \frac{T_{wj,l+1}^{\ n} - (\nu_l + 1)T_{wj,l}^{\ n} + \nu_l T_{wj,l-1}^{\ n}}{\frac{1}{2}\triangle z_l \triangle z_{l-1}(\nu_l + 1)} \tag{2.84}$$

with $\nu_l = \triangle z_l / \triangle z_{l-1}$. Doubling the grid spacing sets $\nu_l = 2$, and $\triangle z_l = 2\triangle z_{l-1}$. Therefore

$$\frac{\partial^2 T_w}{\partial z^2} = \frac{4}{3}\left(\frac{T_{wj,l+1}^{\ n} - 3T_{wj,l}^{\ n} + 2T_{wj,l-1}^{\ n}}{(\triangle z_l)^2}\right) \tag{2.85}$$

As a result, a general finite-difference form for the 1-D heat conduction equation is

$$T_{wj,l}^{\ n+1} = s_{wl}^{\ n}\nu_l T_{wj,l-1}^{\ n} + (1 - s_{wl}^{\ n}(\nu_l + 1))T_{wj,l}^{\ n} + s_{wl}^{\ n} T_{wj,l+1}^{\ n} \tag{2.86}$$

with

$$s_{wl}^{\ n} = \frac{2\kappa_w \triangle t^n}{(1 + \nu_l)\triangle z_{l-1}\triangle z_l}$$

So the form of the FDM for this case is

$$T_{wj,l}^{\ n+1} = 2S_{wl}^{\ n} T_{wj,l-1}^{\ n} + (1 - 3S_{wl}^{\ n})T_{wj,l}^{\ n} + S_{wl}^{\ n} T_{wj,l+1}^{\ n} \tag{2.87}$$

for $l = 1, L-1$ where

$$S_{wl}^{\ n} = \frac{4}{3}\frac{\kappa_w \triangle t^n}{(\triangle z_l)^2}$$

The trade-off for using a non-uniform grid is a change in the size of the truncation error to $O(\triangle z)$ for a grid spacing that doubles in size, but it has been shown that a non-uniform grid can be more accurate than uniform grids (and obviously much faster) when modelling profiles such as this (see Noye [33]).

The boundary conditions for the wall now include one for the outside surface, in that the temperature is considered to be constant there, ie,

$$T_{wj,L}^{\ n} = T_{w,\text{outside}}, \tag{2.88}$$

where the outside wall temperature is taken to be 40°C. The other boundary condition, at the wall/furnace interface, is found from equation (2.82). Using

a simple forward-space discretisation with rearrangement gives

$$T_{wj,0}^{n+1} = T_{wj,1}^{n+1} - \frac{1}{k_w}\triangle z_0 (Q_{gw_j}^{n+1}/P_w) \tag{2.89}$$

where

$$Q_{gw_j}^{n+1} = \mu(T_{sj}^{n+1})^4 + \nu(T_{gj}^{n+1})^4 + \xi(T_{wj,0}^{n})^4 + H_{wj}(T_{gj}^{n+1} - T_{wj,0}^{n}). \tag{2.90}$$

The wall temperature from the nth time step is used, rather than an iterative procedure, to find $T_{wj,0}^{n+1}$, because there is only a small change in the wall temperature from one time step to the next, and hence only a small change in Q_{gw}.

This wall-finite difference model was compared to those found in Stone & Morrison [51] with good agreement, justifying its use here.

2.4.2 Dynamic wall model equations

Having constructed a finite-difference method for the case of the dynamic wall, the equations explaining the transient situation in the annealing furnace for real furnace operation are complete. They are equations (2.37), (2.38) and (2.81) and are reproduced here, ie

$$\frac{\partial T_s}{\partial t} - V_s\frac{\partial T_s}{\partial x} = \frac{Q_{gs}}{\rho_s w_s d_s c_{ps}}, \tag{2.91}$$

$$\frac{\partial T_g}{\partial t} + V_g\frac{\partial T_g}{\partial x} = \frac{Q_{comb} - Q_{gs} - Q_{gw}}{\rho_g(w_f d_f - w_s d_s)c_{pg}}, \tag{2.92}$$

$$\frac{\partial T_w}{\partial t} - \kappa_w\frac{\partial^2 T_w}{\partial z^2} = 0, \tag{2.93}$$

where

$$\begin{aligned} Q_{comb} &= \dot{M}(h_{ad} - h_g), \\ Q_{gs} &= \alpha T_s^4 + \beta T_g^4 + \gamma T_w^4 + H_s(T_g - T_s) \\ &= P_s(B_{gs} - B_s + q_{s,c}), \\ Q_{gw} &= \mu T_s^4 + \nu T_g^4 + \xi T_w^4 + H_w(T_g - T_w) \\ &= P_w(B_{gw} - B_w + q_{w,c}), \end{aligned}$$

recalling that the x direction is upwards in the furnace with $x = 0$ at the furnace base, and z is into the wall (perpendicular to x), with $z = 0$ the furnace boundary with the wall. The boundary conditions for these equations are, for the strip at the top of the furnace, $x = l$,

$$T_s(l,t) = T_{s0}(l); \tag{2.94}$$

for the gas at the boot of the furnace, the Q_{gw} term is now included, so

$$\frac{\partial T_g}{\partial t} = \frac{Q_{comb} - Q_{gs} - Q_{gw}}{\rho_g(w_f d_f - w_s d_s)c_{pg}} \text{ at } x = 0, \tag{2.95}$$

and for the wall at the inside and outside interfaces,

$$-k_w \frac{\partial T_w}{\partial z} = Q_{gw}/P_w \text{ at } z = 0 \tag{2.96}$$

$$T_w(d_w,t) = T_{w,\text{outside}} \text{ at } z = d_w \tag{2.97}$$

where d_w is the thickness of the wall.

The finite-difference forms of the equations for the dynamic wall are very similar to those for the adiabatic wall, with the major difference being the inclusion of the wall heat flux in the gas equation. The form of equations (2.73), (2.74), (2.75) and (2.76) is the same for the dynamic wall case, as is the right hand side of the strip equation shown in (2.77). The right hand side of the gas equation (2.78), with the wall included, becomes

$$\begin{aligned} \text{RHS}_g = {} & (\dot{M}(h_{ad} - h_g) - (\alpha + \mu)T_s^4 - (\beta + \nu)T_g^4 - (\gamma + \xi)T_w^4 \\ & - H_s(T_g - T_s) - H_w(T_g - T_w))/(\rho_g(w_f d_f - w_s d_s)c_{pg}). \end{aligned} \tag{2.98}$$

The finite-difference form for the gas boundary condition at the furnace boot, (2.95), simply involves a forward-time approximation to the time derivative, with the right hand side of the equation evaluated at the (n, j)th grid point. The finite-difference forms for the wall equations have been shown already in equation (2.87), with the boundary conditions (2.88) and (2.89).

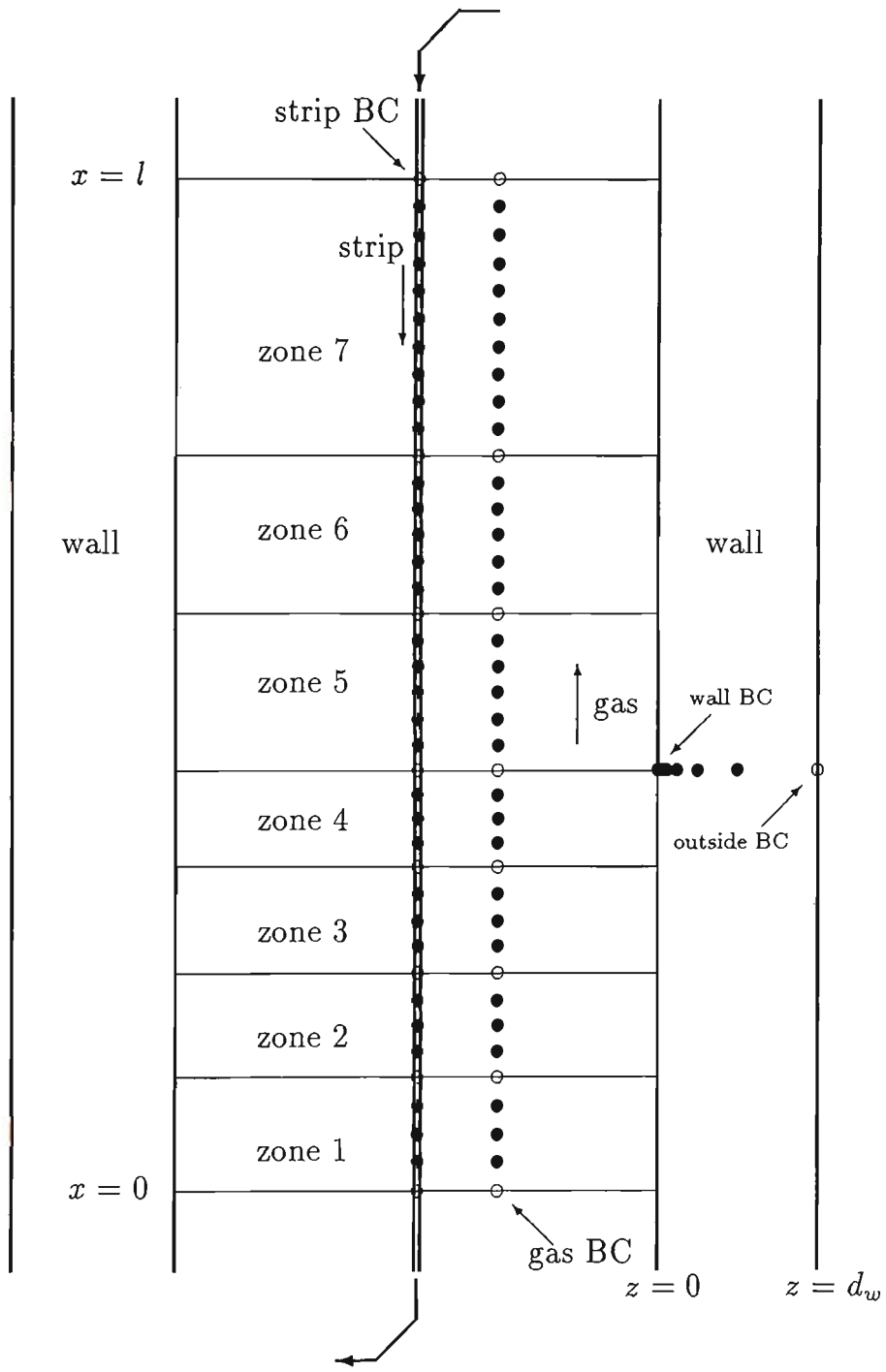

Figure 2.18: Furnace showing 39pt grid, including wall

Because of the inclusion of the finite-difference method for the wall, an extra stability test must be included in the model. The FTCS method used for the wall is stable as long as

$$0 < s_w \leq 1/2,$$

and for a variable grid, stability is guaranteed for the method shown in equation (2.87) so long as the smallest grid spacing meets this criterion. Therefore the condition

$$\triangle t \leq \frac{1}{2}\frac{(\triangle z_0)^2}{\kappa_w}, \tag{2.99}$$

needs to be added to those stated in equations (2.79)-(2.80) to ensure that the method is stable, while still running with the optimal time step.

These finite-difference forms are therefore all that is required to solve the equations describing the furnace. A diagram of the furnace grid arrangement, including the grid spacing in the wall, is shown in Figure 2.18. With initial conditions provided from the furnace steady-state model in Martire [28], these equations can be solved for any transient in the furnace.

2.4.3 Results

This section presents some of the results of the full transient equations for the furnace with the dynamic wall effect included. Six possible types of transients that the galvanising line processes during operation are considered. These transients are as follows:

- cycle change, hard iron to soft iron
- cycle change, soft iron to hard iron
- thickness increase, hard iron cycle
- thickness decrease, hard iron cycle

- thickness increase, soft iron cycle
- thickness decrease, soft iron cycle

The cycle changes include section changes, because practically every cycle change involves coils of different thickness. Thickness changes influence the furnace operation more than width changes, at least where the centreline strip temperature is concerned.

It should be noted here, that when the line data was input to the steady-state program in order to obtain initial values for the transient program, it was found that the steady-state program gave lower values for the gas flows than those that occurred on the line. One reason for this is that the strip emissivity function used by the steady-state program tends to overestimate the strip temperature quite significantly, and hence requires less gas to heat the strip to a higher temperature. A more realistic emissivity/absorptivity function found in Stone & Morrison [51] is implemented into the model for the DFF on MCL6, as well as for the radiant tube furnace model of Chapter 3. In the present CGL2 DFF model, however, percentage changes to the gas flows were used instead. The actual values from the lines are displayed in the tables shown in this chapter, but these values were not the values used in the steady-state and transient programs. Using the percentage change is a valid test for checking whether this model is successful or not when comparing it to the line data.

Another factor was the unavailability, at the time, of any more reliable data than that shown. The measured data had to be interpreted by hand, as there was no numerical data acquisition system available on CGL2. It is intended that most of BHP's galvanising lines should be equipped with facilities that generate data for all relevant furnace parameters, but when this project was carried out, CGL2 did not have that capacity. The more modern MCL6 line does provide this information as is seen in later chapters.

quantity	old	new
line speed (m/min)	74.0	67.2
zone 1 gas flow (m^3/hr)	190	190
zone 2 gas flow (m^3/hr)	195	195
zone 3 gas flow (m^3/hr)	107	130
zone 4 gas flow (m^3/hr)	0	90
zone 5 gas flow (m^3/hr)	0	0
zone 6 gas flow (m^3/hr)	0	0
strip thickness (mm)	0.75	0.55
strip width (mm)	983	944
set point temp (°C)	460	650
air:fuel ratio	8.5:1	8.5:1

Table 2.3: Dynamic wall model - old and new settings - cycle change, hard to soft

The results shown compare the output of this model with the experimental data given from CGL2 at Springhill works, Port Kembla. The data shown from the line follows the variation of the boot strip temperature over time; hence the comparison is made between that variation given by the experimental data as well as by the model. The results of these comparisons are given in the remainder of this chapter. It should be noted that the line output shown in the following figures all have time increasing *from right to left*. Also, in all of the graphs where the boot strip temperature from the line and the model are compared, the line data is represented by the dashed line, and the model data by the solid line.

The first case considered is for a cycle change from a hard iron to a soft iron cycle. The cycle change involved a line speed decrease of around 10% and the gas flows were increased by around 5%. The actual old and new

settings used on the lines are shown in Table 2.3. There is a large section decrease involved in this cycle change also. In the program, it was decided to set the weld initially to be 30 m away from the top of the furnace, and to change the line speed after 30 s. The gas flows were changed when the program commenced. The program was run for seven minutes, because the data from the lines shown in Figure 2.19 indicated that the transient lasted for about that length of time. The result of the model for this situation for the variance of the boot strip temperature over time is shown in Figure 2.20.

When comparing Figures 2.19 and 2.20, the similarities are clear. The combination of lower line speed, increased gas flow and smaller section cause the boot strip temperature on the line to climb rapidly initially, and then slowly decay to the new value. This trend and the final temperature reached is close to that obtained by the model. It is seen that after seven minutes, the model and line data are very similar in the value given for the final temperature reached.

The second example is for a cycle change from a soft to hard iron cycle, with the initial and final values from the line given in Table 2.4. The line data shown in Figure 2.21 is not as clearly defined as in the previous example, because the gas flows are varied more than once, rather than a step change being used. The increase in thickness and width of the strip contributes to a further fall in the strip temperature several minutes later. In this case, the line speed remained unchanged and the gas flows were reduced by about one-third.

In this instance for the model, the weld was set initially at 25 m away from the top of the furnace, and the gas flows were again changed as soon as the program began. The program was allowed to run for ten minutes this time, and the results from the model compare well with those from the line. The initial large drop from the graph of the model data against the line data shown in Figure 2.22 is caused by the decrease in the gas flows, and then

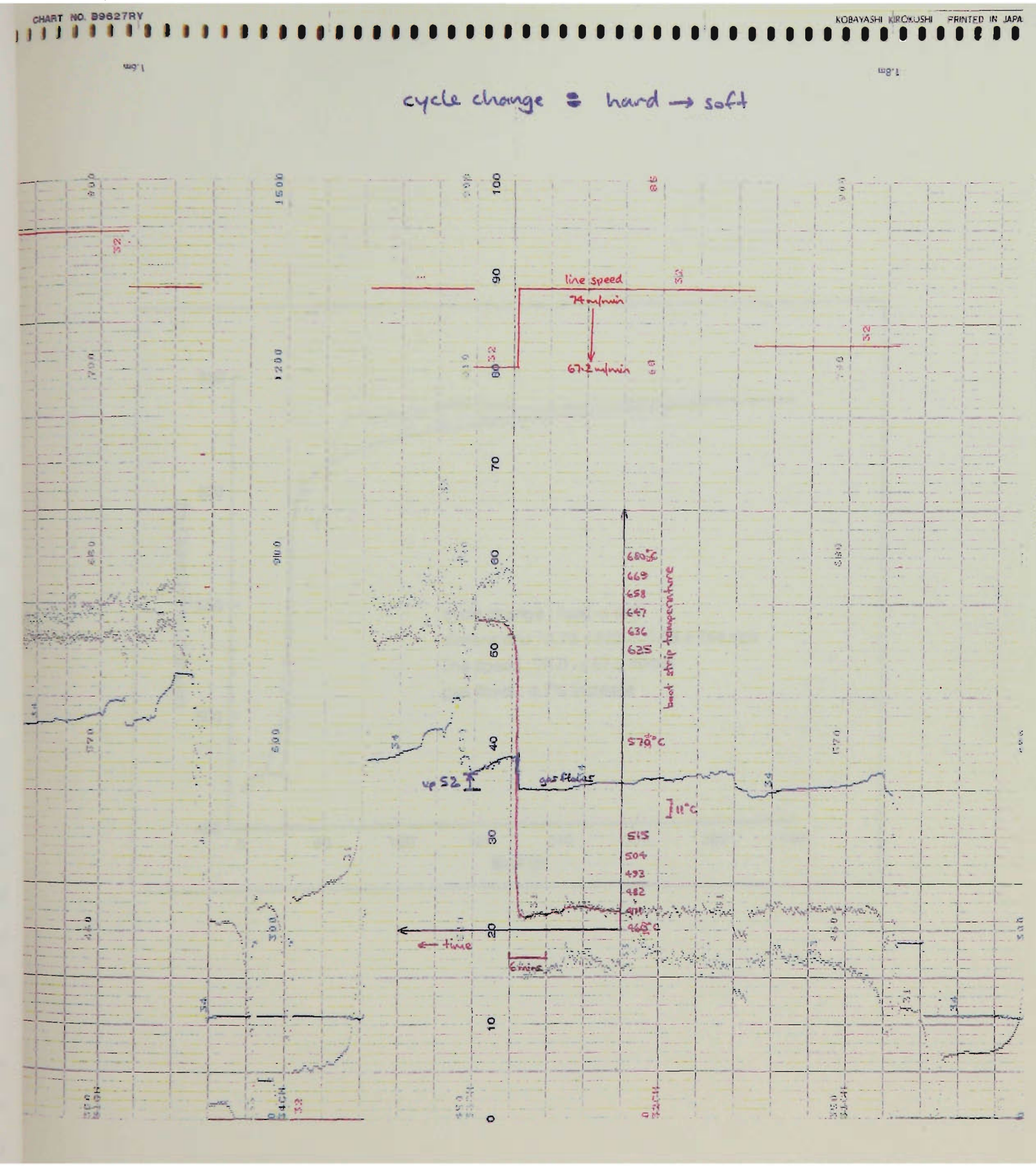

Figure 2.19: From line : boot strip temperature - cycle change, hard to soft

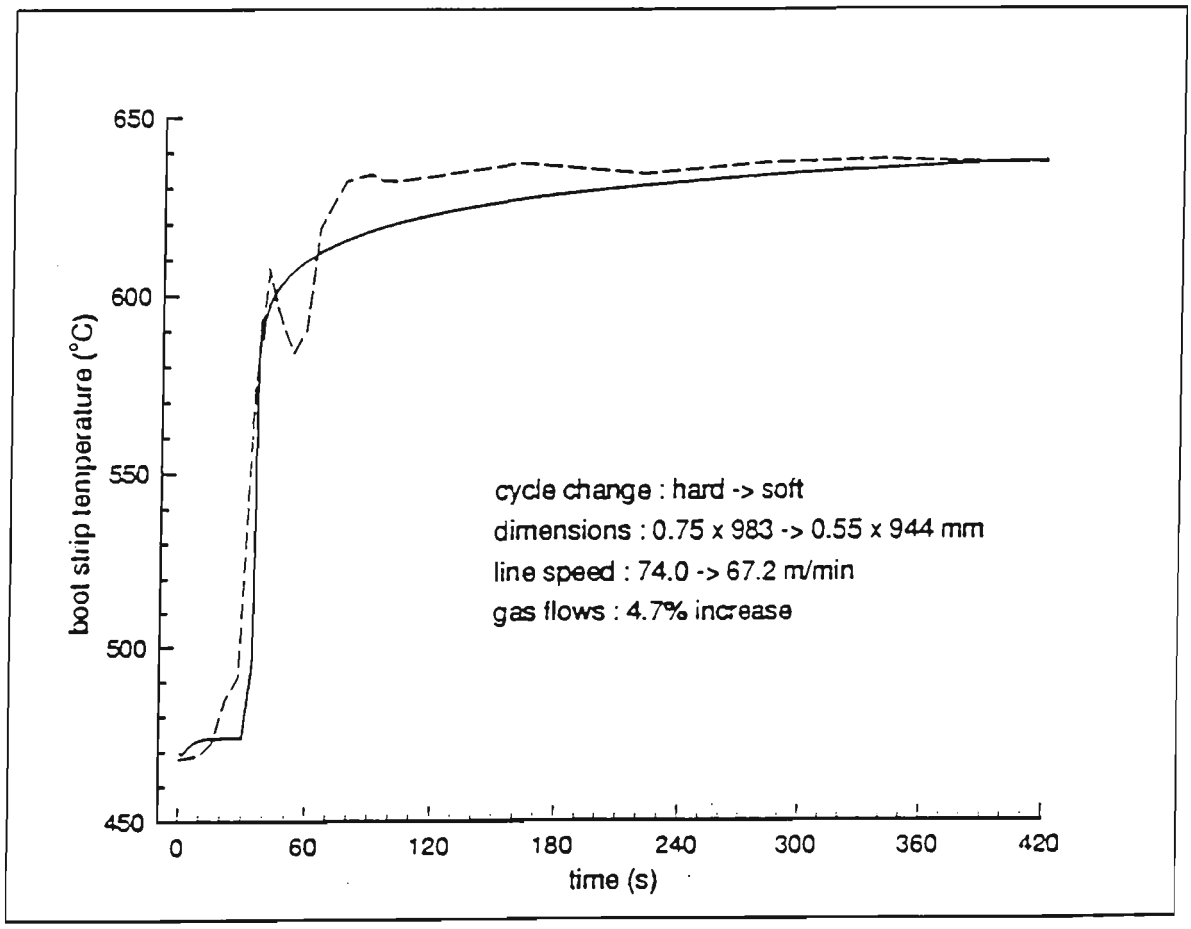

Figure 2.20: From model : boot strip temperature - cycle change, hard to soft

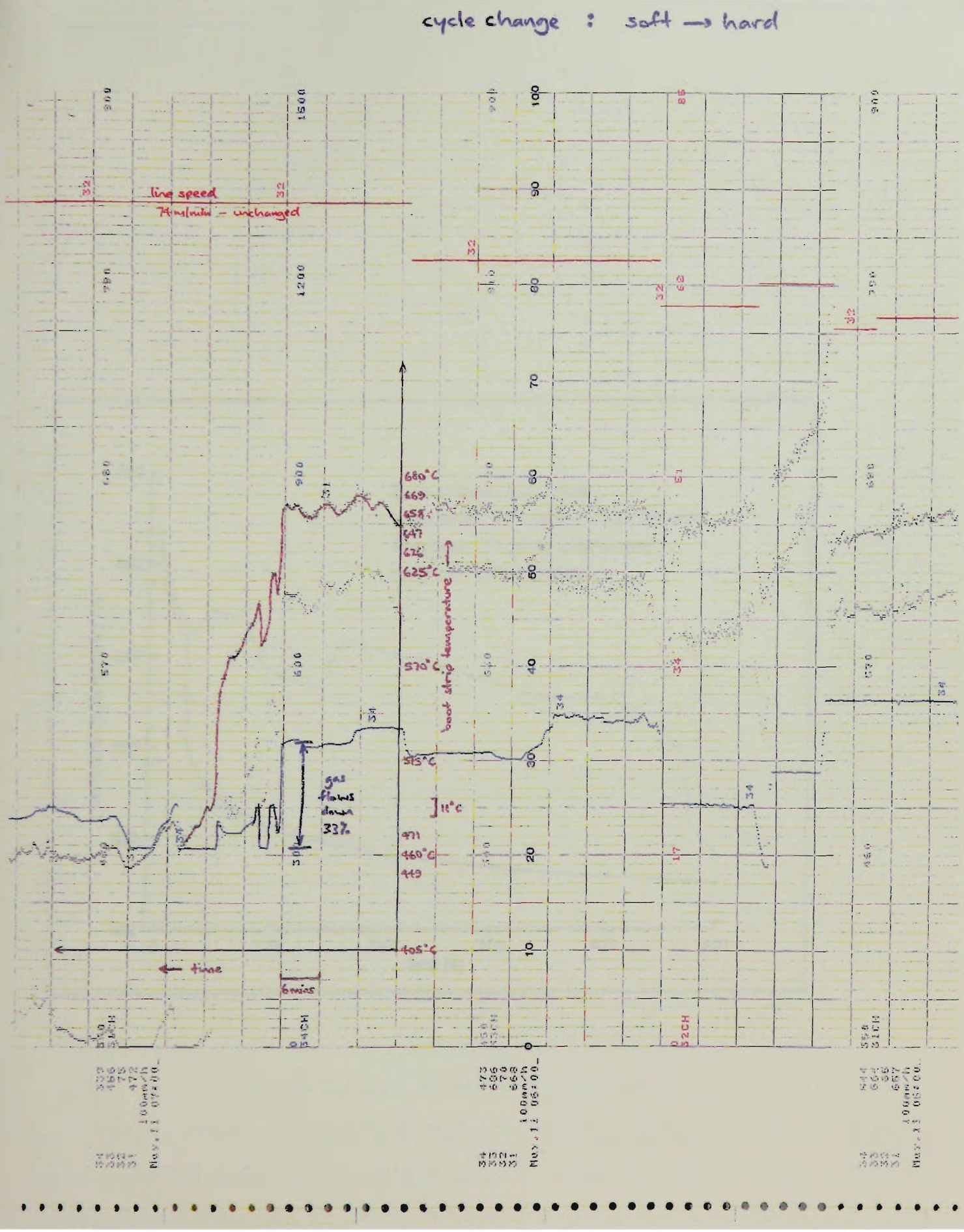

Figure 2.21: From line : boot strip temperature - cycle change, soft to hard

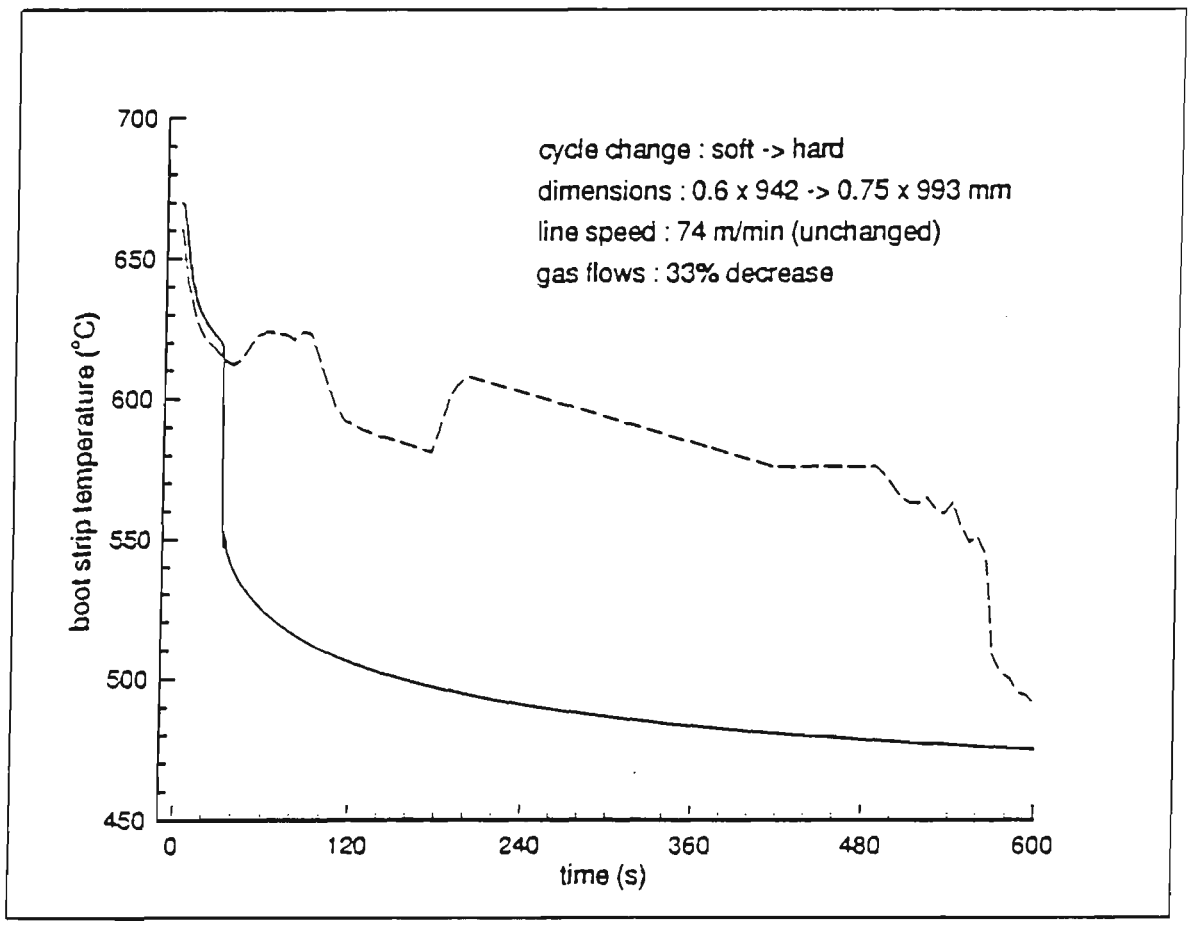

Figure 2.22: From model : boot strip temperature - cycle change, soft to hard

quantity	old	new
line speed (m/min)	74.0	74.0
zone 1 gas flow (m^3/hr)	191	191
zone 2 gas flow (m^3/hr)	159	112
zone 3 gas flow (m^3/hr)	99	0
zone 4 gas flow (m^3/hr)	0	0
zone 5 gas flow (m^3/hr)	0	0
zone 6 gas flow (m^3/hr)	0	0
strip thickness (mm)	0.6	0.75
strip width (mm)	942	993
set point temp (^{o}C)	670	460
air:fuel ratio	9.0:1	9.0:1

Table 2.4: Dynamic wall model - old and new settings - cycle change, soft to hard

the further sudden drop is caused by the weld passing the boot of the furnace. The model converges to a final value for the boot strip temperature of around 475^{o}C, which is very similar to that from the line. If the total change in the gas flow rates over the period examined was introduced as a step change instead, then the line output would look similar to the model output.

Having looked at cycle changes, the more frequent case of thickness changes is considered. The values used in the program for the first of these are given in Table 2.5. For this transient, the line speed was decreased and the gas flows slightly increased. In the model, the weld was set to be 10 m away from the furnace, the line speed changed after 30 s, and the gas flows changed when the program began. The line data is shown in Figure 2.23 and the results of the model compared with the line data in Figure 2.24.

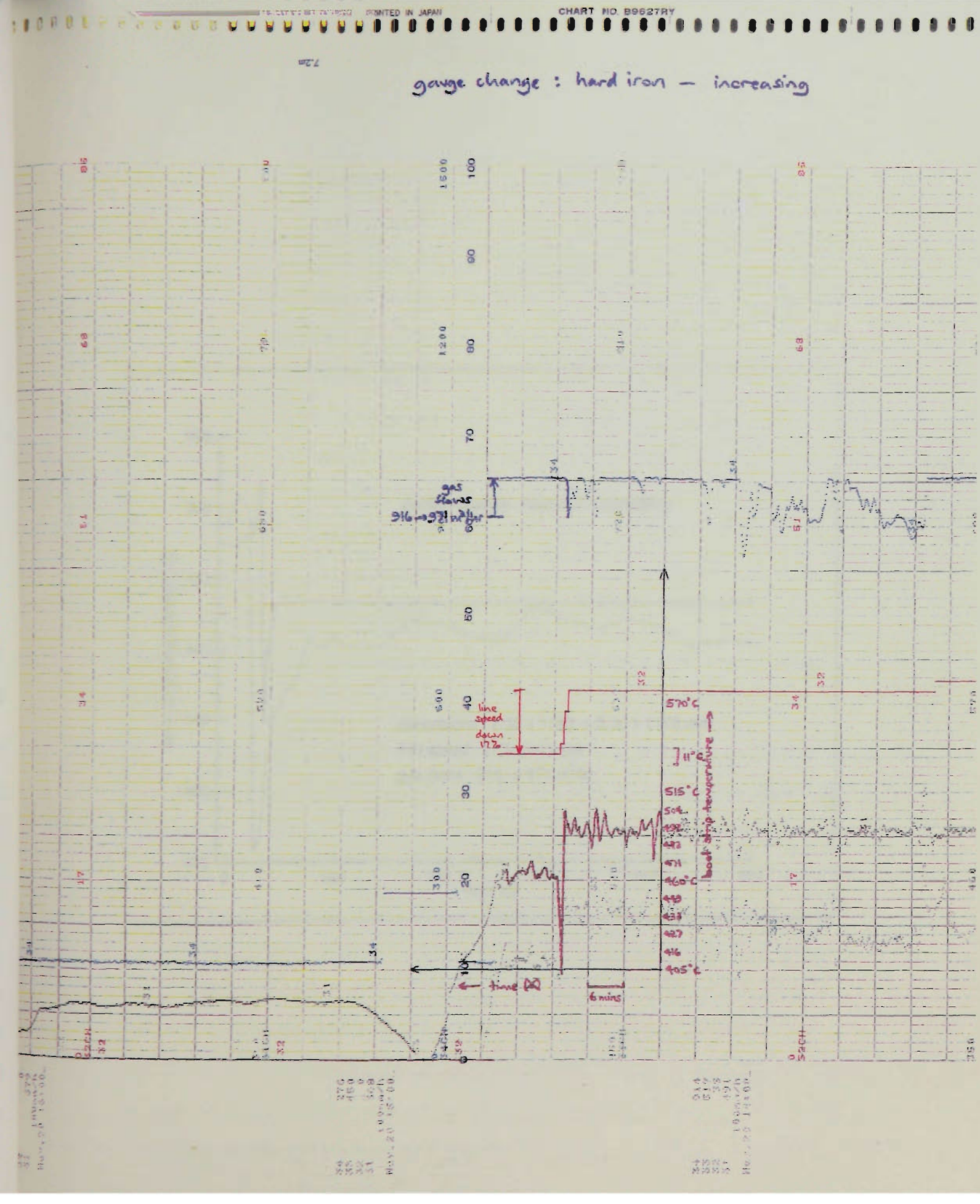

Figure 2.23: From line : boot strip temperature - increasing thickness, hard iron

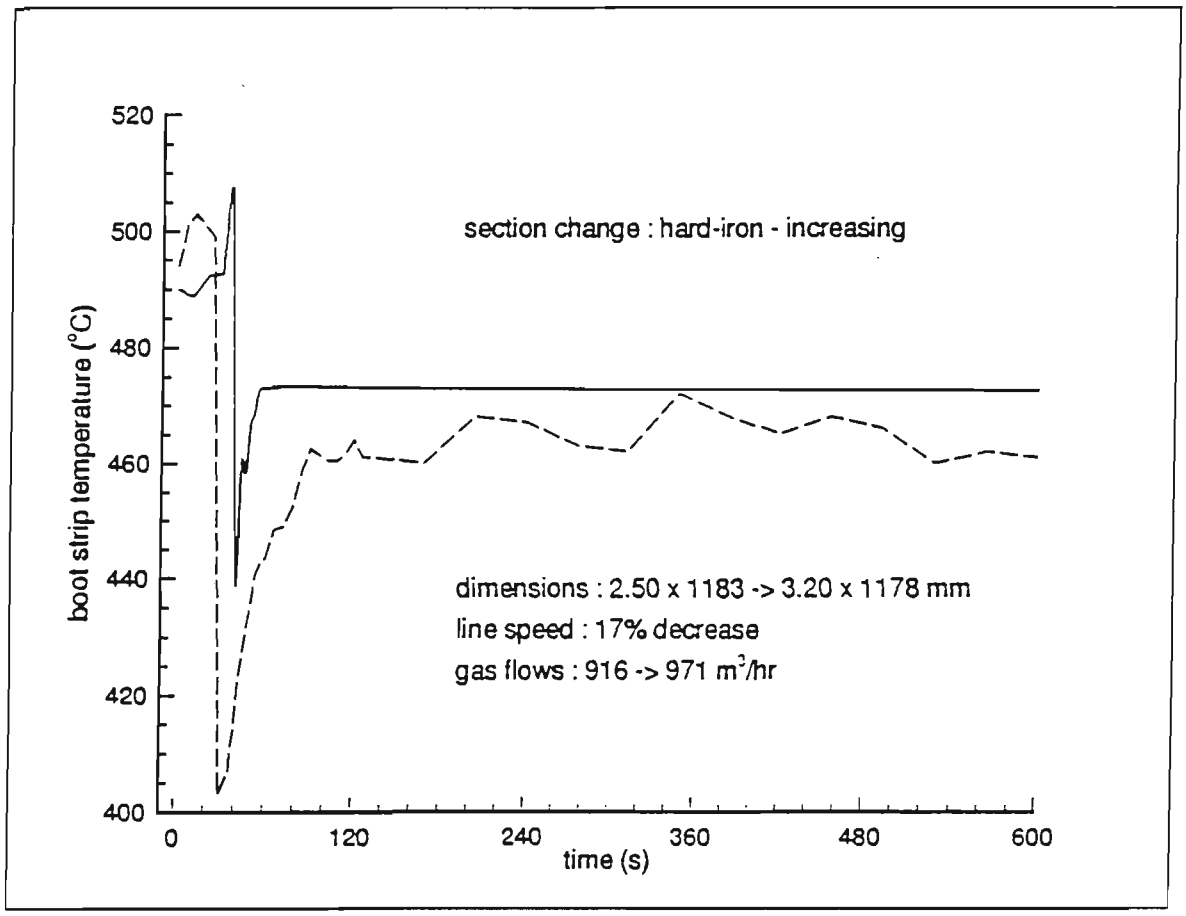

Figure 2.24: From model : boot strip temperature - increasing thickness, hard iron

quantity	old	new
line speed (m/min)	35.1	29.1
zone 1 gas flow (m^3/hr)	191	191
zone 2 gas flow (m^3/hr)	195	195
zone 3 gas flow (m^3/hr)	190	190
zone 4 gas flow (m^3/hr)	150	150
zone 5 gas flow (m^3/hr)	190	245
zone 6 gas flow (m^3/hr)	0	0
strip thickness (mm)	2.50	3.20
strip width (mm)	1183	1178
set point temp (°C)	470	450
air:fuel ratio	8.5:1	8.5:1

Table 2.5: Dynamic wall model - old and new settings - thickness increase, hard iron

Again the comparison between the two is good. It is difficult to know exactly how far the weld is away from the furnace initially; since this distance is not recorded, it must be guessed. The model output in Figure 2.24 indicates a small rise at first, due to the small increase in gas flows, followed by a larger rise due to the decrease in line speed. The presence of the weld passing the furnace boot then causes a large drop in temperature of around 70 K over a very short time, before the effect of the line speed and gas flow changes return the temperature to near the desired set point value. The line data output also shows a large drop in the strip temperature due to the weld, and a return to a value around 20-30 K lower than the initial value. The usefulness of the model is again demonstrated in these results.

For a thickness decrease on a hard iron cycle, the line and the model both converge to a similar temperature eventually, but the model shows

quantity	old	new
line speed (m/min)	30.3	37.8
zone 1 gas flow (m^3/hr)	193	190
zone 2 gas flow (m^3/hr)	194	195
zone 3 gas flow (m^3/hr)	97	140
zone 4 gas flow (m^3/hr)	0	0
zone 5 gas flow (m^3/hr)	0	0
zone 6 gas flow (m^3/hr)	0	0
strip thickness (mm)	2.40	2.00
strip width (mm)	1097	1093
set point temp (°C)	460	460
air:fuel ratio	8.5:1	8.5:1

Table 2.6: Dynamic wall model - old and new settings - thickness decrease, hard iron

a large initial drop in the strip temperature and the line data a large rise. This difference was the result of a deliberate choice and is used to illustrate a point about the usefulness of such a model.

The values used for this run are shown in Table 2.6, the line data in Figure 2.25 and the comparison of the line data and the model data in Figure 2.26. The weld is initially set at 10 m away, the line speed changed after 10 s, and the gas flows changed at the start of the program. The line data shows a large drop at first, then an even larger rise, before returning to near the initial temperature. The large rise is caused by the smaller loading of steel in the furnace as a result of the weld passing the furnace boot. However, it is likely that this steel became non-prime first time (NPFT) steel, because it was heated to around 540°C, which is near the recrystallisation temperature of steel. It seems that the increase in the line speed started when the weld was too

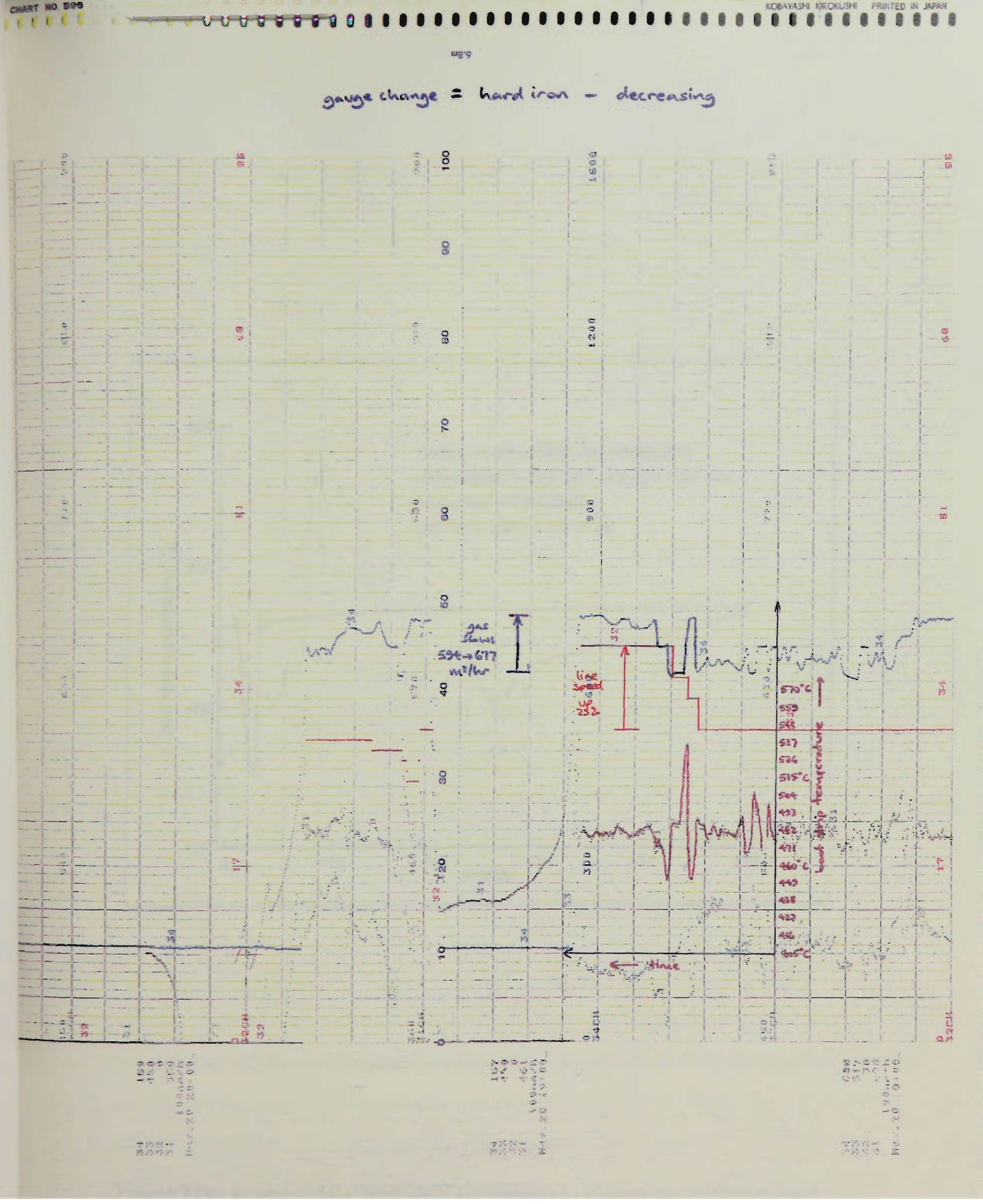

Figure 2.25: From line : boot strip temperature - decreasing thickness, hard iron

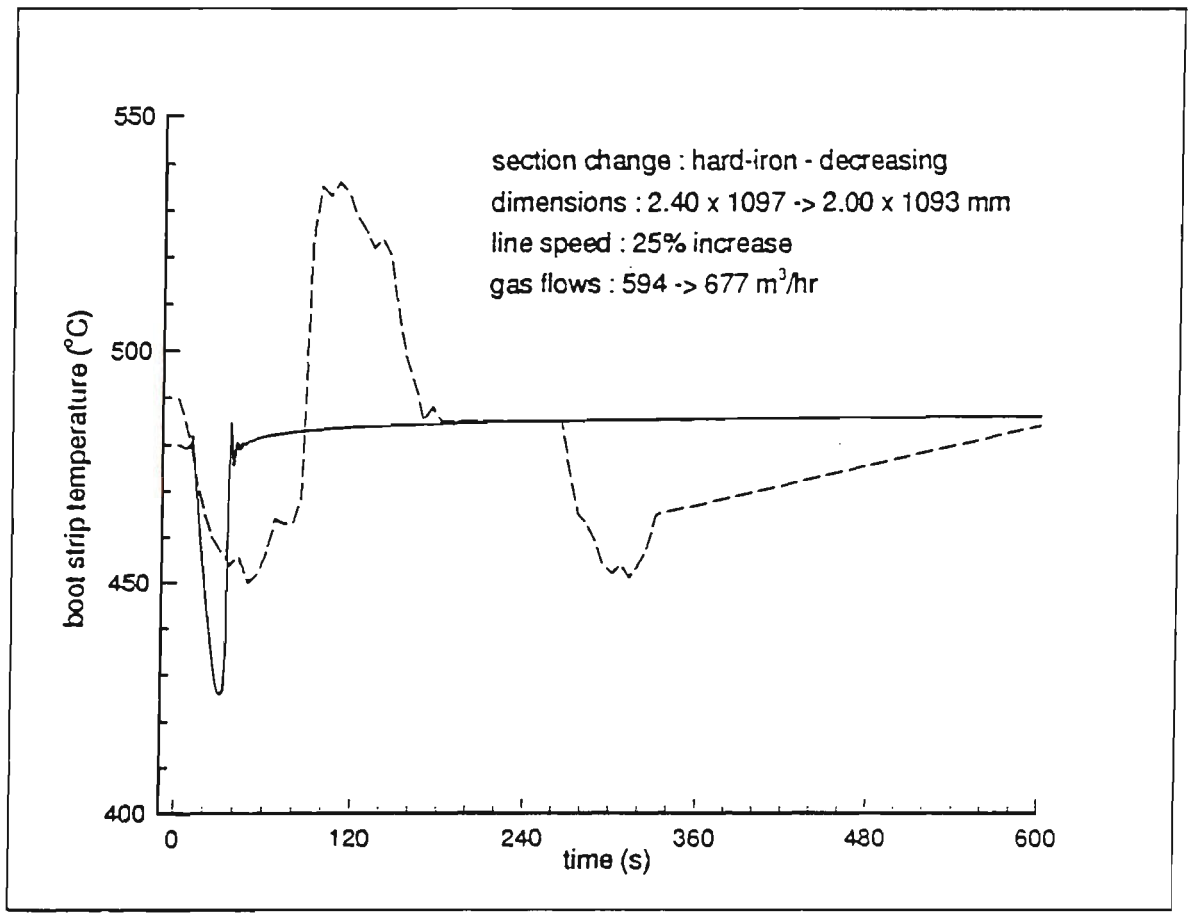

Figure 2.26: From model : boot strip temperature - decreasing thickness, hard iron

close to the furnace entry, and hence the strip reached a higher temperature than was expected when the thinner strip entered. It is seen from the line data that the gas flows were then rapidly decreased around this time to reduce the temperature of the strip back to 'safer' levels. In the model, the line speed is increased before the weld enters the furnace, and so the strip cools to well below the recrystallisation temperature. The decreased thickness of the strip then causes the temperature to rise again to near the original value. As a result, the transient is successfully completed without any danger of the steel recrystallising and becoming too soft for it to remain hard-iron cycle steel. Care must still be taken, however, because other problems may occur if the steel passes through the furnace without getting hot enough.

The main point of this exercise is to indicate that the model can be used to determine how best to run the line and so avoid the dangers of NPFT steel. By experimenting with the position of the weld and the times to change the line speeds and gas flows, the model can tell the operators when to change the parameter settings as well as telling them what new values to set, which was one of the aims of this work.

The results for a thickness increase during a soft-iron cycle run are shown next, and this transient also involved a slight rise in the boot strip temperature. The weld was 5 m away initially, and both the line speed and gas flows were changed as soon as the program started running. The other values used are shown in Table 2.7. The program was run for ten minutes.

The line data is shown in Figure 2.27, and the comparison of the model and line data in Figure 2.28. The temperature increase is much greater in the model data, mainly because the gas flows and line speeds have been changed together. In this instance, it may have been wiser to set the weld closer to the furnace initially, or to change the gas flows and line speeds at a later time. If either of these options were implemented, then the weld would

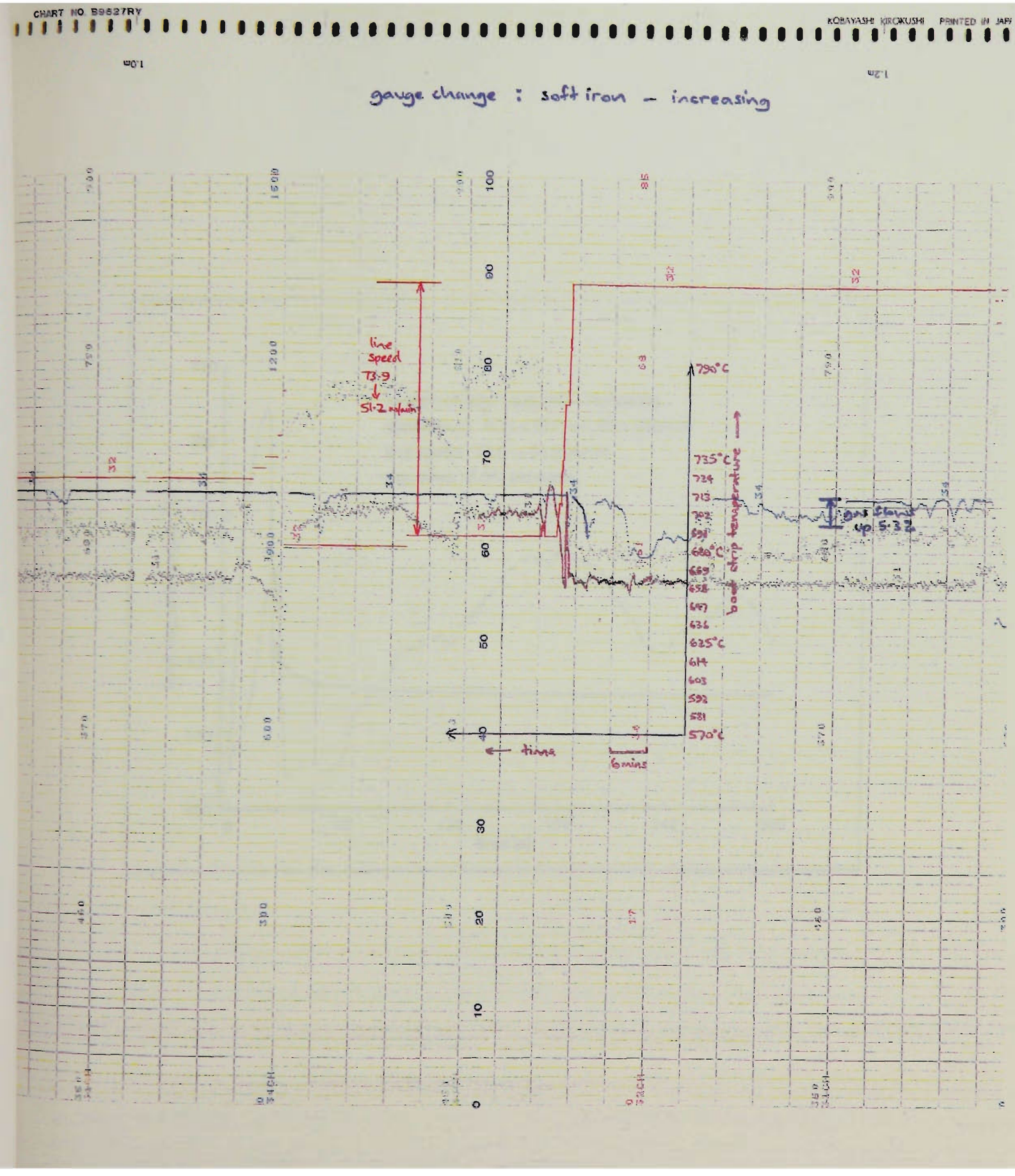

Figure 2.27: From line : boot strip temperature - increasing thickness, soft iron

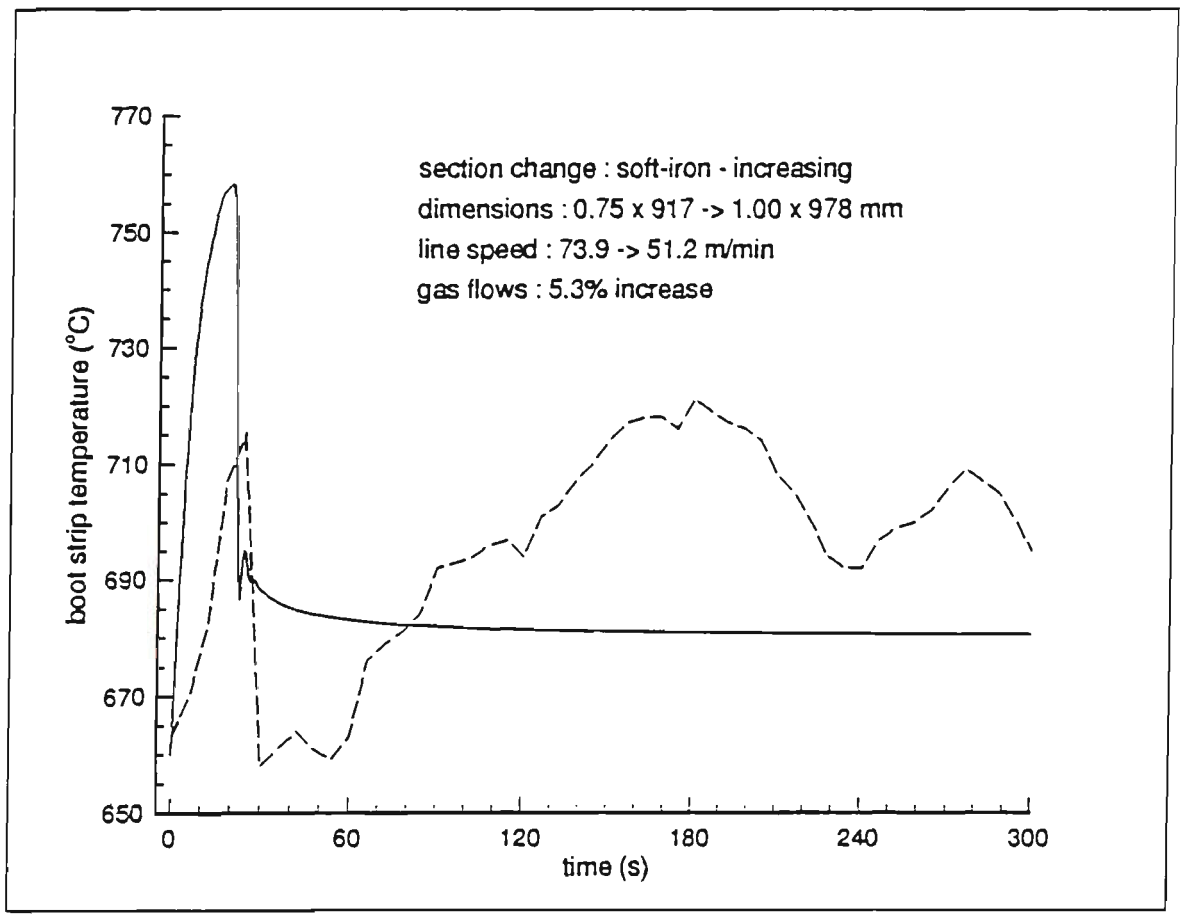

Figure 2.28: From model : boot strip temperature - increasing thickness, soft iron

quantity	old	new
line speed (m/min)	73.9	51.2
zone 1 gas flow (m^3/hr)	191	191
zone 2 gas flow (m^3/hr)	195	195
zone 3 gas flow (m^3/hr)	151	151
zone 4 gas flow (m^3/hr)	142	142
zone 5 gas flow (m^3/hr)	232	248
zone 6 gas flow (m^3/hr)	0	0
strip thickness (mm)	0.75	1.00
strip width (mm)	917	978
set point temp (°C)	660	700
air:fuel ratio	8.5:1	8.5:1

Table 2.7: Dynamic wall model - old and new settings - thickness increase, soft iron

have passed through at an earlier stage and the temperature would not have risen by as much. This example shows the flexibility of the model in its capacity to change the values of parameters (such as the time at which to change the line speed). By using the model in this way, it can indicate that the weld should enter the furnace at an earlier stage than it does in the results shown in Figure 2.28.

The model also appears to slightly underestimate the final temperature given by the line data, but part of the reason for this is that the exact change in the gas flows is not clear. The values shown in Table 2.7 may be an underestimate of the actual initial values of the gas flows, and if they are, then choosing smaller initial gas flows would make the final strip temperature value more realistic.

quantity	old	new
line speed (m/min)	58.7	64.7
zone 1 gas flow (m^3/hr)	191	191
zone 2 gas flow (m^3/hr)	195	195
zone 3 gas flow (m^3/hr)	151	151
zone 4 gas flow (m^3/hr)	144	144
zone 5 gas flow (m^3/hr)	247	247
zone 6 gas flow (m^3/hr)	0	0
strip thickness (mm)	0.9	0.8
strip width (mm)	1223	1134
set point temp (°C)	660	660
air:fuel ratio	8.5:1	8.5:1

Table 2.8: Dynamic wall model - old and new settings - thickness decrease, soft iron

The final example is for a thickness decrease on a soft iron cycle. The details of this are found in Table 2.8, the line data for this transient in Figure 2.29 and the model data in Figure 2.30. The weld is set to be only 5 m away, the gas flows are left unchanged and the line speed is changed as the program begins for this ten-minute run.

The increase in line speed causes the initial fall in the strip temperature in the model data, and the decrease in section causes it to rise above its initial value by around 20 K. This is also shown clearly in the line data, with a large initial drop followed by a larger rise due to the weld. Once more, the results of the model appear to agree reasonably well with experiment.

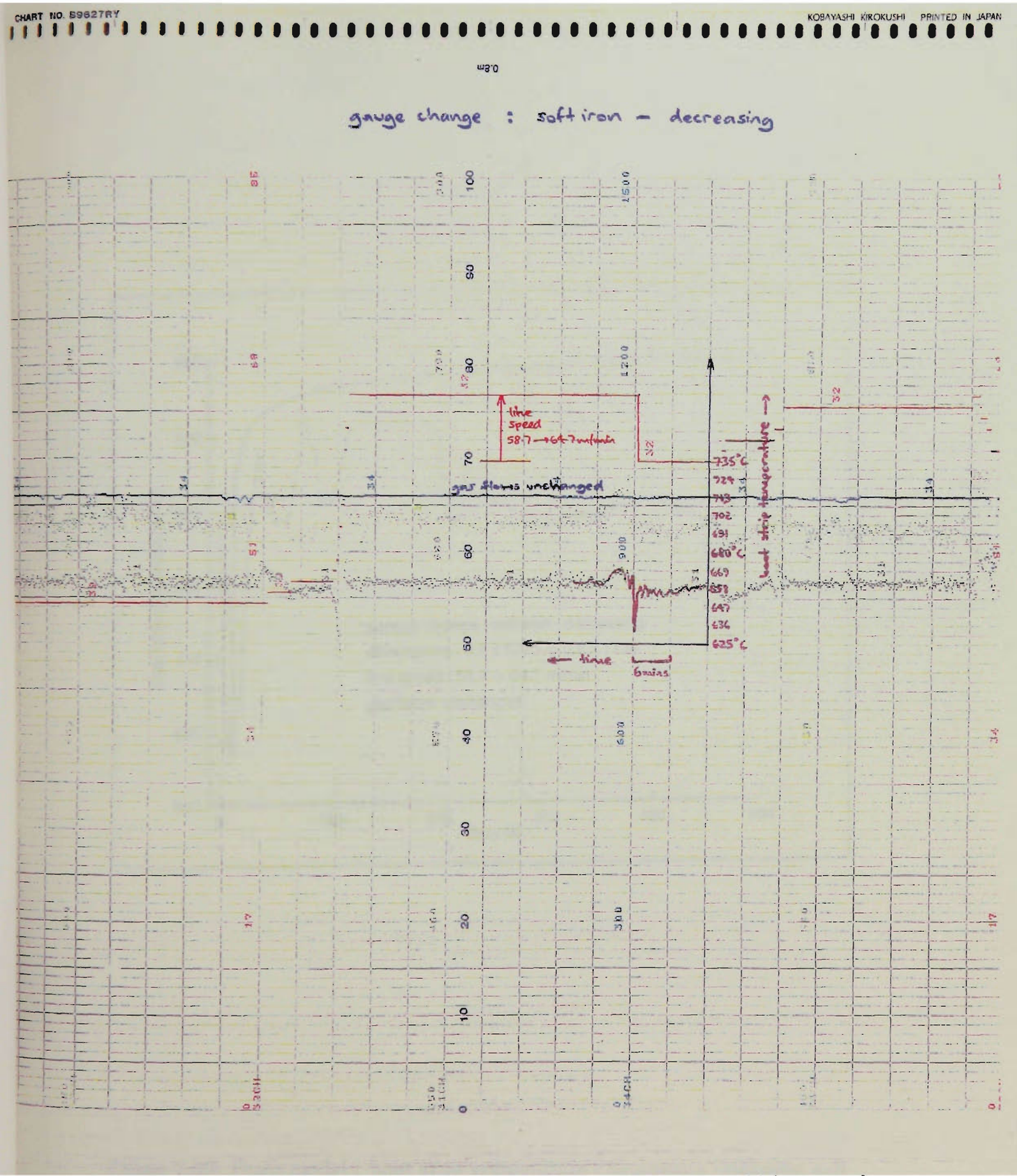

Figure 2.29: From line : boot strip temperature - decreasing thickness, soft iron

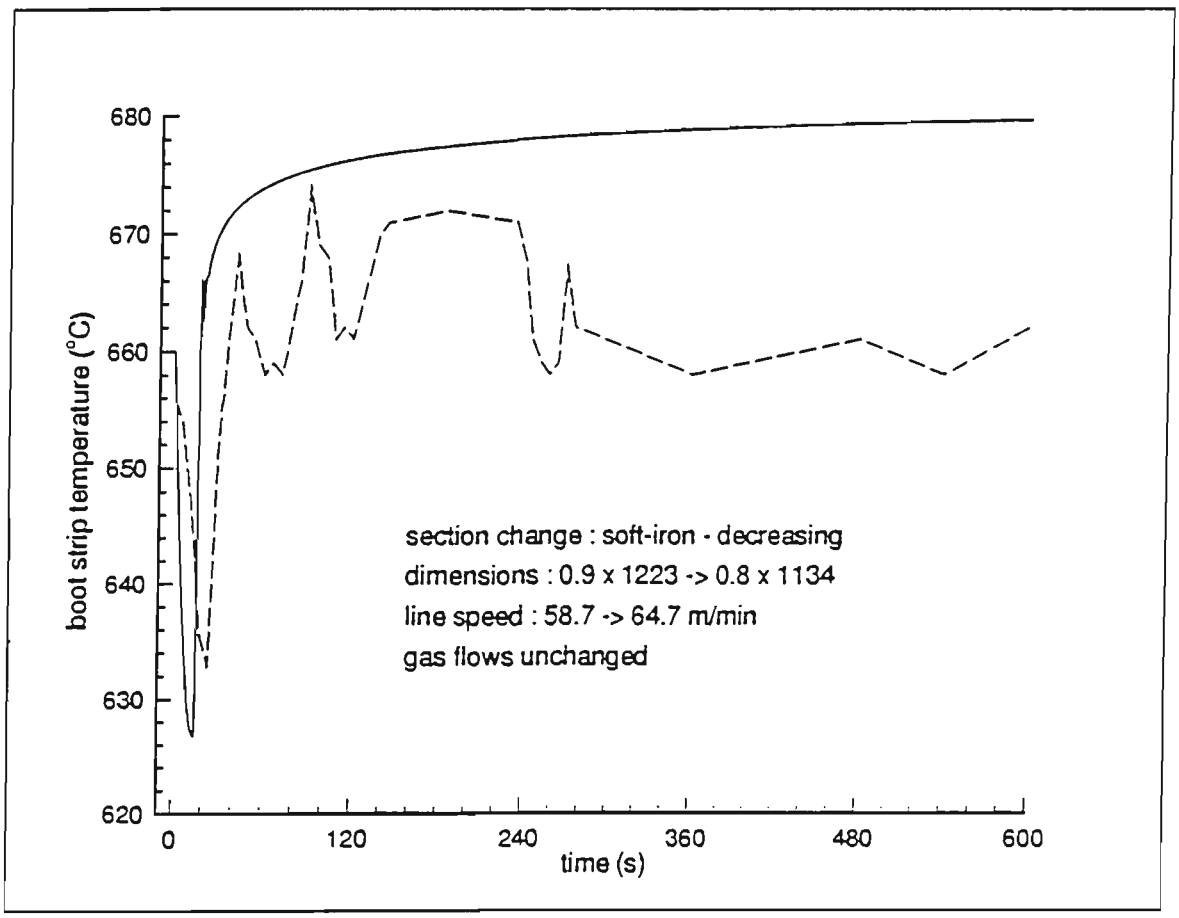

Figure 2.30: From model : boot strip temperature - decreasing thickness, soft iron

2.4.4 Summary

The results presented clearly show the success of this work in its ability to simulate the behaviour of the direct-fired furnace in all possible types of transient situations. The model is found to be accurate enough to be reliable in this capacity, and can therefore be used to model the transient operation of the furnace in an off-line role. Although the model is not fast enough to be used on-line, these results prove that it is accurate enough to make predictions about previously unused transients, rather than just confirming for the line operators the correct parameter settings for standard transients.

This part of the thesis was designed to explain the origin, derivation, implementation and results of work that successfully models the transient operation of the direct-fired furnace on CGL2. Initially, it was thought that this model would be implemented off-line on MCL6 at Westernport. However, the work has been extended since then, especially as continuous data has become available. More on the expansion of the model to run on MCL6 is explained in chapter 4.

Chapter 3

Modelling of the radiant tube furnace (RTF)

3.1 Introduction

After the steel strip travels through the direct-fired furnace on BHP's No. 6 Metal Coating Line (MCL6) at Westernport, it passes through the radiant tube furnace. A diagram of MCL6 is shown in Figure 2.1. The need for a model for the RTF arose from BHP's desire to have a control model for all furnaces on MCL6, including the direct-fired furnace (DFF) and the radiant tube furnace. At present, control is via PID (proportional integral derivative) loops, but a model-based feed-forward control mechanism offers considerable improvement to furnace operation. Because the line is very new (operation began in August 1992), its features include relatively state-of-the-art equipment for data measurement and collection, and it is therefore easier to test the MCL6 model than the CGL2 model. A description of the model and some results are included in this chapter.

The radiant tube furnace on MCL6 is approximately 22 metres high, 5 metres wide and 3 metres deep. A diagram of the furnace is shown in

Figure 3.1. The RTF is divided into two sections, the radiant tube heat section (RTH) and the radiant tube soak section (RTS). There is a thin insulating wall separating the RTH from the RTS. The strip enters from the bottom of the furnace, and moves up and down five times before exiting from the top of the furnace. The length of strip in the furnace at any one time is approximately 100 metres, with the roll-to-roll distance approximately 20 metres. The walls of the furnace are made from a thick insulating blanket (with an inner lining of stainless steel) to ensure that a minimal amount of heat is lost by conduction through the furnace walls. Pyrometers are placed at the exit to the RTH and RTS to provide input temperatures for the furnace PID control loops, as well as allowing the operators to know the current strip temperature at these positions. The operators can therefore compare the measured temperature to the desired strip temperature (setpoints), enabling them to determine if any parameters need to be adjusted.

The function of the RTH is to ensure that the temperature of the steel is raised to that desired for metallurgical conditioning of the steel, while the RTS acts to maintain the strip at or near the RTH temperature. For interstitial free steels (heated to around 750°C), the RTH is especially important, because temperatures this high cannot be reached in the DFF without oxidising the strip surface. There are two kinds of tubes used in the furnace, known as U-tubes and W-tubes, with the tubes shaped like the letter it is named for. The tubes are made from Inconel 601 and have an outer diameter of 190 mm and a wall thickness of 3 mm, with the U-tubes about 5 m long and the W-tubes about 10 m long. Hence the U-tubes radiate more heat in a concentrated area and are used only in the RTH to heat the strip, whereas the W-tubes cover a larger area, are slightly more efficient and are used mainly in the RTS simply to maintain the strip at its temperature. The tubes are placed at right angles to the side wall of the furnace, so that each tube protrudes into

the furnace and 'sees' all of the strip. The tubes protrude into the furnace from both the left-hand wall (drive side) and the right-hand wall (operator side), being placed in the furnace so that they alternate from the drive side to the operator side as the furnace height is traversed. The diagram in Figure 3.1 faces the operator side of the furnace, where the tubes are designated by small circles, with each 'pair' of circles representing one tube. The dotted circles signify tubes that originate from the operator side, and the crossed circles for tubes from the drive side. The W-tubes are those with the circles in each 'pair' located further apart than for the U-tubes. The burner section within which the tubes are located is about 14.5 m high, 5.0 m wide and 2.6 m thick, and is positioned roughly in the middle of the furnace.

The main difference between the direct-fired furnace and the radiant tube furnace is that the RTF does not combust the gas directly into the furnace. Instead, the gas is mixed with air inside large tubes in the furnace, and the gas is combusted within the tubes. The heat generated by this combustion is then conducted through the tube and radiated into the furnace — hence the furnace name. Convection is not included in this model, whereas it is included by Somers *et al.* [48], because ambient gas flows inside the radiant tube furnace are small and the line speeds considered in [48] are typically about three to four times those encountered in this work. The interactions between the strip, walls and the radiant tubes are the major effects that need to be considered.

3.2 The model

Modelling the radiant tube furnace is a difficult task. Even in the absence of gas flows in the RTF, the five passes of the strip and the arrangement of the tubes in the furnace make precise modelling a complex matter. The heat transfer

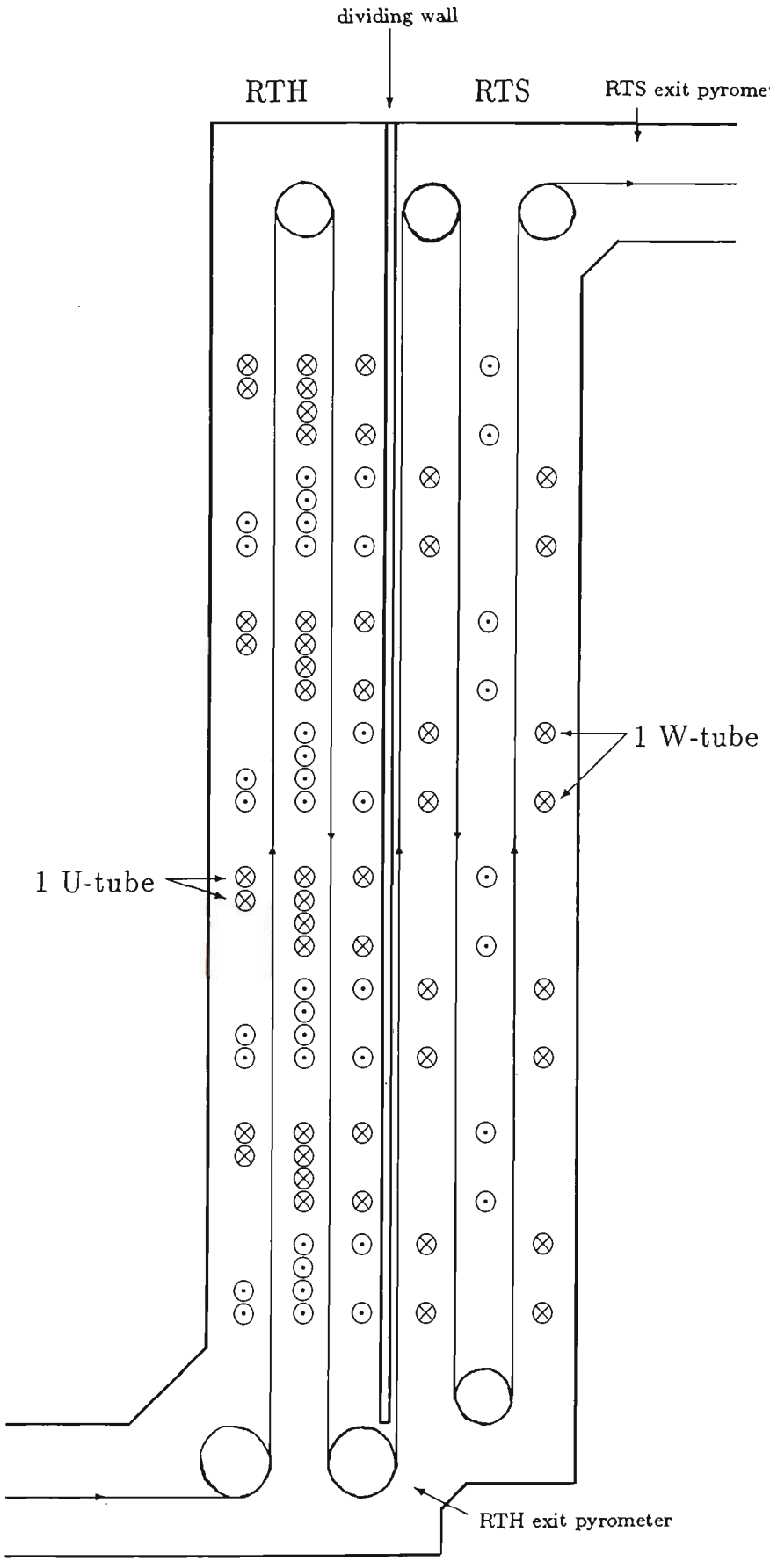

Figure 3.1: Diagram of the radiant tube furnace

between the furnace walls, tubes, strip and the rolls is complicated, and the determination of important heat transfer parameters is difficult, especially for parameters such as the shape factors between the tubes and the strip, as well as between the tubes themselves.

In order to simplify the model, the walls, tubes, turn-around rolls and the rest of the furnace are taken as one body. That is, they are lumped together, and the model then becomes a two-body problem between the 'walls' and the strip. This is acceptable, because the temperature difference between the tubes and the furnace walls is small, and the sum of the individual fluxes from each body is virtually identical to that of the combined flux if the wall, tubes and furnace are taken as one body. The thermal inertia of the insulating material is much less important in the RTF model, because the insulating wool used in the RTF walls is a better insulator and has a lower heat capacity than the brickwork found in the DFF. Most of the effective wall inertia comes from the stainless steel lining, which is not insulated from the strip any more than the radiant tubes and the rolls. The RTF is also a very slow reacting furnace, with only one quarter of the heating capacity of the DFF, but four times the thermal inertia. A two-body problem is obviously simpler than a three-body or higher problem, for it reduces the radiation interaction between the different surfaces. One of the benefits of the simplicity of the model is the speed of execution, which is important if the model is to be used for real-time control of the galvanising line.

Having said this, however, the model does separate part of the turn-around rolls in the furnace from both the wall components and the strip. The reason for this is that contact between the strip and the roll leads to a partial equilibration of the strip and roll temperatures. Data files from MCL6, which display data every five seconds, show that the strip temperature does oscillate on such small time intervals. Without an equilibration of strip and

roll temperatures, the strip temperature varies far more in the model than in reality. Hence the mass of the roll in direct contact with the strip is not included in the thermal mass of the furnace, and is instead used separately to calculate roll temperatures for all six of the turn-around rolls. Those parts of the rolls that lie outside the edges of the strip are included in the total thermal mass of the wall.

The model splits the furnace up into segments, with each vertical pass of the strip (about 20 metres long) included in one segment — therefore there are five segments in all. The first and the last segments have larger thermal masses, because they include all of the tubes on the end walls, as well as the end walls themselves. The three rolls in the RTH are split such that segment 1 and segment 2 each have $1\frac{1}{2}$ rolls, and the three RTS segments have one roll each. The boundary between segment 2 (in the RTH) and segment 3 (in the RTS) is taken to be the curtain separating the two furnace sections, so that segment 2 receives heat solely from the RTH and segment 3 only from the RTS. The gas flows are evenly divided in the RTH, where each segment receives half of the RTH gas flow. The RTS gas flows are split according to the segment orientation; eg, segment 3 receives less than the others, because the strip passing through it only receives radiation directly from 4 W-tubes, whereas segments 4 & 5 receive radiation from 8 W-tubes each. Equally distributing the RTS gas flows between all three RTS segments is another possible partition, but investigations found that both methods gave virtually identical values for the RTF exit temperature. In this way, the fluxes between the walls and the strip can be calculated and a model constructed for the variation of strip temperature with distance and time in the furnace. The breakdown of the furnace into segments is shown in Figure 3.2. It is clear from this diagram that the length of the strip in the last two segments is less than in the first three because of the position of the bottom roll in the RTS — however, the

simplicity of the model does not demand exactness, and keeping the segment lengths equal simplifies the calculations.

The model uses an output data file from MCL6 as input data. This data contains around 80 different values per line, and a new line of data is written into the file every 5 seconds. In general, this means that the model only uses every third or fourth line of data, because the time interval between iterations is about 15-20 seconds. If the line is running at its maximum speed of 150 m min^{-1}, however, the time interval will be only 8 seconds, which means that it will process around two out of every three lines of data. The line of data that is read into the program is the one whose time corresponds to the lowest multiple of 5 seconds below the current time, which is the length of time since the beginning of the iteration. For example, if the current time is 24.2 seconds, then the line of data for 20 seconds will be used. The data set contains all sorts of information, including the time, line speed, strip dimensions, gas and air flows and, importantly, measured strip temperatures for the exit of the DFF, the RTH and the RTS. This means that the temperatures that the model predicts can be compared directly with the measured temperatures. Not only this, but temperature predictions using a filtering technique can also be used to guess what the temperature might be at some specified time in the future. The filtering technique is included in the model, and can generally predict very accurately what the RTF exit temperature might be in one or two minutes, as is shown in the results in section 3.4.

When a section change occurs, the model allows for this by tracking the position of the weld in the RTF. The weld position is actually given relative to the DFF entry position in the input data; an adjustment is made so that the program 'knows' when it then enters the RTF. When the exact position of the weld in a segment is known, all segments that it has yet to pass through are set to the old coil values of strip thickness and width, while all segments it

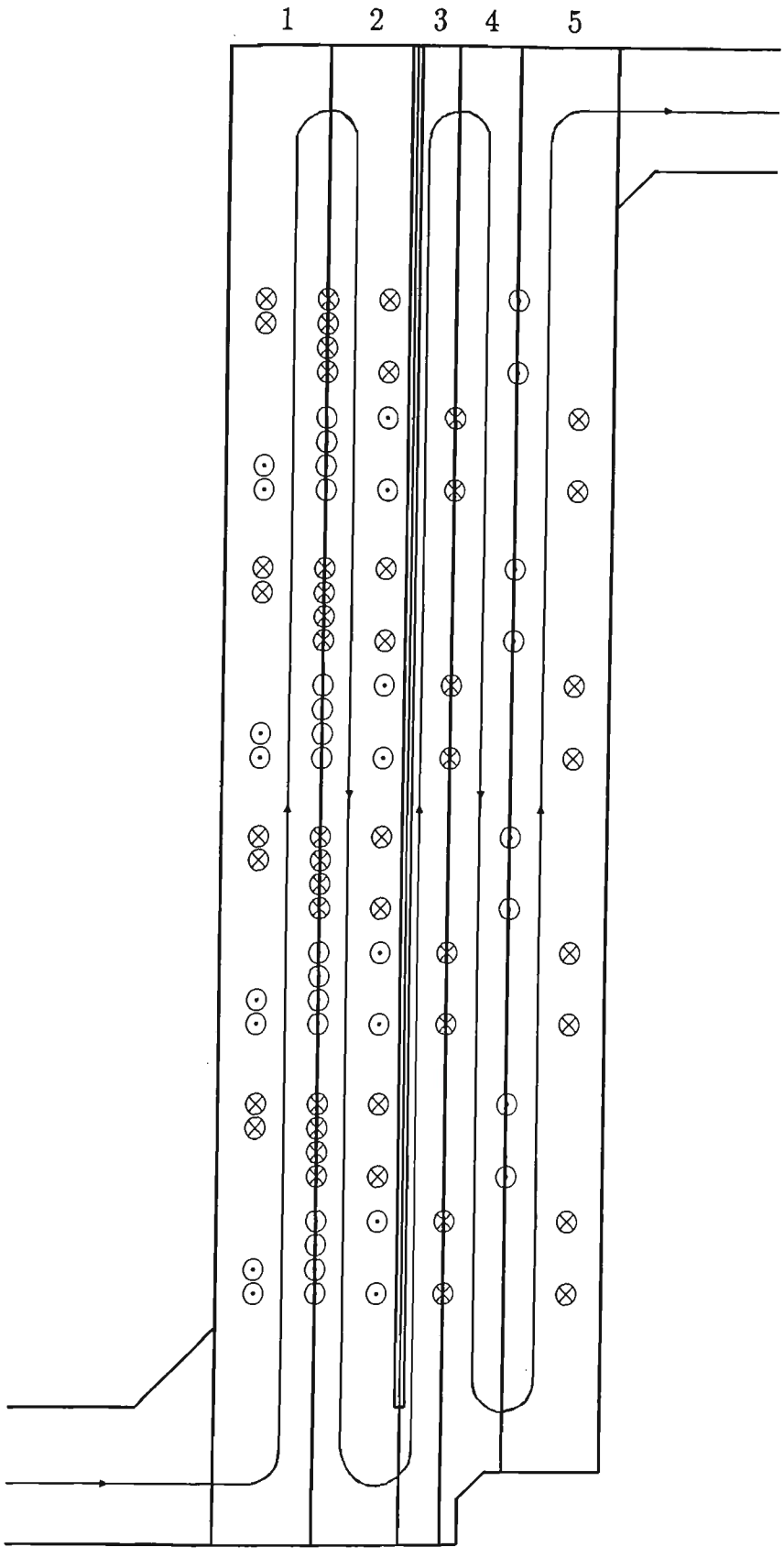

Figure 3.2: Diagram of the RTF showing segments (without rolls)

has already passed through are given the new values of thickness and width. This is a similar procedure to that used in the DFF model. For the segment that the weld is in, the value of thickness and width is taken to be that of the coil that fills the greatest proportion of the segment.

The time interval, Δt, is the time taken for the strip to travel the length of one segment. This means that the higher the line speed, the lower the time interval and vice versa. When the line speed decreases below a certain value, it is assumed that a line stoppage has occurred, and the model reads the input data (without using it in the program) until the velocity returns to a value above the minimum value. If the duration of the line stoppage exceeds a certain set time, then the values are re-initialised, or else the previous values of the temperatures are used if this critical value is not exceeded.

The program completes one run of approximately four hours of data (output every 5 seconds) in around only 15-20 seconds of real time on a SUN sparc 10 workstation. With the filtering procedure mentioned in section 3.3.3 increasing its accuracy, the model works very well. This compares with a run-time of about 3 minutes for only ten minutes worth of data for the CGL2 DFF model (which is an off-line model).

3.3 Model equations

Two different equations for the heat flow rate from the wall to the strip, q_{ws}, are presented here, which both give almost identical results for the strip temperature. The values for q_{ws} are then used in the model equations in section 3.3.2.

3.3.1 The heat transfer between the strip and the wall

Let the furnace be viewed from above, as shown in Figure 3.3, and let it be partitioned into segments as before. Each segment therefore includes one

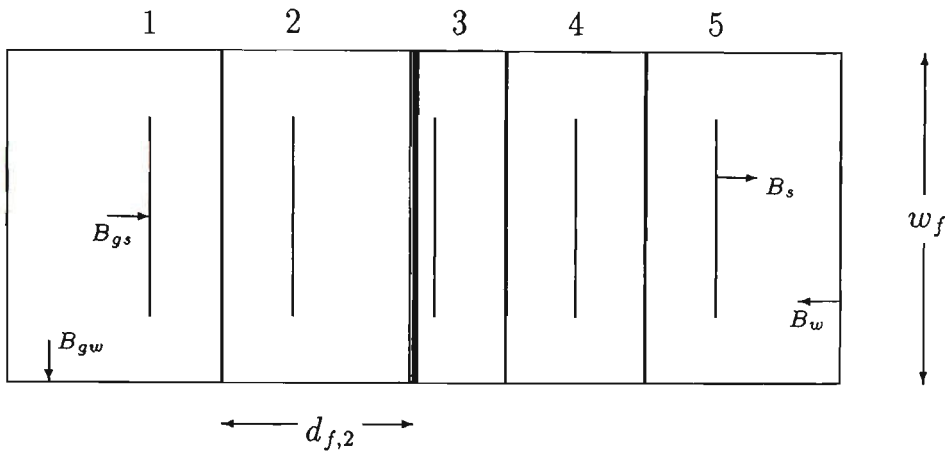

Figure 3.3: View of RTF from above

segment length of the strip, the wall on the drive side and operator side, and the other 'wall' of the segment including the tubes (except for the first and last segments which also include the end walls). The tubes are then taken to be a solid 'wall' that radiation cannot pass through, yet the four sides of the 'wall' can still 'see' each other and the strip. If it is assumed that the strip and the wall are a set of parallel plates of infinite length and finite width, then the shape factors are calculated to be

$$F_{sw} = 1, \tag{3.1}$$

$$F_{ws} = \frac{w_s + d_s}{w_f + d_{f,j}}, \tag{3.2}$$

$$F_{ww} = 1 - \frac{w_s + d_s}{w_f + d_{f,j}}, \tag{3.3}$$

using shape factor algebra, for each segment j.

Radiosities can be used to determine the heat flux to and from each surface in each segment, and the fluxes are assumed to pass through an imaginary surface next to the strip and the wall. If the medium through which the radiation passes to cross these surfaces is called the 'gas', then the radiosities are given by

$$B_s = \varepsilon_s \sigma T_s^4 + \rho_s B_{gs}, \tag{3.4}$$

$$B_w = \varepsilon_w \sigma T_w^4 + \rho_w B_{gw}, \tag{3.5}$$

$$B_{gw} = \frac{P_s}{P_w} F_{sw} B_s + F_{ww} B_w, \tag{3.6}$$

$$B_{gs} = \frac{P_w}{P_s} F_{ws} B_w, \tag{3.7}$$

where the P terms represent the perimeters of the strip and the wall, and $\rho_s = \rho_s(T_w)$. The wall perimeter is taken to be the furnace width and thickness in the burner section of the furnace, which are both smaller than for the whole furnace. This is because the heat transfer that is modelled by the radiosities occurs only within the burner section.

These equations can now be written in terms of B_{gs} and B_{gw}. The total heat transferred between the strip and the wall is given in terms of these radiosities, ie,

$$q_{ws} = P_s \triangle x (B_{gs} - B_s),$$

$$q_{sw} = P_w \triangle x (B_{gw} - B_w).$$

Therefore the heat transferred to the strip from the wall is given by

$$q_{ws} = \triangle x \left(\frac{(\rho_w (F_{ws} F_{sw} + F_{ww}) - 1) P_s \varepsilon_s \sigma T_s^4 + ((1 - \rho_s) F_{ws}) P_w \varepsilon_w \sigma T_w^4}{1 - \rho_w (\rho_s F_{sw} F_{ws} + F_{ww})} \right), \tag{3.8}$$

where $F_{ws} F_{sw} + F_{ww} = 1$. The heat transferred from the strip to the wall is now

$$q_{sw} = \triangle x \left(\frac{((1 - \rho_w) F_{sw}) P_s \varepsilon_s \sigma T_s^4 + (\rho_s F_{sw} F_{ws} + F_{ww} - 1) P_w \varepsilon_w \sigma T_w^4}{1 - \rho_w (\rho_s F_{sw} F_{ws} + F_{ww})} \right), \tag{3.9}$$

From these equations, $q_{ws} + q_{sw} = 0$, which is required for energy to be conserved in each segment.

The alternative method for finding q_{ws} uses a heat flow rate condition found in Holman [16], which contains an equation for the radiation interchange between two surfaces, with no other surface or medium involved. In the case of the RTF, the two surfaces are the wall (ie, all of the furnace

walls, the parts of the rolls not contacting the strip, and the tubes), and the strip, with the calculation performed in each segment. The equation, which describes the energy flow from the wall to the strip, q_{ws}, is

$$q_{ws} = \frac{\sigma(T_w^4 - T_s^4)}{(1-\epsilon_w)/\epsilon_w A_w + 1/A_w F_{ws} + (1-\epsilon_s)/\epsilon_s A_s}. \tag{3.10}$$

If $A_w = P_w \triangle x$ and $A_s = P_s \triangle x$, where the perimeters are defined for each segment as before, then there is virtually no difference between the temperature values derived from using equation (3.10) or equation (3.8). From here on, the expression for q_{ws} shown in equation (3.8) is used in all calculations.

3.3.2 Dynamic Model

The basic form of the equations to be solved is as follows. For the whole strip in the RTF,

$$\frac{\partial T_s}{\partial t} + V_s \frac{\partial T_s}{\partial x} = \frac{q_{ws}}{m_s c_{ps}}, \tag{3.11}$$

and for each segment of the wall,

$$\frac{\partial T_{w,j}}{\partial t} = \frac{q_{wall,j}}{m_{w,j} c_{pw,j}}, \tag{3.12}$$

where $c_{ps} = c_{ps}(T_s)$ and $c_{pw} = c_{pw}(T_w)$ given in Stone & Morrison [51]. The entry strip temperature, $T_{s,0}$ is known, and the strip temperature at each grid point can be calculated. There are six grid points in all; each one corresponding to a roll position. Firstly, the heat flow rate between the wall and the strip is found using,

$$q_{ws} = \triangle x \left(\frac{(\rho_w - 1) P_s \varepsilon_s \sigma T_s^4 + ((1-\rho_s) F_{ws}) P_w \varepsilon_w \sigma T_w^4}{1 - \rho_w (\rho_s F_{sw} F_{ws} + F_{ww})} \right), \tag{3.13}$$

evaluated for each segment and time step, with the emissivity, strip perimeter and shape factors all varying due to the change in temperature and dimension of the strip. Hereafter, the strip emissivity is calculated using functions from

Stone & Morrison [51]. The strip temperature can be calculated by applying the simple first-order upwind finite difference method to equation (3.11),

$$T_{s_j}^{n+1} = (1 - {c_s}^n)T_{s_j}^n + {c_s}^n T_{s_{j-1}}^n + \frac{{q_{ws}}_j^n \triangle t^n}{{m_{s_j}}^n {c_{ps}}_j^n}, \tag{3.14}$$

where ${c_s}^n = {V_s}^n \triangle t^n / \triangle x$. This finite-difference method is von Neumann stable for $0 < c_s \leq 1$ for the homogeneous case. In this model, the strip is moved forwards by one segment length on every time step, forcing $c_s = 1$. Hence

$$T_s^{\text{raw}\,n+1}{}_j = T_{s_{j-1}}^n + \frac{{q_{ws}}_j^n}{\rho_s (w_s d_s)_j^n (\triangle x) {c_{ps}}_j^n} \triangle t^n, \tag{3.15}$$

where ${m_s}_j^n = \rho_s {w_s}_j^n {d_s}_j^n (\triangle x)$. Therefore the strip gains an amount of heat q_{ws} as it moves through one segment j.

Once the strip temperature has been calculated, it is equilibrated with the roll temperature, as was mentioned previously. A paper by Taylor & Elliott [53] shows that an initial difference between the temperature of a strip and a roll is approximately halved for a wrap angle of 180° (although the roll was a heat source in their analysis). Hence an equilibration was sought that modelled the real dynamic response in strip temperature sufficiently well. The equilibration is performed by firstly averaging the strip and roll temperature at each grid point over the thermal mass at each grid point. Then the final values for the strip and roll temperatures are taken, being the average of the equilibrated temperature and the most recently calculated strip and roll temperature. For the roll, this will be the temperature calculated at the previous iteration, and for the strip it will be the raw temperature calculated on the current iteration. In mathematical terms, the equilibration is

$$T_s^{\text{equil}\,n+1}{}_j \{= T_r^{\text{equil}\,n+1}{}_j\} = \frac{m_{r\to s} c_{pr} T_{r_j}^n + m_s c_{ps} T_s^{\text{raw}\,n+1}{}_j}{m_{r\to s} c_{pr} + m_s c_{ps}}. \tag{3.16}$$

The term $m_{r\to s}$ denotes the mass of the roll in contact with the strip, given by

$$m_{r\to s} = \rho_r w_s d_r C_r I_{r\to s}, \tag{3.17}$$

where C_r is the roll circumference, and $I_{r\rightarrow s}$ is a chosen value between 0 and 1 which represents the amount of interaction between the roll and the strip. Therefore, the value $I_{r\rightarrow s} = 0$ signifies no interaction and $I_{r\rightarrow s} = 1$ complete interaction.

The final values for the strip and roll temperature are then obtained from

$$T_{s_j}^{n+1} = \tfrac{1}{2}(T_{s\ j}^{\mathrm{raw}\,n+1} + T_{s\ j}^{\mathrm{equil}\,n+1}), \tag{3.18}$$

$$T_{r_j}^{n+1} = \tfrac{1}{2}(T_{r_j}^{n} + T_{r\ j}^{\mathrm{equil}\,n+1}). \tag{3.19}$$

In other words, the strip and roll temperatures are allowed to come half-way to equilibrium. For an off-line model, where accuracy rather than speed is more important, a finite-difference method could be included to model this interaction along the lines of that used by Taylor & Elliott [53], but the extra computational time that results from this is not desirable in an on-line model; the empirical method is sufficient.

Having calculated all of the strip temperatures and included the roll/strip interaction, the wall temperature is calculated, using the total heat flow rate to the wall, q_{wall}, which is

$$q_{wall_j}^{n} = q_{in} - q_{out} - q_{waste} - q_{ws}\big]_j^n . \tag{3.20}$$

The heat that the wall receives depends on the amount input to the furnace, and that which is lost to the strip, the uncombusted waste gases and that conducted out through the furnace walls. The total heat flow rate into the furnace, q_{in}, is determined using the relationship

$$q_{in} = \dot{m}_g E, \tag{3.21}$$

where E represents the total energy released by the combustion products at standard temperature and pressure. The input gas flow $\dot{m}_g$ is provided in the data input and is in units of $\mathrm{Nm^3\ hr^{-1}}$ (N $\equiv$ normal). It should be pointed out

that this relationship holds only when there is an excess of air in the furnace, meaning that all of the gas in the furnace is combusted. When there is an excess of gas in the furnace, the amount combusted depends on the amount of oxygen in the furnace, and in this case q_{in} takes the form

$$q_{in} = \frac{\dot{m}_a}{S} E, \tag{3.22}$$

where $\dot{m}_a$ is the air flow rate and $S(= 9.773)$ is the stoichiometric ratio.

For the heat lost through the walls, the steady-state heat conduction formula is used for simplicity,

$$q_{out,j} = k_w A_{w,j}(T_{w,j} - T_a)/d_w, \tag{3.23}$$

where $k_w = k_w(T_{w,j})$ and T_a is the outside wall temperature (taken to be 40°C). The surface area of the wall includes the burner section, where the furnace thickness and width are slightly smaller, as well as the top and bottom sections of the furnace. The total surface area for the furnace is then partitioned between the segments.

The formula for the heat loss by the waste gases is more complex, because the natural gas mixture is made up of many different components, and the composition of the waste gas will vary depending on the furnace air-to-fuel ratio. For example, in a lean atmosphere, where there is an excess of air, all of the gas mixture will be combusted, leaving behind some nitrogen, oxygen and carbon dioxide from the air. In a rich atmosphere, there will be an excess of the gas. This causes all of the oxygen in the air to be consumed, but leaves methane, ethane, propane and other component gases from the gas mixture to exit the furnace as waste gases. When the air-to-fuel ratio is the same as the stoichiometric ratio, the chemical reaction is

$$1 \text{ mole gas} + 9.773 \text{ moles air} \longrightarrow 1.041\ CO_2 + 2.014\ H_2O, \tag{3.24}$$

along with some nitrogen and extra carbon dioxide from the gas mixture. The air is assumed to be 20.95% oxygen and the remainder nitrogen, neglecting

argon. Therefore 9.773 moles of air equates to 2.047 moles of oxygen. For lean mixtures (the most common situation), the component waste gases are N_2, O_2, CO_2 and H_2O, and for rich mixtures, N_2, CO_2, H_2O, CH_4, C_2H_6, C_3H_8 and C_4H_{10}. The heat loss for one component gas is

$$\begin{aligned} q_{waste,i} &= \dot{m}_{g,i} h_{g,i}(T_w), \\ &= \dot{m}_{g,i} \int_{T_{room}}^{T_w} c_{pg,i}(\tau) d\tau, \end{aligned} \tag{3.25}$$

where $T_{room} = 25°C$. Therefore, to calculate the total heat loss,

$$q_{waste} = \sum_i \dot{m}_{g,i} \int_{T_{room}}^{T_w} c_{pg}(\tau) d\tau, \tag{3.26}$$

is used, where i represents each component of the waste gas.

The mass flows for each gas can be determined, based on the reaction shown in (3.24), using a method such as that found in Baumeister [2]. The enthalpies are calculated using the coefficients found in Prothero [40] for the specific heat of various gases. (This data is given in units of cal mol^{-1} for the enthalpies, and it is converted to J m^{-3} by using the fact that one mole of an ideal gas occupies 22.4 L of air at standard temperature and pressure.) The wall temperature is used instead of the gas temperature because the gas is considered to be at the same temperature as the wall by the time it reaches the end of the tube to exit from the furnace. In practice, the waste gas will be somewhat hotter than the wall if there is hot combustion (and somewhat cooler than the wall if there is little or no combustion), so the lumping assumption leads to an overestimate of the furnace efficiency.

Having obtained q_{wall}, the wall temperatures for the current time step for each segment are then obtained using a simple forward-time differencing of equation (3.12), and so

$$T_{w_j}^{n+1} = T_{w_j}^{n} + \frac{q_{wall_j}^{n}}{m_w c_{pw}(T_{w_j}^{n})} \triangle t^n. \tag{3.27}$$

It is recalled that the 'wall' as described here includes

- the stainless steel lining of the burner section (SS),
- the top and bottom sections of the furnace and the parts of the wall outside the burner section ($top\&bot$),
- the parts of the rolls not contacting the strip ($r \neq\!\!\rightarrow s$), and
- the tubes.

As a result, the expression $m_w c_{pw}$, the thermal mass of the 'wall', is a summation of the individual thermal masses that make up the 'wall'. All of the components are assumed to be at the same temperature, but the material from which the components are made are different and so have different values of specific heat. Therefore, in equation (3.27),

$$\begin{aligned} m_w c_{pw}(T_{w_j}^n) &= m_{r\neq\!\!\rightarrow s} c_{pr}(T_{w_j}^n) + m_{tubes} c_{p,tubes}(T_{w_j}^n) \\ &\quad + m_{top\&bot} c_{p,top\&bot}(T_{w_j}^n) + m_{SS} c_{p,SS}(T_{w_j}^n), \end{aligned} \tag{3.28}$$

where $m_{r\neq\!\!\rightarrow s} = m_r - m_{r\rightarrow s}$. The top and bottom sections are taken to have the same stainless steel lining thickness as the furnace walls. This assumption is made because the actual mass of the top and bottom sections is unknown. However, because the largest components of the thermal mass of the wall are the tubes and the rolls, the likely range of mass of the top and bottom sections will not have much effect on the total thermal mass.

This process continues until each wall temperature has been updated. The model then continues the iteration through subsequent time steps until the end of the data file has been reached.

Before the model is run in real time, initial strip and wall temperatures are derived by using the first line of data from the data files. An initialisation procedure is used to obtain these values for the wall and strip temperatures for the various grid points and segments in the furnace. Because data is provided directly from the line, values such as the line speed, gas and

air flows and strip dimensions are known, although not with 100% reliability. Values for the strip thickness and width, for example, have been found to be in error in the past. The temperature at the entry end of the RTF is given by the standby pyrometer, located after the turn-around roll in the direct-fired furnace. Using this value, and the known gas flows in the furnace, values for the wall temperatures and strip temperatures for the whole furnace can be calculated by examining one segment at a time and evaluating for the whole furnace.

Initialising the model can be done in several ways. The method used here is to assume a typical strip and wall temperature profile throughout the RTF as input values, and then feed these into the model until it reaches a steady-state. A good initial guess is to use a linear temperature rise in the RTH, and a smaller linear rise or even a constant temperature in the RTS, and for the walls to be hotter in the RTH than in the RTS. An even simpler method is to use the initially known value of the RTF entry temperature to iterate once through the furnace, calculating the strip and wall temperatures at each grid point and segment as it progresses. This requires setting $q_{ws} = q_{in}$ initially, and rearranging equation (3.8) in terms of T_w. The strip temperature for the next grid point can then be calculated using the steady-state form of equation (3.11). This process can be repeated until the final grid point is reached. This technique usually results in a large over-estimation of the temperatures, especially in the wall. If this is the case, the model can again be used to bring the furnace to a steady-state.

3.3.3 Filtering

The model described is very fast in its execution, but because of its simplicity it lacks some accuracy. In order to make the model more accurate, a simple exponential filtering procedure is also used. Filtering is described further in

Goodwin & Sin [12]. The filtering procedure uses data from a set number of prior time steps, for example, and uses the discrepancy between the predicted and measured data from that time to derive a filtered model value for the current time step. This procedure further improves the accuracy of the model, and enables it to be run at high speeds with the knowledge that it will still give very accurate results. A description of the procedure follows.

The initial 'error' in the model is taken to be the difference between the model temperature and the measured temperature from a specified number of time steps beforehand. At every time step, an 'error' is calculated (using a weighted average of the old 'error' and the new 'error'), which is the difference between the model-predicted temperature and the measured temperature. The value of the weights can vary, but the sum of the weights must be one. The weights of 0.9 on the previous error and 0.1 on the most recently obtained error were found to be satisfactory. In mathematical form:

$$T_{s,err}{}^{n+1} = 0.9T_{s,err}{}^{n} + 0.1(T_{s,pred}{}^{n+1} - T_{s,meas}{}^{n+1}). \tag{3.29}$$

Then, when these values are needed five time steps 'into the future', the filtered value is calculated using

$$T_{s,fil}{}^{n} = T_{s,pred}{}^{n} - T_{s,err}{}^{n-5}. \tag{3.30}$$

Five time steps is chosen because it is the equivalent of the time taken for the strip to advance by one furnace length, and hence is an appropriate choice for line controllers.

The results from the next section indicate the effectiveness of the filtering mechanism. The graphs shown there do not display the actual values of the filtering procedure until a certain number of time steps into the program, so until that time the filtered temperature is 'initialised' at 700°C.

3.4 Results

The MCL6 line at Westernport provides a wealth of data with which the model can be compared to check its accuracy. It is therefore helpful for modelling, unlike CGL2 at the time of the derivation of the DFF model for that line. At the time of writing, there were some problems with the data concerning the accuracy of some values, but these difficulties had to be ignored. Some of the results from the model, showing comparisons with measured data, are now given.

The first set of results is an analysis of data from the data set named *mrl32.dat*. This data was provided from MCL6 every 5 seconds for a period of nearly four hours. Graphs of the variation of gas and air flows, as well as the line speed, strip thickness and strip width, are shown in Figures 3.4 and 3.5. This data set included two section changes — one at about 300 seconds (5 minutes), the other at 1200 seconds (20 minutes), with the line speed increasing from 110 to 120 to 140 metres per minute, and the strip thickness decreasing from 0.75 to 0.6 to 0.4 mm. The strip thickness, width and speed then remain constant for the duration of the data set, but the gas flows are turned on and off in the RTH as shown. This would be expected to cause oscillations in the strip temperature over those times. The reason for the RTH gas turning on and off is that it is controlling to a setpoint temperature, but the fire rate required to maintain the strip at the setpoint is below the minimum fire rate and above zero. The best that the PID controller can do is to provide a pulse width modulated fire rate with a period of about 50 minutes, as shown in Figure 3.4. A period of this duration indicates the magnitude of the RTF inertia.

The graph shown in Figure 3.6 shows the output for several sets of temperature data over time. The bottom line is the temperature given by the standby pyrometer, which is located just after the exit roll of the DFF and is used as the input temperature for the RTF in the program. The different

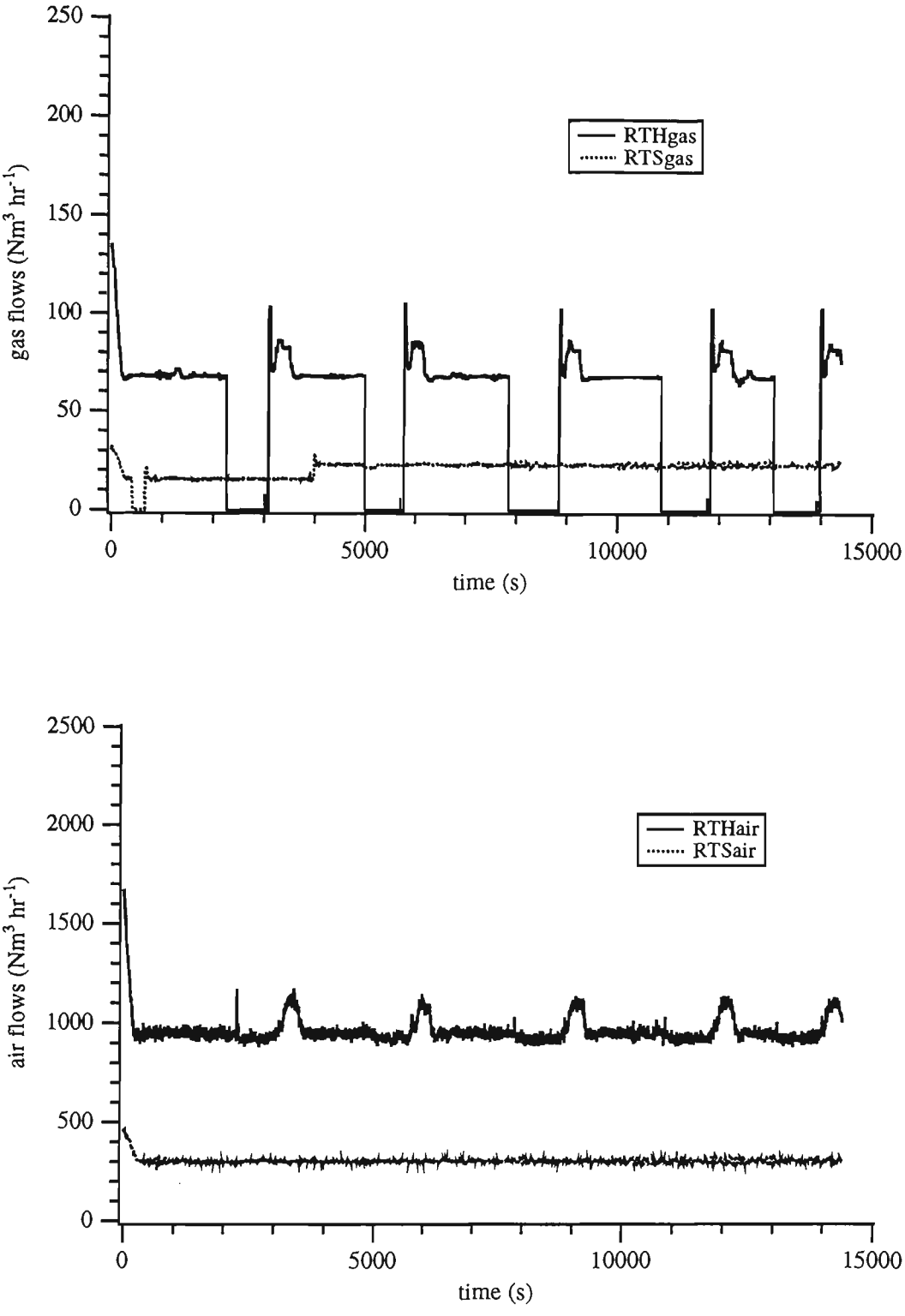

Figure 3.4: Data set mrl32 - gas and air flows

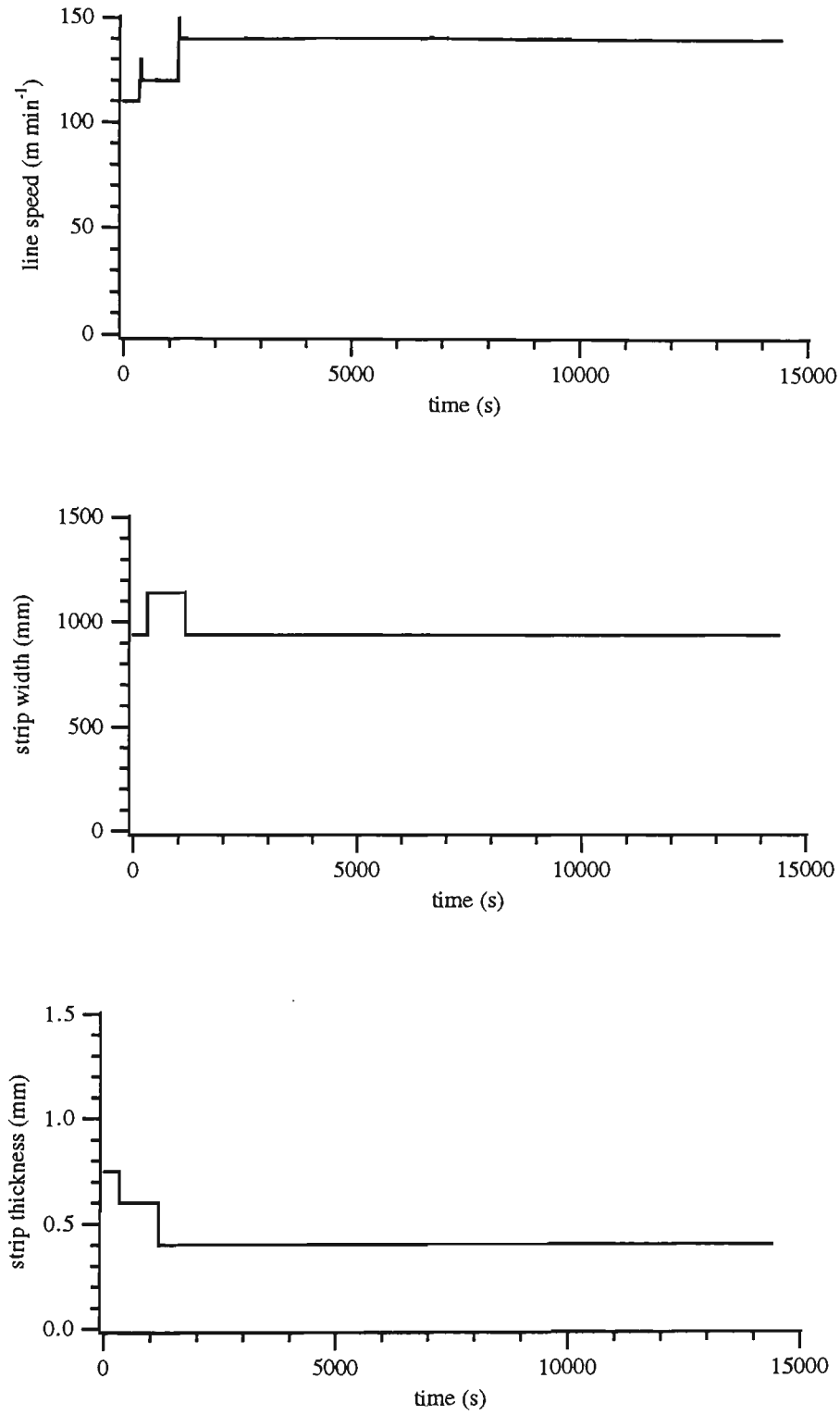

Figure 3.5: Data set mrl32 - line speed, strip width and thickness

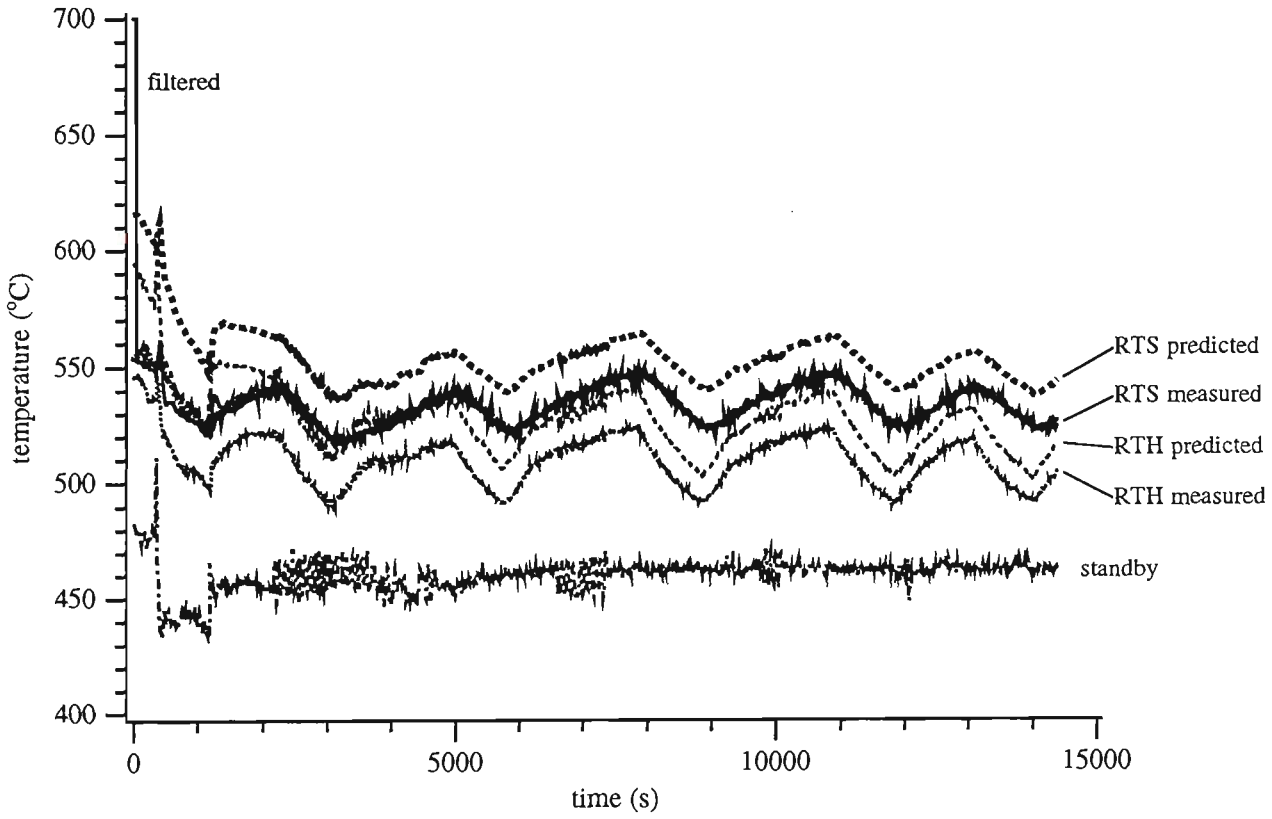

Figure 3.6: Comparison of results for data set mrl32

'smaller'-dashed lines represent the predicted and measured temperatures for the exit from the RTH, while the different 'larger'-dashed lines represent the predicted and measured temperatures for the exit from the RTS. The solid line is the temperature returned by the filtering procedure. The patterns representing each parameter are also indicated on the graphs; either by a legend, or by lines when the parameters are difficult to distinguish.

Results show that the model overpredicts the measured temperature at the RTF exit, but not greatly. The filtered temperature, which uses values from five time steps in arrears (equating to one furnace length), corrects the predicted value well. The initial overprediction results from the model initialising on the first line of data in the data file, with the actual (unrecorded) previous history of the furnace being quite different. After the data has been run for some time, the model maintains the strip temperature at the RTF exit at a value that is within 20 K of the measured temperature.

The importance of including some sort of roll/strip interaction is shown in Figures 3.7, 3.8 and 3.9. These graphs display predicted temperatures for when the roll/strip interaction is taken to be either complete (ie, all of the roll in contact with the strip is involved in heat transfer with it), 50/50, or non-existent (ie, the roll and the strip do not exchange heat), respectively.

In Figure 3.7, it is assumed that there is complete roll/strip interaction; ie, all of the roll mass has thermal contact with the strip. The equilibration procedure, explained previously by equations (3.16)–(3.19), is used here. As a result, there is a complete damping of short-term transients (of the order of 10 s) from one time step to the next, which is an unrealistic situation as the measured temperatures show. These transients are probably caused by minor variations in the thickness of the strip from the constant nominal value that the model uses from the given line data. In Figure 3.8, the graphs for the 50/50 situation are shown. Clearly, the predicted model temperatures

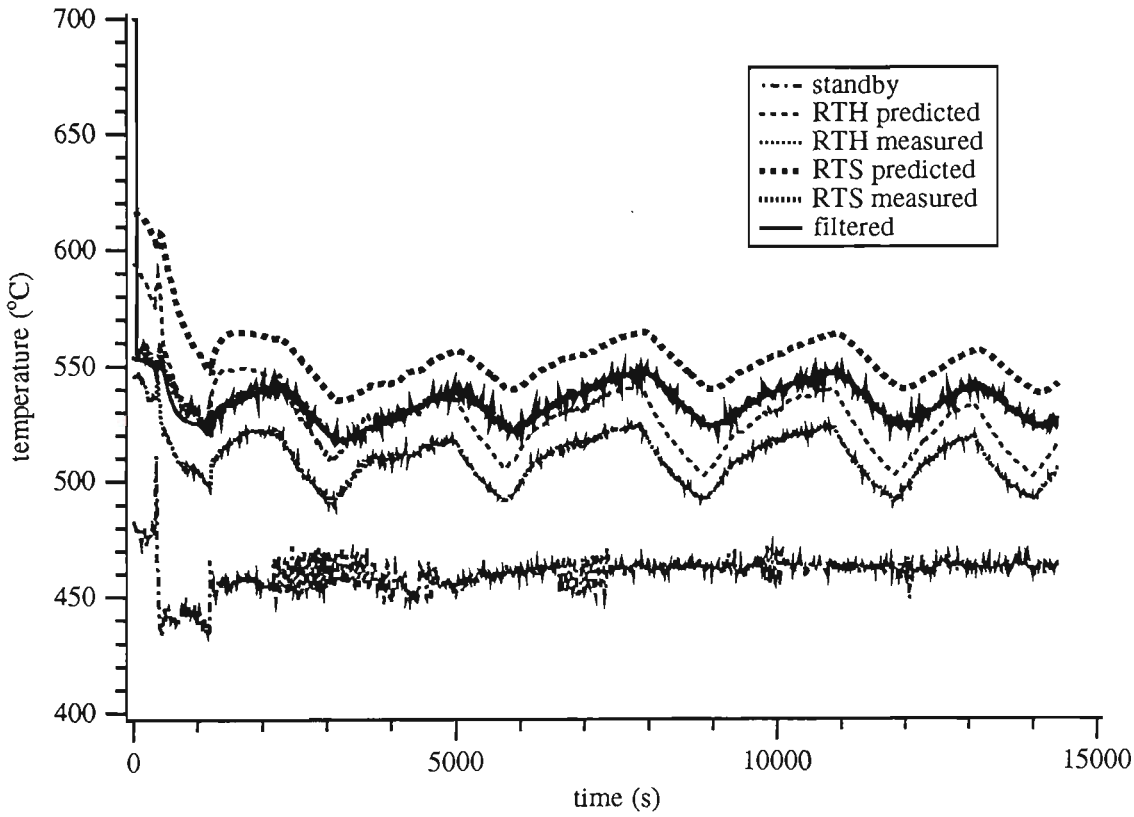

Figure 3.7: Comparison of results for mrl32 - complete roll/strip interaction

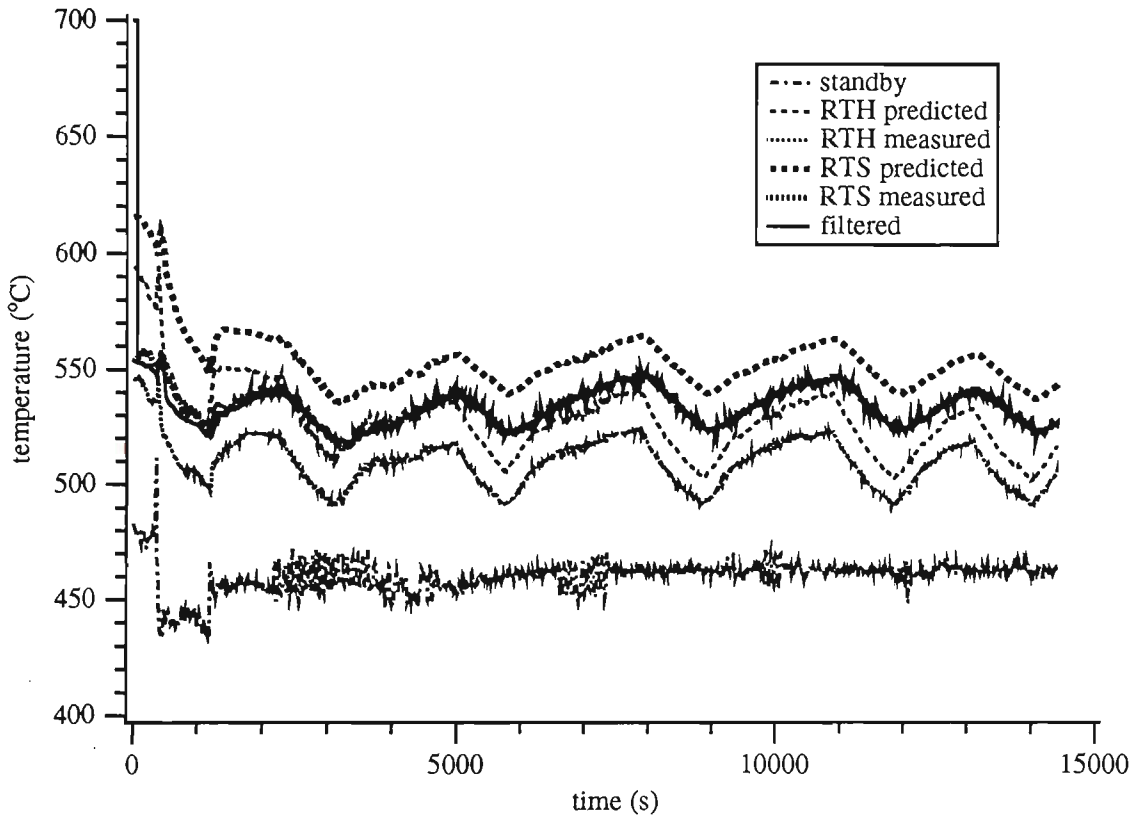

Figure 3.8: Comparison of results for mrl32 - 50/50 roll/strip interaction

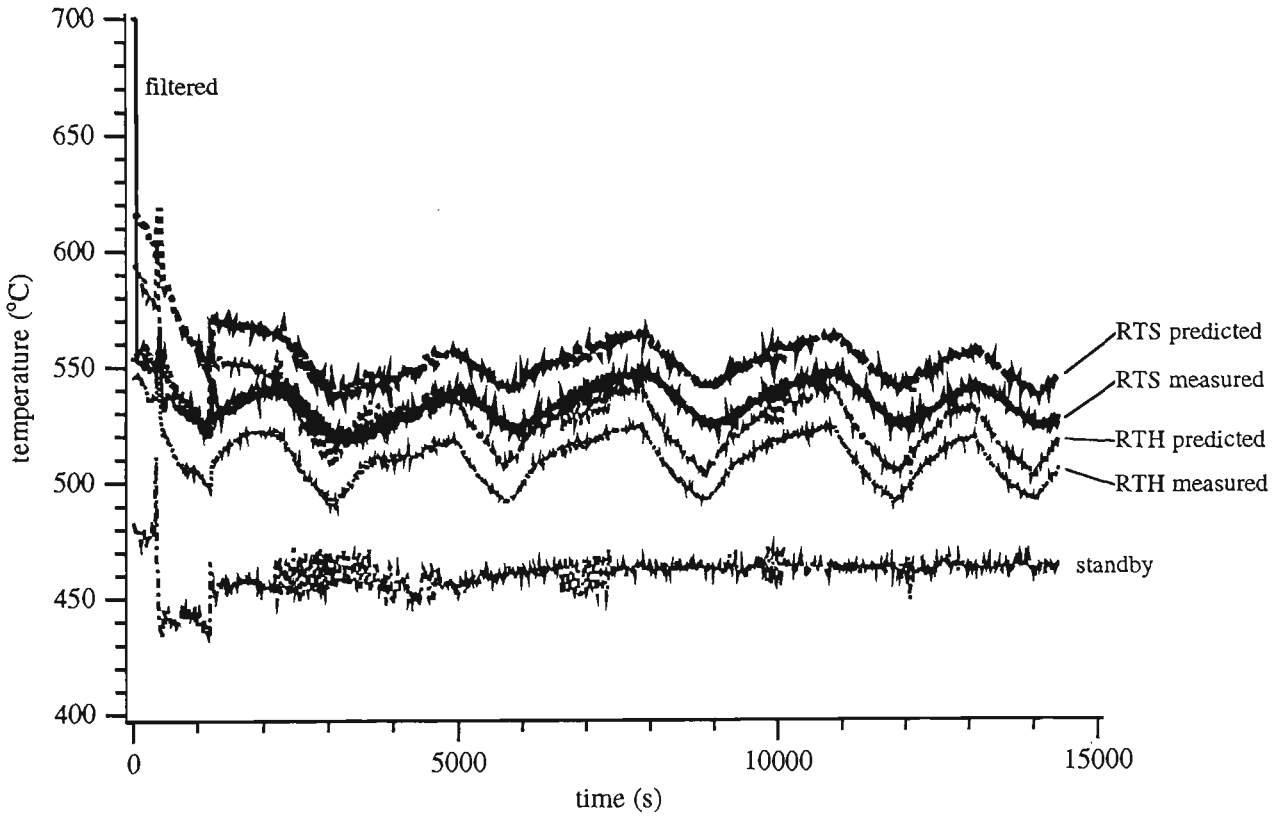

Figure 3.9: Comparison of results for mrl32 - no roll/strip interaction

oscillate in a more realistic manner than in the previous complete-interaction case, because the model more accurately reflects the actual situation on the line. The final graph in Figure 3.9 shows the situation where none of the roll mass is assumed to be in contact with the strip surface. This graph shows that the oscillation in the strip temperature over time is wildly varying, which is also unrealistic as the measured temperatures indicate. Figure 3.6 uses a 25/75 split, where 25% of the roll mass in contact with the strip is transferring heat with it, and the remaining 75% is not. This arrangement is used in the following graphs also, as it is found to represent the real-time strip temperature variation well, although it will vary from case to case depending on such things as the strip/roll contact time, the thermal contact resistivity and the strip thickness. In mathematical terms, $I_{r \rightarrow s} = 0.25$ in equation (3.17).

In Figures 3.10-3.12, an example of a line start-up is given. The data set used here is labelled *mrl33.dat*, and it includes an initial period of around 7300 seconds during which the line is not moving, as seen in the variation of line speed with time in Figure 3.11. The corresponding gas and air flows are displayed in Figure 3.10, and the strip thickness and width in Figure 3.11. As a result, the model only begins operating once the line starts up. The initial large overprediction is again caused by the model initialising on the first line of data, therefore assuming that the low value of line speed has always existed. As the line speeds up, the model predicts more realistic temperatures, and the filtered values again closely follow the measured data values. The model only starts accepting data when the line speed reaches a value greater than or equal to 30 metres per minute. The model could use a lower value for the minimum line speed required for calculations, but for this data set it caused difficulties, because the strip speed is 25 m min^{-1} at about 2300 s only for a short time before being shut down again. Also, the gas flows are not turned on in the RTH at this time, resulting in unrealistic strip and

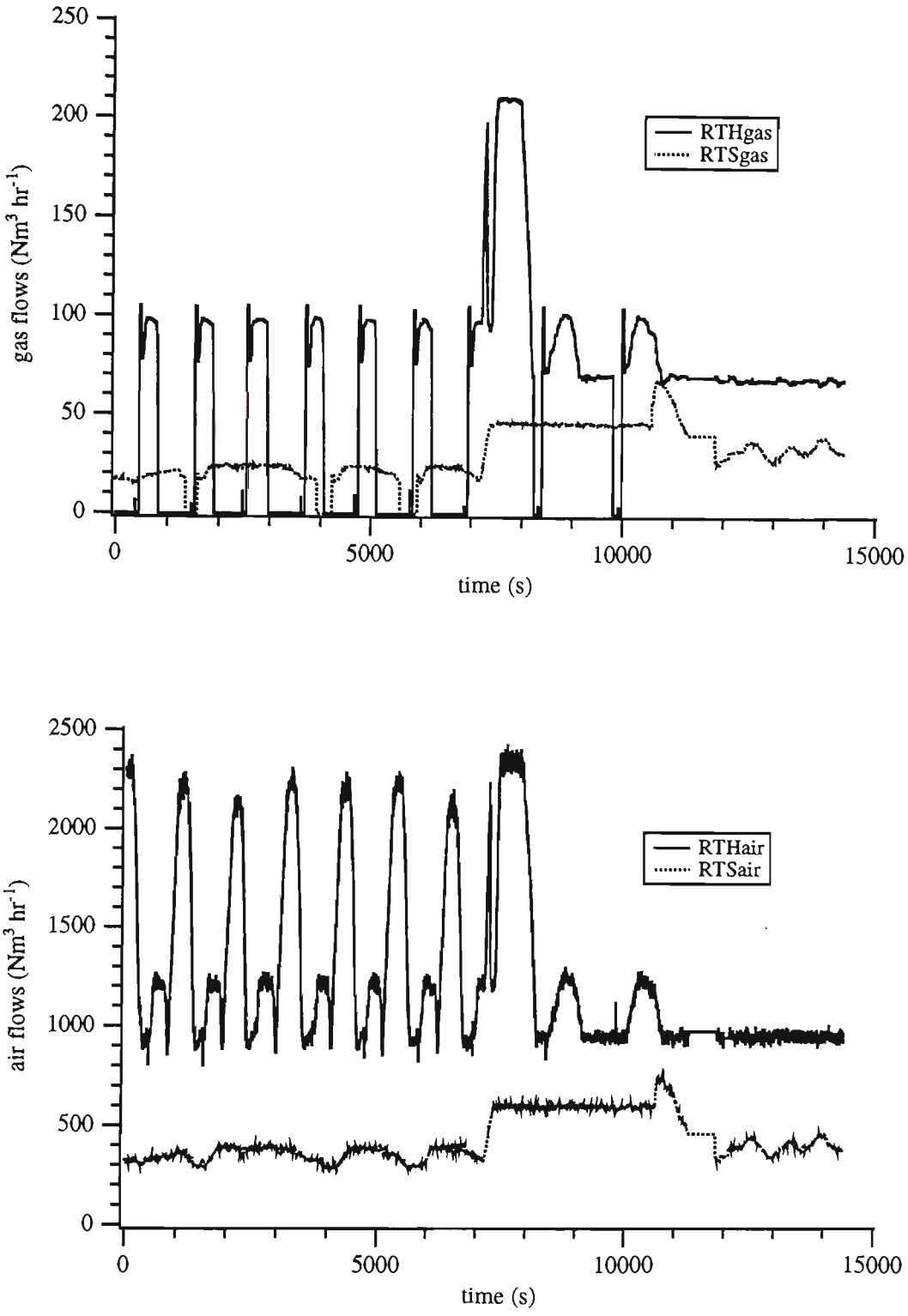

Figure 3.10: Data set mrl33 - gas and air flows

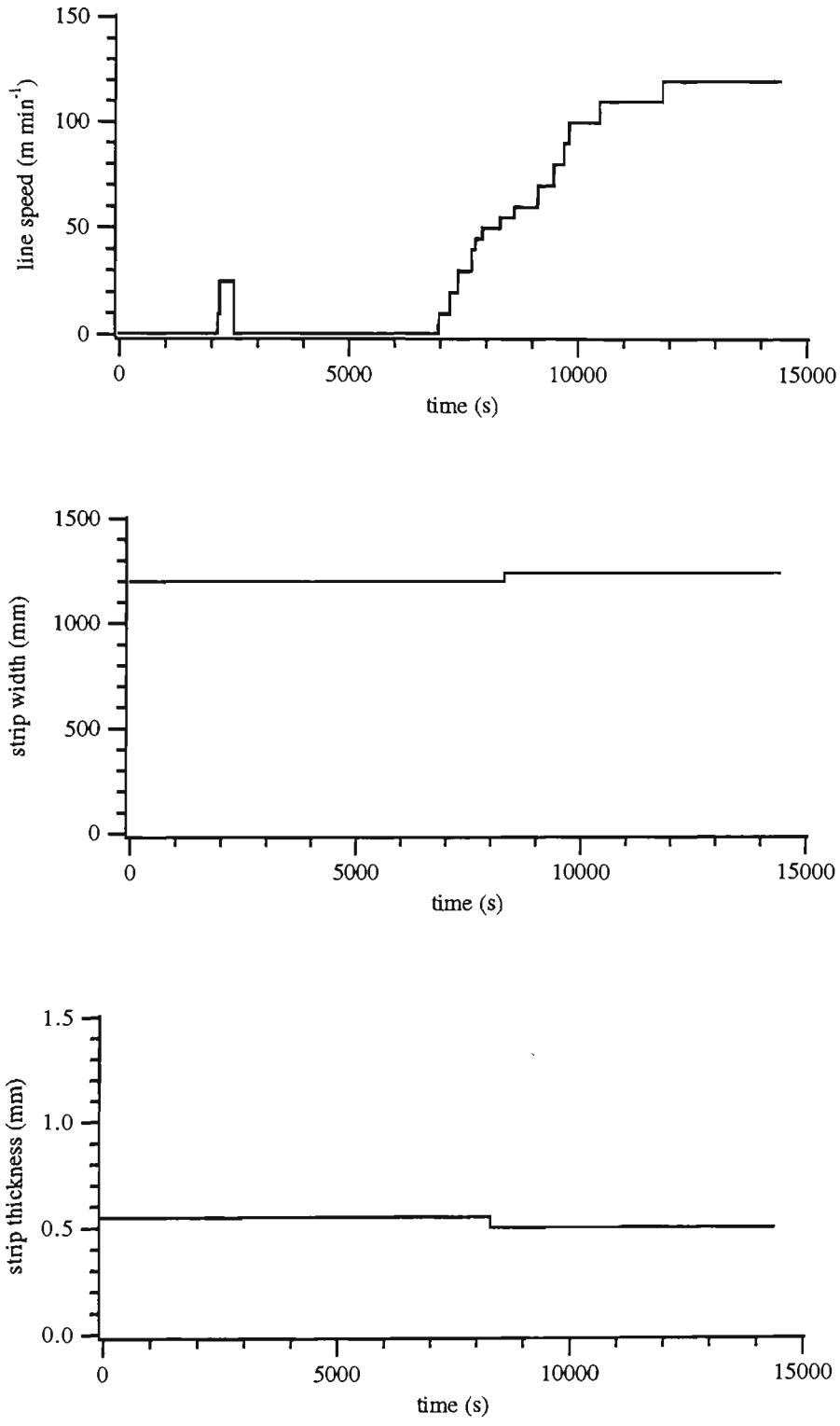

Figure 3.11: Data set mrl33 - line speed, strip width and thickness

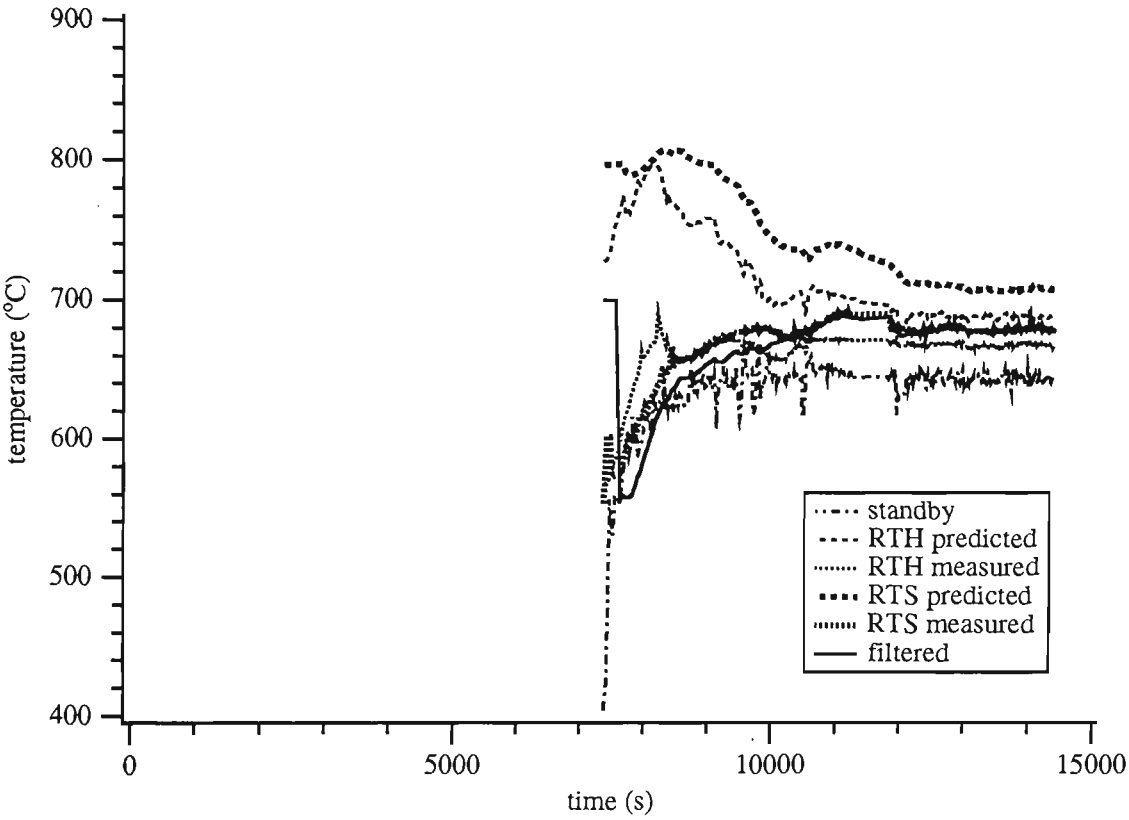

Figure 3.12: Comparison of results for data set mrl33

wall temperature values. The model assumes that the RTH has *never* had any heat input to it, because it has no prior knowledge of furnace conditions.

The next set of graphs is for the data set labelled *mrl35.dat*, shown in Figures 3.13-3.15. The major feature is the cycle change that occurs at approximately 8000 seconds into the data set. This cycle change is due to a drop in the DFF exit temperature from approximately 750°C to 600°C, causing the gas in the RTF tubes to be turned off. When the gas flows are turned back on at around 9200 seconds, the line speed is decreased to 70 metres per minute. There is also a section change here, shown in Figure 3.14, with the thickness increased from 0.75 mm to 1.00 mm, and the width from 900 mm to 1020 mm. Other minor section changes occur for the duration of the data set, but do not result in significantly different strip temperatures. Perhaps the most noticeable is at 10300 seconds, where the strip dimensions change from 1.00×1020 mm to 1.20×1070 mm, accompanied by a line speed decrease from 70 m min^{-1} to 65 m min^{-1} and a substantial initial decrease in gas flow.

Again, it is clear that the model slightly overpredicts the strip temperature for the exit from both the RTH and the RTS. The filtering corrects this difference, as the solid line on the graph shows. The predicted temperatures follow the trends well, even in the period where the gas is turned off when the temperature is decreasing towards its new set point value. The graph indicates that there is virtually the same difference between the predicted and measured data line for the duration of the data set.

For the final data set, labelled *mrl36.dat*, there is very little variation in strip temperature over its duration. There are only two significant thickness changes — one at around 1900 seconds, and the other at 8900 seconds, shown in Figure 3.17. Both of these changes are clearly seen on the graph in Figure 3.18, in the line representing the standby pyrometer temperature. Smaller changes in the standby pyrometer temperature occur at around 4600

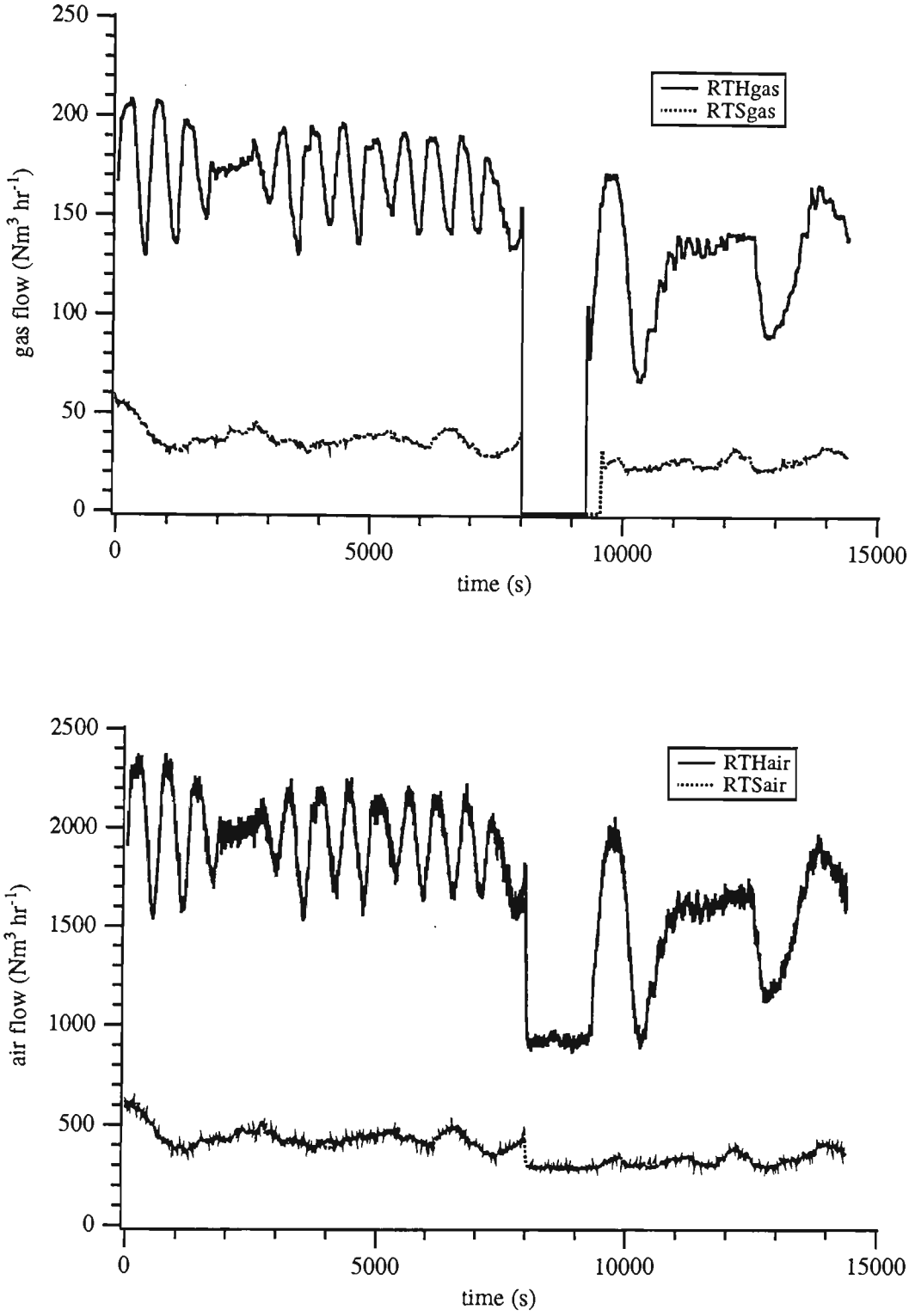

Figure 3.13: Data set mrl35 - gas and air flows

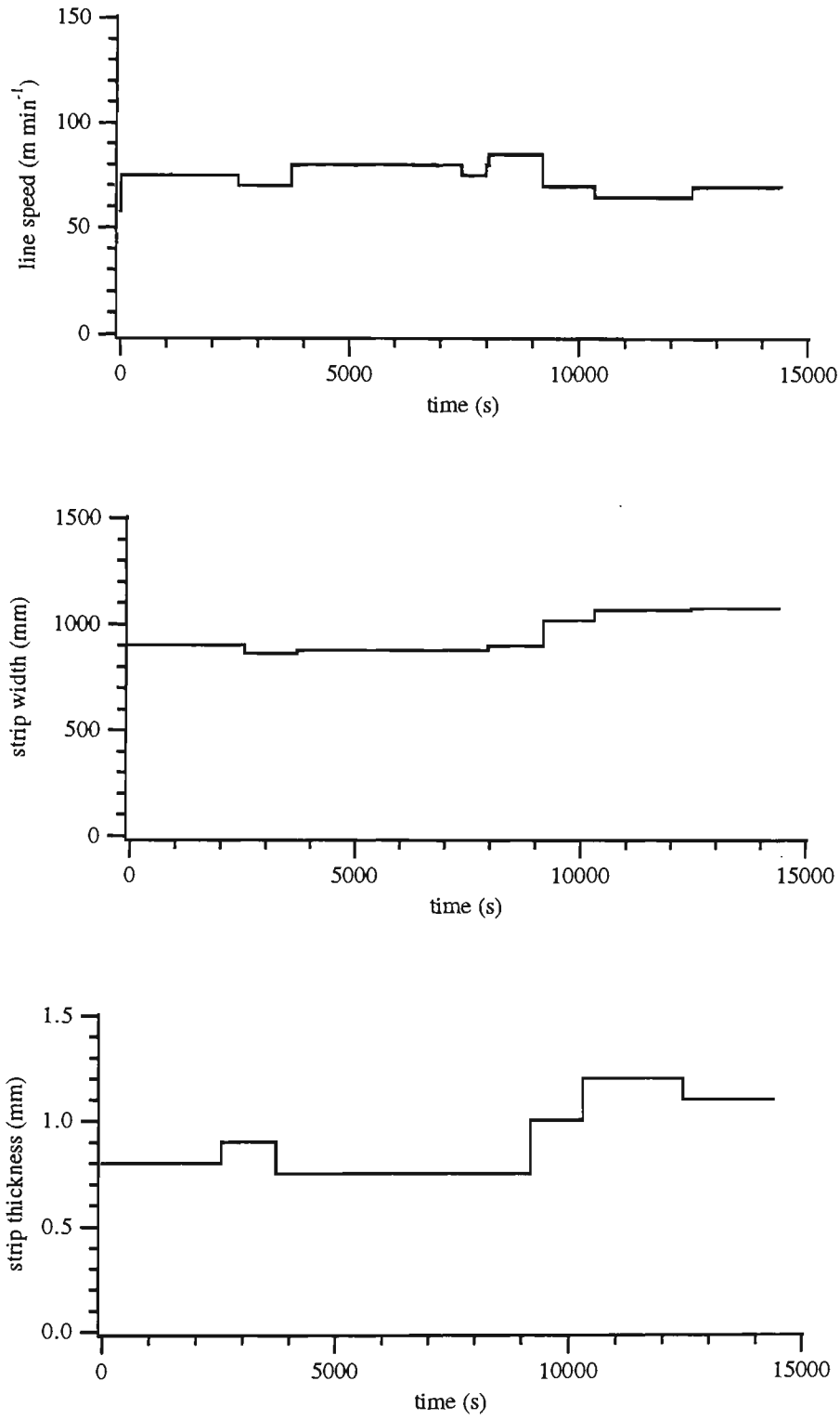

Figure 3.14: Data set mrl35 - line speed, strip width and thickness

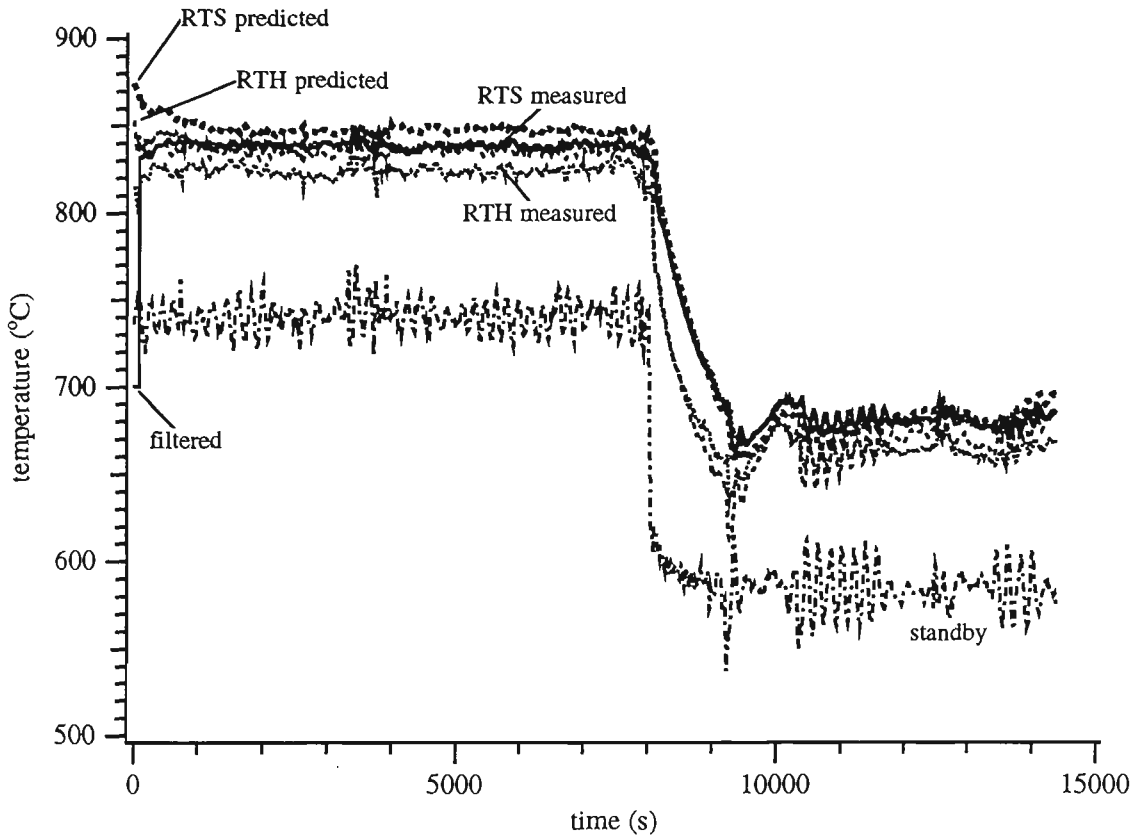

Figure 3.15: Comparison of results for data set mrl35

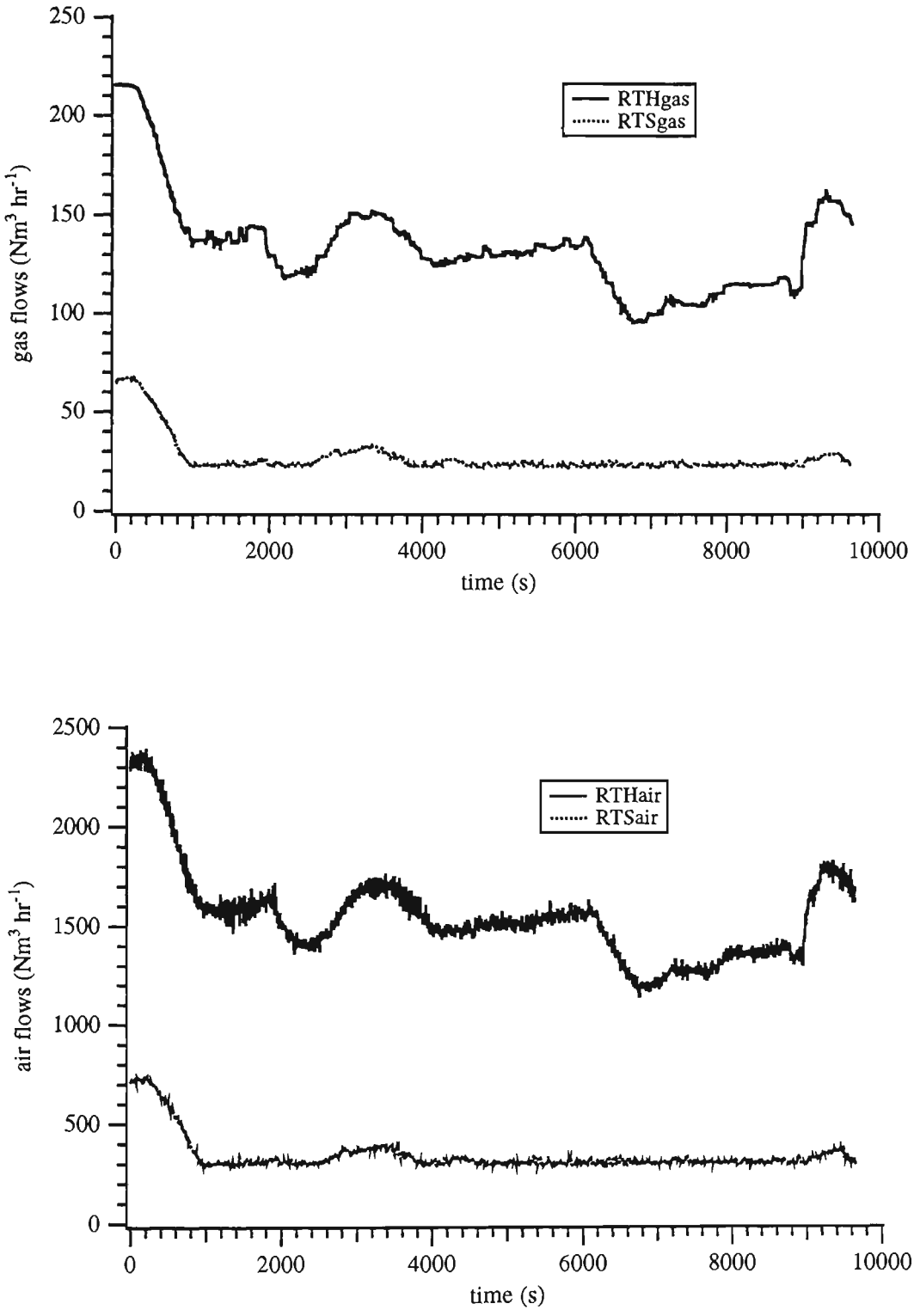

Figure 3.16: Data set mrl36 - gas and air flows

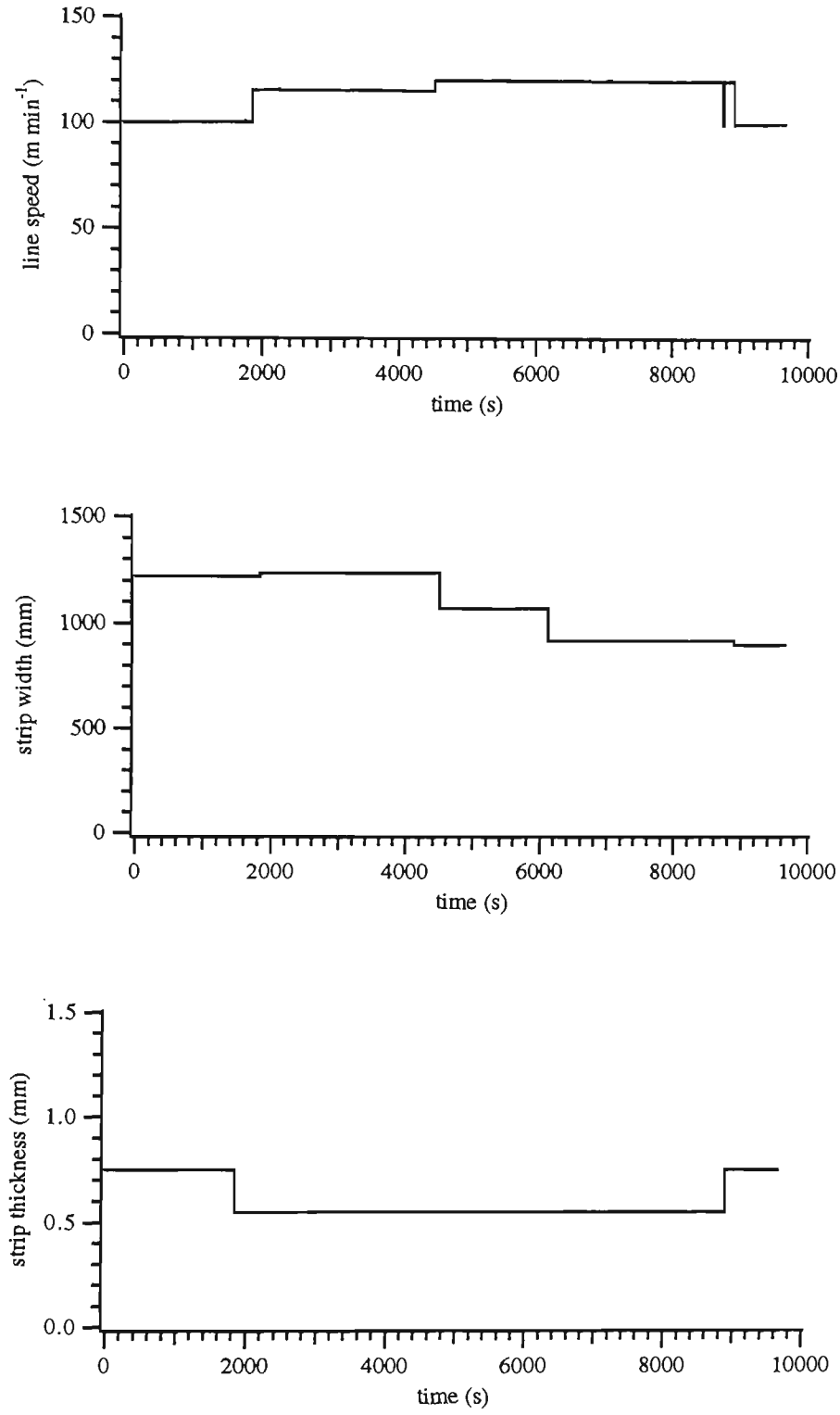

Figure 3.17: Data set mrl36 - line speed, strip width and thickness

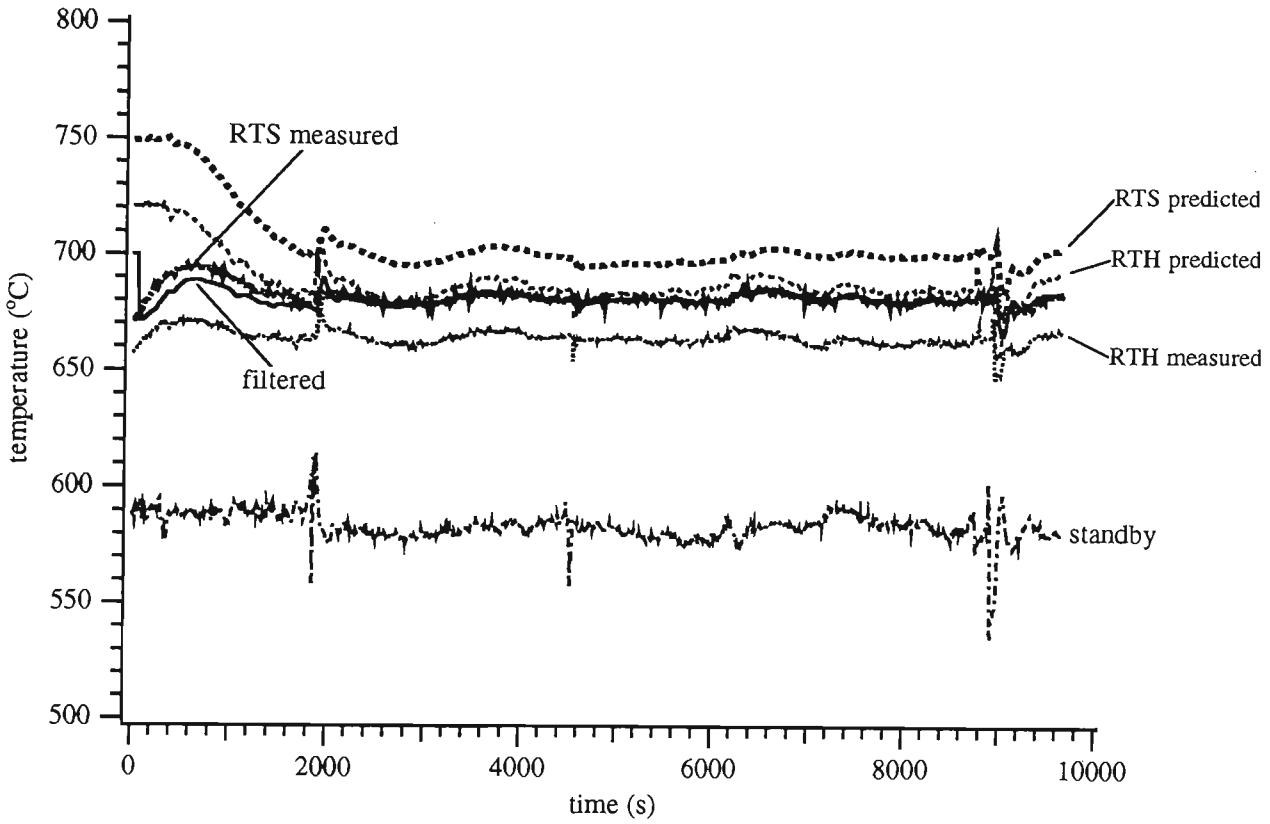

Figure 3.18: Comparison of results for data set mrl36

seconds, coinciding with a slight increase in line speed due to a decrease in the strip width, and at around 6000 seconds with another strip width decrease. The gas flows are high at the beginning of the data set, but are mostly in the range of 100–150 $m^3\ hr^{-1}$ in the RTH and 20–30 $m^3\ hr^{-1}$ in the RTS as shown in Figure 3.16.

The results show that the model again overpredicts at the start, but follows the trend of the data for the duration on the data set, slightly above the measured value. The filtered temperature is never more than 15 K out from the measured value, and during normal operation it almost exactly follows the measured data.

In Figure 3.19, a graph of data set *mrl36.dat* is again given, only this time the iteration has not commenced until about 1000 seconds into the data set. The purpose of this graph is to indicate the influence of the initial conditions on the values that the model obtains at the end of the initialisation. The gas flows for this data set, shown in Figure 3.16, are very high to begin with, before levelling out at around 1000 seconds. As a result, the initial predictions of the model are also much higher. Because the model has no prior knowledge of the values of the line speed, gas flows etc, it assumes that the furnace has been running with the initial conditions for an unlimited time up to that point. However, when the gas flows decrease, the model reflects the decrease in the strip temperature, as shown in Figure 3.18. Figure 3.19 is displayed to indicate that the model would be much closer to the measured values initially if the variation in the model parameters was small to begin with.

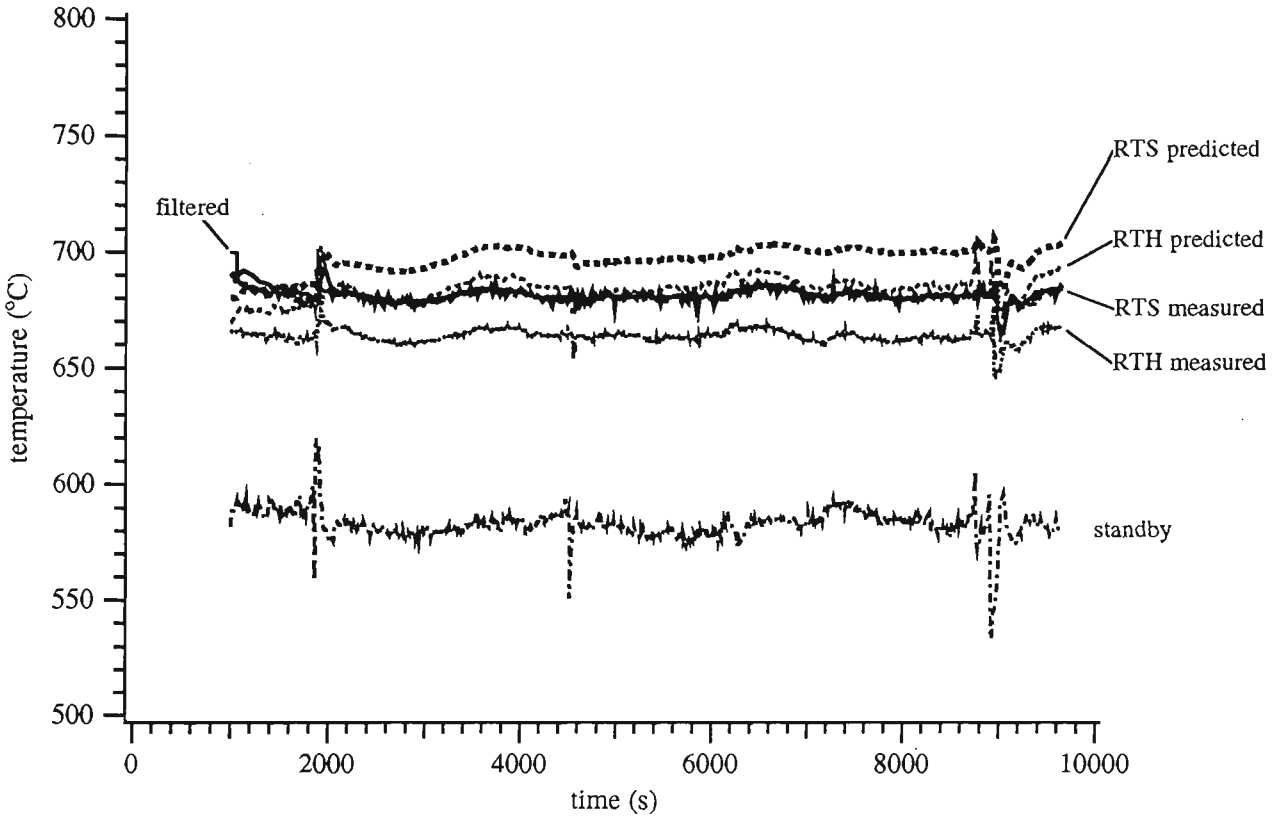

Figure 3.19: Comparison of results for mrl36 using initialisation at 1000s

3.5 Conclusion

This section of the thesis has summarised the development of a model for the operation of the radiant tube furnace on MCL6 at Westernport. The model has the advantage of being extremely quick and hence can be used on-line to control the line. The raw model generally overpredicts the measured strip temperature by around 20 K, but a filtering procedure using feedback from previously obtained data corrects this and enables the model to have both speed and accuracy.

The model could be extended if desired by using a less crude approximation for the heat flow between the walls and the strip, especially by separating out the tubes and the rest of the furnace from the 'wall'. Going into greater depth would cause the model to take longer to run, but improve its accuracy. If BHP wanted to derive an off-line model for this procedure, as has been done for the DFF, then the model could be made more complex and account more for the heat interaction between all of the surfaces and concentrate on the accuracy of the raw predicted data without need for a filtering procedure. For example, a finite-difference method for the roll/strip interaction could be implemented. Also, a more accurate FDM could be used for the evaluation of the strip temperatures and more grid points could be employed, with perhaps 20 grid points per segment rather than just one at each end. This would also require a decrease in the time step, and therefore it would examine more of the data set that is fed into the program, rather than using one in every three or four lines of data as is now the case.

Chapter 4

Modelling the direct-fired furnace on MCL6

The next stage of the project was to adapt and update the direct-fired furnace model from the previous chapters to BHP's newest galvanising line, MCL6 at Westernport in Victoria. During the course of the thesis, data had been made available from MCL6 that could allow the DFF model to be tested more reliably than was the case for CGL2. The input data mentioned in the previous chapter also includes data from the direct-fired furnace, including the initial preheat (entry) temperature and the boot (exit) temperature from the DFF, as well as gas and air flows for all zones. This information, combined with the line speed, gas flows and strip width and thickness which the data also provides, allows the DFF to be modelled with many transients over a duration of hours, rather than just one transient for a few minutes in the case of the CGL2 model. Therefore the major reason for extending the model to the DFF on MCL6 was the greater availability — if not greater accuracy — of data. It also allowed for the model to be extended to examine the strip edges, mentioned in the following chapter.

The model for MCL6 DFF includes the core of the CGL2 DFF

model, combined with the input procedure for the RTF model, so that the model can be run with data being continually input. However, the two direct-fired furnaces are not identical, and the model needs to be adjusted accordingly.

4.1 Description of the MCL6 DFF

The differences between the DFF on CGL2 and MCL6 become more apparent in the diagram of the MCL6 direct-fired furnace in Figure 4.1 [51]. The furnace is now split into three sections — the preheat, the bridge and the DFF proper. (Hereafter, the term 'DFF' is used to represent the *whole* furnace, including the bridge and the preheat, and the term 'DFF proper' will represent the main gas-fired heating section of the furnace.)

The total length of the furnace is about 38 m, with a furnace width of 2.4 m and the furnace depth 0.6 m; except in zone 4 of the DFF proper where it is 0.45 m, and in the preheat section where it is 1 m. The preheat (length $\approx$ 10 m) uses recycled gases from the DFF proper to heat the strip if some preliminary heating is required. For example, when running soft-cycle steel, the preheater needs to be on to ensure that the steel reaches the required temperature (approximately 600°C). For hard-iron product, the set-point temperature is about 500°C, and the preheat may not be needed, although this also depends on the capacity of the furnace. The amount of gas entering the preheater is controlled depending on the type of product that the line is running. The bridge section (length $\approx$ 14 m) simply holds the strip at its entry temperature until it enters the DFF proper; gas does not flow through it. The function of the DFF proper (length $\approx$ 14 m) is to heat the strip to the required set point temperature, and to clean it of impurities — hence these are the same functions performed by the DFF on CGL2. All of these factors must be included in the model. The strip temperature is recorded using an

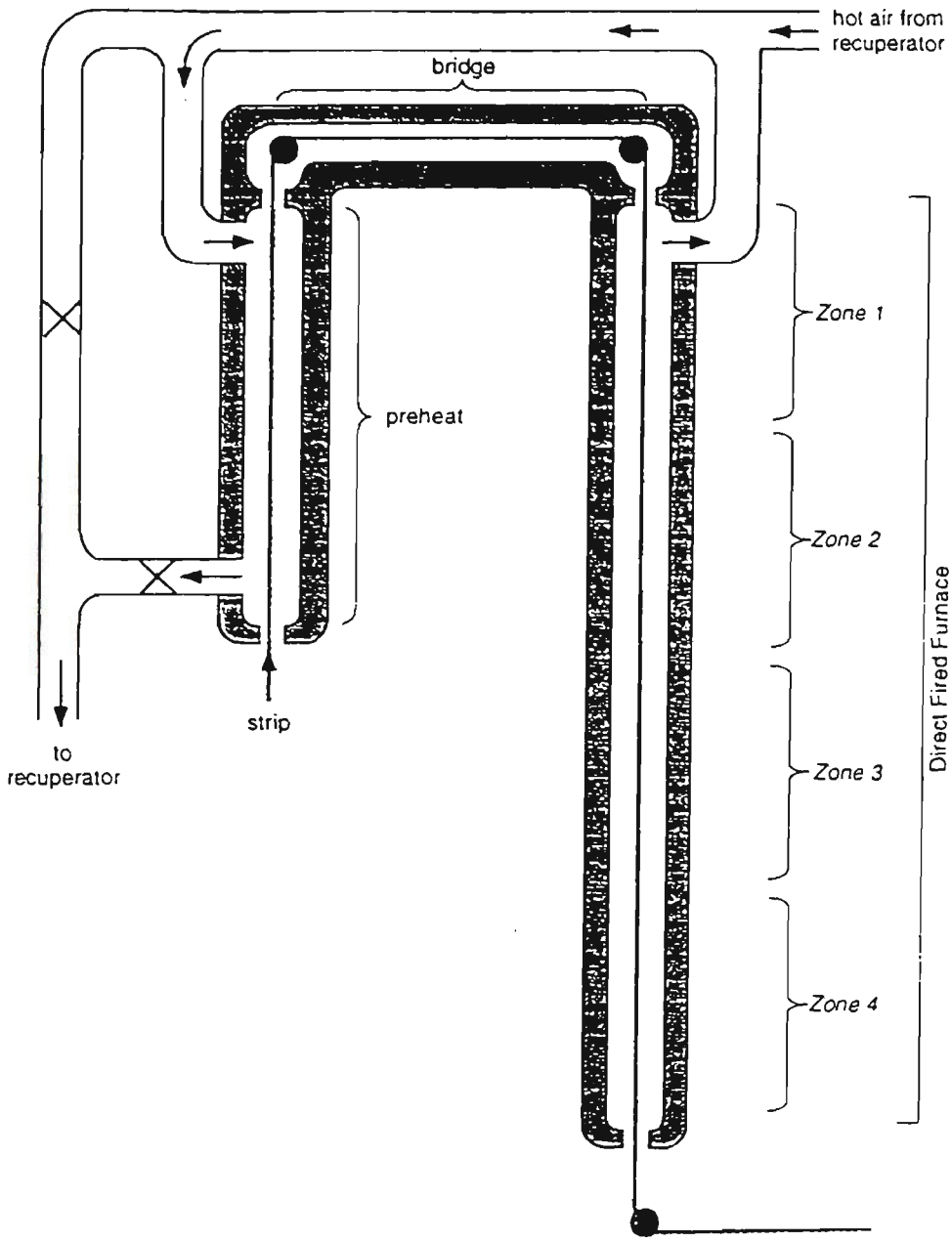

Figure 4.1: Diagram of MCL6 DFF

exit pyrometer at the boot of the DFF and the so-called standby pyrometer, located after the DFF boot roll, which was used in the RTF model.

On MCL6, the DFF proper is split into four gas-producing zones rather than six, and they are numbered from top to bottom rather than bottom to top as for CGL2; hence zone 4 is the bottom zone. Zone 4 is a premix zone and is always turned on (except in the case of a line stoppage) to ensure adequate cleaning of the strip. Zones 1-3 are nozzle mix zones, and so can use recuperated air, whereas zone 4 uses purely combusted air at ambient temperature as for CGL2. The heat demand factor (HDF) is a value which describes the current DFF proper gas flow for all zones as a percentage of the maximum DFF proper gas flow for all zones. The rules for operating the preheater can be described in terms of the HDF as follows;

- if furnace HDF $< 40\%$, preheater is off;
- if $40\% \leq$ furnace HDF $\leq 70\%$, a linear fit for the preheat gas flow is used from 0 to 100% of the gas flow at the top of the DFF proper, and
- if furnace HDF $> 70\%$, a linear fit is used between 100% DFF proper gas flow at HDF $= 70\%$, and 50% DFF proper gas flow at HDF $= 100\%$.

If the gas temperature at the preheat/bridge boundary is greater than 950°C, then the preheater is turned off in order to keep the strip temperature down. If the strip temperature exceeds 240°C in the preheater, it will develop an oxide layer which is too thick to remove later in the furnace.

As was mentioned in Chapter 3, the data values from the input files are not always reliable. Measurements and assumed data from the line are not exactly correct all of the time, and can sometimes be completely wrong. For example, assumed strip thicknesses can be incorrect by only a couple of percent, but this still has a significant influence on the overall strip temperature. Also, when a gas zone is turned off, the value for the gas flow is given as zero in

the data file. However, unless the line is shut down, the gas flow is actually operating at a minimum fire rate of 17% of it maximum value, which equates to about 55 $m^3\ hr^{-1}$. These anomalies are a fact of life, unfortunately, but are allowed for in the model where possible.

4.2 Differences in the models

Some changes had to be made to the original CGL2 model in order to adapt it to the MCL6 direct-fired furnace, aside from the change in the format of the input data from one initial reading to a continuous update of values. For example, a routine for line stoppages was also included in the program, so that the model works in situations such as for data set *mrl33.dat* shown in Figure 3.12.

Recall the equations for the dynamic model;

$$\frac{\partial T_s}{\partial t} - V_s\frac{\partial T_s}{\partial x} = \frac{Q_{gs}}{\rho_s w_s d_s c_{ps}} \tag{4.1}$$

$$\frac{\partial T_g}{\partial t} + V_g\frac{\partial T_g}{\partial x} = \frac{Q_{comb} - Q_{gs} - Q_{gw}}{\rho_g(w_f d_f - w_s d_s)c_{pg}} \tag{4.2}$$

$$\frac{\partial T_w}{\partial t} - \kappa_w\frac{\partial^2 T_w}{\partial z^2} = 0 \tag{4.3}$$

where

$$Q_{comb} = \dot{M}(h_{ad} - h_g) \tag{4.4}$$

$$Q_{gs} = \alpha T_s^4 + \beta T_g^4 + \gamma T_w^4 + H_s(T_g - T_s) \tag{4.5}$$

$$= P_s(B_{gs} - B_s + q_{s,c}) \tag{4.6}$$

$$Q_{gw} = \mu T_s^4 + \nu T_g^4 + \xi T_w^4 + H_w(T_g - T_w) \tag{4.7}$$

$$= P_w(B_{gw} - B_w + q_{w,c}) \tag{4.8}$$

Because of the absence of gas flow in the bridge section, the heat transfer equations omit both the gas temperature and any heat transfer via convection

in this section of the furnace. Therefore, the gas equation (4.2) is excluded, and the Q_{gs} term used in equation (4.1) and the Q_{gw} term used in the boundary condition for the wall (2.96) become

$$Q_{gs} = \alpha T_s^4 + \gamma T_w^4, \tag{4.9}$$

$$Q_{gw} = \mu T_s^4 + \xi T_w^4 \tag{4.10}$$

These equations also hold for the preheater if there is no gas flow there, which occurs in conditions mentioned previously. When the preheater is turned on, the term Q_{comb} is eliminated from the gas equation, because no gas combustion occurs in the preheat section.

During the initial runs of the model using MCL6 data, numerical oscillation was found in the bridge section of the furnace, where gas is absent. The oscillation was greatest in the region close to the boundary of the bridge with the direct-fired furnace proper, and was still present as the time step was lowered. As the grid spacing was decreased, the range of the instability was reduced, but it was still noticeable close to the boundary. The problem at the boundary results from the discontinuity of the gas flow between the DFF proper and the bridge. This problem did not arise for the CGL2 model, because the gas flows through the whole furnace in that example. In section 2.3.3, it is described that the Lax-Wendroff method, given by equation (2.61), is used throughout the furnace, except at the zonal boundaries where the second-order upwind method, equation (2.62), is used. Let b denote the point at the bridge/DFF boundary. At point b, the strip enters the top of the DFF proper from the bridge section, whilst the gas provides heat transfer to the strip. The second-order upwind method is used to find the new strip temperature at point b using points $b+2$, $b+1$ and b. At the point immediately before it from the viewpoint of the strip, $b+1$, the Lax-Wendroff method is used to calculate the

new strip temperature, ie,

$$T_{sb+1}^{n+1} = \tfrac{1}{2}c_{sj}^{n}(1+c_{sj}^{n})T_{sb+2}^{n} + (1-\{c_{sj}^{n}\}^{2})T_{sb+1}^{n} - \tfrac{1}{2}c_{sj}^{n}(1-c_{sj}^{n})T_{sb}^{n} + \triangle t^{n}(\mathrm{RHS}_{s})_{j}^{n}. \quad (4.11)$$

However, the value of T_s at the point b includes the temperature that is influenced by the gas flow at the bridge/DFF boundary. As the Lax-Wendroff method is used for the whole bridge section, the influence of the gas feeds its way back through the furnace, depending on the size of the grid spacing. This causes the numerical oscillation. In response, the usage of the finite-difference methods was altered. For this furnace, the second-order upwind method is used everywhere, except at the first point after a zonal boundary as the strip moves through the furnace. This arrangement is also used for the gas in its opposite direction of motion. Hence the oscillation is removed in the bridge section, as upwind methods only use the values 'behind' it relative to the direction of motion.

In the MCL6 model, updated values for such parameters as the strip emissivity and specific heat are used, which are different from those used in earlier work. Analysis was done in the interim period on these experimental values, and here they are taken from Stone & Morrison [51]. Again, there is some doubt as to the reliability of this experimental work, but these values are used throughout the remainder of the thesis.

Also, the procedure to determine the optimal time interval needs to be updated as the new data is input. As the gas velocity is continually changing with the gas flow and the gas temperature, so the time step can increase or decrease depending on whether the gas flow rate falls or rises. In this way the program runs at its optimal speed for its duration, while always ensuring that stability is maintained using equations (2.79), (2.80) and (2.99).

Some gas parameters also vary with the air-to-fuel ratio, such as the adiabatic flame temperature, the mole fractions of products to reactants, and

the density of products at the adiabatic flame temperature. Initially these were given at discrete values of the air-to-fuel ratio, but because of the variation of the air-to-fuel ratio at different zones in the furnace, functional fits were performed on these data so that they are now 'functions' of the air-to-fuel ratio.

To obtain results, temperatures are initially assumed for the strip, gas and wall at the top and bottom of the furnace, with a linear fit to these points giving temperatures at all discrete points in the furnace. The bridge section, in which there is no gas flow, is not included in the linear fit for the gas temperatures, and at all times the gas temperature at the preheat/bridge boundary is taken to be the same as that at the bridge/DFF proper boundary — ie, the gas does not lose any heat as it passes through the ducts from the DFF proper to the preheater. (Because this may overpredict the gas temperature at the preheat, the condition that the preheat is turned off when $T_g > 950°C$ is neglected.) Using these initial temperatures, the program is run to steady-state conditions, which usually occurs in the time that it takes for the strip to travel two furnace lengths (depending on the line speed). During the initialisation procedure, the wall is assumed to be adiabatic, so the solution for the state of the furnace is a steady-state solution. The resultant state is reasonably indicative of the actual furnace state, although the large time constant for the wall makes it difficult to determine this exactly. Therefore

$$B_{gw} - B_w + q_{w,c} = f(T_w) = 0 \tag{4.12}$$

is solved for T_w using an IMSL routine [19] for finding the root of a polynomial.

4.3 Results

Results of this adaptation of the model to MCL6 are now presented. Graphs are shown to compare the results of the model to the line data for the data sets

mrl32.dat and *mrl35.dat*, both of which were used in the model comparisons for the radiant tube furnace also. These data sets include measured values for the DFF gas and air flow rates, the furnace heat demand factor, the preheat entry temperature and the boot strip temperature.

The first set of results is for the data set *mrl32.dat*. The gas and air flow rates for zones 1-4 are shown in Figure 4.2; the line speed, strip thickness and width values are as shown in Figure 3.5. The predicted model temperature is represented by the dashed line, while the measured temperature taken from the standby pyrometer (also used in the RTF model comparisons) is denoted by the solid line. The boot pyrometer is somewhat unreliable in its readings — for example, it is unable to read temperatures below about 500°C because of stray radiation from the DFF — so the standby pyrometer is used instead for better reliability.

The comparison of the model with the line data is found in Figure 4.3. The initial overprediction is because of the inability of the model to predict what happened prior to the beginning of the data set, and hence the wall temperature is too high initially (as in the case of the radiant tube furnace model). The line data is quite flat in its average profile over the duration of the data set, and the model follows this rather well. The oscillation in the line data is caused by the continuous oscillation in the gas flows, which in turn results from some problems that BHP have had in implementing their control strategy for the line. Because of this, transients occur continuously in the data set, which the model appears to profile well.

The other set of results is shown for data set *mrl35.dat*. The DFF gas and air flows are shown in Figure 4.4, the line speed, strip thickness and width in Figure 3.14, and the comparison of results in Figure 4.5. In this case, the model substantially underpredicts the measured boot strip temperature by around 50-100°C. The offset in temperature remains fairly constant for the

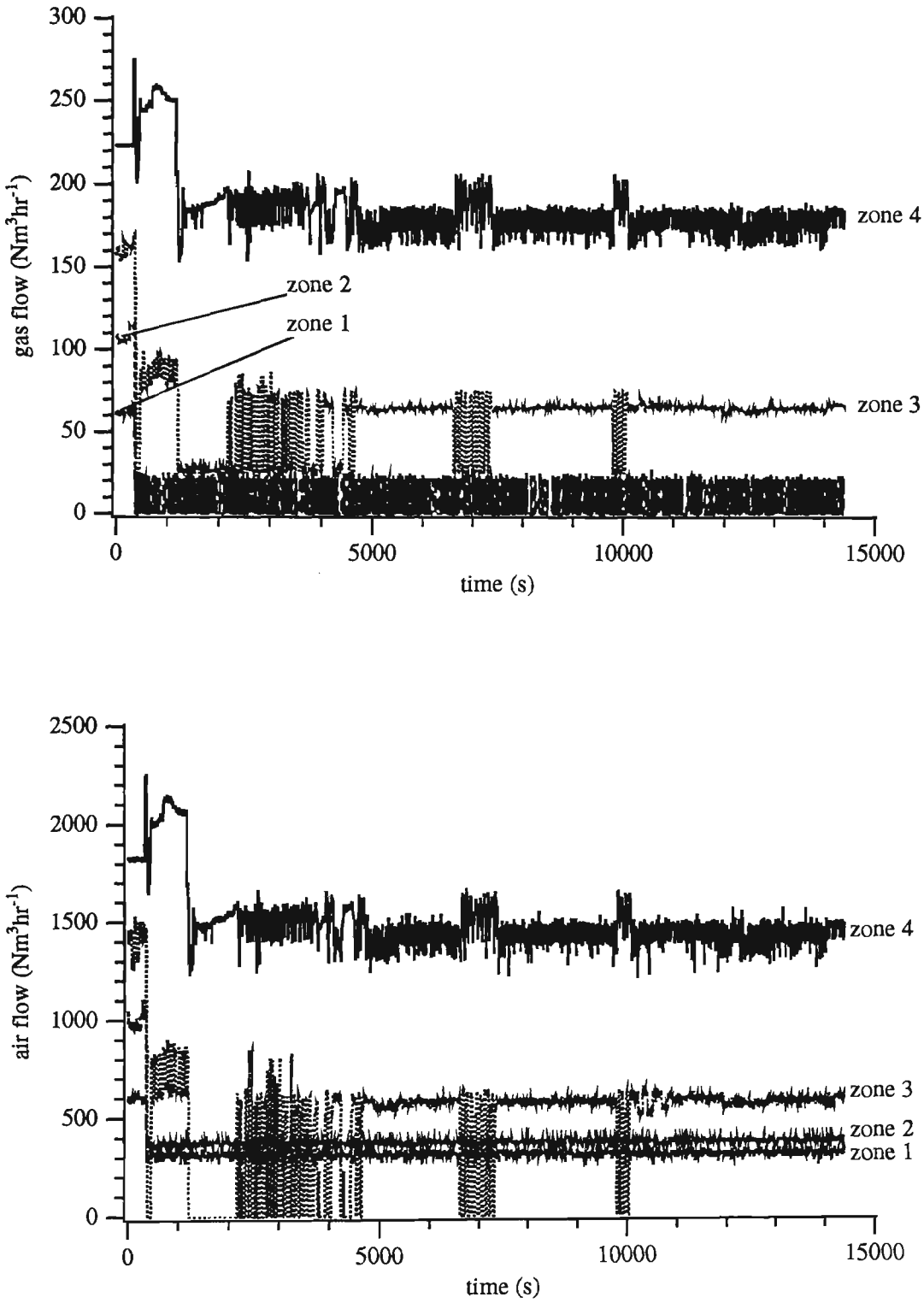

Figure 4.2: DFF gas and air flows for data set mrl32

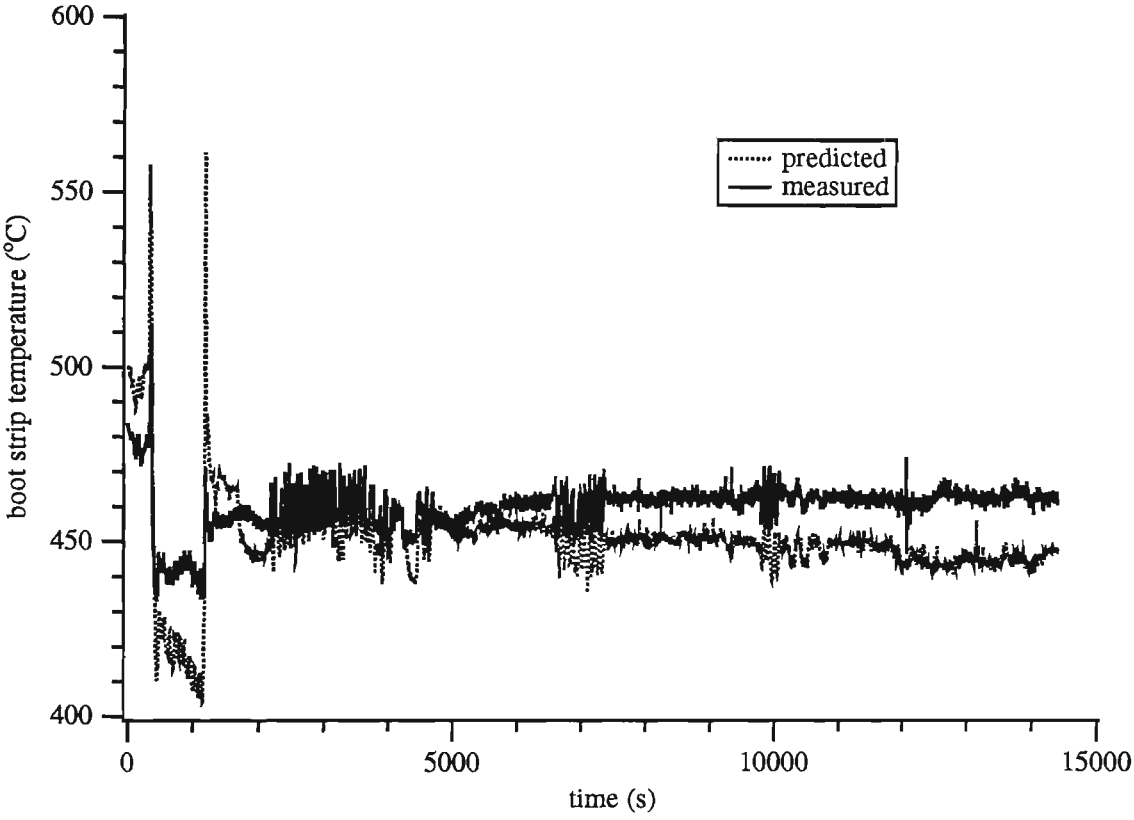

Figure 4.3: MCL6 DFF model - data set mrl32

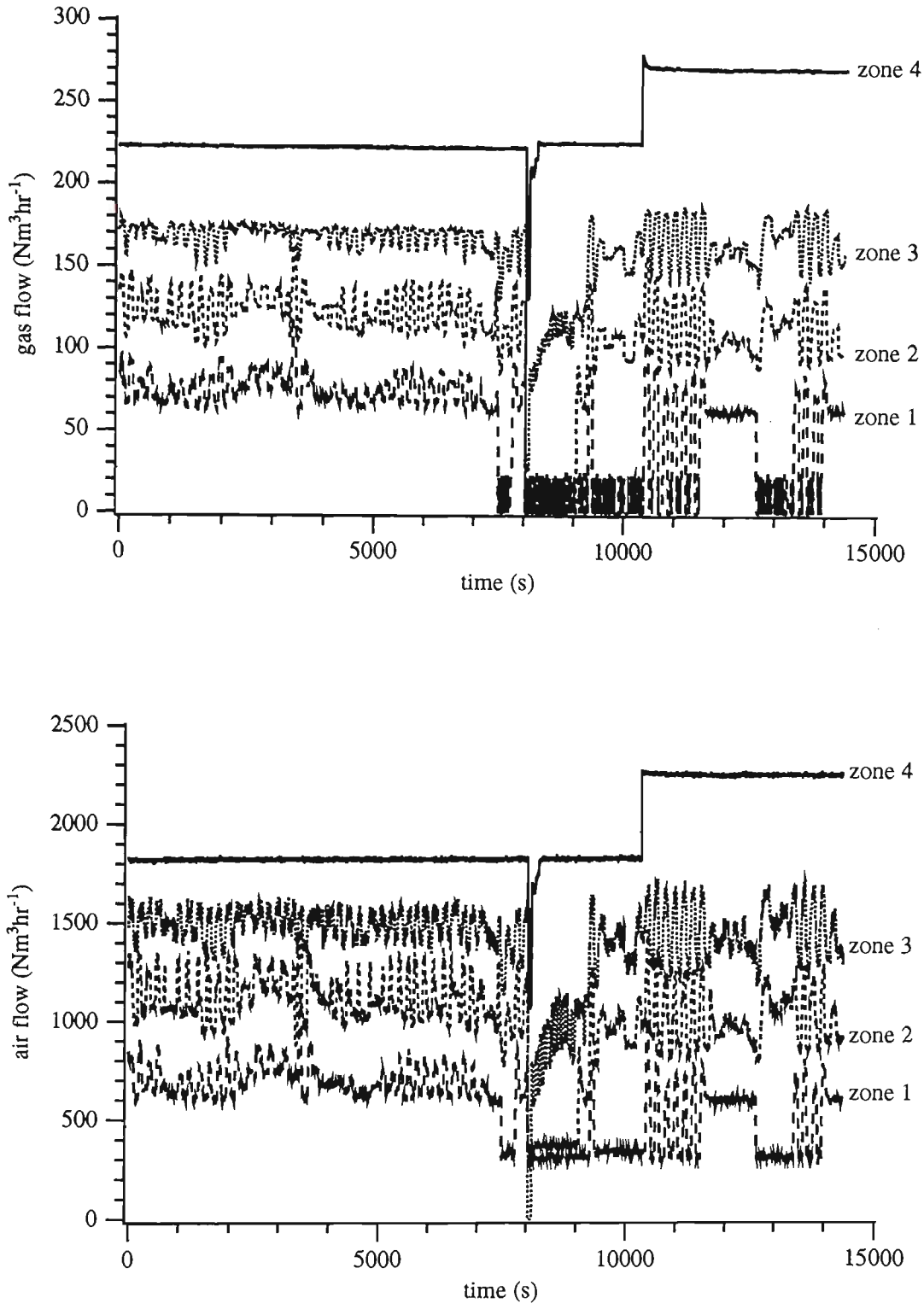

Figure 4.4: DFF gas and air flows for data set mrl35

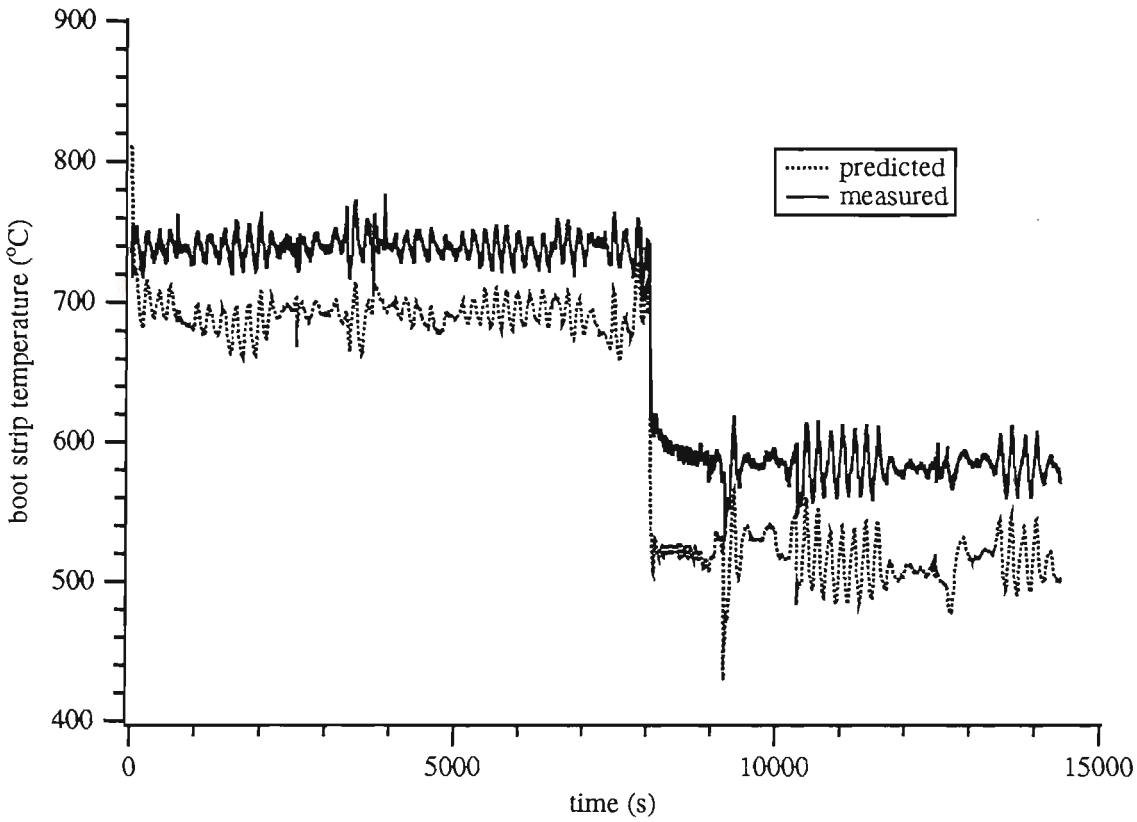

Figure 4.5: MCL6 DFF model - data set mrl35

duration of the data set. The trends in the data set are again well reflected, but obviously a discrepancy of this magnitude is unsuitable for implementation on a line, especially as an off-line model such as this. For an on-line control model, an offset error is not a problem, provided it is relatively constant across section and cycle changes. On a SUN sparc 10 workstation, the model can process the whole data set in around 15-20 minutes.

This data set reveals the need for further work, both on the model and on the data set itself, which has revealed problems with accuracy in the past. Dummy test runs of the model seemed to reflect what would be expected to occur. For example, a 10% drop in line speed caused a temperature rise of around 9%. Similar tests on the strip thickness gave similar results. A 10% drop in the strip width caused a lesser rise in strip temperature of $\approx 6\%$, because reducing the strip width reduces the area through which the strip can absorb heat. Changing the gas flows also gave expected results. Therefore further work is needed to find any deficiencies in the model (although the model of Chapter 2, of which this is an extension, appears to work well), or to gauge if some furnace parameters are not being modelled accurately. Some functions for parameters such as the strip emissivity may also be inaccurate and need further investigation. It is also desirable that more reliable data sets be available — one data set that was provided gave a value of the strip thickness approximately 20% lower than reality, causing the temperature to be about 100 K higher.

It is also noted that numerical checks were performed to test the convergence of the model. These checks also hold for the CGL2 model, because the MCL6 model is an adaptation of the CGL2 model. The data used was taken from data set *mrl35.dat* shown in Figure 4.5, and the results of the convergence test, showing the boot strip temperature at various times, are shown in Table 4.1. To estimate the error in the numerical solution, Richardson

grid pts	$t = 0$	$t = 2000$	$t = 5000$	$t = 12000$	$t = t_f$
43	810.244	708.033	689.231	508.333	500.081
81	807.021	703.341	684.256	503.133	494.574
161	804.606	699.937	680.667	499.354	490.660
322	803.373	698.247	678.932	497.762	488.962

Table 4.1: Convergence test on MCL6 DFF model

extrapolation is used. With the finite-difference methods to calculate the strip temperature of $O\{(\triangle x)^2\}$ accuracy, the error therefore quadruples in size as the grid spacing doubles. The exact temperature can be approximated using

$$\begin{aligned} 490.660 &= T_{exact} + 4\epsilon, \\ 488.962 &= T_{exact} + \epsilon, \end{aligned} \tag{4.13}$$

where ϵ is the error, in the example where $t = t_f$ for 161 and 322 grid points. This gives $T_{exact} = 488.393$, which means that the numerical solution obtained with 43 grid points of 500.081 has an error of about $2\frac{1}{2}\%$. The results for 43 grid points in the furnace are used here and in chapter 5 because of its faster execution time — the 322 grid point model took over nine hours to run on the same computer.

4.4 Summary

This chapter describes the adaptation of the original DFF model; from CGL2 with the capacity to handle one transient, to MCL6 with the ability to run continuously and model any number of transients over any specified duration. It is principally an extension of the earlier work, but a necessary one, because it allows the model to run for lengths of time equivalent to those that are used by BHP to record data from their lines. This allows real-time comparisons to be made between the line data and the model. It also allows the model to be

extended to study other phenomena in real time. Further work is obviously required, and at the time of writing was being carried out by personnel at BHP Research. More data was becoming available at the time of writing, but time constraints did not permit their inclusion in this work.

Chapter 5

The temperature variation across the strip

The final part of the thesis involved the examination of the effect, if any, that the heat transfer in the MCL6 direct-fired furnace has on the edges of the steel strip when compared to the rest of the strip. For several reasons, the edges are expected to be slightly hotter than the rest of the strip. If the edges of the strip are found to be hotter, this has ramifications for the whole strip. Even a difference of a few Kelvin is important in the heat treatment of steel strip. If hard-iron steel is near its recrystallisation temperature in the middle of the strip, a difference of a few degrees out to the edges may mean that the steel there has already recrystallised. This leads to inconsistencies in the metallurgical properties of the steel, and may involve patches of soft edges, resulting in imperfect product. Therefore, any good estimation as to the temperature difference across the steel strip will enable BHP to accommodate for this in its heat treating process.

Some of the reasons why the edges are thought to be hotter than the rest of the strip are

- **the greater surface area at the strip edge.** Although the strip is

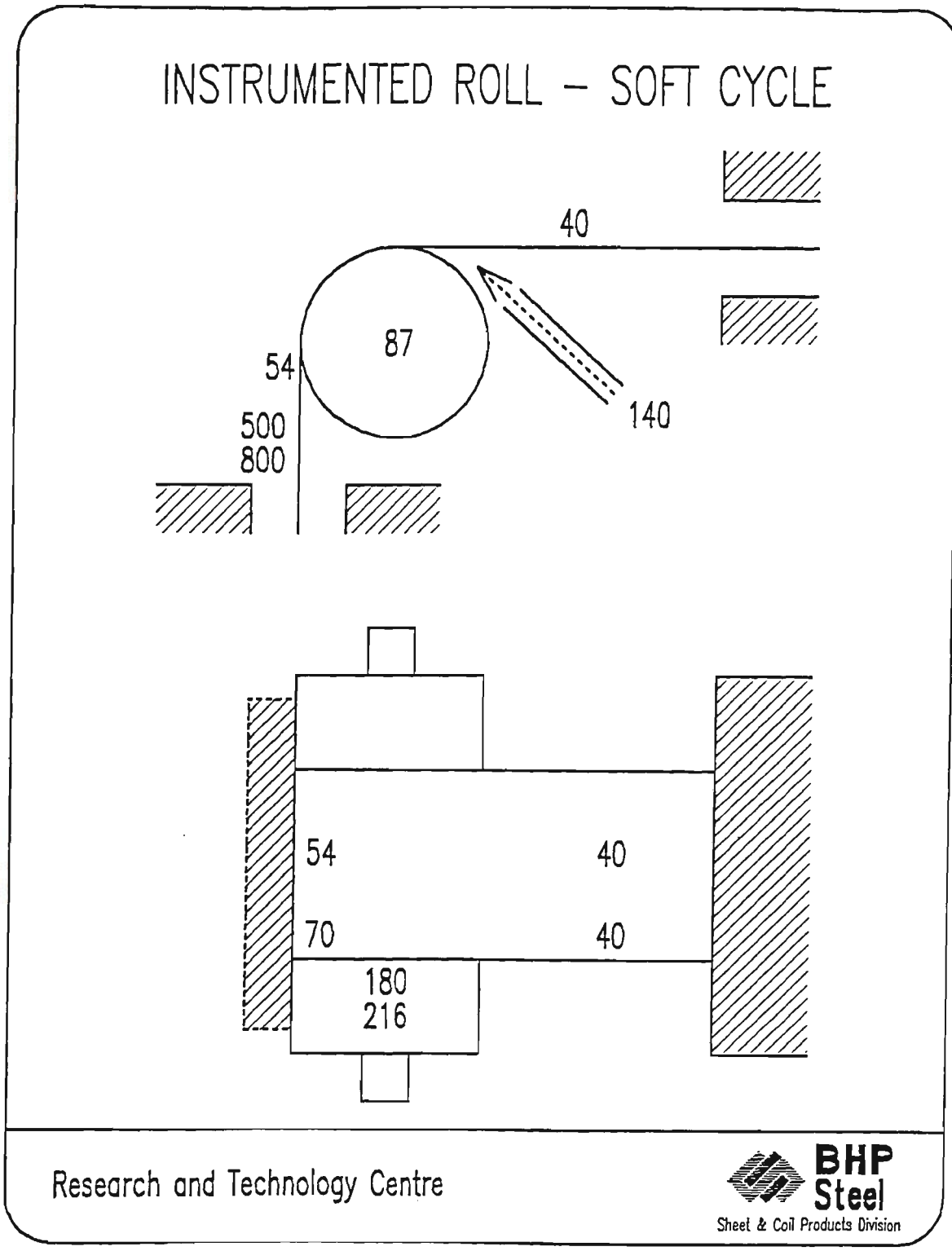

Figure 5.1: BHP diagram showing hotter edges at rolls

very thin (of the order of 0.5 mm) compared to its width, the extra area exposed is expected to absorb some heat.

- **the decrease in strip thickness from the middle of the strip to the edges**, known as *edge drop*. This phenomenon occurs during the rolling of the steel (both hot rolling and cold rolling), where the steel is rolled from a slab about 150 mm thick to the strip thickness of around 0.5 mm. The thickness decreases markedly close to the edge owing to the action of the rolls on the steel as it is being shaped. This phenomenon is treated widely in the literature. Papers exist on models of the thickness profile, both during cold rolling (Larkiola *et al.* [26] and Vermot des Roches & Janczak [59]), and in hot rolling (Zambrano & Colás [65] and Mäntylä *et al.* [27]). The thickness of the steel is found to taper away significantly after rolling is performed. Other papers consider ways of overcoming this edge drop by using slightly tapered rolls (for example, Ozaki *et al.* [35], Campas *et al.* [5] and Kitamura *et al.* [25]); a method which appears to be successful in reducing the effects of edge drop.

  Any change in uniform strip thickness has been seen in previous examples throughout this thesis to substantially change the strip temperature, so steel strip that is only one or two percent thinner at the edges is expected to cause a 5-10 K temperature rise.

- **direct radiation influence from the side-on walls.** To this stage in the thesis, the strip and the walls have each been modelled as one surface, though these 'surfaces' realistically have more than one side. Most of the radiation from the wall to the strip originates from the walls that are facing the strip front-on, because the gas burners are located there. Therefore, the front-on walls would be thought to be hotter than the walls that are side-on to the main face (ie, the width) of the strip.

At the same time, the walls that are side-on to the width of the strip are front-on to the edge of the strip, and the radiation shape factor from the side walls to the strip edge would be relatively high compared to that from the front walls to the strip edge. The front-on and side-on walls therefore need to be separated to model this, increasing the complexity of the model by adding more surfaces that radiate heat.

- **conduction across the strip rolls.** Observations by BHP on the temperature variation across the strip when the strip passes around a roll show that heat conducts from the rolls across the strip edges, affecting the temperature profile there. The temperature across the roll width is not uniform either, and therefore knowing the temperature gradient in the roll is important in determining how much heat crosses the edge of the strip. A diagram indicating the order of the observed difference is shown in Figure 5.1. (This diagram is of the turn-around roll at the top of ZAL1, with gas leaving the furnace below directly heating the roll. On MCL6 however, the rolls are located in parts of the furnace where there is little or no gas present.) A change in the strip width could also have a substantial effect; parts of the roll with a different temperature may suddenly become either covered by an increase, or exposed by a decrease, in strip width, both changes influencing the roll temperature and, by conduction, the strip temperature.

Other papers examine the temperature profile across the strip during rolling. Khloponin *et al.* [24] examine the transverse temperature profile of steel strip in a hot rolling mill, finding a decrease in temperature at the edges. Buffenoir *et al.* [4] mention that the edges are about 70 K cooler than the centreline temperature after hot rolling. In these situations, the edge temperatures are actually lower than the temperatures away from the edge whereas in the direct-fired furnace the edges are expected to be hotter. As was mentioned

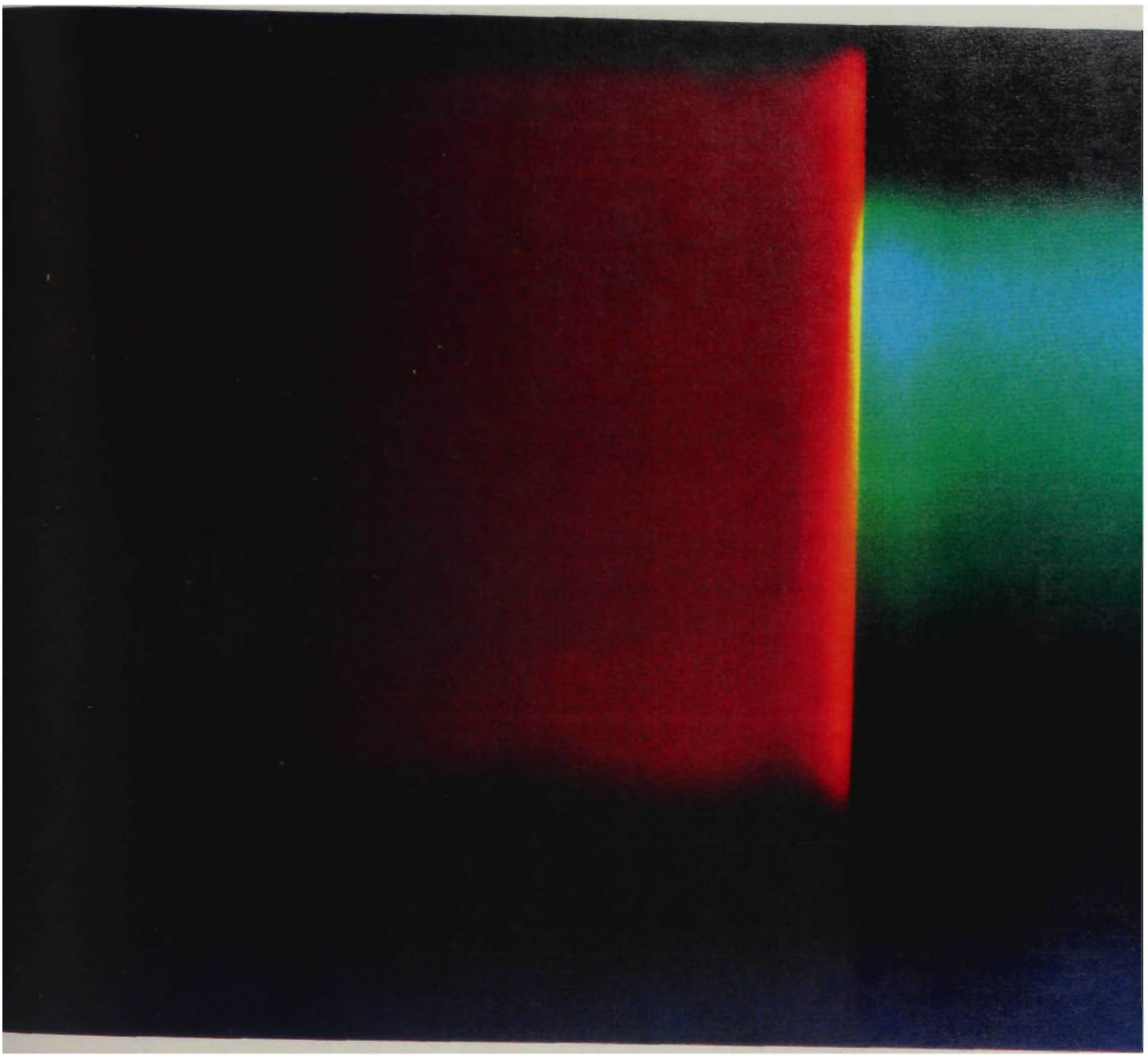

Figure 5.2: Photograph showing hotter strip edges in the DFF

earlier, the non-homogeneity of the temperature causes non-uniformity in the metallurgical properties of the steel.

Indeed, the photograph in Figure 5.2 of the strip near the furnace boot shows how hot the edges can become under normal conditions. This was taken at one of BHP's galvanising lines at Port Kembla, with the line running soft-iron product. The heat glow for a short distance in from the edge indicates that the strip is markedly hotter there. The aim of the model is to find out how much hotter the edges are.

5.1 Modelling the strip in 2-d

To model the edge effects, an extension to the extra dimension across the strip, denoted by y, is required, plus an alternative solution method to the equations and additional boundary conditions. The inclusion of the variation of thickness with width is represented by the $d_s(y)$ term. Symmetry can be assumed across the strip, and so the domain of y is from the middle ($y = 0$) to the edge ($y = \frac{1}{2}w_s$) of the strip. Therefore the strip equation (4.1) becomes

$$\frac{\partial T_s}{\partial t} - V_s\frac{\partial T_s}{\partial x} - \frac{1}{\rho_s c_{ps}}\frac{\partial}{\partial y}\left(k_s\frac{\partial T_s}{\partial y}\right) = \frac{2w_s(B_{gs} - B_s + q_{s,c})}{\rho_s w_s d_s(y) c_{ps}}, \tag{5.1}$$

or

$$\frac{\partial T_s}{\partial t} - V_s\frac{\partial T_s}{\partial x} - \frac{1}{\rho_s c_{ps}}\frac{dk_s}{dT_s}\left(\frac{\partial T_s}{\partial y}\right)^2 - \kappa_s\frac{\partial^2 T_s}{\partial y^2} = \frac{2w_s(B_{gs} - B_s + q_{s,c})}{\rho_s w_s d_s(y) c_{ps}}, \tag{5.2}$$

where $\kappa_s = k_s/(\rho_s c_{ps})$. The boundary condition for the strip edge at $y = \frac{1}{2}w_s$ takes the form

$$k_s d_s \left.\frac{\partial T_s}{\partial y}\right|_{y=\frac{1}{2}w_s} = d_s(B_{gs} - B_s + q_{s,c}), \tag{5.3}$$

while at the strip centre, negligible transverse heat flow is expected, so

$$\left.\frac{\partial T_s}{\partial y}\right|_{y=0} = 0. \tag{5.4}$$

The $Q_{gs} = P_s(B_{gs} - B_s + q_{s,c})$ term used previously has been split between the strip face and the strip edge, with the major proportion of the heat entering the strip through the face. The d_s terms are included in equation (5.3) merely to illustrate that the strip thickness represents the 'perimeter' through which the heat enters the strip edge. This separation of the heat between the edge and the rest of the strip is necessary in order to ensure that the strip still receives an amount of heat equal to $B_{gs} - B_s + q_{s,c}$ into its 'perimeter' $P_s = 2(w_s + d_s)$.

It is also observed in equation (5.2) that the term involving the variable thermal conductivity is much smaller than the constant thermal conductivity term. The expression for dk_s/dT_s is small compared to k_s for steel at temperatures of the range considered here (ie, hundreds of degrees Kelvin). Numerical tests on the model also showed that including the variable thermal conductivity term had a very small effect (which actually reduced the strip edge temperature slightly since $dk_s/dT_s < 0$ over the region of interest). Therefore the dk_s/dT_s term is neglected and the equation to be solved becomes

$$\frac{\partial T_s}{\partial t} - V_s\frac{\partial T_s}{\partial x} - \kappa_s\frac{\partial^2 T_s}{\partial y^2} = \frac{2w_s(B_{gs} - B_s + q_{s,c})}{\rho_s w_s d_s(y) c_{ps}}. \tag{5.5}$$

Values for the strip thermal conductivity were taken by assuming a functional fit to data found in Weast [61] for the thermal conductivity of iron (due to the very low percentage of other products in the steel). At a strip temperature of 800 K (ie, about 530°C, which is near the recrystallisation temperature for steel), $k_s = 42.3$ $\mathrm{Wm^{-1}K^{-1}}$. The functional form is shown in equation (B.1) in Appendix B.

A further change is that the value for T_s used in calculating the radiation and convection for the strip is taken as the average temperature across the strip width, rather than just using the centreline strip temperature. Therefore, in equations such as (2.41) and (4.5) to calculate the heat flux to

the strip,

$$T_s = \frac{1}{\frac{1}{2}w_s}\left(\sum_{k=0}^{E-1}\tfrac{1}{2}(T_{s,k}+T_{s,k+1})\triangle y_k\right), \tag{5.6}$$

at each grid height j in the furnace, for the E grid points across the strip. More on the finite-difference solution method is explained in section 5.5.

5.2 Including the edge drop

To model the variation of strip thickness across the width, a function is fitted to data indicating how large the deformation is. Campas *et al.* [5] state that the edge drop phenomenon occurs in the last 25 mm of the strip width for 150 mm wide strip, and that the edge drop can be as much as 4% from the strip centre to a point 5 mm from the edge. According to BHP [64], the strip thickness decreases by 10μm from the middle of the strip to a point some 50mm from the edge, and a further 10μm from that point to the strip edge, which also represents a drop of 4%. The edge drop varies with the strip thickness (the 10μm drop is for strip that is 0.5 mm thick), but is independent of the strip width.

A good function to represent the edge drop according to BHP is

$$d_s(y) = Ay^{16} + By^2 + Cy + D, \tag{5.7}$$

because most of the strip has a parabolic shape until the steep decline near the edge. This is similar to that used by Mäntylä *et al.* [27], where a quadratic is used to model the thickness profile from the centre to a point 25 mm from the edge. With the slope at the middle of the strip ($y = 0$) equal to zero and the thickness at the middle equal to d_s (the given strip thickness), this causes $C = 0$ and $D = d_s$. The percentage drop in the thickness change from the middle of the strip to a point a certain distance in from the edge is represented by d_{pos}, which is between 0 and 1. The remaining $(100(1 - d_{pos}))\%$ of the thickness

drop occurs from that point to the edge, where that distance is denoted by w_{pos}. Let d_{per} represent a value between 0 and 1 which is the percentage change in the strip thickness between the centre and the edge. As a result, the edge drop function passes through the points $(0, d_s)$, $(\frac{1}{2}w_s - w_{pos}, d_s(1 - d_{per}d_{pos}))$ and $(\frac{1}{2}w_s, d_s(1 - d_{per}))$. There is now enough information to find A and B. Therefore, if $W = \frac{1}{2}w_s$ and $X = \frac{1}{2}w_s - w_{pos}$, then the strip thickness at any point across the width $w_s(y)$ is given by

$$\begin{aligned} d_s(y) &= 2\left(\frac{\frac{1}{2}d_s d_{per}(X^2 - d_{pos}W^2)(w_s(y))^{16}}{W^2X^{16} - W^{16}X^2}\right. \\ &\quad \left. - \frac{\frac{1}{2}d_s d_{per}(X^{16} - d_{pos}W^{16})(w_s(y))^2}{W^2X^{16} - W^{16}X^2} + \frac{1}{2}d_s\right). \end{aligned} \tag{5.8}$$

In this way, various values for the edge drop can be input to examine the influence of the edge drop on the strip temperature. With this procedure, care should be taken to ensure that the value of $d_s(y)$ does not exceed the actual strip thickness d_s at any point across the width.

5.3 Including the side walls

Including the side walls (the walls that the edge of the strip is facing) separately from the front walls (the walls that the width of the strip is facing) adds an extra body to the equations, resulting in extra complexity of the calculations. For example, extra shape factors are needed between the bodies. A cross-section of the furnace is shown in Figure 5.3, including all of the bodies : the strip (s), the front wall (wf) and the side wall (we), as well as the gas which is present both in the preheater (when it is turned on) and the direct-fired furnace proper.

In the MCL6 direct-fired furnace, the side walls are made of Fiberfrax AL1400 blanket [51], with different thermal properties from the brick-insulation front wall. In reality, the Fiberfrax material is only found on one

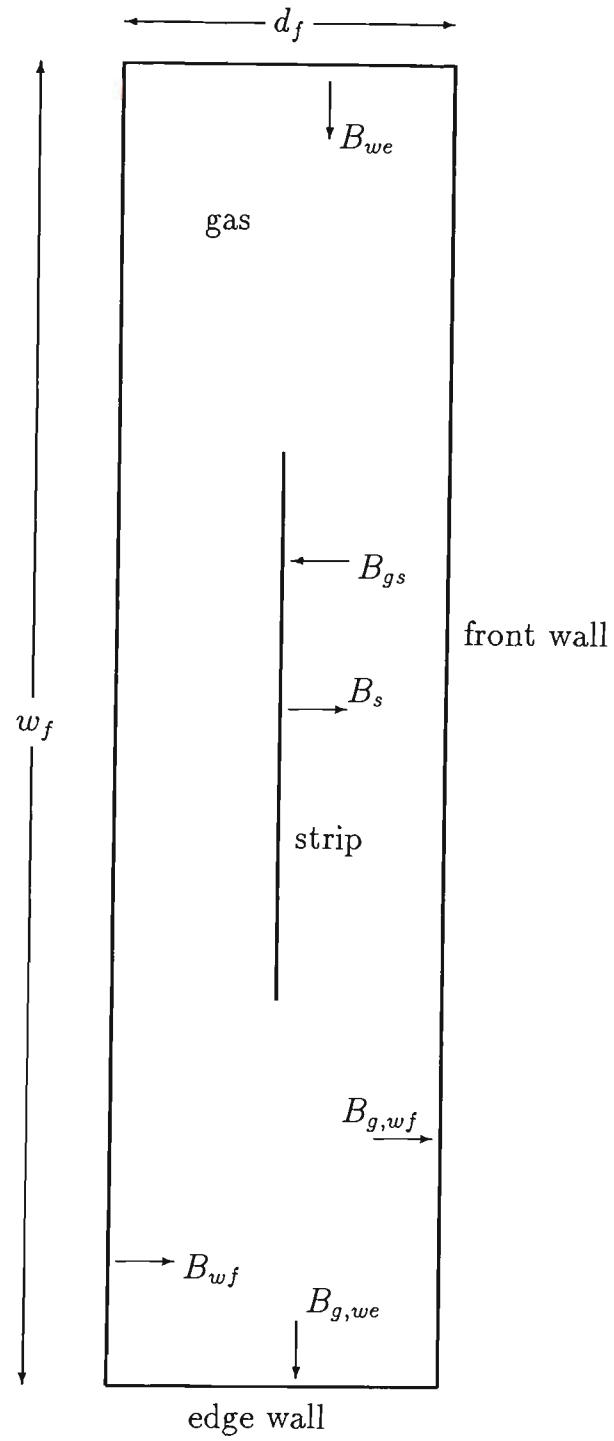

Figure 5.3: Cross-section of the furnace with separate walls

side of the wall in the DFF, except in the top zone of the DFF proper, where the whole wall is made up of the blanket. For simplicity and symmetry, the side wall is assumed to be made of only the blanket, and the front wall solely of the brick insulation.

Even though the front wall has two 'parts', one on either side of the strip, whatever heat transfer is occurring in one wall is expected to be occurring in the opposite wall because of the symmetry of the furnace (assuming that the strip is in the exact centre of the furnace). The same assumption holds for the side walls. Perimeters are used here, as before, but with this assumption, the wall is split into its four faces with the two front walls and the two side walls, so that the perimeters are $P_{we} = d_f$ for *each* side wall, and $P_{wf} = w_f$ for each front wall. The strip is also separated to an extent, with the strip edge being separated from the main face for some calculations. The symmetry assumption across the strip is retained, but the two faces of the strip are taken as one — therefore $P_{se} = d_s$ and $P_{sf} = 2w_s$. This separation enables the study of the radiation between the walls and the strip edge. However, for the bulk of the calculations, the strip is taken to be *one* body, as was the case in the MCL6 centreline temperature model and the CGL2 model. This is done for two reasons:

- completely separating the strip edge and strip face causes another body to be added to an already algebraically complex problem, and
- the average strip temperature across its width is much closer to the centreline temperature than to the edge temperature.

Therefore, the strip can be treated as one body when calculating the radiation flux between itself, the gas and the front and side walls, with $T_{sf}(\equiv T_s)$ calculated using equation (5.6).

The crossed-string method, as described in Siegel & Howell [46] and elsewhere, is used to determine the shape factors for the bodies. The

application of the crossed-string method to finding the shape factor from the front wall to the strip face, $F_{wf,sf}$, gives

$$F_{wf,sf} = \frac{l-c}{w_f}, \tag{5.9}$$

where

$$l = \left(\left(\frac{1}{2}(w_f + w_s)\right)^2 + \left(\frac{1}{2}(d_f - d_s)\right)^2\right)^{\frac{1}{2}}, \tag{5.10}$$

$$c = \left(\left(\frac{1}{2}(w_f - w_s)\right)^2 + \left(\frac{1}{2}(d_f - d_s)\right)^2\right)^{\frac{1}{2}}. \tag{5.11}$$

From this expression for $F_{wf,sf}$, the shape factors can be found for $F_{sf,wf}$, $F_{sf,we}$ and $F_{we,sf}$ using both the reciprocity relation $P_i F_{ij} = P_j F_{ji}$ between bodies i and j, and the fact that $2F_{sf,wf} + 2F_{sf,we} = 1$. It can be shown that

$$F_{we,sf} = \frac{w_s}{d_f}\left(1 - \frac{l-c}{w_s}\right). \tag{5.12}$$

Again using the crossed-string method, the shape factor between the side wall and the strip edge can be calculated, ie,

$$F_{we,se} = \frac{b-c}{d_f}, \tag{5.13}$$

where

$$b = \left(\left(\frac{1}{2}(w_f - w_s)\right)^2 + \left(\frac{1}{2}(d_f + d_s)\right)^2\right)^{\frac{1}{2}}, \tag{5.14}$$

and c is as in equation (5.11). Using further reciprocity and shape factor summation relations such as $F_{se,we} + 2F_{se,wf} = 1$,

$$F_{wf,se} = \frac{1}{2}\frac{d_s}{w_f}\left(1 - \frac{b-c}{d_s}\right), \tag{5.15}$$

can be found. The shape factors from the front wall and side wall to the whole strip are therefore

$$F_{wf,s} = F_{wf,sf} + 2F_{wf,se} = \frac{1}{w_f}\left(l - c + d_s\left(1 - \frac{b-c}{d_s}\right)\right), \tag{5.16}$$

$$F_{we,s} = F_{we,sf} + F_{we,se} = \frac{1}{d_f}\left(b - c + w_s\left(1 - \frac{l-c}{w_s}\right)\right). \tag{5.17}$$

Using reciprocity,

$$F_{s,wf} = \frac{1}{P_s}\left(l - c + d_s\left(1 - \frac{b-c}{d_s}\right)\right), \tag{5.18}$$

$$F_{s,we} = \frac{1}{P_s}\left(b - c + w_s\left(1 - \frac{l-c}{w_s}\right)\right). \tag{5.19}$$

Determining the remaining shape factors between the walls themselves is rather more difficult. The presence of the strip in the middle of the furnace has a significant effect on the amount of radiation between the walls. To find these values, imagine that the strip is extended all the way to the furnace walls, as in the diagram in Figure 5.4, with the new 'surface' called a. Then, to find the shape factor between the front walls, $F_{wf,wf}$, the shape factors for $F_{wf,a}$ and $F_{a,wf}$ are determined and then multiplied together. Both $F_{wf,a}$ and $F_{a,wf}$ can be found using shape factor algebra. The value of $F_{wf,wf}$ then becomes

$$F_{wf,wf} = \frac{((w_f^2 + (\frac{1}{2}d_f)^2)^{\frac{1}{2}} - \frac{1}{2}d_f - (l-c))^2}{w_f(w_f - w_s)}. \tag{5.20}$$

In a similar way, $F_{wf,we}$ can be calculated by splitting the side wall into two equal halves either side of a, $we\frac{1}{2}$ and $we\frac{2}{2}$, and solving, ie,

$$F_{wf,we} = F_{wf,we\frac{1}{2}} + F_{wf,a}F_{a,we\frac{2}{2}}. \tag{5.21}$$

Standard formulae exist [46] to find the component values on the right-hand side of equation (5.21).

The summation of the calculated values of $F_{wf,wf} + 2F_{wf,we} + F_{wf,s}$ using equations (5.20), (5.21) and (5.16) is not exactly one, but over the range of strip widths processed by BHP in the furnace, the calculated error is less than 1%, decreasing to zero for wider strips. The reason is that not all of the radiation can be accounted for in the furnace using this method. At surface a, for example, most of the radiation will 'travel' to the nearest side wall, we, and to the front wall directly facing it, wf, but surface a can still 'see' the

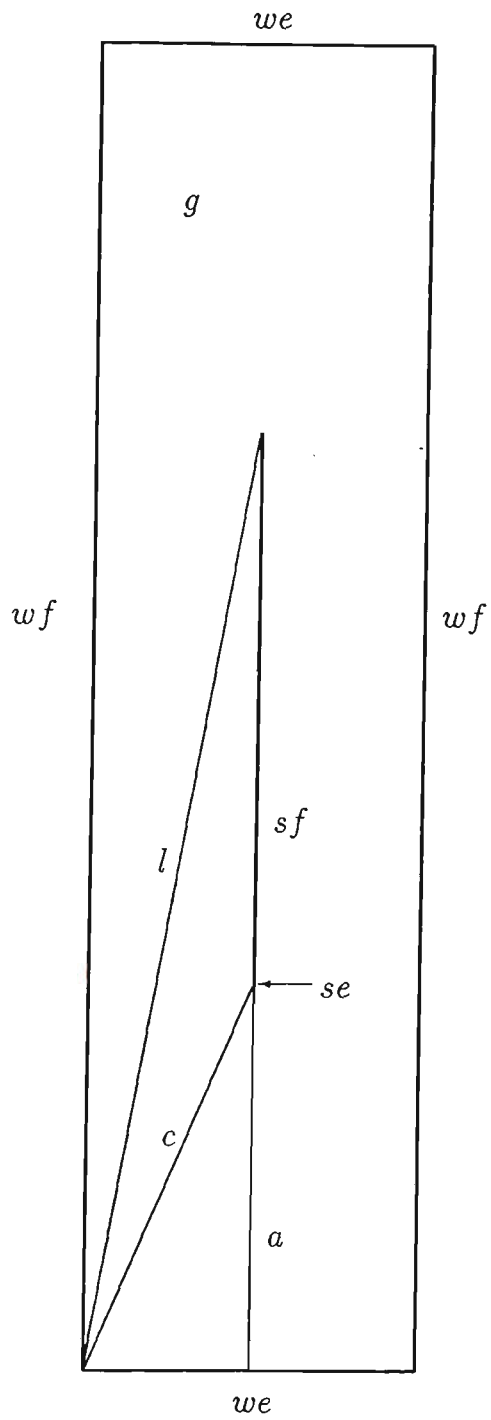

Figure 5.4: Finding the shape factors for the separated wall model

opposite side wall we, albeit only slightly. However, the front wall wf cannot directly see that side wall using this method. As a result, there is this slight error, but it is small enough to be neglected. To simplify the calculations, the other shape factors between the walls are determined using shape factor algebra. Therefore, $F_{wf,we}$ is obtained using

$$F_{wf,we} = \tfrac{1}{2}(1 - F_{wf,s} - F_{wf,wf}), \tag{5.22}$$

instead of equation (5.21). Also

$$F_{we,wf} = w_f F_{wf,wf}/d_f, \tag{5.23}$$

$$F_{we,we} = 1 - 2F_{we,wf} - F_{we,s}. \tag{5.24}$$

Now that the shape factors between the surfaces have been found, the radiosities from each surface can be determined also. They are

$$B_{sf} = \varepsilon_{sf}\sigma T_{sf}^4 + \rho_{sf}B_{g,sf}, \tag{5.25}$$

$$B_{se} = \varepsilon_{se}\sigma T_{se}^4 + \rho_{se}B_{g,se}, \tag{5.26}$$

$$B_{wf} = \varepsilon_{wf}\sigma T_{wf}^4 + \rho_{wf}B_{g,wf}, \tag{5.27}$$

$$B_{we} = \varepsilon_{we}\sigma T_{we}^4 + \rho_{we}B_{g,we}. \tag{5.28}$$

Here ρ_{sf} is a function of the gas temperature in the sections of the furnace where gas is flowing (ie, in the DFF proper, and in the preheater according to the conditions explained in section 4.1), and a function of the side and front wall temperatures in the bridge, where there is no gas flow. Analogous expressions arise for the strip edge reflectivity ρ_{se}. The radiosities from the gas to each surface are,

$$P_{sf}B_{g,sf} = P_{sf}\varepsilon_g\sigma T_g^4 + 2P_{wf}F_{wf,sf}\tau_g B_{wf} + 2P_{we}F_{we,sf}\tau_g B_{we}, \tag{5.29}$$

$$P_{se}B_{g,se} = P_{se}\varepsilon_g\sigma T_g^4 + 2P_{wf}F_{wf,se}\tau_g B_{wf} + P_{we}F_{we,se}\tau_g B_{we}, \tag{5.30}$$

$$P_{wf}B_{g,wf} = P_{wf}\varepsilon_g\sigma T_g^4 + 2P_{we}F_{we,wf}\tau_g B_{we}$$

$$+ P_{wf}F_{wf,wf}\tau_g B_{wf} + P_s F_{s,wf}\tau_g B_s, \tag{5.31}$$

$$P_{we}B_{g,we} = P_{we}\varepsilon_g \sigma T_g^4 + 2P_{wf}F_{wf,we}\tau_g B_{wf} + P_{we}F_{we,we}\tau_g B_{we} + P_s F_{s,we}\tau_g B_s. \tag{5.32}$$

In the situation where a section of the furnace has no gas flow, the gas transmissivity τ_g is 1 and the terms involving T_g disappear. The '2' terms signify that each face of the wall can see the two walls on either side of itself, as well as the opposing wall. The whole strip can also see both faces of the front wall and the side wall. However, the edge of the strip only sees one of the side walls and hence there is no '2' preceding the B_{we} term in the expression for $B_{g,se}$. Also, the substitution

$$f_{i,j} = P_i F_{i,j}\tau_g / P_j \tag{5.33}$$

for bodies i and j is made from here on to reduce the number of terms in the equations to follow.

As can be seen, deriving expressions for the radiosities in terms of temperatures requires care. Ultimately, these expressions can be written as functions of $B_{g,wf}$ and $B_{g,we}$, as shown below.

$$\begin{aligned}
&B_{g,wf} \\
&= [[f_{s,wf}(1 - f_{we,we}\rho_{we} - 2f_{we,s}f_{s,we}\rho_s\rho_{we}) \\
&+ f_{s,we}(2f_{we,wf}\rho_{we} + 2f_{s,wf}f_{we,s}\rho_s\rho_{we})]\varepsilon_s\sigma T_{sf}^4 \\
&+ [(1 + f_{s,wf}\rho_s)(1 - f_{we,we}\rho_{we} - 2f_{we,s}f_{s,we}\rho_s\rho_{we}) \\
&+ (1 + f_{s,we}\rho_s)(2f_{we,wf}\rho_{we} + 2f_{s,wf}f_{we,s}\rho_s\rho_{we})]\varepsilon_g\sigma T_g^4 \\
&+ [(2f_{we,wf} + 2f_{s,wf}f_{we,s}\rho_s)(1 - f_{we,we}\rho_{we} - 2f_{we,s}f_{s,we}\rho_s\rho_{we}) \\
&+ (f_{we,we} + 2f_{s,we}f_{we,s}\rho_s)(2f_{we,wf}\rho_{we} + 2f_{s,wf}f_{we,s}\rho_s\rho_{we})]\varepsilon_{we}\sigma T_{we}^4 \\
&+ [(f_{wf,wf} + 2f_{s,wf}f_{wf,s}\rho_s)(1 - f_{we,we}\rho_{we} - 2f_{we,s}f_{s,we}\rho_s\rho_{we}) \\
&+ (2f_{wf,we} + 2f_{s,we}f_{wf,s}\rho_s)(2f_{we,wf}\rho_{we} + 2f_{s,wf}f_{we,s}\rho_s\rho_{we})]\varepsilon_{wf}\sigma T_{wf}^4] \\
&/[(1 - f_{we,we}\rho_{we} - 2f_{we,s}f_{s,we}\rho_s\rho_{we})(1 - f_{wf,wf}\rho_{wf} - 2f_{wf,s}f_{s,wf}\rho_s\rho_{wf})
\end{aligned}$$

$$- (2f_{we,wf}\rho_{we} + 2f_{s,wf}f_{we,s}\rho_s\rho_{we})(2f_{wf,we}\rho_{wf} + 2f_{s,we}f_{wf,s}\rho_s\rho_{wf})] \quad (5.34)$$

$$B_{g,we}$$

$$= [[f_{s,wf}(2f_{wf,we}\rho_{wf} + 2f_{s,we}f_{wf,s}\rho_s\rho_{wf})$$

$$+ f_{s,we}(1 - f_{wf,wf}\rho_{wf} - 2f_{wf,s}f_{s,wf}\rho_s\rho_{wf})]\varepsilon_s\sigma T_{sf}^4$$

$$+ [(1 + f_{s,wf}\rho_s)(2f_{wf,we}\rho_{wf} + 2f_{s,we}f_{wf,s}\rho_s\rho_{wf})$$

$$+ (1 + f_{s,we}\rho_s)(1 - f_{wf,wf}\rho_{wf} - 2f_{wf,s}f_{s,wf}\rho_s\rho_{wf})]\varepsilon_g\sigma T_g^4$$

$$+ [(2f_{we,wf} + 2f_{s,wf}f_{we,s}\rho_s)(2f_{wf,we}\rho_{wf} + 2f_{s,we}f_{wf,s}\rho_s\rho_{wf})$$

$$+ (f_{we,we} + 2f_{s,we}f_{we,s}\rho_s)(1 - f_{wf,wf}\rho_{wf} - 2f_{wf,s}f_{s,wf}\rho_s\rho_{wf})]\varepsilon_{we}\sigma T_{we}^4$$

$$+ [(2f_{wf,we} + 2f_{s,we}f_{wf,s}\rho_s)(1 - f_{wf,wf}\rho_{wf} - 2f_{wf,s}f_{s,wf}\rho_s\rho_{wf})$$

$$+ (f_{wf,wf} + 2f_{s,wf}f_{wf,s}\rho_s)(2f_{wf,we}\rho_{wf} + 2f_{s,we}f_{wf,s}\rho_s\rho_{wf})]\varepsilon_{wf}\sigma T_{wf}^4]$$

$$[(1 - f_{we,we}\rho_{we} - 2f_{we,s}f_{s,we}\rho_s\rho_{we})(1 - f_{wf,wf}\rho_{wf} - 2f_{wf,s}f_{s,wf}\rho_s\rho_{wf})$$

$$- (2f_{we,wf}\rho_{we} + 2f_{s,wf}f_{we,s}\rho_s\rho_{we})(2f_{wf,we}\rho_{wf} + 2f_{s,we}f_{wf,s}\rho_s\rho_{wf})] \quad (5.35)$$

The other radiosities can be determined from these expressions by substitution into the equations for B_{we}, B_{wf}, $B_{g,se}$, $B_{g,sf}$, B_{se} and B_{sf} listed previously. Expressions for the convective heat transfer from the gas are also required. They are

$$q_{se,c} = h(T_g - T_{se}), \quad (5.36)$$

$$q_{sf,c} = h(T_g - T_{sf}), \quad (5.37)$$

$$q_{we,c} = h(T_g - T_{we}), \quad (5.38)$$

$$q_{wf,c} = h(T_g - T_{wf}), \quad (5.39)$$

where the heat transfer coefficient h is calculated from equations (2.52)-(2.56), using the furnace dimensions for MCL6.

The conduction equations for the walls are also separated into the side and front wall components. Therefore,

$$\frac{\partial T_{we}}{\partial t} - \kappa_{we}\frac{\partial^2 T_{we}}{\partial z_{we}^2} = 0, \quad (5.40)$$

$$\frac{\partial T_{wf}}{\partial t} - \kappa_{wf}\frac{\partial^2 T_{wf}}{\partial z_{wf}^2} = 0, \tag{5.41}$$

where $\kappa_{we} = k_{we}/(c_{p,we}\rho_{we})$ and $\kappa_{wf} = k_{wf}/(c_{p,wf}\rho_{wf})$. The z_{we} and z_{wf} variables are used to distinguish between the different directions of the two z coordinates used here, even though the actual directions are of no consequence.

The equation for the strip in the case of the two-wall model now becomes

$$\frac{\partial T_s}{\partial t} - V_s\frac{\partial T_s}{\partial x} - \kappa_s\frac{\partial^2 T_s}{\partial y^2} = \frac{Q_{g,sf}}{\rho_s w_s d_s(y) c_{ps}}, \tag{5.42}$$

where $Q_{g,sf} = 2w_s(B_{g,sf} - B_{sf} + q_{sf,c})$, and the boundary condition for the strip edge now takes the form

$$k_s \left.\frac{\partial T_s}{\partial y}\right|_{y=\frac{1}{2}w_s} = Q_{g,se}/d_s, \tag{5.43}$$

where $Q_{g,se} = d_s(B_{g,se} - B_{se} + q_{se,c})$.

Changes are also required to the gas equation (4.2), with the Q_{gs} and Q_{gw} components split, ie,

$$\frac{\partial T_g}{\partial t} + V_g\frac{\partial T_g}{\partial x} = \frac{Q_{comb} - Q_{g,sf} - 2Q_{g,se} - 2Q_{g,wf} - 2Q_{g,we}}{\rho_g(w_f d_f - w_s d_s(y))c_{pg}}, \tag{5.44}$$

with

$$Q_{g,we} = P_{we}(B_{g,we} - B_{we} + q_{we,c}), \tag{5.45}$$

$$Q_{g,wf} = P_{wf}(B_{g,wf} - B_{wf} + q_{wf,c}). \tag{5.46}$$

The '2' appears in front of the $Q_{g,se}$ term because of the two strip edges that are in the furnace, even though only one half of the strip is considered in the strip edge calculations. The same reasoning holds for the two front and side walls, whereas the two strip faces are taken as one body in the calculations. Because the perimeters of the wall defined here are for only one face of the wall, the Q_{gw} terms in the gas equation must be multiplied by two to include

all four faces of the wall. Boundary conditions too are required for each wall at the wall/furnace interface ($z_{we} = 0$ and $z_{wf} = 0$), ie,

$$-k_{we}\frac{\partial T_{we}}{\partial z_{we}} = B_{g,we} - B_{we} + q_{we,c}, \tag{5.47}$$

$$-k_{wf}\frac{\partial T_{wf}}{\partial z_{wf}} = B_{g,wf} - B_{wf} + q_{wf,c}. \tag{5.48}$$

The above equations (5.40)–(5.48) are used to solve the problem when considering the separation of the wall into front wall and side wall, and in the roll analysis that follows. The equations (5.5) and (5.3) are used when examining the effect of both the extra surface area and the edge drop on the strip temperature.

Including the extra wall component in the program doubles the number of wall points involved and, because the wall requires the largest number of grid points, the run time of the system is approximately doubled also. In the initialisation procedure, it is now required that both wall components are adiabatic, ie,

$$B_{g,we} - B_{we} + q_{we,c} = f(T_{we}, T_{wf}) = 0,$$

$$B_{g,wf} - B_{wf} + q_{wf,c} = f(T_{we}, T_{wf}) = 0.$$

Another IMSL [19] routine is used to find the roots of this system of equations.

5.4 Including the rolls

There are three rolls in the DFF on MCL6, as can be seen in Figure 4.1; two in the bridge section, and one located immediately after the strip exits the direct-fired furnace (actually 1.45 m after the point taken as the DFF exit). The large heat capacity of the rolls is expected to have a significant effect on the strip temperature, especially with heat transferred across the strip edges. The rolls can either increase or decrease the edge temperature, depending on

whether the rolls are hotter or cooler than the strip. The main interest is on the boot roll, which is subject to greater variability in temperature due to the presence of the DFF proper immediately above it.

Perhaps the greatest influence affecting heat transfer across the strip edges when in contact with the rolls is a change in the strip width. Before a change occurs, a basic strip and roll temperature profile develops for a particular strip width. If this width changes, then the temperature profile also changes; how it changes depends on whether the strip width increases or decreases, and on the temperature of that part of the roll that is covered or exposed. When there is a width increase, a section of the roll that was previously exposed only to radiation from the wall is now covered by the strip; as a result it will attain a similar temperature profile to the strip that is now in contact with it, due to the heat coupling that occurs. At the same time, this profile will depend on the roll temperature. For example, if the roll temperature initially increased up to a certain value past the strip edge, then that part of the strip now covering the formerly exposed section will also become hotter as a result — ie, near the edges. If the roll temperature is lower, the coupling effect is expected to decrease the strip temperature. The results later in this chapter investigate some of these possibilities.

The rolls in the furnace are 2.15 m across and have a radius of 0.4 m, with their outer stainless steel shell thickness being 22 mm. With the roll diameter of 0.8 m therefore being greater than the furnace 'thickness' of 0.6 m, the part of the furnace where the roll is located has a furnace thickness greater than 0.6 m. A diagram showing a cross-section of the part of the furnace incorporating the roll is found in Figure 5.5. The furnace thickness here, denoted by $d_{f,r}$, is approximately 1.7 m.

By including the rolls, there is a further increase in the computation time for the program, with extra grid points both across the roll face and into

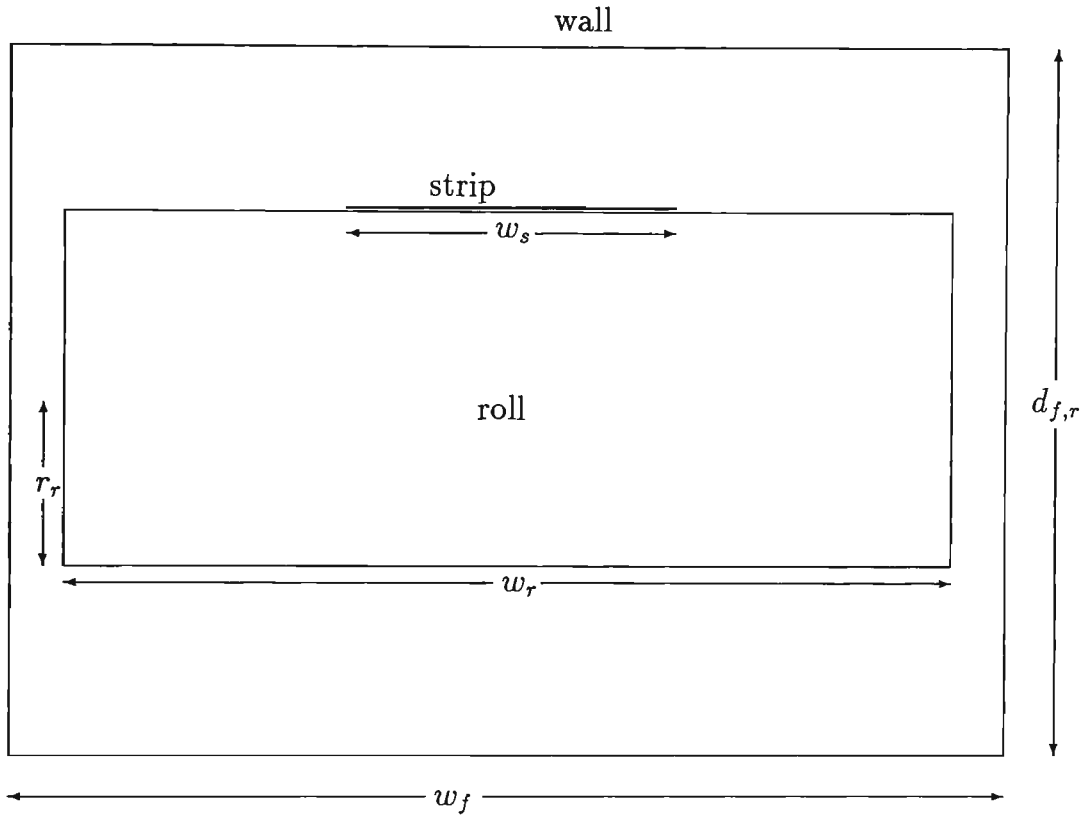

Figure 5.5: Roll area cross-section

the roll shell. In fact, together with the extra grid points across the strip and the extra wall, the number of grid points will increase approximately 3-4 times for the 2-d strip model. The extra calculations involved also act to increase the program's run time. Since the presence of the roll also adds another body to the model, compensation is made by the wall being assumed to be one body in the sections where the rolls are found, instead of being split into the front and side wall components. In the furnace sections where there is no gas flow present, the walls are found to be approximately the same temperature anyway, so this assumption appears to be justified. Also, the position of the strip on only one side of the roll means that the symmetry assumption used previously when splitting the walls no longer holds. This adds even more bodies into the problem if all of these surfaces are to be included. Therefore the whole wall, the roll and the strip are the participating surfaces in the heat transfer in those parts of the furnace where the rolls are present.

Even though the roll is cylindrical in shape, a roll perimeter is used here for consistency, as perimeters have been used throughout the construction of the models. Not all of the roll is in contact with the strip at any one time. A substantial part of it receives radiated heat from the wall surrounding it, although this amount will not be large because of the virtual absence of gas flow in this section. In fact, the only roll exposed to any heat flow from the gas is the boot roll, which receives a small amount of heat from the gas that leaks into the furnace from the RTF. However, this amount is small enough to be neglected here.

As for the side wall example, shape factors are required between all surfaces. Most of these are fairly straightforward to derive, as the strip and the roll only see the wall, and therefore $F_{rw} = 1$ and $F_{sw} = 1$. The remaining shape factors can then be calculated thus:

$$F_{ws} = \frac{P_s F_{sw}}{P_w} = \frac{P_s}{P_w}, \tag{5.49}$$

$$F_{wr} = \frac{P_r F_{rw}}{P_w} = \frac{P_r}{P_w}, \tag{5.50}$$

$$F_{ww} = 1 - F_{wr} - F_{ws} = 1 - \frac{P_r + P_s}{P_w}, \tag{5.51}$$

where the perimeters represent those parts of the surfaces that are directly exposed to radiation, therefore,

$$P_s = w_s + 2d_s, \tag{5.52}$$

$$P_r = 2(w_r + 2r_r) - w_s, \tag{5.53}$$

$$P_w = 2(w_f + d_{f,r}), \tag{5.54}$$

where $d_{f,r}$ is the furnace thickness in the sections of the furnace including the rolls as mentioned previously.

The radiosities between the surfaces are

$$B_s = \varepsilon_s \sigma T_s^4 + \rho_s B_{gs}, \tag{5.55}$$

$$B_r = \varepsilon_r \sigma T_r^4 + \rho_r B_{gr}, \tag{5.56}$$

$$B_w = \varepsilon_w \sigma T_w^4 + \rho_w B_{gw} \tag{5.57}$$

from each surface, and

$$P_s B_{gs} = P_w F_{ws} B_w, \tag{5.58}$$

$$P_r B_{gr} = P_w F_{wr} B_w, \tag{5.59}$$

$$P_w B_{gw} = P_w F_{ww} B_w + P_r F_{rw} B_r + P_s F_{sw} B_s \tag{5.60}$$

into each surface. Again, T_s is used in these calculations as in equation (5.6), and T_r is derived in a similar way for the K grid points across the roll, ie,

$$T_r = \frac{1}{\frac{1}{2}w_r} \left(\sum_{k=0}^{K-1} \tfrac{1}{2}(T_{r,k} + T_{r,k+1}) \triangle y_k \right). \tag{5.61}$$

The roll emissivity, specific heat and thermal conductivity are also calculated using this average value for T_r. The functional forms for these parameters are listed in Appendix B.

Solving for these radiosities is simpler than for the case of splitting the front and side walls, but nonetheless involves many different expressions. The solution can be found in terms of B_{gw}, ie,

$$B_{gw} = \frac{f_{sw}\varepsilon_s\sigma T_s^4 + f_{rw}\varepsilon_r\sigma T_r^4 + (f_{sw}\rho_s f_{ws} + f_{rw}\rho_r f_{wr} + f_{ww})\varepsilon_w\sigma T_w^4}{1 - \rho_w(f_{sw}\rho_s f_{ws} - f_{rw}\rho_r f_{wr} - f_{ww})}, \quad (5.62)$$

where $f_{ij} = P_i F_{ij}/P_j$ as in equation (5.33). From this, B_w can be determined using equation (5.57), and then $B_{gs} = f_{ws}B_w$ and $B_{gr} = f_{wr}B_w$.

The heat flow rate per unit length onto the exposed roll surface, Q_{gr} is then found using

$$\begin{aligned} Q_{gr} &= P_r(B_{gr} - B_r) \\ &= P_r[(1 - \rho_r(T_w))B_{gr} - \varepsilon_r\sigma T_r^4]. \end{aligned}$$

When initialising the model, both the roll and the wall in the vicinity of the roll are taken to be adiabatic to obtain the initial temperatures. This is similar to the two-wall problem, and the same IMSL routine is used to find the roll and wall temperatures, using the equations

$$B_{gr} - B_r = f(T_r, T_w) = 0, \quad (5.63)$$

$$B_{gw} - B_w = f(T_r, T_w) = 0, \quad (5.64)$$

recalling that there is negligible gas flow in the sections of the furnace where the rolls are located and therefore convection is ignored there.

The basic equation for the heat transfer in the roll is

$$\begin{aligned} \frac{\partial T}{\partial t} &= \frac{1}{\rho_r c_{pr}}\nabla(k_r \nabla T_r) \\ &= \frac{1}{\rho_r c_{pr}}\frac{dk_r}{dT_r}\left(\left(\frac{\partial T_r}{\partial y}\right)^2 + \left(\frac{\partial T_r}{\partial R}\right)^2\right) + \kappa_r\left(\frac{\partial^2 T_r}{\partial y^2} + \frac{\partial^2 T_r}{\partial R^2}\right), \quad (5.65) \end{aligned}$$

where $\kappa_r = k_r/(\rho_r c_{pr})$ (with ρ_r the density in this case) and R represents the direction into the roll surface. In dealing with the roll, it is found that the term involving the derivative of the thermal conductivity is much smaller if

compared to the second derivative in the temperature term, so the dk_r/dT_r term is neglected in a way analogous to the treatment of the variation in strip thermal conductivity. Therefore,

$$\frac{\partial T}{\partial t} = \kappa_r \left(\frac{\partial^2 T_r}{\partial y^2} + \frac{\partial^2 T_r}{\partial R^2} \right), \tag{5.66}$$

is the equation to be solved.

Boundary conditions for the roll are necessary in the middle of the roll, where symmetry requires that

$$\frac{\partial T_r}{\partial y}(0, R) = 0; \tag{5.67}$$

also at the end of the roll, $y = \frac{1}{2} w_r$,

$$\frac{\partial T_r}{\partial y}(\tfrac{1}{2} w_r, R) = 0, \tag{5.68}$$

where in both instances there is assumed to be no heat flow across the boundaries.

For the R direction, two boundary conditions are used: one for the part of the roll covered by the strip and one for the part not covered by the strip. For the roll/strip interface,

$$-k_r \frac{\partial T_r}{\partial R}(y, 0) = C(T_s - T_r), (0 \leq y \leq \tfrac{1}{2} w_s), \tag{5.69}$$

is used to account for the heat coupling between the strip and the roll. This expression is taken from Taylor & Elliott [53], where the value C is the conductance of the interface, taken for cold-rolled steel strip at low contact pressure to be 5678 $\mathrm{Wm^{-2}K^{-1}}$. For the uncovered roll,

$$-k_r \frac{\partial T_r}{\partial R}(y, 0) = B_{gr} - B_r, (\tfrac{1}{2} w_s < y \leq \tfrac{1}{2} w_r), \tag{5.70}$$

where B_{gr} and B_r are as obtained previously. At the interior of the roll, the roll 'sees' only the rest of the roll interior. As a result, there is no net gain or loss of heat at the roll interior boundary. Therefore

$$\frac{\partial T_r}{\partial R}(y, d_r) = 0. \tag{5.71}$$

The equation for the strip also changes when in contact with the roll. Not only does it receive heat at a flow rate per metre of $Q_{gs} = P_s(B_{gs} - B_s)$, with P_s as defined in equation (5.52), but the direct coupling between it and the roll directly beneath it is denoted by Q_{sr}, where

$$Q_{sr} = w_s(C(T_s - T_r)). \tag{5.72}$$

Therefore the strip equation (5.5) when the strip is on a roll becomes

$$\frac{\partial T_s}{\partial t} - V_s\frac{\partial T_s}{\partial x} - \kappa_s\frac{\partial^2 T_s}{\partial y^2} = \frac{Q_{gs} - Q_{sr}}{\rho_s w_s d_s(y) c_{ps}}. \tag{5.73}$$

In the radiant tube furnace model, the use of a finite-difference method to analyse the roll effect was rejected because of the negative influence that the accompanying increase in computational time would have on the on-line model. In this case, the speed is not an important consideration, and so finite-difference equations are used.

The boundary condition at the strip edge now has an extra component as well, that being the heat conducted across the strip edge from the roll. Therefore,

$$k_s\frac{\partial T_s}{\partial y} = k_r\frac{\partial T_r}{\partial y} + B_{gs} - B_s, (y = \tfrac{1}{2}w_s), \tag{5.74}$$

where the conductance term is sufficiently dominant for the radiation terms to be neglected if desired.

5.5 Solution method

With the extension to two dimensions across the strip surface, an accompanying increase in the number of calculations occurs. Most explicit finite-difference methods to solve the 2-d transport equation of the form (5.5) have reduced stability criteria to those found in 1-d equations. One way to solve this is to

use a time-splitting method (described by Noye [33] and Richtmyer & Morton [43]), which bypasses these additional stability criteria by first splitting the original equations into n component equations, then solving each equation over $(1/n)$th of a full time step. In this case, equation (5.5) is split in two, ie

$$\frac{1}{2}\frac{\partial T_s^{(1)}}{\partial t} - V_s\frac{\partial T_s^{(1)}}{\partial x} = \frac{2w_s(B_{gs} - B_s + q_{s,c})}{\rho_s w_s d_s(y) c_{ps}}, \tag{5.75}$$

$$\frac{1}{2}\frac{\partial T_s^{(2)}}{\partial t} - \kappa_s\frac{\partial^2 T_s^{(2)}}{\partial y^2} = 0. \tag{5.76}$$

If equation (5.75) is solved over the first half of a full time step, and equation (5.76) over the second half, then this is equivalent to solving both

$$\frac{\partial T_s^{(1)}}{\partial t} - V_s\frac{\partial T_s^{(1)}}{\partial x} = \frac{2w_s(B_{gs} - B_s + q_{s,c})}{\rho_s w_s d_s(y) c_{ps}}, \tag{5.77}$$

$$\frac{\partial T_s^{(2)}}{\partial t} - \kappa_s\frac{\partial^2 T_s^{(2)}}{\partial y^2} = 0, \tag{5.78}$$

over a full time step, because a $\frac{1}{2}\triangle t$ term appears in place of the ∂t term when the equations are discretised, cancelling out the $\frac{1}{2}$ in front of the time derivative. This is very convenient for many reasons, eg,

- equation (5.77) is virtually identical to the strip equation (4.1), which means no major programming changes are necessary and the new strip temperature can be found as before,
- the stability range for the strip equation remains the same when using the same finite-difference methods, and
- equation (5.78) is the basic 1-d heat conduction equation, for which analytical and numerical solutions are readily available.

The numerical scheme for the advection part of the equation is chosen as the same combination of the Lax-Wendroff method with the second-order upwind method as presented in Chapter 4. The difference now is that the advection terms only constitute half of the solution at each time step. Also,

the extra dimension across the strip needs to be included and is represented by the k subscript. Therefore, with the $n+\frac{1}{2}$ representing the solution after the first half of the time step, the Lax-Wendroff equation (2.73) and second-order upwind equation (2.74) become respectively

$$\begin{aligned} T_{s_{j,k}}^{n+\frac{1}{2}} &= -\tfrac{1}{2}c_{s_j}^{n}(1-c_{s_j}^{n})T_{s_{j-1,k}}^{n} + (1-\{c_{s_j}^{n}\}^2)T_{s_{j,k}}^{n} \\ &\quad +\tfrac{1}{2}c_{s_j}^{n}(1+c_{s_j}^{n})T_{s_{j+1,k}}^{n} + \triangle t^n(\mathrm{RHS}_s)_{j,k}^{n}, \qquad (5.79) \\ T_{s_{j,k}}^{n+\frac{1}{2}} &= -\tfrac{1}{2}c_{s_j}^{n}(1-c_{s_j}^{n})T_{s_{j-2,k}}^{n} + c_{s_j}^{n}(2-c_{s_j}^{n})T_{s_{j-1,k}}^{n} \\ &\quad +\tfrac{1}{2}(1-c_{s_j}^{n})(2-c_{s_j}^{n})T_{s_{j,k}}^{n} + \triangle t^n(\mathrm{RHS}_s)_{j,k}^{n}. \qquad (5.80) \end{aligned}$$

The grid to solve the diffusion part of the equation across the strip width is chosen in a similar way to the wall grid as explained in section 2.4.1. It is expected that the greatest temperature rise will take place at or near the strip edge, so the grid is arranged in the same way as for the wall; that is, doubling in size from the strip edge inwards to the middle of the strip. This method is found to be quite suitable when examining the edge effects. The finite-difference method for the strip therefore takes a similar form to that for the wall as shown in equation (2.87), except that in this case the strip grid points are halving in size between the strip centre $k=0$ and the strip edge $k=E$. Therefore,

$$T_{s_{j,k}}^{n+1} = s_{s_k}^{n}T_{s_{j,k-1}}^{n+\frac{1}{2}} + (1-3s_{s_k}^{n})T_{s_{j,k}}^{n+\frac{1}{2}} + 2s_{s_k}^{n}T_{s_{j,k+1}}^{n+\frac{1}{2}}, \qquad (5.81)$$

for $k=1, E-1$, where the strip diffusion number is

$$s_{s_k}^{n} = \frac{4}{3}\frac{\kappa_s \triangle t^n}{(\triangle y_{k-1})^2}. \qquad (5.82)$$

Using this combination of finite-difference methods allows the strip temperature to be calculated at every grid point across the strip width and throughout the strip length. The gas and wall equations are solved as before, with the separation of the walls into two different bodies having no effect on the basic form of the equations.

However, at the points where the rolls are included in the calculations, extra complexity arises. It is expected that the major variation in the roll temperature will also be at or near the edges of the strip, both at the points on the roll underneath the strip and at the roll points just outside the strip edge. Hence a similar arrangement is desired for the roll grid points, with the grid spacing doubling from the points at the strip edge to the end roll point, $k = K$. This in turn causes other problems, both in evaluating the roll temperature at the point directly underneath the strip edge, and also in the case of a strip width change. The time-splitting method is again used to solve for the roll temperature. In this case, diffusion occurs both across the roll and into the roll. Therefore, the roll equation (5.66) is solved using

$$T_{r\,k,m}^{\,n+\frac{1}{2}} = s_{r\,k}^{\,n}\nu_k T_{r\,k-1,m}^{\,n} + (1 - s_{r\,k}^{\,n}(\nu_k + 1))T_{r\,k,m}^{\,n} + s_{r\,k}^{\,n} T_{r\,k+1,m}^{\,n} \quad (5.83)$$

$$T_{r\,k,m}^{\,n+1} = s_{r\,m}^{\,n}\nu_m T_{r\,k,m-1}^{\,n+\frac{1}{2}} + (1 - s_{r\,m}^{\,n}(\nu_m + 1))T_{r\,k,m}^{\,n+\frac{1}{2}} + s_{r\,m}^{\,n} T_{r\,k,m+1}^{\,n+\frac{1}{2}} \quad (5.84)$$

where

$$s_{r\,k}^{\,n} = \frac{2\kappa_r \triangle t^n}{(1+\nu_k)\nu_k(\triangle y_{k-1})^2}, \quad (5.85)$$

$$s_{r\,m}^{\,n} = \frac{2\kappa_r \triangle t^n}{(1+\nu_m)\nu_m(\triangle R_{m-1})^2}, \quad (5.86)$$

with $\triangle R_m$ increasing in size from the outside to the inside of the roll shell. The other parameter $\nu_k (= \triangle y_k / \triangle y_{k-1})$ depends on whether the grid positions being determined are between the strip centre and the strip edge, or between the strip edge and the edge of the roll. The value of ν_k in the roll region under the strip will be the same as the value of ν_k for the strip (< 1), and the value for ν_k in the uncovered roll region is greater than one, since $\triangle y_k$ increases from the strip edge to the roll edge.

Consider the diagram in Figure 5.6. When a change in the strip width occurs, the grid spacing has to be reset both for the strip and the roll. If the number of grid points is set as a constant for the duration of the program

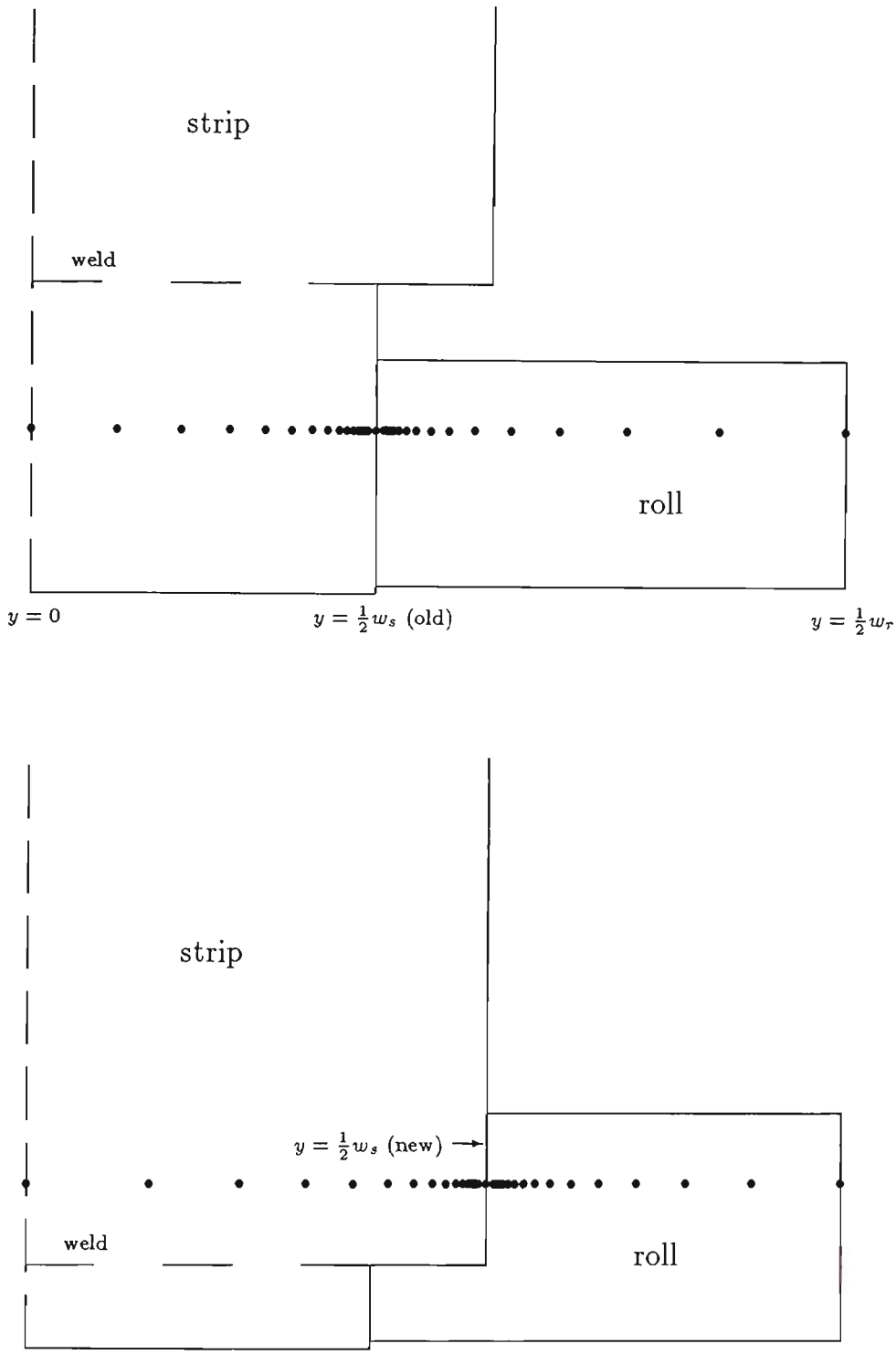

Figure 5.6: Diagram showing the grids for a weld passing a roll

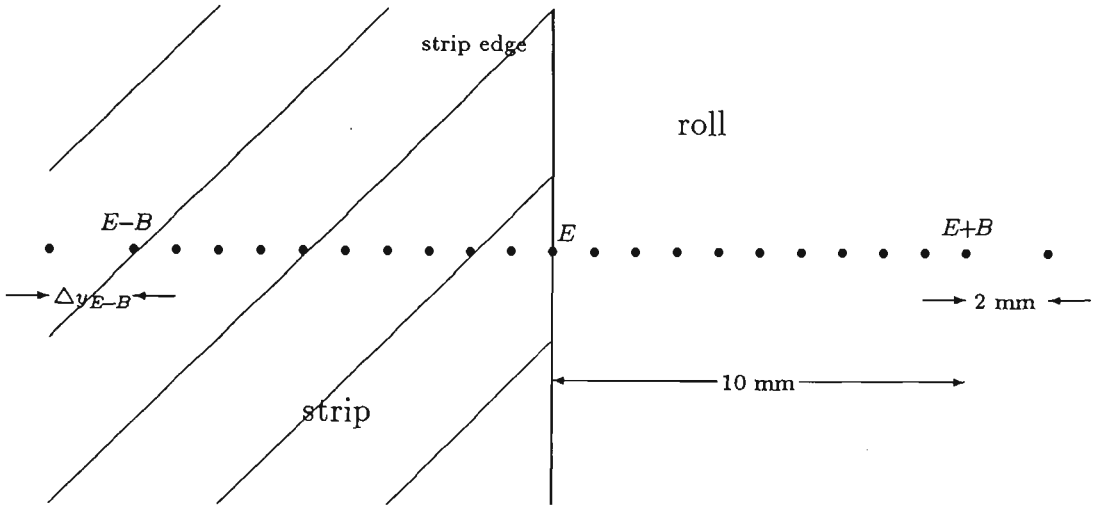

Figure 5.7: Diagram showing the grid around the strip edge

across the strip and the roll, then a change in the strip width means that all grid spacings change size. The problems with calculating the roll temperature at the point underneath the strip edge lies with the accuracy and stability of the finite-difference method used there. Interpolation formulae that are used need to be two orders of accuracy higher than the finite-difference method used across the strip in order to maintain the overall accuracy of the method [33]. Even when an interpolation formula is used, it is not necessarily stable for all cases.

To overcome this, the part of the roll that is 10 mm either side of the strip edge is treated separately from the rest of the grid, as shown in Figure 5.7. Here, grid points are placed 1 mm apart so that the grid spacing is uniform and no problems with accuracy or stability arise other than the standard FTCS stability restriction that $0 < s \leq \frac{1}{2}$. This removes the need for an interpolation formula to find the temperatures at the strip edge. This also gives excellent resolution of the temperature profile immediately around the strip edge. Outside of this region, the grid spacing increases out to the middle

of the roll/strip on one side and the edge of the roll on the other. At the first point outside this boundary region, the grid spacing is fixed at 2 mm. This is therefore an integer multiple of the grid spacing within the strip boundary region, and as a result, the accuracy of the method within the boundary region (which is $O\{(\triangle y)^2\}$) is maintained [33]. Therefore, if the domain across the strip/roll surface extends from $k = 0, K$, with $k = E$ denoting the strip edge, and B the number of points in the boundary region, then

$$T_{sj,E-B}^{n+1} = s_{sk-1}^{n} T_{sj,E-B-1}^{n+\frac{1}{2}} + (1 - 2s_{sk-1}^{n}) T_{sj,E-B}^{n+\frac{1}{2}} + s_{sk-1}^{n} T_{sj,E-B+2}^{n+\frac{1}{2}}, \quad (5.87)$$

for the strip near the edge, with $s_{sk}^{n} = \kappa_s \triangle t^n / (\triangle y_k)^2$. The expression for the roll in this region is

$$T_{rE-B,m}^{n+\frac{1}{2}} = s_{rk-1}^{n} T_{rE-B-1,m}^{n} + (1 - 2s_{rk-1}^{n}) T_{rE-B,m}^{n} + s_{rk-1}^{n} T_{rE-B+2,m}^{n}. \quad (5.88)$$

For the roll outside the strip edge,

$$T_{rE+B,m}^{n+\frac{1}{2}} = s_{rk}^{n} T_{rE+B-2,m}^{n} + (1 - 2s_{rk}^{n}) T_{rE+B,m}^{n} + s_{rk}^{n} T_{rE+B+1,m}^{n}, \quad (5.89)$$

where $s_{rk}^{n} = \kappa_r \triangle t^n / (\triangle y_k)^2$.

The grid spacing for the remaining distance out to the edge is determined by finding the lowest positive real root of the equation

$$\left(\sum_{k=E+B}^{K-1} \nu^{k-(E+B)} \right) \triangle y_{E+B+1} = \tfrac{1}{2}(w_r - w_s) - w_{bdy}, \quad (5.90)$$

for the roll region outside the strip edge, and

$$\left(\sum_{k=0}^{E-B-1} \nu^{k} \right) \triangle y_{E-B} = \nu^{E-B-1} (\tfrac{1}{2} w_s - w_{bdy}), \quad (5.91)$$

for the strip and the roll region underneath it, where $w_{bdy} = 10$ mm represents the width of the boundary region. Therefore in equation (5.83), $\nu_k < 1$ for $k = 0, E-B-1$, and $\nu_k > 1$ for $k = E-B, K-1$. The values for $\triangle y_{E-B}$ and $\triangle y_{E+B+1}$ are known because they are adjacent to the boundary region, and

are therefore integer multiples of the grid spacing within the region. In this case, $\triangle y_{E-B} = 2\triangle y_{E-B+1}$ and $\triangle y_{E+B+1} = 2\triangle y_{E+B}$. Another IMSL routine [19] is used to find ν.

The consequence of this is that the grid spacing is no longer exactly doubling in size on either side of the grid. Therefore the strip finite-difference method for the diffusion part of the equation now takes the general form

$$T_{sj,k}^{n+1} = s_{sk}^{n}\nu_k T_{sj,k-1}^{n+\frac{1}{2}} + (1 - s_{sk}^{n}(\nu_k + 1))T_{sj,k}^{n+\frac{1}{2}} + s_{sk}^{n}T_{sj,k+1}^{n+\frac{1}{2}} \tag{5.92}$$

with

$$s_{sk}^{n} = \frac{2\kappa_s \triangle t}{(1+\nu_k)\triangle y_{k-1}\triangle y_k}. \tag{5.93}$$

As a result, there are three different solution regions for the roll across its surface — between the strip centre and the strip edge ($k = 0, E-B$), between the strip edge and the roll edge ($k = E+B, K$), and in the region 10 mm either side of the strip edge ($k = E-B, E+B$). The strip also has a separate region 10 mm in from the boundary, and from there the grid spacing increases in size towards the centre of the strip according to the value of ν for $k = 0, E-B$.

With the re-meshing of the grid when the width change occurs, the temperatures at these new points on the roll need to be evaluated also. This is currently done by taking a linear fit between the roll temperatures using the old grid, and then finding the temperatures that correspond to the new grid points. This is probably the main difficulty with this approach, because the roll temperature profile may not be accurately retained when the new grid is formed. The temperature profile, at the point where the strip edge had been, remains for some time, while a new profile forms at the changed position of the strip edge. One way to overcome this would be to have another boundary area, similar to the one just described, at both the old and new boundary areas, with the grid at the old one being removed after the temperature profile flattens out. This would also cause problems, however, since a varying grid

would need to be chosen between the two boundaries, as well as the varying grids either side of the boundaries. If there is a strip width increase, the strip grid will change with the roll grid, causing it to have two boundaries also. These varying grids would introduce accuracy problems and possibly stability problems for the finite-difference method. In the results shown for the rolls, the grid spacing and number of grid points are chosen so that the roll temperature profile is retained as accurately as possible, by ensuring that at least one grid point lies in the old boundary region.

Using a grid of this form appears to be a good compromise between accuracy and computation time. It is noted that there are small numerical oscillations in the solution near the middle of the strip and the edge of the roll; but since these are of the order of 1 K they are quite insignificant, being barely noticeable in the graphs that are shown. These oscillations do not increase in time, and result from numerical errors caused by the combination of a decreasing, uniform and increasing grid across the one solution domain, each with different orders of accuracy. The other alternative is to choose a grid spacing of the order of 1 mm across the whole roll, and hence the whole strip, which becomes unacceptably expensive in computation time. For the roll model, this grid for the strip with the boundary region near the edge is used for all heights in the furnace, with the extra grid points also ensuring greater accuracy.

The occurrence of a width change in the furnace means that the advection terms in the strip equation cannot be used for the points across the strip in the immediate vicinity of the weld. With the re-meshing of the strip grid, the strip points before and after the weld do not 'line up', except for the centreline strip grid point. The model overcomes this by tracking the weld position, and when the weld is in the furnace, the model uses advection only to calculate the half-time step centreline strip temperature, and then diffusion

across the strip at all points as before. Currently, a deficiency in the data means that the weld does not travel a distance that is equivalent to $V_s \triangle t$ metres over one time interval of $\triangle t$ seconds in the data file. At other times, the weld just 'appears' in the furnace with the new values of strip thickness and width. Because of this, the model actually changes the dimensions of the strip instantaneously throughout the furnace when the data indicates that the weld has entered it, rather than progressively changing the dimensions as the weld travels through the furnace. This routine is included in the model, however, being available for application when the data is more reliable.

With the addition of many extra equations, several boundary conditions (BCs) have been added to the finite-difference scheme. With these boundary conditions, care must again be taken concerning their stability when incorporating them into the FDM. During the analysis of these BCs, it was found that there were problems with their stability, especially when the side wall was introduced. The thermal conductivity of the Fiberfrax blanket is lower than that of the brick insulation on the adjacent wall, so the side wall boundary condition gives a lower stability range than the front wall for the same time step. Because the radiation heat transfer entering the wall is non-linear in mathematical form, it is very difficult to determine the stability accurately. When numerical tests were conducted to test the stability range, it was found that the numerical BC used for the wall in equation (2.89) was unstable when the number of grid points was reduced (hence the size of the first grid spacing $\triangle z_0$ at the boundary was increased).

As a result, numerical boundary approximations were constructed so they might match the truncation error of the BC with that of the finite-difference method used across the domain [33]. The basic form of the matched truncation error BC, for a derivative boundary condition

$$a_0^n T_0^n - b_0^n \left.\frac{\partial T}{\partial y}\right|_0^n = c_0^n, \tag{5.94}$$

with a and b positive, evaluated at $y = 0$, is

$$T_0^{n+1} = (1 - 2s(1 + a_0^n \triangle y_0 / b_0^n))T_0^n + 2sT_1^n - 2sc_0^n \triangle y_0 / b_0^n. \qquad (5.95)$$

This is obtained by taking a centred-difference about the boundary, giving a value for the fictitious grid point T_{-1}^n, and by substituting this value into the finite-difference method used across the solution domain. Using this procedure, explained in Hildebrand [15], overcame the stability problems at the boundary for reduced numbers of grid points. Therefore, all finite-difference forms of the derivative boundary conditions for diffusion across the strip, wall and roll were constructed in this manner.

Another way to obtain some idea of the stability bounds is to linearise the equations about the region of interest. For example, the strip boundary condition (5.3) can be linearised about the strip temperature at the edge; it does not vary markedly between time steps since the size of the time step is small. Therefore linearising:

$$\begin{aligned} k_s \frac{\partial T_s}{\partial y} &= B_{gs} - B_s + q_{s,c}, \\ &= (\alpha T_s^4 + \beta T_g^4 + \gamma T_w^4 + H_s(T_g - T_s))/P_s \end{aligned}$$

using $T_s = T_{se} + T_s'$, with T_{se} the edge strip temperature, gives

$$k_s \frac{\partial T_s'}{\partial y} = T_s'((4\alpha T_{se}^3 - H_s)/P_s + (\alpha T_{se}^4 + \beta T_g^4 + \gamma T_w^4 + H_s(T_g - T_{se}))/P_s, \qquad (5.96)$$

with the Von Neumann stability condition for T_s' when using a boundary approximation of the form (5.95) of

$$s_{s,max} = \frac{1}{2 + ((-4\alpha T_{se}^3 + H_s)\triangle y_{E-1}/(P_s k_s))}, (\alpha < 0). \qquad (5.97)$$

The value of $s_{s,max}$ differs from 0.5 by less than 0.1% when 8 grid points across the strip are used, meaning that $\triangle y_{E-1} \approx 2$ mm if the grid spacing is doubled from the edge to the centre, as is done when the roll/strip interaction is not

being examined. Therefore the influence of the strip boundary condition on stability is negligible.

Analogous expressions exist when linearising the wall boundary conditions. For example, equation (5.47) for the side wall can be linearised about the side wall temperature at the wall/furnace boundary using $T_{we} = T_{we,0} + T'_{we}$, so

$$s_{we,max} = \frac{1}{2 + (4\xi_{we}T^3_{we,0} + h)\triangle z_0/k_{we}}, \tag{5.98}$$

where ξ_{we} is the coefficient of T^4_{we} in the expressions for B_{we} and $B_{g,we}$ as given in equations (5.28) and (5.35), and h is the coefficient of the convection term in equation (5.38).

The roll boundary condition (5.69), however, is linear in form and the stability bounds can be calculated exactly when using equation (5.95). The bound is

$$s_{rR,max} = \frac{1}{2 + C\triangle R_0/k_r}, \tag{5.99}$$

which varies with $\triangle R_0$. This bound is included in the routine that evaluates the optimal time step.

The stability range of the overall method is further restricted with the addition of these new parameters. On top of the gas advection restriction (2.79), the strip advection restriction (2.80), and the wall diffusion restriction (2.99), come criteria for the strip across its width, the side wall and the roll. Across the strip, it is

$$\triangle t \leq \frac{1}{2}\frac{(\triangle y_k)^2}{\kappa_s}, \tag{5.100}$$

where y_k is the smallest grid spacing used, which is either the one at the strip edge, or, when the strip is on a roll, at any point within the boundary region. For the side wall,

$$\triangle t \leq \frac{1}{2}\frac{(\triangle z_0)^2}{\kappa_{we}}, \tag{5.101}$$

grid pts	$\triangle z_0$	$s_{we,max}$ (BC)	s_{we} (FDM)
8	1.10 mm	0.1832	0.0167
9	0.55 mm	0.2683	0.0672
10	0.27 mm	0.3493	0.2694
11	0.14 mm	0.4113	≈ 0.5

Table 5.1: Stability at side wall boundary

grid pts	$\triangle R_0$	$s_{rR,max}$ (BC)	s_{rR} (FDM)
3	3.14 mm	0.3342	0.0091
4	1.47 mm	0.4060	0.0421
5	0.71 mm	0.4496	0.1781
6	0.35 mm	0.4739	≈ 0.5

Table 5.2: Stability at roll exterior boundary

with the expression for the front wall being the same as that in equation (2.99), since $\kappa_{wf} \equiv \kappa_w$. For the roll, the stability criterion is

$$\triangle t \leq \frac{1}{2}\frac{(\triangle y_k)^2}{\kappa_r}, \tag{5.102}$$

across the roll, where y_k is a point within the boundary region. Into the roll,

$$\triangle t \leq \frac{1}{2}\frac{(\triangle R_0)^2}{\kappa_r}, \tag{5.103}$$

since $\triangle R_0$ represents the smallest grid spacing for the grid into the roll.

The model shows that as the number of grid points used in the strip, wall and roll diffusion equations is decreased, then these time-dependent stability criteria begin to influence the overall stability conditions more than the boundary conditions. Consider the Tables 5.1 and 5.2, which compare the maximum stable value for s at the boundary when using a boundary equation of the form (5.95), with the value of s at the boundary grid point using the finite-difference equation (2.87) for the wall and (5.84) for the roll. If the

number of grid points into the side wall in Table 5.1 is reduced by one, while the grid is arranged to double its spacing, then the value of s for the side wall is reduced to about one-quarter of its previous value (changing with $(\triangle z)^2$). This keeps it well below the upper bound determined by the BC, s_{max} (changing with $\triangle z$), for the same time step $\triangle t$. For eleven grid points with the same time step, $s_{we} > s_{we,max}$, so the time step must be decreased to ensure stability. However, the further reduction in a time step that is already small in order to retain stability is not desired. A similar situation occurs for the grid spacing into the roll in Table 5.2. Therefore, the number of grid points is chosen to ensure that the method for each parameter is stable, without having to significantly reduce the time step. These extra limitations, coupled with the additional number of calculations involved, acts to substantially increase the run time of the model. A data file of around 4 hours duration (as most of those used here are) now takes around 8 hours of computation time to complete, compared to only about 15 minutes for the centreline model of Chapter 4.

5.6 Results

The first set of results considers only the effect of the exposed strip edge surface on the edge temperature. Three examples are given using different strip thicknesses and widths at various line speeds and gas flow rates. In the initial graphs, only 8 grid points are used across the strip width, with the grid spacing doubling from the centre to the edge. This causes some lack of resolution in the profile shown.

The first graph in Figure 5.8 shows the variation of strip temperature over its width from the centre of the strip to the edge (therefore the actual strip width is twice the figure given at the edge while the same profile is assumed at the other edge). This graph was taken at the end of the data file

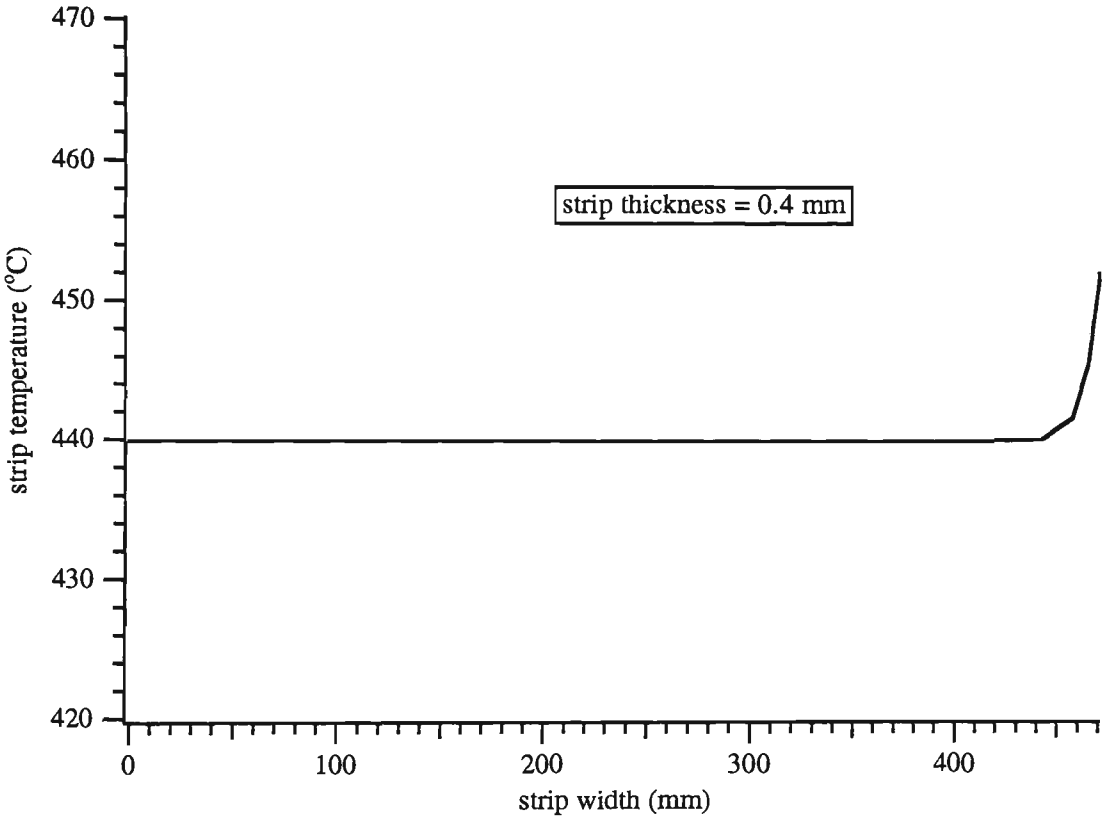

Figure 5.8: Exposed edge surface area - at end of *mrl32.dat*

mrl32.dat with the strip thickness at 0.4 mm and the strip width at 940 mm. The gas flows and line speed are found in Figures 4.2 and 3.5 respectively.

The strip profile is clearly quite flat for most of the strip width until the edge is reached, when the temperature increases by around 13 K at the edge. The main area of interest is certainly in the last 20-30 mm, where the heat entering the edge according to equation (5.3) is diffused inwards by the strip from the edge.

The second example is taken with the data from the end of the data set *mrl35.dat*. The gas flows as shown in Figure 4.4 are much higher; as a result the temperature increase at the edge is also higher at around 25 K. Again the main variation in temperature occurs within about 30 mm of the strip edge. The line speed at this time is 70 metres per minute and the strip width is 1080 mm.

The final graph in Figure 5.10 is taken with the same data set *mrl35.dat*, but this time the model was stopped after 2000 seconds. The value here of the strip thickness is 0.8 mm and the strip width is 903 mm. Again the gas flows are higher that in the first example, though slightly less than for the second example. This leads to a temperature rise again of about 25 K, but the centreline strip temperature is over 700°C, so the percentage rise is less when compared with the previous example.

All of these graphs reveal a temperature rise at the strip edge which is dependent on the amount of heat entering the furnace, which in turn is dependent to some degree on the gas flow. If the centreline strip temperature is slightly less than the recrystallisation temperature of the steel, then the temperature at the edge may be slightly higher than the recrystallisation temperature, causing problems in the quality of the steel. The difference in the strip centreline temperature obtained using this model and the one in chapter 4 is negligible.

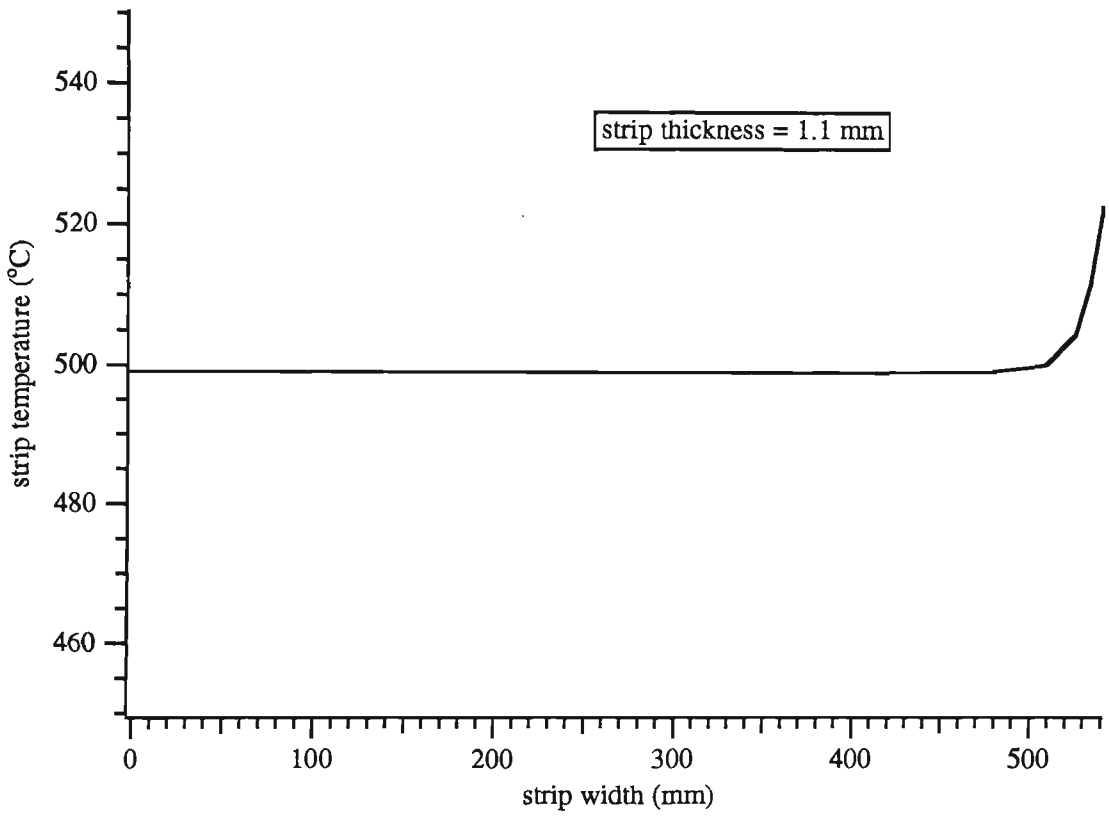

Figure 5.9: Exposed edge surface area - at end of *mrl35.dat*

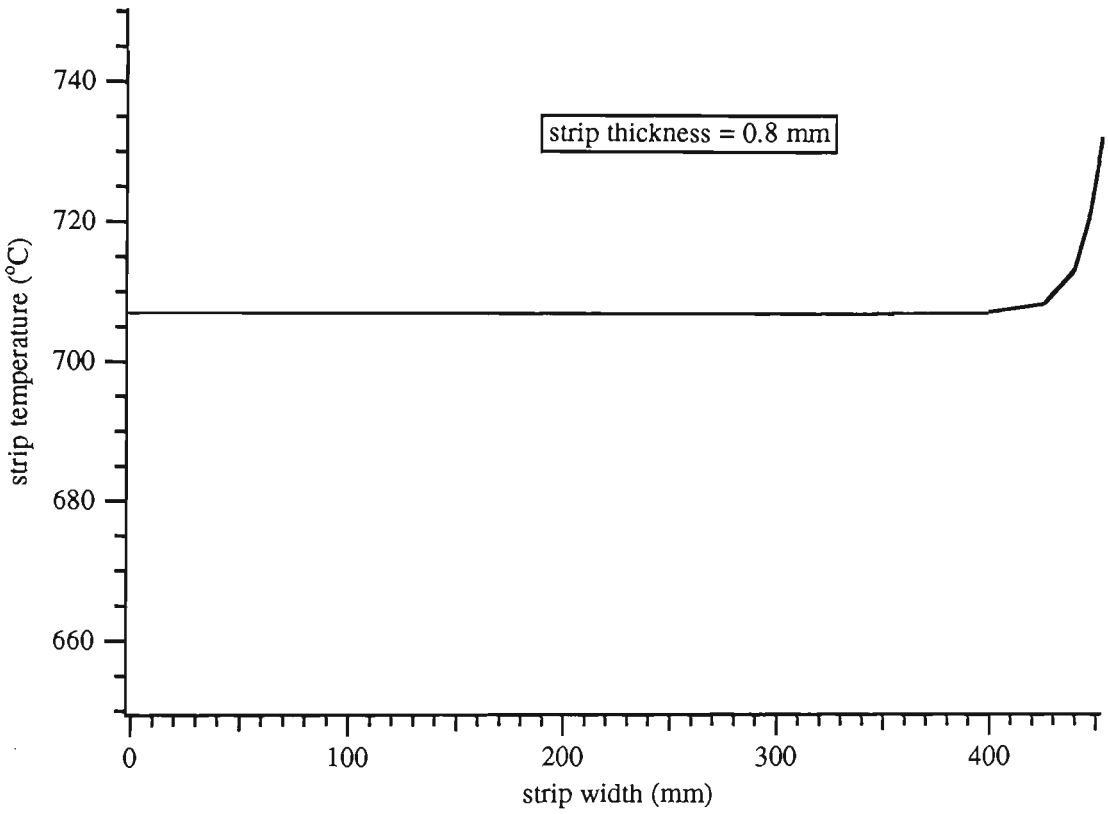

Figure 5.10: Exposed edge surface area - *mrl35.dat* after 2000s

The size of the 'boundary layer' region that is observed in these results can be approximated using the same analytical technique as shown in section 2.2, except that the strip is substituted for the wall. By analogy, equation (2.28) becomes

$$\delta = \frac{3k_s(T_{s,edge} - T_{s,\infty})}{B_{gs} - B_s + q_{s,c}}, \tag{5.104}$$

where $T_{s,edge}$ is the edge strip temperature and $T_{s,\infty}$ represents the centreline strip temperature. In the example shown in Figure 5.10 at $t = 2000$ s, the flux to the strip $B_{gs} - B_s + q_{s,c} = 76135$ Wm^{-2}, $k_s = 34.0$ Wm^{-1}K^{-1}, $T_{s,edge} = 732.3^{o}$C and $T_{s,\infty} = 707.0^{o}$C. This gives

$$\delta = \frac{3(34)(25.3)}{76135} = 33.9 \text{ mm}, \tag{5.105}$$

which, when compared with Figure 5.10, gives a good approximation for the size of the boundary region.

The next set of results looks at the effect of edge drop on the edge temperature. The edge drop effect is coupled with the surface area effect in the following graphs.

Figure 5.11 shows the thickness profiles used to calculate the strip temperatures displayed in Figure 5.12. The amount of edge drop modelled is for the percentage changes shown on the graphs, with the value of d_{pos} chosen to be 0.5 and $w_{pos} = 60$ mm as used in equation (5.8). This profile was derived at the same time as that given in Figure 5.10 — ie, for data set *mrl35.dat* at $t = 2000$ s.

As is expected, the decreasing strip thickness has a substantial effect on the strip temperature, both at the edge and at all points in between except for the centreline temperature, depending on the edge drop. For the 5% edge drop case, the temperature difference is around 50 K. If this were a truly representative profile, then at certain temperatures there would be substantial non-uniformities in the metallurgical properties over the strip width. Even

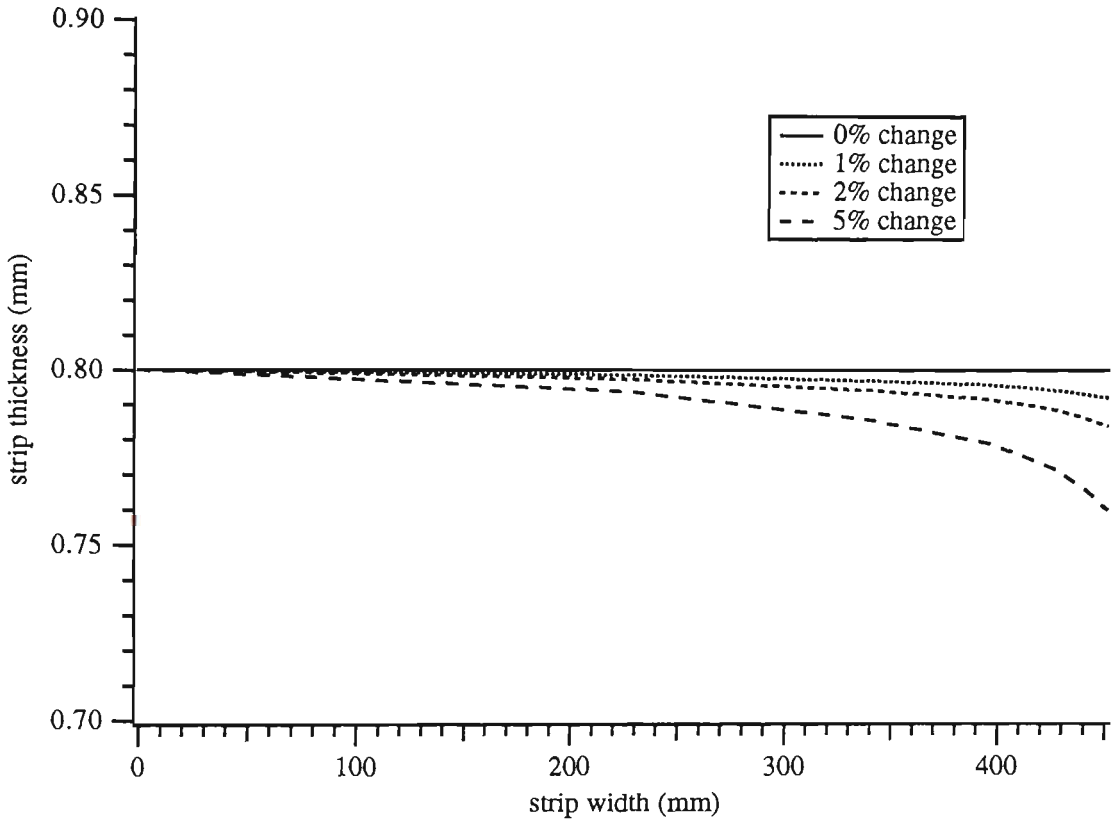

Figure 5.11: Thickness profiles for edge drop - *mrl35.dat* after 2000s

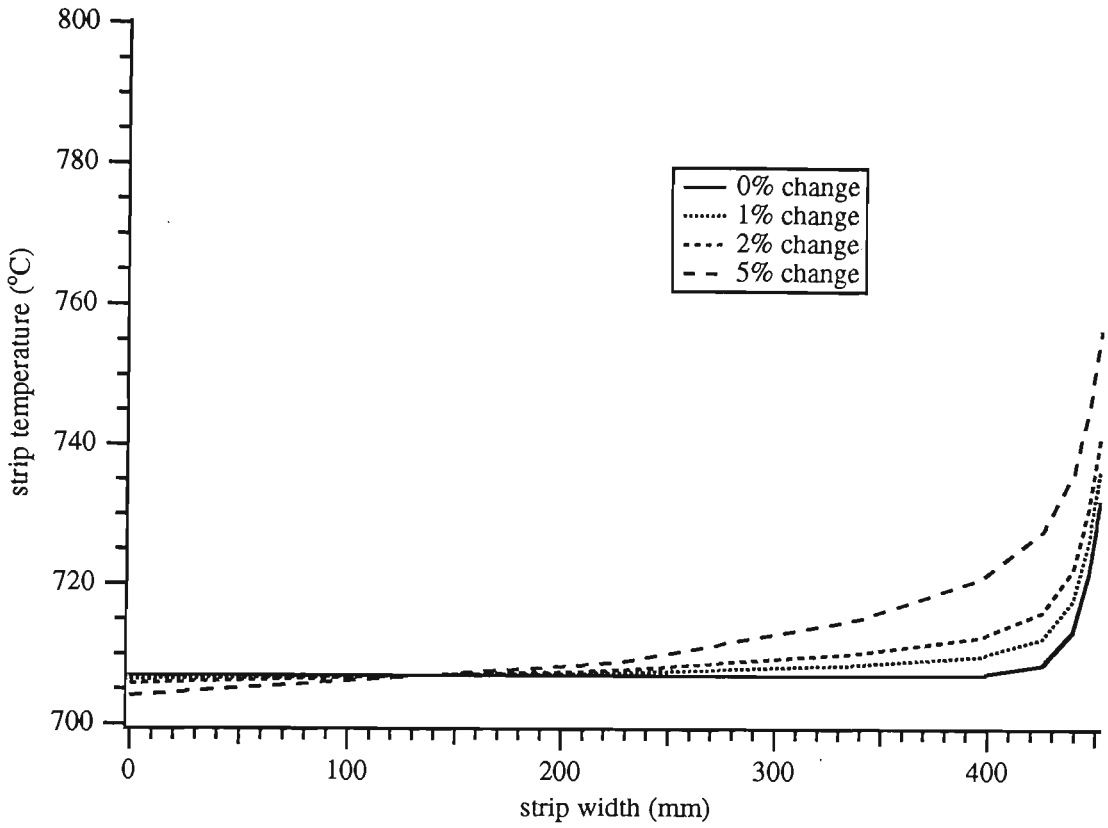

Figure 5.12: Effect of edge drop on temperature - *mrl35.dat* after 2000s

in the 1% and 2% drop examples, the temperature rises by around 5 K per percentage drop; therefore, there is an approximate 1% temperature rise for every 1% thickness drop. It is clear that the temperature profile closely follows the thickness profile.

Next, the influence of the side walls is examined. In the graphs that follow, comparisons are made between the temperature profiles of the strip for both the one-wall model and the split two-wall model. The graphs compared are for data sets already examined, that being for data set *mrl35.dat* after a time of 2000 s. Comparisons are made assuming an edge drop of 0% in Figure 5.13, 1% in Figure 5.14 and 2% in Figure 5.15. The solid line represents the profiles shown previously for these examples, while the dashed line gives the profile of the separated wall model.

Contrary to what was expected, separating the side walls from the front walls appears to have a very small effect on the strip edge temperature in comparison to the extra edge surface area and the edge drop effect. The difference in temperature between the centre and the edge for the one-wall and two-wall models is very slight. In Figure 5.13, the one-wall model gives a temperature difference of 25.26 K, and the two-wall model 27.10 K. For Figure 5.14, the differences are 30.64 K and 33.01 K, and for Figure 5.15, 36.08 K and 39.02 K. Therefore, when the separated-wall model is included, its effect accounts for less than 10% of the total temperature difference.

The reasons for this small influence probably relate to the fact that the edge is already hotter than the rest of the strip, as shown when examining the effect of the extra surface area exposed and the edge drop. The difference in temperature between the edge and the source of heat transfer to it is less than it is between the strip face — at a lower temperature than the edge — and the same source. Therefore the heat transferred by radiation and convection will be less to the strip edge than to the strip face. Also, even though the

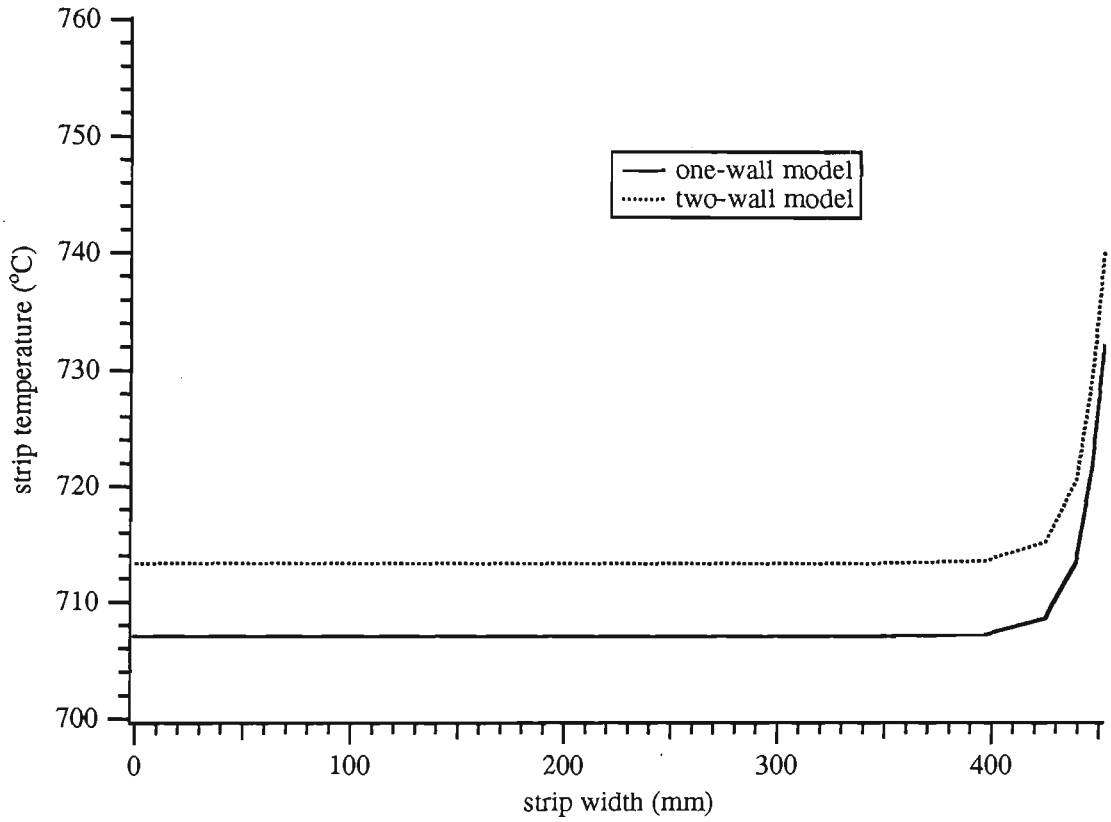

Figure 5.13: Comparison of one-wall and two-wall models — 0% edge drop

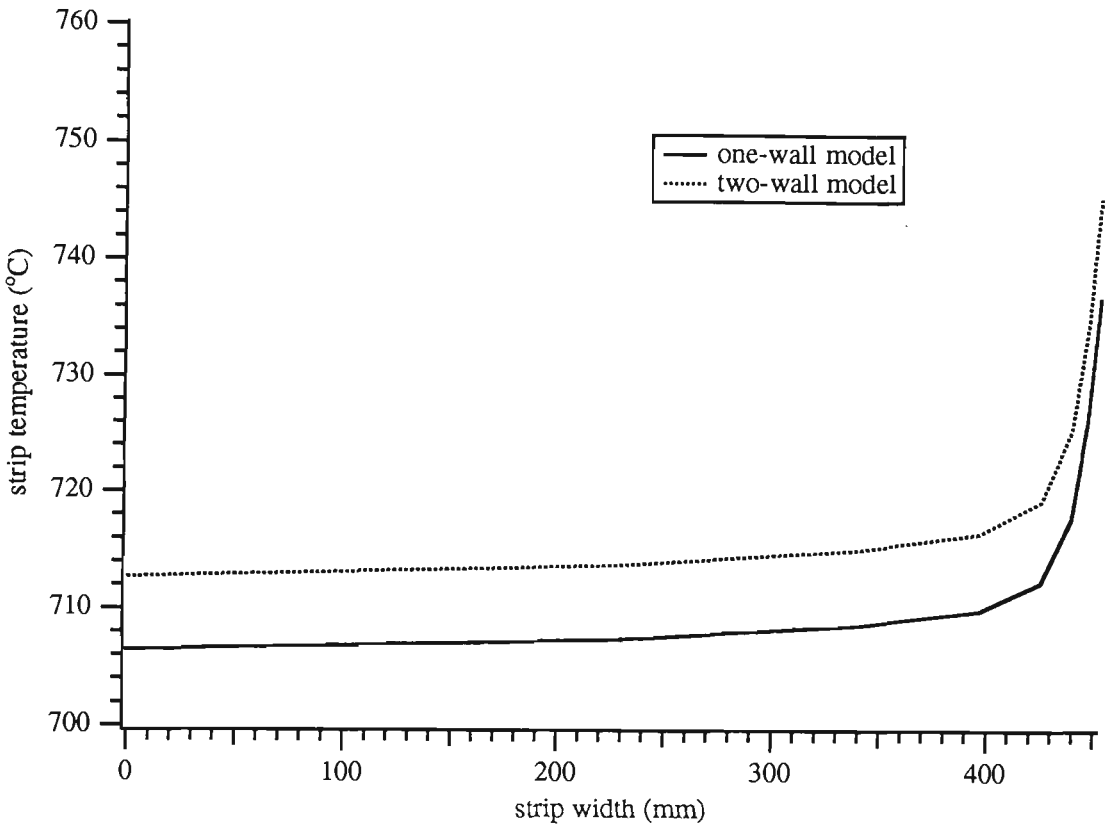

Figure 5.14: Comparison of one-wall and two-wall models — 1% edge drop

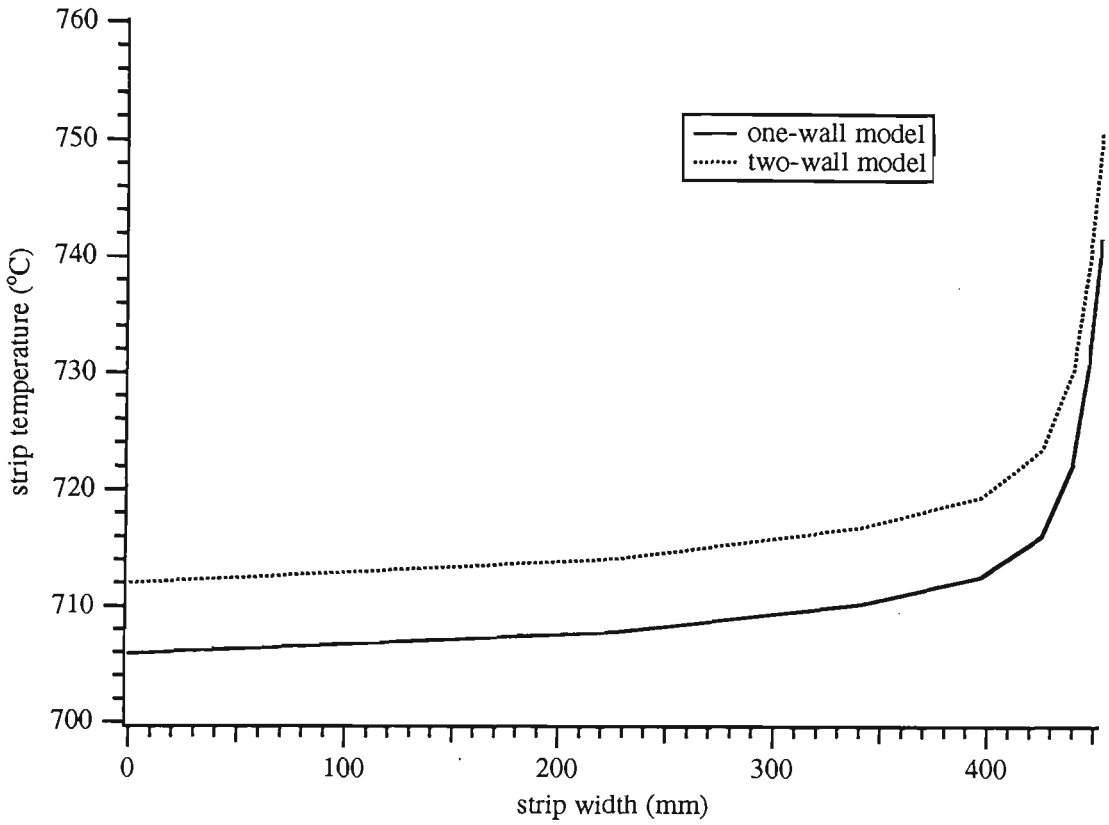

Figure 5.15: Comparison of one-wall and two-wall models — 2% edge drop

radiation shape factor between the side wall and the strip edge $F_{we,se}$ is much larger in a relative sense than between the front wall and the strip edge $F_{wf,se}$, it still has a very small absolute value (0.00066 for strip 1 m wide and 1 mm thick according to equation (5.15)). Therefore, only a very small proportion of the heat from the walls is received by the strip edge.

However, the two-wall model is itself somewhat deficient. The model actually suggested that the side walls were hotter than the front walls, which is certainly not expected in the furnace since the gas burners are located on the front walls. The direct exposure of the front walls to the strip means that the strip obtains most of its heat from the front walls, reducing the temperature to below that of the side walls. Some quick tests in allocating some of the heat of combustion Q_{comb} directly into the front wall rather than into the gas was found to increase the overall strip temperature and increase the front wall and side wall temperatures. The opportunity exists for further work in this area.

The final set of results examines the effect of the rolls on the strip temperature variation across the strip width. A change in the strip width has been found to play a less important part in the variation of strip temperature than the strip thickness change throughout the thesis, but in this section on the rolls, the variation in strip width is shown to markedly influence the temperature profile across the strip. All of the examples shown here are in the case of transients, when a new coil enters the furnace with a different width. The solid line in the graphs to follow represents the strip temperature on the roll, and the dashed lines represent the internal grid points in the roll, from the surface at $R = 0$ to the inside of the shell, $R = d_r$. Five internal roll grid points were used in the following graphs. All cases considered assume a strip edge drop of 2%, with the same values for d_{pos} and w_{pos} as used previously.

The first case considered is that of a decreasing strip width, with

the roll temperature outside the strip edge at a lower temperature than the strip. The data set used in this example is *mrl36.dat*. The width change occurs at 4495 s into the data set, with the old coil 1235 mm wide and the new coil 1070 mm wide. For this run, 26 grid points were chosen across the strip and 50 across the roll (both including the points in the boundary region). With this choice, a grid point after the width change is located 612.5 mm from the centre of the roll, when re-meshing using equation (5.90). Considering that the edge of the old strip coil was 617.5 mm from the centre, the roll temperature profile in this region should be retained well.

The graph shown in Figure 5.16 is that of the strip and the roll before the weld occurs at $t = 4490$ s. The strip temperature profile is similar to that seen in the graphs of the edge drop in Figure 5.12. The major difference is at the very edge, where there is a slight peak due to the heat conduction over the strip edge from the strip to the lower roll temperature in accordance with equation (5.74). This peak does not extend further in toward the centre of the strip over time, because the strip already has the basic temperature profile from advection before it reaches the roll, and the contact time with the roll is too short. Outside the strip edge, the roll temperature is virtually uniform throughout the roll thickness, and under the strip the profile closely follows that of the strip. Also, as suggested, the numerical oscillations in the roll temperature toward the end of the roll are negligible. This initial graph can also be interpreted as a typical 'steady-state' profile for the strip in contact with a roll, for the example when the roll is cooler than the strip outside the strip edge.

The next graph, Figure 5.17, is taken five seconds after the weld passes the roll. Two peaks in the roll temperature are now evident — one where the strip edge was, and one where the strip edge is. The strip temperature profile is basically unchanged. The high thermal mass of the roll means that

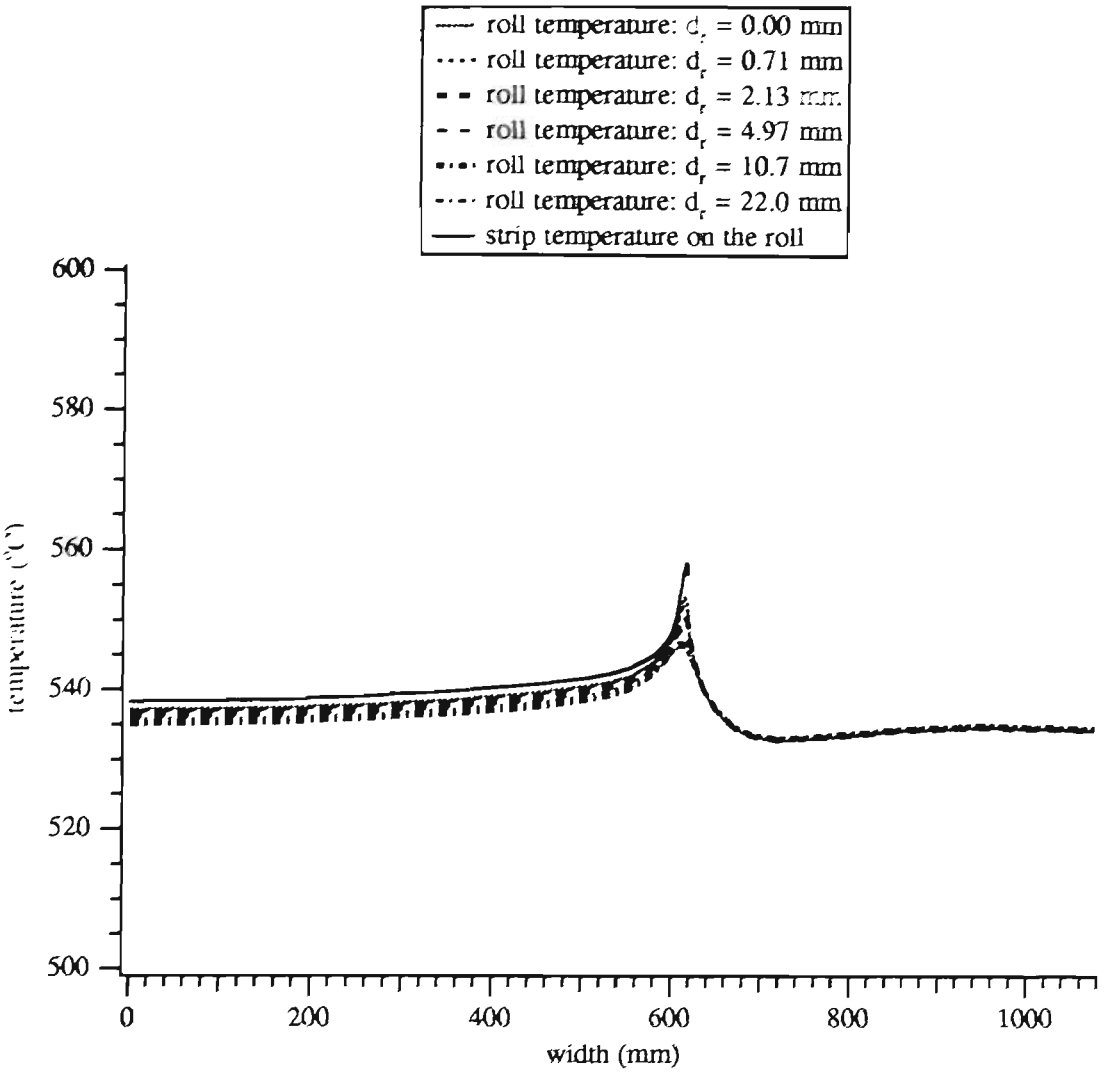

Figure 5.16: Decreasing width, lower roll temperature — before width change

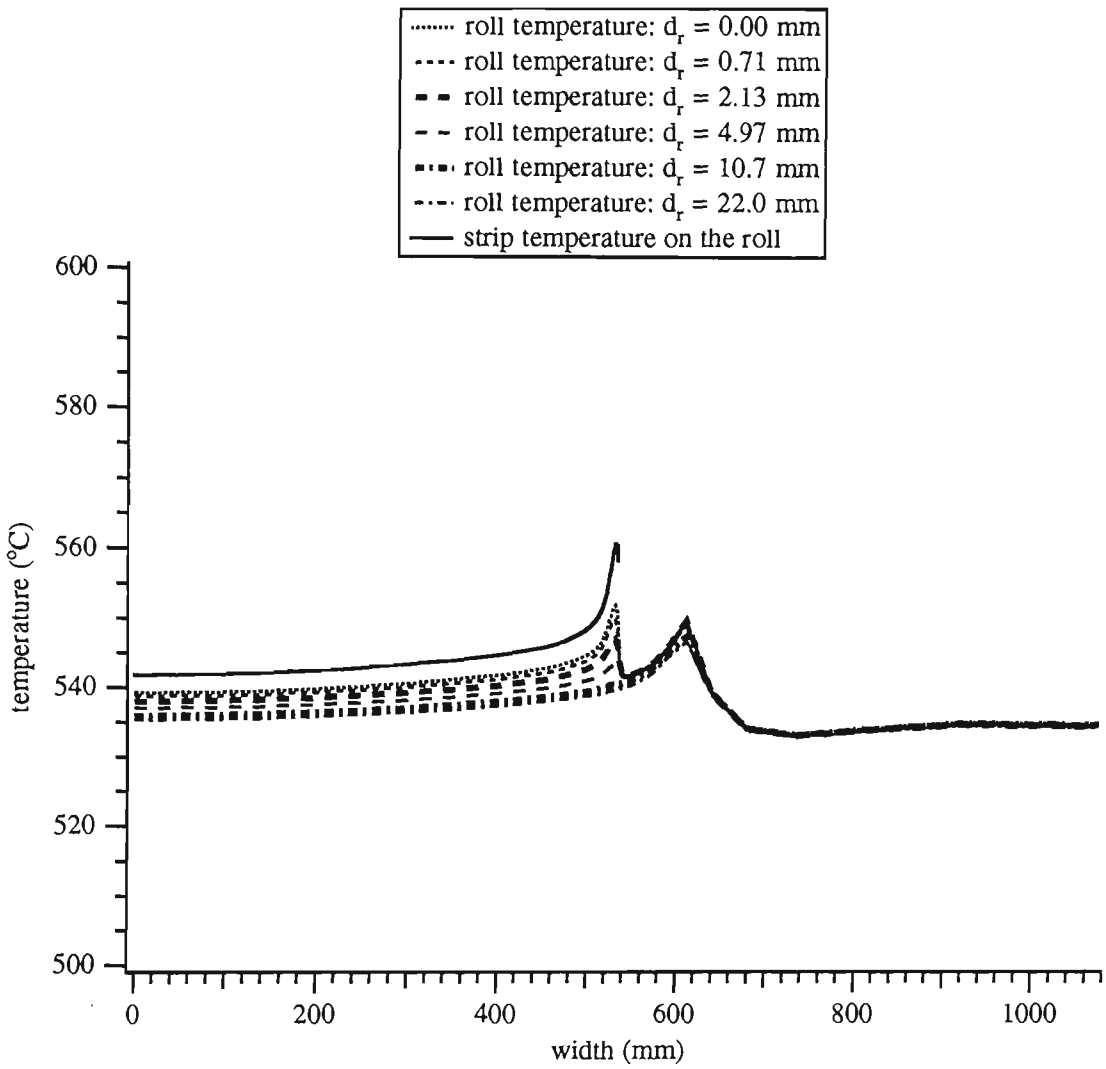

Figure 5.17: Decreasing width, lower roll temperature — 5 s after width change

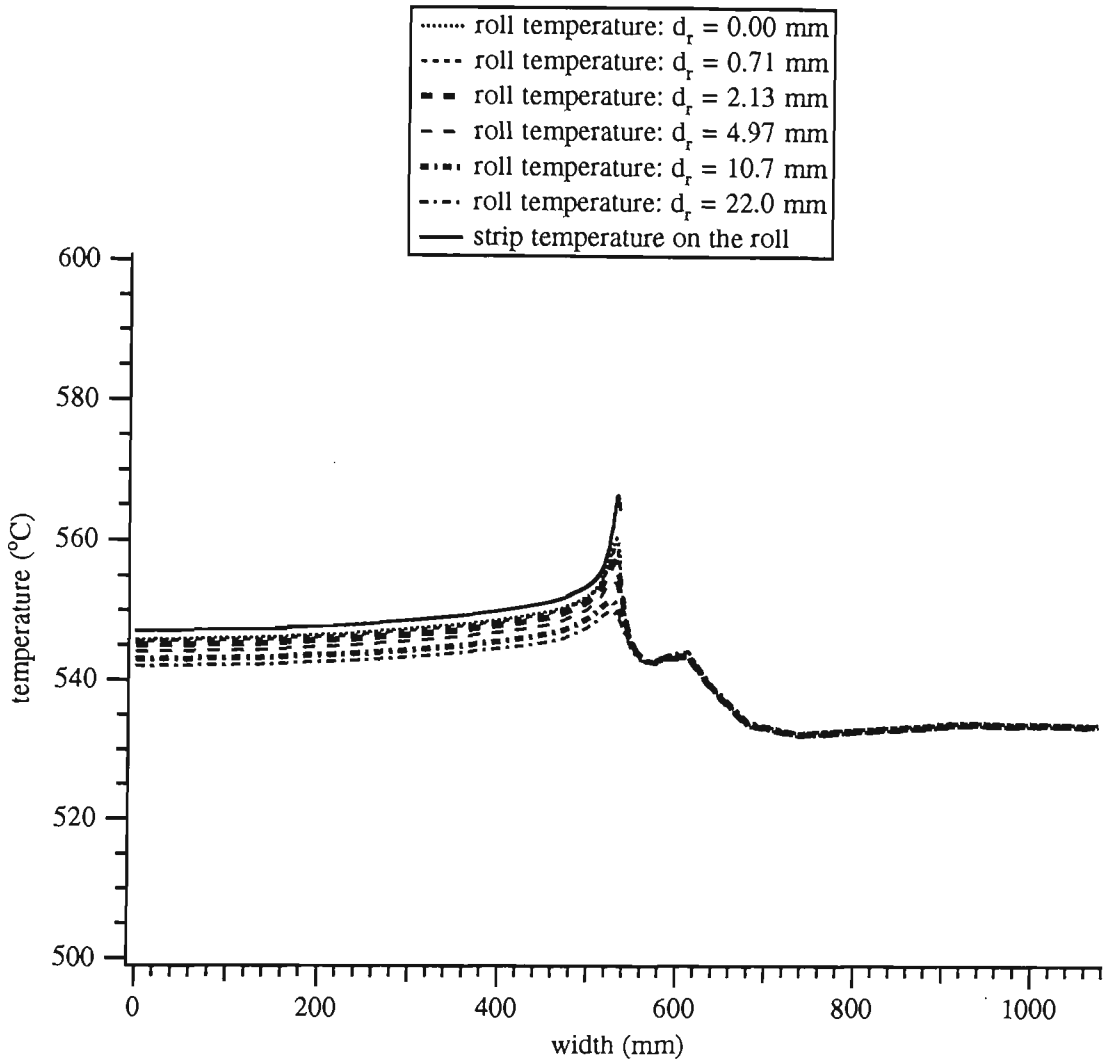

Figure 5.18: Decreasing width, lower roll temperature — 100 s after width change

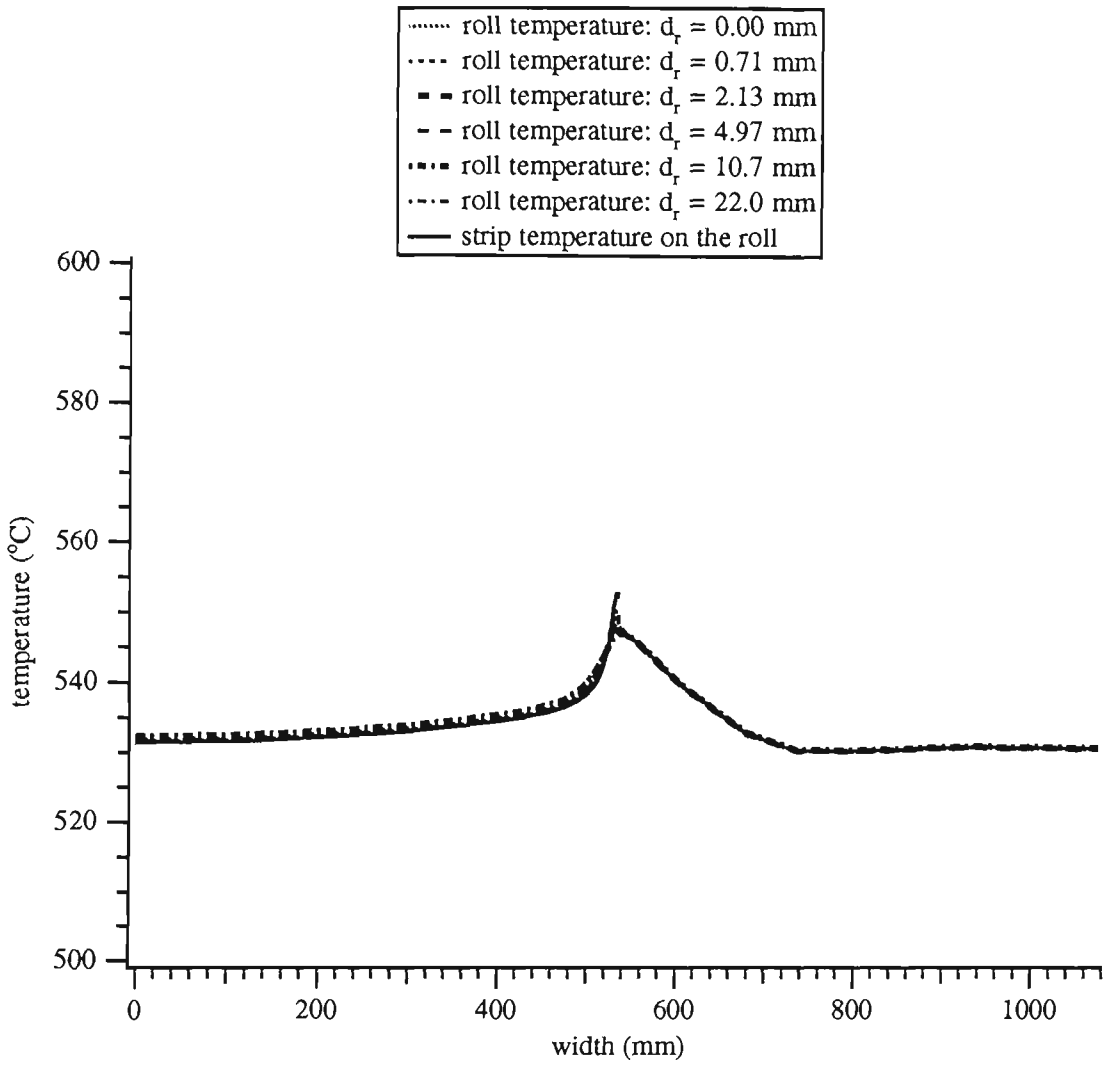

Figure 5.19: Decreasing width, lower roll temperature — 500 s after width change

it takes a substantial amount of time for this peak to disappear as the heat diffuses and radiates away. Figures 5.18 and 5.19 are taken 100 and 500 seconds after the weld change respectively, and evidence of the peak still exists in these cases. The centreline strip temperature continues to vary as a consequence of the heat transfer processes occurring in the DFF above the roll.

Of more importance is what happens when a strip width increase occurs, because of its effect on the strip temperature. Two cases of this are now considered — the cases when the roll temperature is higher and lower than the strip temperature.

The situation where the width increase covers an area of higher roll temperature is shown in Figures 5.20, 5.21, 5.22 and 5.23. The data set examined is *mrl35.dat*, and the width change examined occurs at 9182 s into the data set. In this example, 26 grid points across the strip and 50 grid points across the roll were chosen. The width increase is from 900 mm to 1020 mm. Therefore, the eighth grid point is at 449.6 mm from the centre of the strip after the width change, which is only 0.4 mm from the position of the previous edge. The profile taken two seconds prior to the width increase, and graphed in Figure 5.20, shows a typical strip width temperature profile, with the roll underneath coupled closely to it and the roll outside the edge still at a temperature of over 700°C. The cycle change that brought the strip temperature down occurred at just after 8000 s according to Figure 4.4, with the roll cooling slowly because of its high thermal mass. Figure 5.20 shows a typical profile when the strip is in contact with a roll that is hotter outside the edge — there is no 'peak' in the strip temperature near the edge in this example.

After the strip width increase occurs, as shown in Figure 5.21, the heavy coupling between the strip and roll causes the roll temperature to begin equilibrating with the strip, in accordance with equation (5.69), with

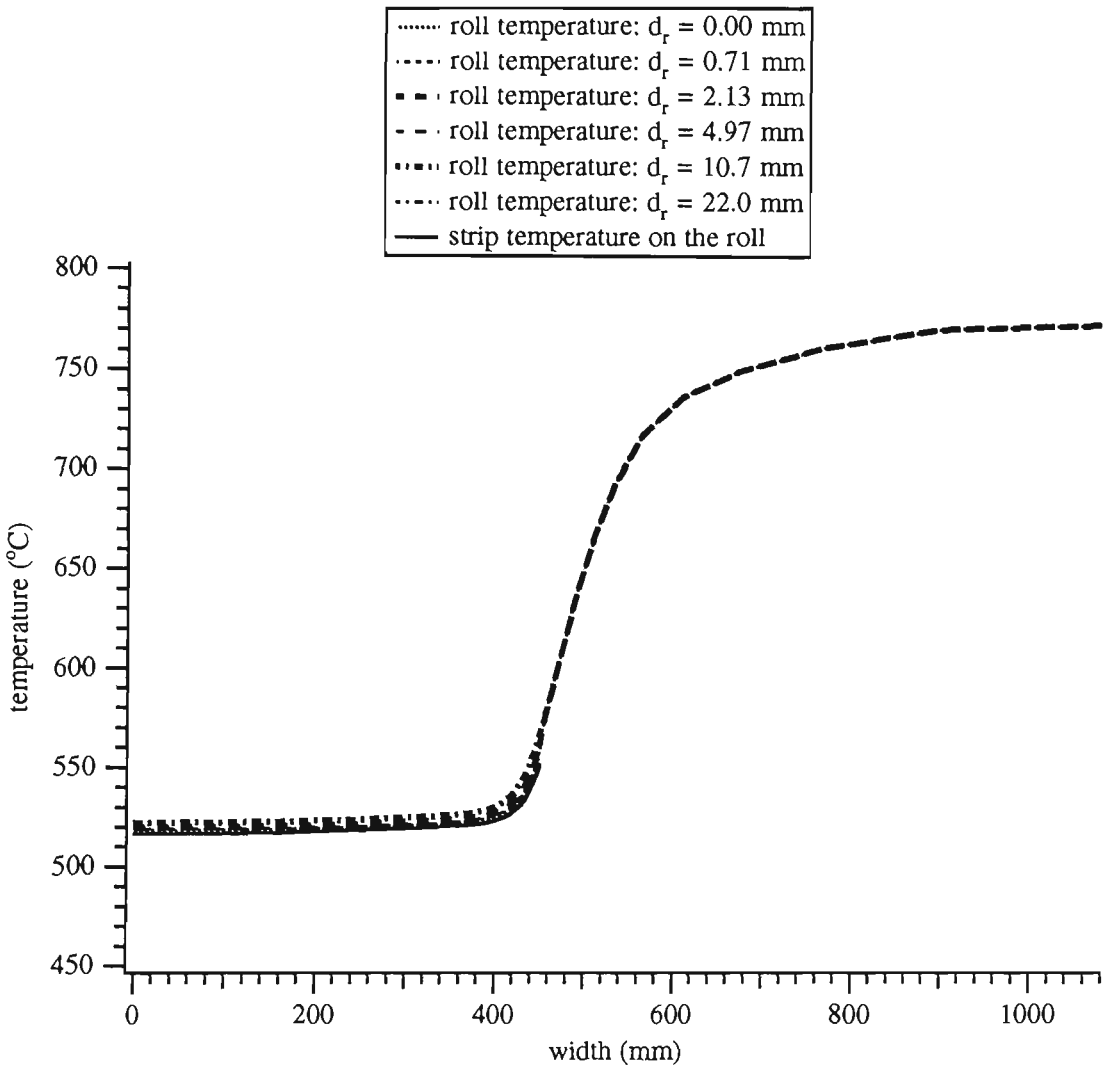

Figure 5.20: Increasing width, higher roll temperature — before width change

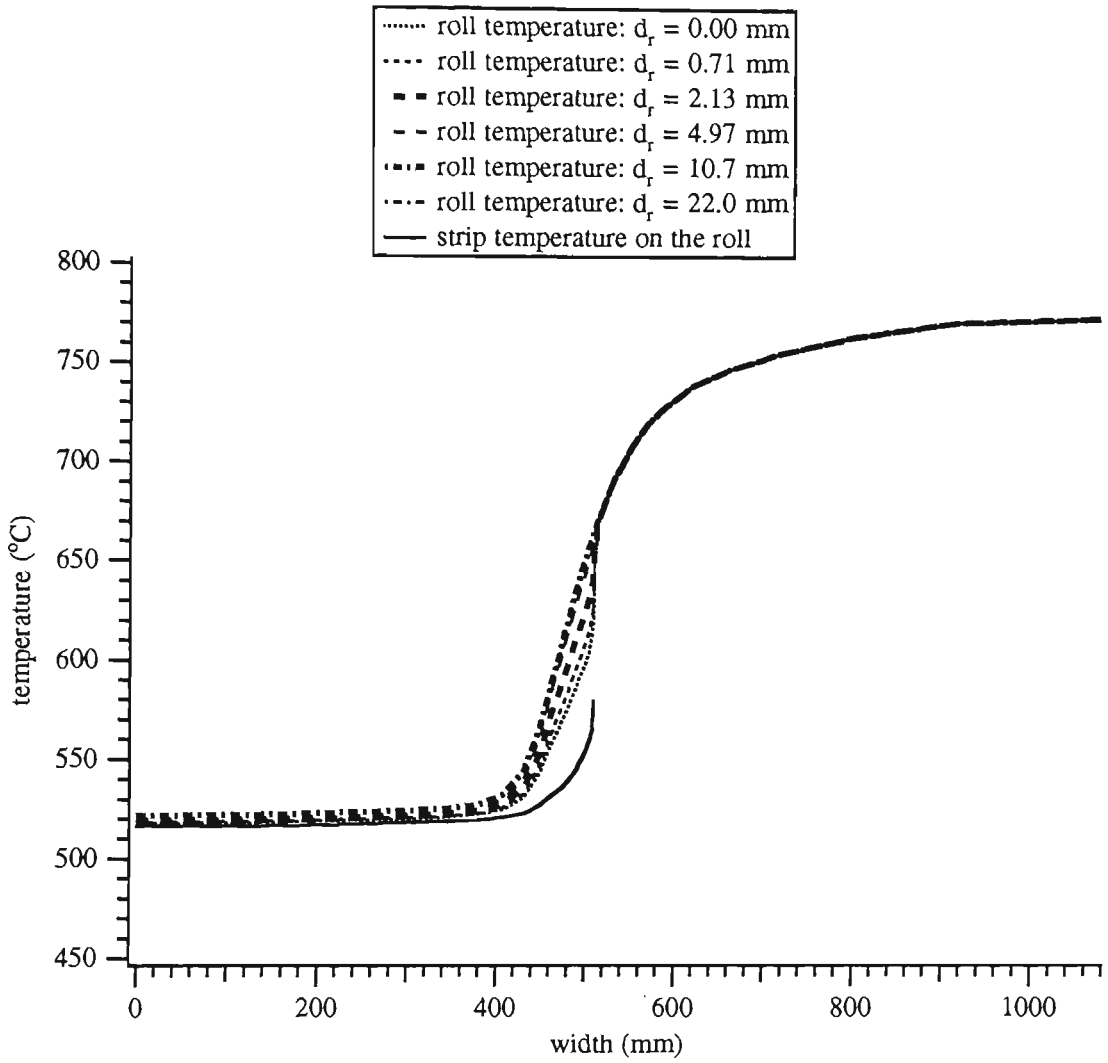

Figure 5.21: Increasing width, higher roll temperature — 3 s after width change

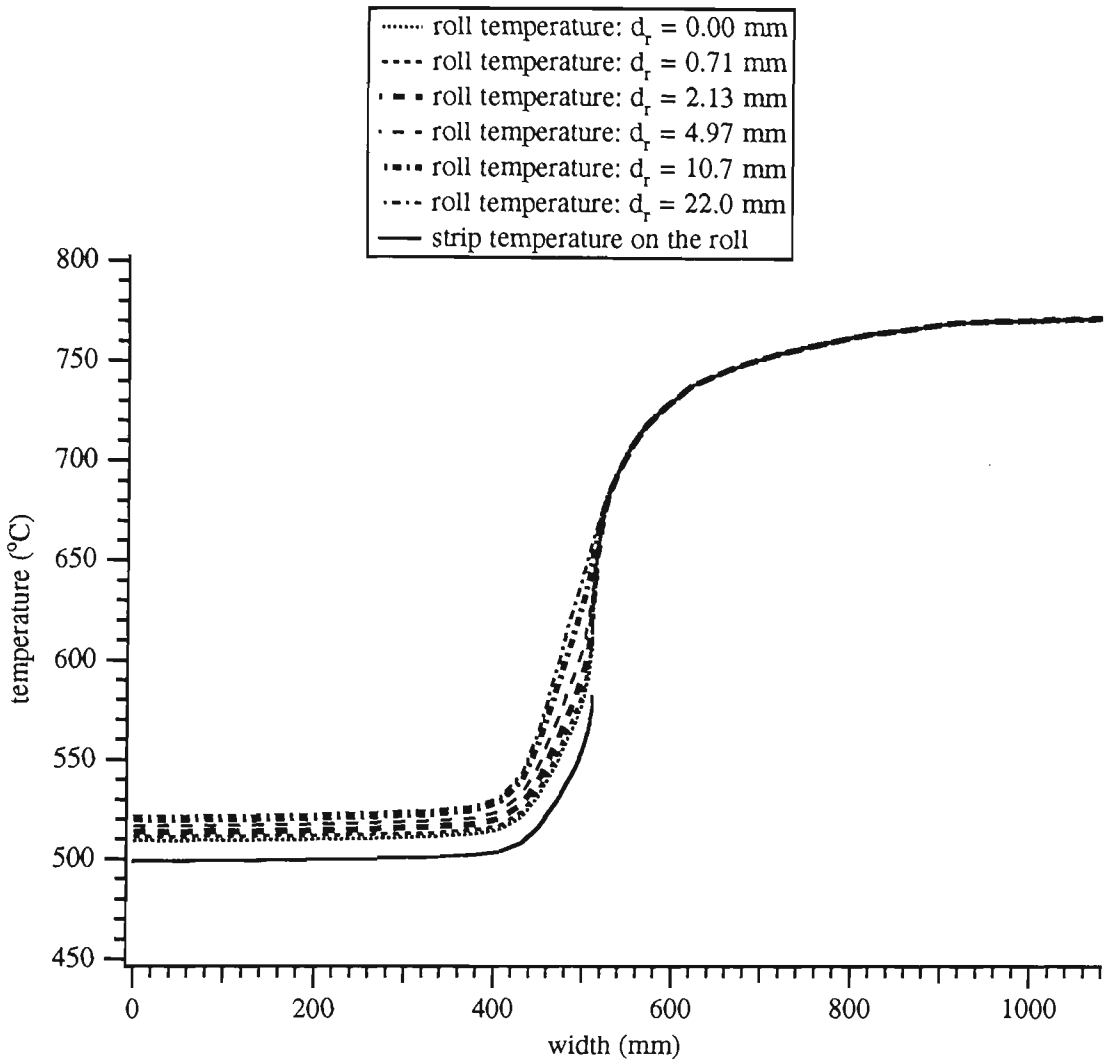

Figure 5.22: Increasing width, higher roll temperature — 18 s after width change

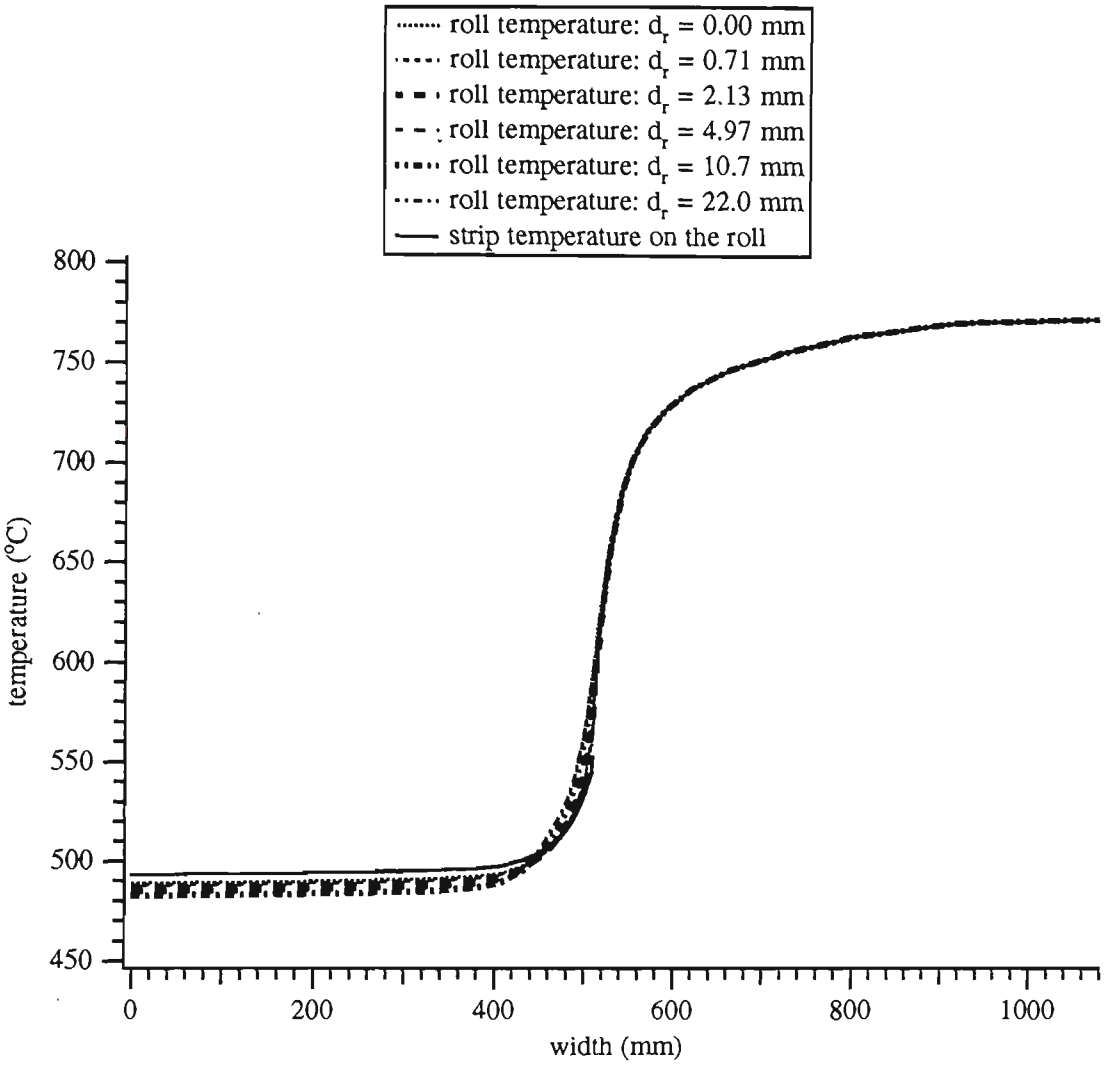

Figure 5.23: Increasing width, higher roll temperature — 118 s after width change

the fastest response at the roll surface. The consequence of this coupling is that the strip profile not only includes a peak at the strip edge, but the strip temperature in the region straddling the old and new strip width (between 900 and 1020 mm) is also higher than normal. This means that not only is the region of the strip within 30 mm or so of the edge at a possibly different metallurgical state, but so is the region that extends to the point corresponding to the old strip width. The edges themselves are also seen to be gaining a substantial amount of heat via conduction over the strip edges from the roll outside of it, as well as from the coupling with the roll underneath it. The equilibration is still found to be occurring 18 seconds later in Figure 5.22, and it is nearly completed about two minutes after the width change according to Figure 5.23. The line speed over this period is about 70 metres per minute, so if it takes two minutes for the strip profile to return to 'normal', then it is possible that over 100 m of defective steel has been produced.

The final example is in the case of a strip width increase over a region of the roll that is at a lower temperature. The data set *mrl34.dat* is used in this case and the values are initialised from 3060 s into the data set, in which the roll is cooler than the strip. The width increase from 1210 mm to 1550 mm occurs at 3668 s into the data set. In this example, 29 points across the strip and 55 points across the roll were chosen. This arrangement positioned a grid point at 598.2 mm from the centre, which is shown to retain the old roll temperature profile well. The initial strip profile is shown in Figure 5.24 and is similar to that previously shown before a weld change as in Figure 5.16. The next graph (Figure 5.25) shows the profile just half a second after the weld change passes the roll. The line speed is 60 metres per minute and the gas flows remain unchanged for the period examined here. The strip thickness is 1.5 mm, changing to 0.9 mm 20 seconds later (another example of the problems with the data sets — the width and thickness should change simultaneously).

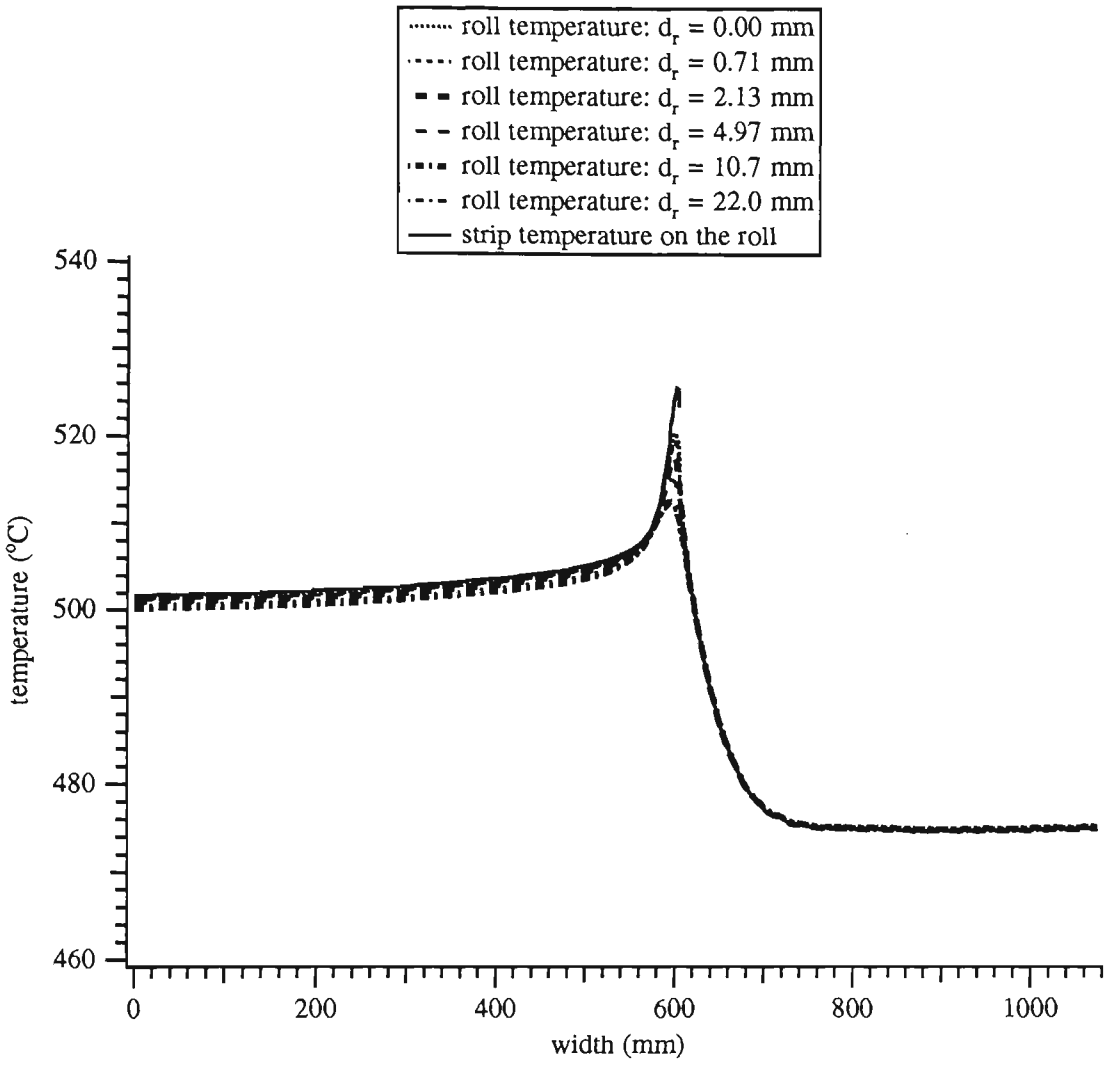

Figure 5.24: Increasing width, lower roll temperature — before width change

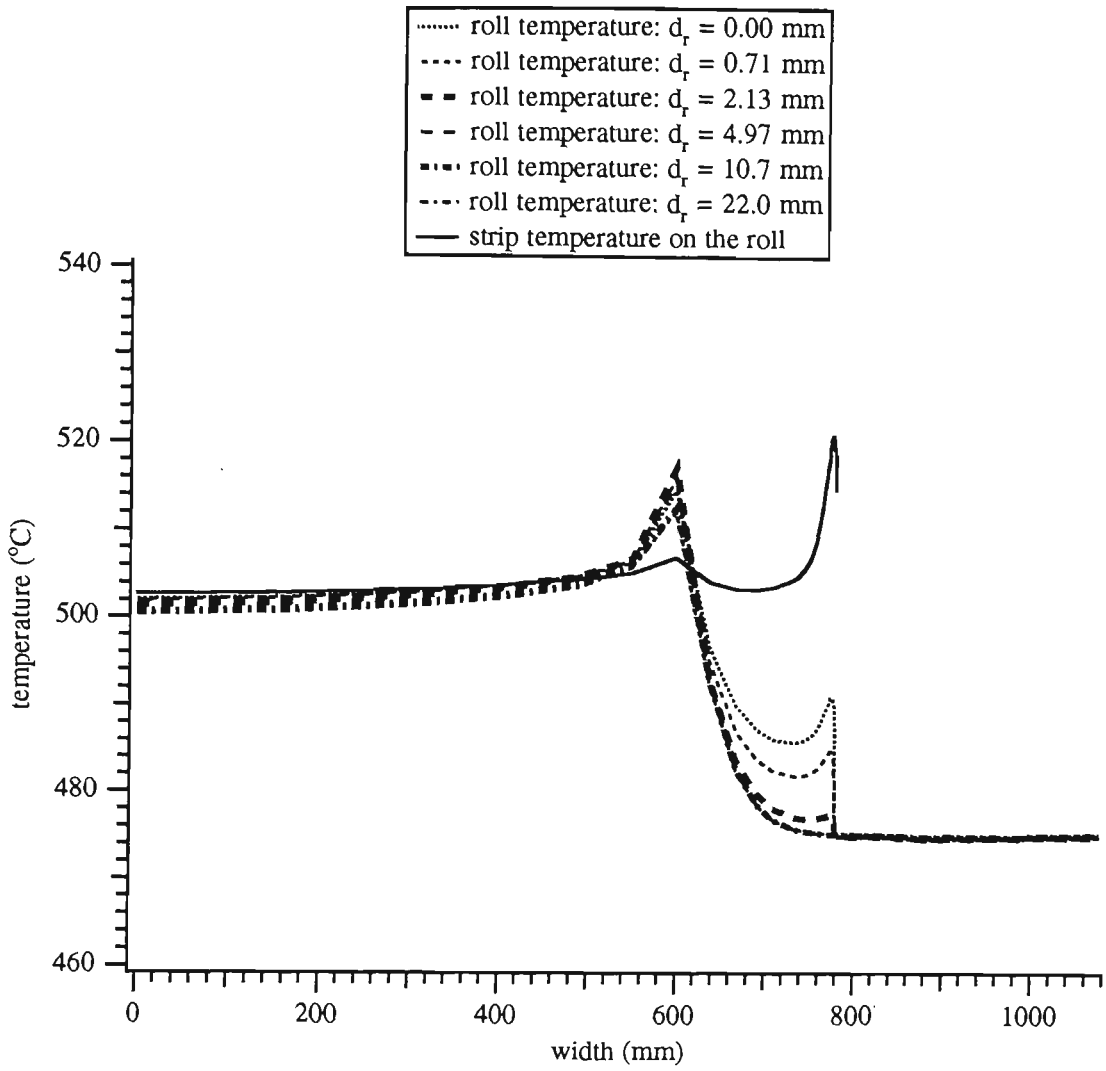

Figure 5.25: Increasing width, lower roll temperature — 0.5 s after width change

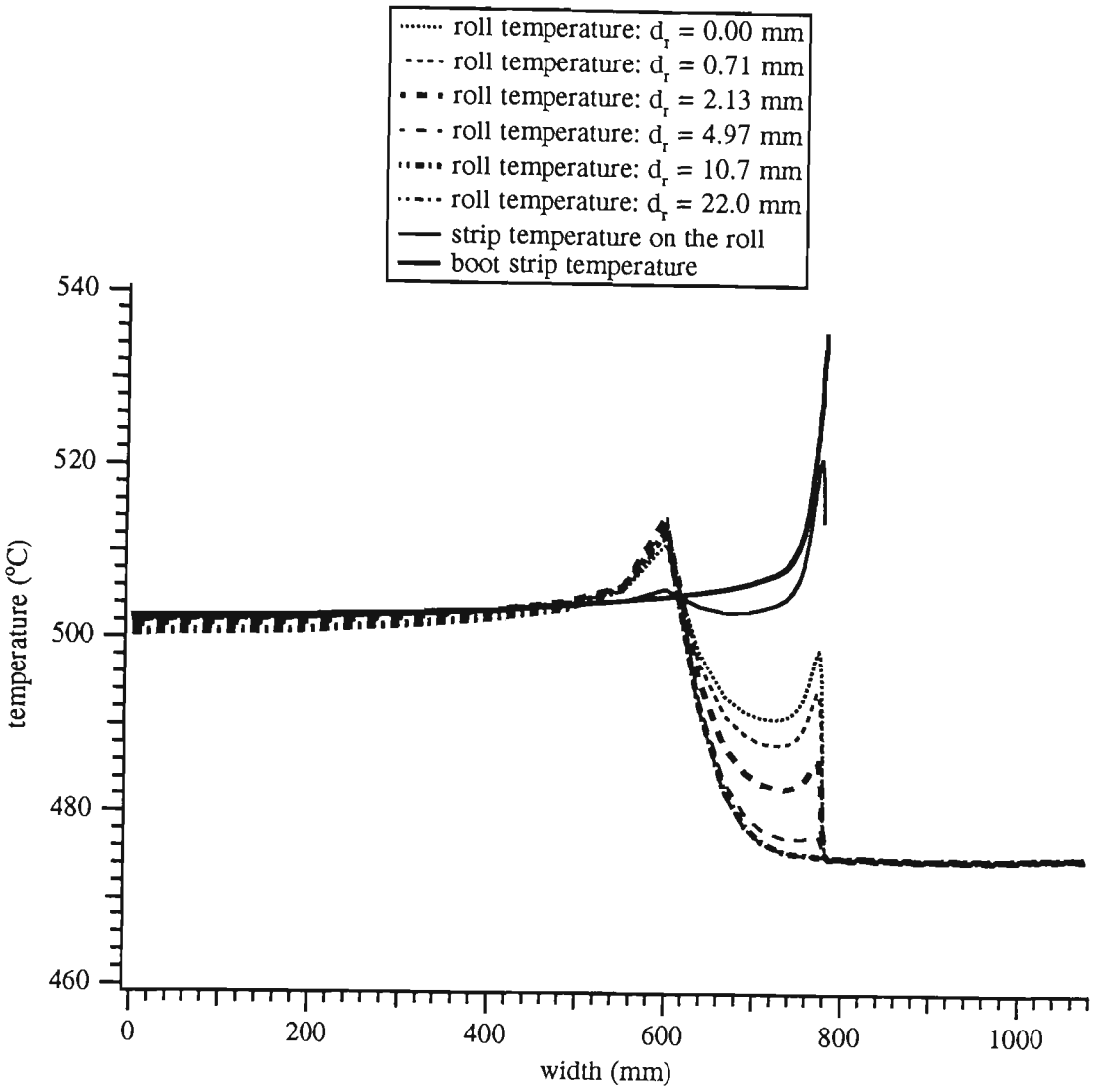

Figure 5.26: Increasing width, lower roll temperature — 2 s after width change

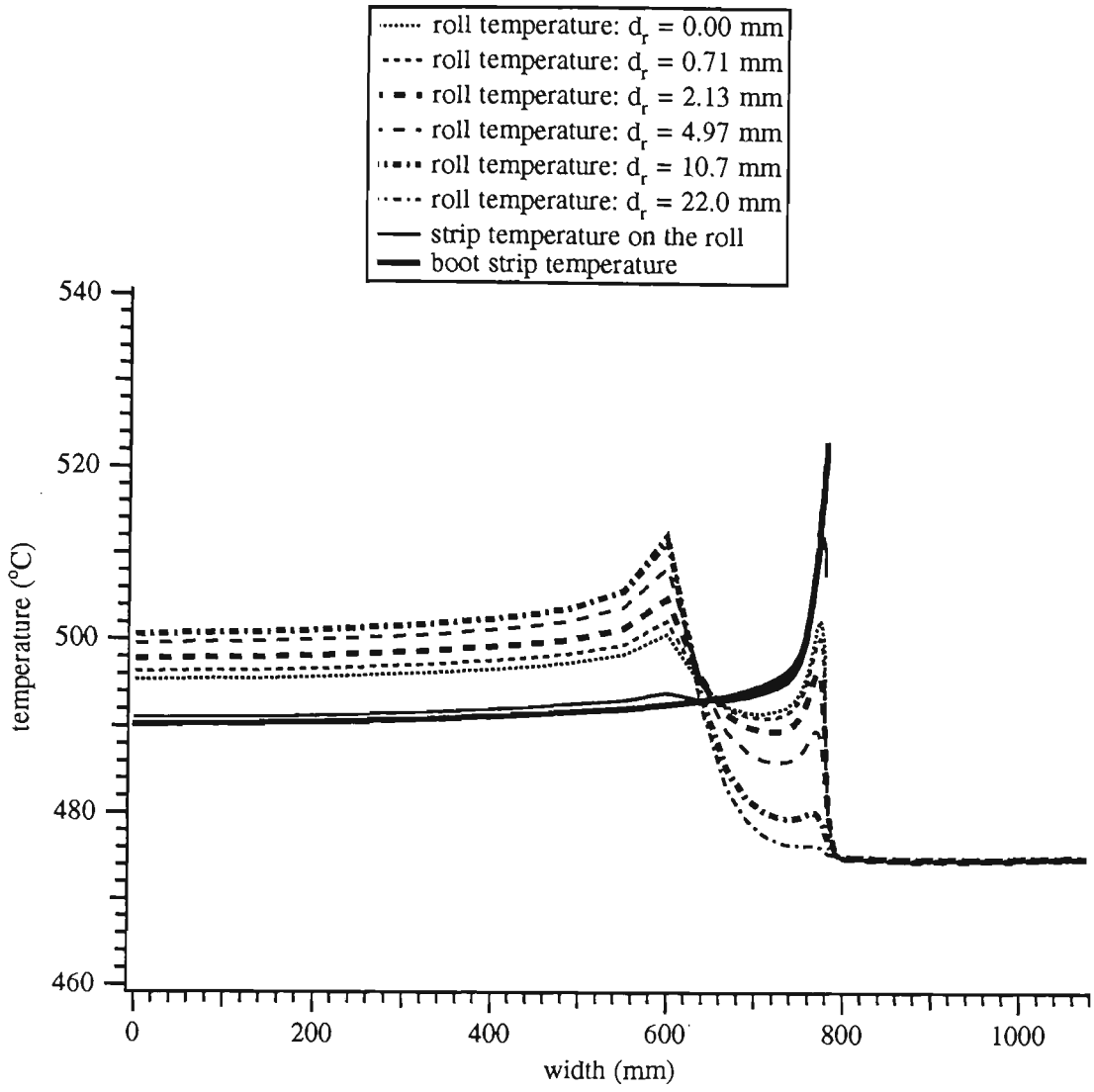

Figure 5.27: Increasing width, lower roll temperature — 12 s after width change

The results from this case are very interesting. The strip now physically covers the old peak in the roll temperature, and the advection onto the strip in the furnace means that the edge strip profile is also similar, but with a deeper dip at the very edge because of the conductive effect there. At the same time, the presence of the strip over a previously uncovered section of the roll causes a rapid equilibration of the strip and the roll in this newly coupled section. Perhaps the most peculiar effect is at the point where the old strip edge was. Again there is equilibration occurring between the strip and the roll, but it is in such a way that the result is the double peak in the strip seen in Figure 5.25. The strip temperature has therefore been raised by the coupling at the point of the previous strip edge, and lowered by the coupling at the points in between the old and new edge. Evidence of the peak is still seen in Figures 5.26 and 5.27 taken 2 s and 12 s after the weld change respectively, although the extra peak appears to die out quickly with the rapid coupling. Immediately after this, a large increase occurs in the centreline strip temperature, primarily caused by the strip thickness decrease. Therefore, further comparisons were not possible with this data set, so it is not known how long the influence of the double peak lasts. From the graphs shown, it appears that the double peak would subside fairly rapidly due to the heavy coupling between the strip and the roll.

Also included in Figures 5.26 and 5.27 is the boot strip temperature, taken respectively 0.5 and 10.5 seconds after the weld change, when the piece of strip shown contacting the roll in these diagrams was at the boot. These graphs show the coupling effect between the roll and the strip. The negligible gas flow in the boot section also causes the edge temperature to decrease slightly — in this example, it results in a drop of around 5 K before the strip contacts the roll. The rest of the decrease, as well as the peak in the strip temperature on the roll, is caused by the coupling effect.

The consequence of these results is that the strip region corresponding to the old strip width may be hotter than the parts of the strip directly around it. This could also cause metallurgical deficiencies in the strip if the temperatures are in the critical region near the recrystallisation temperature. The situation could arise that there is an 'island' of steel a certain distance in from the edge that has been treated differently to the rest of the steel. This would mean that that entire section of strip would have to be scrapped.

These results show that care obviously needs to be taken when treating the strip in the furnace. The measured and controlled centreline strip temperature should be set to ensure an adequate safety margin under normal processing conditions (except perhaps, during cycle changes), and the temperature should be kept low enough or high enough to ensure that the metallurgical property of the steel at the edges is not too different from that elsewhere.

It should also be mentioned briefly that the other two rolls located in the bridge section of the furnace have similar temperature profiles in the cases just described, although the temperatures found there are much lower than at the boot. Therefore the metallurgical implications are not as significant for the bridge rolls. The profile quickly dies out as the strip travels through the bridge because of the absence of gas flow.

5.7 Summary

This chapter of the thesis has examined the temperature differences at the edges of the strip and the mechanisms which cause these differences. In summary:

- the extra surface area at the strip edge, when exposed to heating in the furnace, results in significantly higher temperatures at the edge, where

the temperature rise depends on the amount of heat available in the furnace;

- the effect of the decrease in strip thickness across its width (edge drop) also has a significant effect on the strip edge temperature, in proportion to the percentage change in thickness from the centre to the edge;

- the side walls do not affect the edge strip temperature in a significant way, although this may be a deficiency of the model; and

- the rolls, especially the boot roll, can have quite a sizeable impact on the edge temperature, especially when a change in the strip width occurs, both in increasing or damping the edge temperature. This effect can occur over an area that relates to the location of the old and new strip edges (in the case of a strip width increase).

During the investigation of the edge effects, it was found that the centreline strip temperatures derived using these models of the edge effects differ by a maximum of 15 K from the centreline temperatures obtained in the 1-D strip model of Chapter 4. Because of the very large increase in computational time caused by the extensions to the model, with the small differences in the centreline strip temperatures that result, it may be advisable to have two separate models — one to determine the centreline strip temperature, and one for the edge temperature. This would save a substantial amount of time if the edge analysis was unnecessary for some reason.

Chapter 6

Conclusion

This thesis has involved the development and implementation of mathematical models for steel processing furnaces found on some of BHP Steel's continuous galvanising lines. Of course, the models are by no means complete, and further work can be done to improve them. For example, the derivation of more accurate values for some of the heating parameters, such as strip and gas emissivity, would enable more accurate testing of the models. At present, these values are, at best, educated guesses, but even a slight change, especially in the strip emissivity, was found to change significantly the results of the strip temperature in the models. For the radiant tube furnace, an analysis of the strip edge temperature there could produce some interesting results. The walls are very hot everywhere in the RTF, and the exposure of the edge to radiation, as well as the edge drop effect and the presence of six hot participating turn-around rolls, could be expected to affect the edge temperature. A more detailed off-line RTF model could be developed also, with a resultant greater emphasis on accuracy. This could include a separation of the tubes and the wall, and an increase in the number of grid points with the incorporation of finite-difference methods to solve the equations more accurately. Using implicit finite-difference methods should increase the stability range and hence the run-time of the

model of the edge effects, which would be advantageous. If this is done, a much finer grid could be used to obtain better resolution of the variation in the roll and strip temperature, although computation time would still be reasonably large.

To summarise the thesis: the original direct-fired furnace model for CGL2 was found to be in good agreement with the experimental data that was available at the time. The on-line radiant tube furnace model for MCL6 was reasonably accurate, while the use of an in-built filtering mechanism acted to further reduce errors during the run-time — indeed, the model is to be implemented by BHP as part of their control strategy for the whole MCL6 furnace section. When adapting the original CGL2 model to the direct-fired furnace on MCL6, an underprediction of the actual strip temperature occurred, but this adaptation allowed the model to be extended and tested in two dimensions across the strip. The final piece of work on the temperature differences across the strip showed that the edges can become substantially hotter than the middle; an effect which can have considerable repercussions on the metallurgical quality of the steel. This was caused mainly by the exposure to radiation of the extra surface area of the strip at the edge, and by the decrease in the thickness of the strip across the width. It was found that the boot roll also influenced the strip edge temperature markedly, especially during an increase in the strip width. The temperature profile between the positions of the old and new strip edge depends on whether the part of the roll newly covered by the strip was hotter or cooler than the strip before being covered. These results for the edges have important implications; they suggest an edge temperature consistently hotter than the centreline strip temperature, and that during width changes, the boot roll can influence an even larger area of the strip than just the edge.

Appendix A

Nomenclature

Symbols - English alphabet.

A	surface area (m^2)
B	radiosity (W m^{-2})
C	roll conductance (W m^{-2} K^{-1})
c	Courant number
c_p	specific heat (J kg^{-1} K^{-1})
d	thickness (m)
D_H	hydraulic diameter (m)
F	radiation shape factor
H	convection coefficients in Q_{gs} and Q_{gw} (W m^{-1} K^{-1})
h	enthalpy (J kg^{-1})
h	heat transfer coefficient (W m^{-2} K^{-1})
k	thermal conductivity (W m^{-1} K^{-1})
l	length (m)
m	mass (kg)
$\dot{m}$	mass flow rate (kg s^{-1}) [m^3 hr^{-1} in Chapter 3]
$\dot{M}$	addition rate of combusted gas (kg m^{-1} s^{-1})
Nu	Nusselt number

P	perimeter (m)
Pr	Prandtl number
q	heat flow rate (W) [W m^{-2} in section 2.2]
$q_{\_,c}$	convective heat flux to surface '_' (W m^{-2})
Q	heat flow rate per unit length (W m^{-1})
Re	Reynolds number
s	diffusion number
T	temperature (K)
t	time (s)
V	velocity (m s^{-1})
w	width (m)

x	furnace co-ordinate (parallel to strip flow) (m)
y	furnace co-ordinate (perpendicular to strip flow) (m)
z	furnace co-ordinate (into the wall) (m)
R	furnace co-ordinate (into the roll) (m)

Symbols - Greek alphabet.

α	absorptivity
δ	penetration distance (m)
ε	emissivity
κ	thermal diffusivity (m^2 s^{-1})
μ	dynamic viscosity (kg m^{-1} s^{-1})
ν	multiple change in grid spacing
ρ	density (kg m^{-3})
ρ	reflectivity
σ	Stefan-Boltzmann constant ($5.67 * 10^{-8}$ W m^{-2} K^{-4})

τ	transmissivity
α, β, γ	radiation coefficients in Q_{gs} (W m^{-1} K^{-4})
μ, ν, ξ	radiation coefficients in Q_{gw} (W m^{-1} K^{-4})

All other symbols used that are not denoted here are explained where they occur.

Subscripts.

a	air
ad	at adiabatic flame temperature
$comb$	combustion
f	furnace
g	gas
r	roll
s	strip
se	strip edge
sf	strip face
w	wall
we	side-on wall
wf	front-on wall
in	into the furnace (RTF)
out	out from the furnace via wall conduction (RTF)
$waste$	out from the furnace via waste gases (RTF)
j	grid point in x-direction
k	grid point in y-direction
l	grid point in z-direction
m	grid point in R-direction
n	time step (superscript)

Combinations of any of these signifies a transfer from one to the other. For example, B_{gs} denotes the radiosity from the gas to the strip; $F_{we,wf}$ is the shape factor from the side-on wall to the front-on wall, and so on.

Furnace name abbreviations.

All for continuous coating lines run by BHP Steel Sheet & Coil Products Division.

ZAL1	ZINCALUME Line No. 1
CGL2	Continuous Galvanising Line No. 2
DCL3	Dual Coating Line No. 3
ZAL4	ZINCALUME Line No. 4
ZAL5	ZINCALUME Line No. 5
MCL6	Metal Coating Line No. 6

Appendix B

Values of various parameters

Most functions used in this thesis for parameters such as the emissivity and specific heat are taken from Martire [28], and Stone & Morrison [51]. Those taken from the general literature are shown below.

Strip

Thermal Conductivity (W m^{-1} K^{-1}) (Weast [61]), T_s in K :

$$k_s = 4.1978 * 10^{-5} T_s^2 - 0.12099 T_s + 112.27. \tag{B.1}$$

Roll

Emissivity (Touloukian [56]), T_r in K :

$$\varepsilon_r = 0.11225 + 1.9679 * 10^{-4} T_r - 5.4596 * 10^{-8} T_r^2. \tag{B.2}$$

Specific Heat (J kg^{-1} K^{-1}) (Peckner & Bernstein [38]), T_r in K :

$$c_{pr} = 419.27 + 0.44914 T_r - 2.6382 * 10^{-4} T_r^2. \tag{B.3}$$

Thermal Conductivity (W m^{-1} K^{-1}) (Peckner & Bernstein [38]), T_r in ^{o}C :

$$k_r = 11.714 + 1.0597 * 10^{-2} T_r + 1.4019 * 10^{-6} T_r^2. \tag{B.4}$$

Bibliography

[1] N. G. Barton (ed.), *Proceedings of the 1990 Mathematics-in-Industry Study Group*, CSIRO Australia, 1990, p1-14.

[2] T. Baumeister (ed. in chief), *Marks' Standard Handbook for Mechanical Engineers*, 9th edition, McGraw-Hill, New York, 1987.

[3] F. G. Blottner & P. J. Roache, *Nonuniform Mesh Systems*, J. Comp. Phys., **8**, 1971, p498-499.

[4] M. Buffenoir, J. Giusti, G. Bonavia, G. Hurel, J.-N. Pezant & G. Roux, *Sollac FOS Hot Strip Mill : New Developments in Dimensional Control - An Integrated Approach*, in *5th International Rolling Conference, Dimensional Control in Rolling Mills*, The Institute of Metals, London, 1990, p198-204.

[5] J.-J. Campas, S. Terreaux, L. Vermot des Roches, D. Janczak & B. Bonvier, *New On-Line Gauge for Edge Drop Measurement. Effect of Tapered Work Rolls on a Pilot Mill and Tandem Cold Mill*, in *METEC Congress 94. 2nd European Continuous Casting Conference. 6th International Rolling Conference*, Vol 2, Düsseldorf, 1994, p273-280.

[6] K. S. Chapman, S. Ramadhyani & R. Viskanta, *Modeling and Analysis of Heat Transfer in a Direct-Fired Batch Reheating Furnace,* in *Heat Trans-*

fer Phenomena in Radiation, Combustion and Fires, ASME HTD v106, New York, 1989, p265-274.

[7] K. S. Chapman, S. Ramadhyani & R. Viskanta, *Modeling and Parametric Studies of Heat Transfer in a Direct-Fired Continuous Reheating Furnace,* Metall. Trans. B., **22B**, August 1991, p513-521.

[8] H. J. Crowder & C. Dalton, *Errors in the Use of Nonuniform Mesh Systems,* J. Comp. Phys., **7**, 1971, p32-45.

[9] P. Docherty & R. J. Tucker, *The influence of wall emissivity on furnace performance,* J. Inst. Energy, **35**, March 1986, p35-37.

[10] V. G. Goman & V. E. Krivosheev, *Influence of Position of Radiant Tubes in Furnace on Uniformity of Charge Heating*, Steel in the USSR, **19**, Jan 1989, p43-45.

[11] T. R. Goodman, *Applications of integral methods to transient non-linear heat conduction*, in *Advances in Heat Transfer*, T. F. Irvine & J. P. Hartnett (eds.), **1**, Academic Press, Orlando, 1964, p51-122.

[12] G. C. Goodwin & K. S. Sin, *Adaptive Filtering Prediction and Control*, Prentice-Hall, Englewood Cliffs, 1984.

[13] R. F. Harder, S. Ramadhyani & R. Viskanta, *Evaluation and Modeling of Gas-Fired Radiant Tubes*, in *ASME Proceedings of the 1988 National Heat Transfer Conference*, ASME HTD v96, ASME, New York, 1988, p67-77.

[14] *Heat Cleaning Steel Strip Continuously,* Heat Technology, Fall 1979, p6-10.

[15] F. B. Hildebrand, *Finite-Difference Equations and Simulations*, Prentice-Hall, Englewood Cliffs, 1968.

[16] J. P. Holman, *Heat Transfer, SI Metric Edition*, McGraw-Hill, Singapore, 1989.

[17] H. C. Hottel & A. F. Sarofim, *Radiative Transfer*, McGraw-Hill, New York, 1967.

[18] M. Imose, *Heating and Cooling Technology in the Continuous Annealing*, Trans. ISIJ, **25**, 1985, p911-932.

[19] IMSL Math/Library, FORTRAN Subroutines for Mathematical Applications, Version 1.1, IMSL, December 1989.

[20] A. S. Jamaluddin & W. A. Fiveland, *Radiative Transfer in Multi-Dimensional Enclosures with Specularly Reflecting Walls*, in *Radiation Heat Transfer: Fundamentals & Applications*, ASME HTD v137, ASME, New York, 1990, p95-100.

[21] S. Kanetoh, S. Iwadoh, N. Matsui, M. Yamasaki, A. Honda & Y. Kuze, *The Equipment and Operation of NKK Fukuyama No. 3 CAL,* NKK Tech. Rev., **56**, 1989, p49-57.

[22] E. E. Khalil, P. Hutchinson & J. H. Whitelaw, *The Calculation of the Flow and Heat-Transfer Characteristics of Gas Fired Furnaces*, in 18^{th} *Symposium (International) on Combustion*, The Combustion Institute, Pittsburgh, 1981, p1927-1938.

[23] E. E. Khalil & J. S. Truelove, *Calculation of Radiative Heat Transfer in a Large Gas-Fired Furnace*, Letters in Heat and Mass Transfer, **4**, 1977, p353-365.

[24] V. N. Khloponin, E. I. Latukhin & S. A. Burlakov, *Transverse temperature profile of strips*, Steel in the USSR, **16**, March 1986, p135-136.

[25] K. Kitamura, I. Yarita, N. Suganuma, T. Nakanishi & K. Toyoshima, *Edge-Drop Control of Hot and Cold Rolled Strips by a Tapered-Crown Work Roll Shifting Mill*, Kawasaki Steel Technical Report, Number 27, November 1992, p5-12.

[26] J. Larkiola, J. Nylander & A. S. Korhonen, *Experiments on the Modelling of Profile in the Cold Rolling of Strips*, in *1st International Conference on Modelling of Metal Rolling Processes*, The Institute of Metals, London, 1993, p462-474.

[27] P. Mäntylä, R. Korhonen & N.-G. Jonsson, *Improved Thickness and Shape Accuracy with Advanced Pass Scheduling in Plate Rolling*, Journal of Materials Processing Technology, **34**, 1-4, September 1992, p255-263.

[28] B. Martire, *Program Documentation and Users Guide: Model for Steady-State Heat Transfer in the Selas Furnace,* BHP Steel, Coated Products Division, Research & Technology Centre, Report No. 1100, July 1991.

[29] E. A. Mizikar & E. A. Upton, *Thermal and Metallurgical Optimization of a Continuous Galvanizing Process*, presented at the AIME Annual Meeting, February 22-26, 1976, 31pp.

[30] P. R. Mould, *An Overview of Continuous Annealing Technology for Steel Sheet Products,* J. Metals, May 1982, p18-28.

[31] NAG Fortran library manual, Mark 11, Numerical Algorithms Group, Oxford, 1984.

[32] M. Nakayama, K. Sekiguchi, M. Yamazaki, H. Yoshida, M. Abe & Y. Ise, *Application of Direct Fired Furnace to NKK-CAL/CGL,* NKK Tech. Rev., **64**, 1992, p8-14.

[33] B. J. Noye, *Finite-Difference Methods for Partial Differential Equations,* Honours Applied Mathematics Course Notes, University of Adelaide, 1990, 290pp.

[34] W. J. Ottersbach, *Hot-dip galvanizing line with vertical annealing furnace,* Metall. Plant and Tech. Int., **4**, 1991, p132-144.

[35] D. Ozaki, F. Fujita, S. Iwadoh & T. Sharyoh, *A Technology for Minimizing the Feather Edge in Cold Rolling by Utilization of Work Roll Shifting Mill,* in *5th International Rolling Conference, Dimensional Control in Rolling Mills*, The Institute of Metals, London, 1990, p270-277.

[36] M. N. Özişik, *Boundary Value Problems of Heat Conduction*, International Textbook Company, Scranton, 1968.

[37] Ph. Paulus, J. Mignon & P. Laval, *Flexible Continuous Annealing : An European Answer to Intricate Product Mixes*, in *Hot & Cold-Rolled Sheet Steels*, R. Pradhan & G. Ludkovsky (eds.), The Metallurgical Society, 1988, p73-94.

[38] D. Peckner & I. M. Bernstein (eds.), *Handbook of Stainless Steels*, McGraw-Hill, New York, 1977.

[39] V. A. Pikashov & V. A. Velikodnyy, *Effect of the Emissive Properties of the Surface on the Effective Radiation in Various Heat Transfer Models*, Heat Transfer - Soviet Research, **19**, 4, July-August 1987, p110-118.

[40] A. Prothero, *Computing with Thermochemical Data*, Combustion & Flame, **13**, Aug 1969, p399-408.

[41] H. Ramamurthy, S. Ramadhyani & R. Viskanta, *Modeling of Heat Transfer in Indirectly-Fired Batch Reheating Furnace*, in *ASME/JSME Thermal Engineering Proceedings*, Volume 5, ASME, New York, 1991, p205-215.

[42] H. Ramamurthy, S. Ramadhyani & R. Viskanta, *Modeling of Heat Transfer in Indirectly-Fired Continuous Reheating Furnace*, in *Transport Phenomena in Materials Processing*, ASME HTD v146, ASME, New York, 1990, p37-46.

[43] R. D. Richtmyer & K. W. Morton, *Difference Methods for Initial-Value Problems*, Second Edition, Interscience Publishers, New York, 1967.

[44] G. F. C. Rogers & Y. R. Mayhew, *Engineering Thermodynamics: Work and Heat Transfer*, 2nd edition, Longman Group Ltd., London, 1967.

[45] K. Sekiguchi, N. Gunji, Y. Ise, M. Shoji, K. Araki & M. Ogawa, *New Technology and Products of No. 3 Continuous Galvanizing Line at Keihin Works,* Nippon Kokan Tech. Rep., Overseas No. 40, 1984, p17-27.

[46] R. Siegel & J. R. Howell, *Thermal Radiation Heat Transfer*, 2nd edition, Hemisphere Publishing Corp., Washington, 1981.

[47] R. R. Somers & G. T. Pallone, *Verification of a Heat-Transfer Model for Predicting Strip Temperature in a Continuous Furnace*, Iron and Steel Engineer Year Book, 1970, p503-507.

[48] R. R. Somers, G. T. Pallone & E. J. Patula, *A Heat Transfer Model for Predicting Strip Temperature*, Iron and Steel Engineer Year Book, 1969, p510-513.

[49] T. H. Song & R. Viskanta, *Interaction of Radiation with Turbulence: Application to a Combustion System*, J. Thermophysics & Heat Transfer, **1**, 1, Jan 1987, p56-62.

[50] T. H. Song & R. Viskanta, *Prediction of the Thermal Performance of an Industrial Natural Gas-Fired Furnace*, Gas Wärme Int., **37**, 1, Jan-Feb 1988, p22-30.

[51] P. Stone & B. Morrison, *MCL6 Control Project Progress Report*, The Broken Hill Proprietary Co. Ltd., Feb 1993, Confidential.

[52] K. Taya, I. Ueda & M. Honjoh, *Development of the Strip Temperature Control Technique for a Continuous Annealing Line*, in *Developments in the Annealing of Sheet Steels*, R. Pradhan & I. Gupta (eds.), The Minerals, Metals and Materials Society, Warrendale, 1992, p133-142.

[53] H. L. Taylor & J. D. Elliott, *Heat Transfer between Continuous Strip and a Roll*, in *Flat Rolled Products III*, E. W. Earhart (ed), Interscience Publishers, New York, 1962, p85-96.

[54] N. E. Thompson & B. Martire, *A Qualitative Study of the Selas Furnace,* BHP Steel, Coated Products Division, Research & Technology Centre, Report No. 993, May 1989.

[55] N. E. Thompson & B. Martire, *Steady-State Equations for the Selas Furnace. I. Derivation,* BHP Steel, Coated Products Division, Research & Technology Centre, Report No. 1003, June 1989.

[56] Y. S. Touloukian (ed.), *Thermophysical Properties of High Temperature Solid Materials. Volume 3 : Ferrous Alloys*, Macmillan, New York, 1967.

[57] R. J. Tucker & R. Lorton, *Mathematical Modelling of Load-Recuperative Gas-Fired Furnaces*, in *Institute of Chemical Engineers Symposium Series No. 86*, 1984, p1035-1046.

[58] F. G. van Dongen, *Heat Transfer in Gas-Fired Furnaces. A Semi-Empirical Model Combining the Zone Method for Radiation and an Integral Technique for the Flow Pattern*, J. Inst. Energy, **56**, 429, Dec 1983, p184-190.

[59] L. Vermot des Roches & D. Janczak, *An Elementary Approach of the Numerical Modelling of the Edge Drop Effect in Cold Rolling of Strips*, in *5th International Rolling Conference, Dimensional Control in Rolling Mills*, The Institute of Metals, London, 1990, p79-88.

[60] R. Wang, *Direct-fired heating in continuous hot-dip galvanising lines*, Metall. Plant and Tech. Int., **4**, 1991, p126-130.

[61] R. C. Weast (ed.), *CRC Handbook of Chemistry and Physics*, 62nd edition, CRC Press, Boca Raton, 1981-82.

[62] K. Yahiro, H. Shigemori, K. Hirohata, T. Ooi, M. Haruna & K. Nakanishi, *Development of Strip Temperature Control System for a Continuous Annealing Line*, in *Proceedings of the IECON '93. International Conference on Industrial Electronics, Control and Instrumentation*, Volume 1, IEEE, New York, 1993, p481-486.

[63] N. Yoshitani, *Modelling and Parameter Estimation for Strip Temperature Control in Continuous Annealing Processes*, in *Proceedings of the IECON '93. International Conference on Industrial Electronics, Control and Instrumentation*, Volume 1, IEEE, New York, 1993, p469-474.

[64] W. Y. D. Yuen, 1994, private correspondence.

[65] P. del C. Zambrano & R. Colás, *Profile and Shape Evolution During Hot Rolling of Steel Strip*, in *1st International Conference on Modelling of Metal Rolling Processes*, The Institute of Metals, London, 1993, p502-510.

Publications of the author

1. D. O. Marlow, *A Transient Model for Annealing Furnace Operation,* Fifth Australian Heat & Mass Transfer Conference, The University of Queensland, Brisbane, Qld, 6-9 Dec 1993, preprints of papers, p 32-1 to 32-6.

2. D. O. Marlow, *Modelling Direct-Fired Furnaces for Transient Operations,* Applied Mathematical Modelling; accepted 23 Nov 1994.

3. D. O. Marlow, B. R. Morrison & P. M. Stone, *An on-line mathematical model for a radiant tube furnace,* in preparation.

4. D. O. Marlow, *Analysis of the temperature variation across steel strip during heat treatment in a direct-fired furnace,* in preparation.

Papers 1 and 2 contain work included in Chapter 2 of this thesis. Paper 3 is derived from Chapter 3, and paper 4 summarises the work of Chapter 5.